Rare Event Estimation and Robust Optimization Methods with Application to ORC Turbine Cascade

Nassim Razaaly

NNT : 2019SACLX027

THÈSE DE DOCTORAT

de

L'UNIVERSITÉ PARIS-SACLAY

École doctorale de mathématiques Hadamard (EDMH, ED 574)

Établissement d'inscription : École polytechnique

Laboratoire d'accueil : Centre de mathématiques appliquées de Polytechnique, UMR 7641 CNRS

Équipe : EPC INRIA DEFI

Spécialité de doctorat : Mathématiques appliquées

Nassim RAZAALY

Rare Event Estimation and Robust Optimization Methods with Applications to ORC Turbine Cascade

Thèse présentée et soutenue publiquement à Palaiseau, *le* 12 Juillet 2019

Devant le jury composé de MM.

Paola CINNELLA,	Professeur, ENSAM	Président
Pietro Marco CONGEDO,	Chargé de Recherche, INRIA	Directeur de thèse
Omar KNIO,	Professeur, KAUST	Examinateur
Olivier LE MAÎTRE,	Directeur de Recherche, CMAP-CNRS	Examinateur
Francesco MONTOMOLI,	Professeur, Imperial College London	Rapporteur
Fabio NOBILE	Professeur, École polytechnique fédérale de Lausanne	Rapporteur
Giacomo PERSICO	Professeur, Politecnico di Milano	Examinateur

Abstract

This thesis aims to formulate innovative Uncertainty Quantification (UQ) methods in both Robust Optimization (RO) and Reliability-Based Design Optimization (RBDO) problems. The targeted application is the optimization of supersonic turbines used in Organic Rankine Cycle (ORC) power systems.

Typical energy sources for ORC power systems feature variable heat load and turbine inlet/outlet thermodynamic conditions. The use of organic compounds with a heavy molecular weight typically leads to supersonic turbine configurations featuring supersonic flows and shocks, which grow in relevance in the aforementioned off-design conditions; these features also depend strongly on the local blade shape, which can be influenced by the geometric tolerances of the blade manufacturing. A consensus exists about the necessity to include these uncertainties in the design process, so requiring fast UQ methods and a comprehensive tool for performing shape optimization efficiently.

This work is decomposed in two main parts. The first one addresses the problem of rare events estimation, proposing two original methods for failure probability (metaAL-OIS and eAK-MCS) and one for quantile computation (QeAK-MCS). The three methods rely on surrogate-based (Kriging) adaptive strategies, aiming at refining the so-called Limit-State Surface (LSS) directly, unlike Subset Simulation (SS) derived methods. Indeed, the latter consider intermediate threshold associated with intermediate LSSs to be refined. This direct refinement property is of crucial importance since it enables the adaptability of the developed methods for RBDO algorithms. Note that the proposed algorithms are not subject to restrictive assumptions on the LSS (unlike the well-known FORM/SORM), such as the number of failure modes, however need to be formulated in the Standard Space. The eAK-MCS and QeAK-MCS methods are derived from the AK-MCS method and inherit a parallel adaptive sampling based on the weighted K-Means algorithm. MetaAL-OIS features a more elaborate sequential refinement strategy based on MCMC samples drawn from a quasi-optimal ISD. It additionally proposes the construction of a Gaussian mixture ISD, permitting the accurate estimation of small failure probabilities when a large number of evaluations (several millions) is tractable, as an alternative to SS. The three methods are shown to perform very well for 2D to 8D analytical examples popular in structural reliability literature, some featuring several failure modes, all subject to very small failure probability/quantile level ($O(10^{-5} - 10^{-9})$). Accurate estimations are performed in the cases considered using a reasonable number of calls to the performance function (15-150).

The second part of this work tackles original Robust Optimization (RO) methods applied to the Shape Design of a supersonic ORC Turbine cascade. A comprehensive Uncertainty Quantification (UQ) analysis accounting for operational, fluid parameters and geometric (aleatoric) uncertainties is illustrated, permitting to provide a general overview over the impact of multiple effects and constitutes a preliminary study necessary for RO. Then, several mono-objective RO formulations under a probabilistic constraint are considered in this work, including the minimization of the mean or a high quantile of the Objective Function. A critical assessment of the (Robust) Optimal designs is finally investigated.

Keywords Gaussian Processes • Failure Probability • Extreme Quantile • Robust Optimization • ORC Turbine • Geometric Manufacturing Variability

Acknowledgments

I first would like to express my deepest gratitude to my advisor, Pietro Marco Congedo for fruitful years of collaboration, guidance and financial support. I am greatly indebted to him for having introduced me to the academic world and convinced me to achieve this PhD. He gave me a lot of freedom, while constantly wisely coaching me, providing me research opportunities and yet he was always available to discuss new ideas.

I would like to thank my examiners Prof. Francesco Montomoli and Prof. Fabio Nobile for many insighful comments on the manuscript and for taking the time to read it. I would like to thank the members of my PhD committee for taking interest on my research work and for participating to the final oral examination.

I would like to thank Prof. Giacomo Persico, for having introduced me to the passionating world of design shape optimization for turbomachinery, starting from an intense discussion on the sidelines of my first conference.

I would like to thank Prof. Gianluca Iaccarino who permitted to make two rich visiting experiences at the CTR, Stanford, where I could benefit from his excellent academic knowledge. I would like to thank Daan Crommelin for have warmly welcomed me at CWI, and for the many interesting discussions we exchanged, typically starting from a question around a coffee and ending up in an hour long discussion next to his whiteboard.

Finally, I would like to thank my family for always supporting me through good and difficult times in the past years, and dedicate this manuscript to my mother.

Publications

Journal Papers

[-] **N. Razaaly**, G. Gori, G. Persico, P.M. Congedo, *Quantile-based robust optimization of a supersonic nozzle for Organic Rankine Cycle turbine*, Submitted, April 2019.
[-] **N. Razaaly**, D. Crommelin, P.M. Congedo, *A Efficient Kriging-Based Extreme Quantile Estimation suitable for expensive performance function*, Submitted, April 2019.
[-] **N. Razaaly**, P.M. Congedo, *Extension of AK-MCS for the efficient computation of very small failure probabilities*, Submitted, January 2019.

[1] **N. Razaaly**, G. Persico, P.M. Congedo, *Impact of geometric, operational, and model uncertainties on the non-ideal flow through a supersonic ORC turbine cascade*, Energy, Volume 169, Pages 213-227, 2019.
[2] **N. Razaaly**, P.M. Congedo, *Novel Algorithm using Active Metamodel Learning and Importance Sampling: application to multiple failure regions of low probability*, Journal of Computational Physics, Volume 368, Pages 92-114, 2018.
[3] **N. Razaaly**, G. Persico, P.M. Congedo, *Uncertainty Quantification of Inviscid Flows Through a Supersonic ORC Turbine Cascade*, Energy Procedia, Elsevier, Volume 129, Pages 1149–55, 2017.
[4] **N. Razaaly**, P.M. Congedo, *Computation of tail probabilities for non-classical gas-dynamic phenomena*, Journal of Physics: Conference Series, IOP Publishing, Volume 821, Number 1, 2017.

Proceedings

[1] **N. Razaaly**, G. Gori, G. Iaccarino, P.M. Congedo, *Optimization of an ORC supersonic nozzle under epistemic uncertainties due to turbulence models*, GPPS Zurich19, 2019.
[2] **N. Razaaly**, G. Gori, O. Le Maître, G. Iaccarino, P.M. Congedo, *Robust optimization of ORC turbine cascades operating with siloxane MDM*, CTR Proceedings of the Summer Program 2018.

International Conferences

[1] **N. Razaaly**, P.M. Congedo, *AK-MCS extension for the Efficient Estimation of Extreme Quantiles and Failure Probabilities*, UQOP 2019, Paris, France, March 2019.

[2] **N. Razaaly**, G. Gori, G. Iaccarino, P.M. Congedo, *Optimization of an ORC supersonic nozzle under epistemic uncertainties due to turbulence models*, GPPS 2019, Zurich, Switzerland, January 2019.
[3] **N. Razaaly**, P.M. Congedo, Efficient Computation of Rare Events: Failure Probability and Quantile, MATHIAS-Seminar Total 2018, Serris, France, October 2018.
[4] **N. Razaaly**, G. Persico, G. Gori, P.M. Congedo, Robust Optimization of a Supersonic ORC Turbine Cascade under a probabilistic constraint: a Quantile Formulation, NICFD 2018, Bochum, Germany, October 2018.
[5] **N. Razaaly**, G. Persico, G. Gori, P.M. Congedo, Robust Optimization of a Supersonic ORC Turbine Cascade: a Quantile-based Approach, MASCOT 2018, Roma, Italy, October 2018.
[6] **N. Razaaly**, G. Persico, G. Gori, P.M. Congedo, Robust Optimization of a Supersonic ORC Turbine Cascade: a Quantile-based Approach, ECFD 7 - 7th European Conference on Computational Fluid Dynamic, Glasgow, UK, June 2018.
[7] **N. Razaaly**, P.M. Congedo, An Efficient Reliability Analysis Tool for the Computation of Low Tail Probabilities and Extreme Quantiles in Multiple Failure Regions: Application to Organic Rankine Cycles, SIAM UQ 2018 - SIAM Conference on Uncertainty Quantification, Garden Grove, California, USA, April 2018.
[8] **N. Razaaly**, P.M. Congedo, Robust Optimization of ORC blades turbines under a low quantile constraint, ORC International Conference 2017 - 4th International Seminar on Organic Rankine Cycle Power System, Milano, Italy, September 2017.
[9] **N. Razaaly**, P.M. Congedo, A Gradient Based Local Multivariate Interpolation Regression Surrogate Model for scattered data sets, UNCECOMP 2017 - 2nd International Conference on Uncertainty Quantification in Computational Sciences and Engineering, Rhodes, Greece, June 2017
[10] **N. Razaaly**, P.M. Congedo, Computation of Tail Probabilities for non-classical Gasdynamic Phenomena: Rarefaction Shock Wave Experiment, NICFD 2016 for Propulsion and Power, Varenna, Italy, October 2016.

Seminar

[1] **N. Razaaly**, P.M. Congedo, Efficient Computation of Rare Events: Failure Probability and Quantile, CWI UQ Seminar, Amsterdam, Netherlands, January 2019.

Contents

List of Figures

List of Tables

Nomenclature

Simulation Tool/Engineering Systems

BOP Balance of Plant, page 14

CAD Computer-Aided Design, page 13

CAM Computer-Aided Manufacturing, page 13

CFD Computational Fluid Dynamics, page 24

DES Detached Eddy Simulation, page 14

EOS Equations of State, page 13

LES Large Eddy Simulation, page 14

NICFD Non-Ideal Compressible Fluid Dynamics, page 14

NRBC Non-Reflecting Boundary Conditions, page 136

ORC Organic Rankine Cycles, page 11

PRSV Peng-Robinson-Stryjek-Vera, page 3, , page 13

Reynolds-averaged Navier–Stokes, page 14

Soave-Redlich-Kwong, page 3, , page 13

Shear Stress Transport, page 135

Trailing Edge, page 141

Van der Waals, page 134

Waste Heat Recovery, page 12

lengthscales a.k.a. scales parameters, page 35

Artificial Neural Network, page 60

Best Linear Unbiased Predictor, page 30

Cross-Validation, page 37

Gaussian Processes, page 17

Leave-One-Out, page 38

Introduction en Français

–1 Contexte

Dans le secteur de l'énergie, la production d'énergie décentralisée suscite un regain d'intérêt. Étant donné que les sources renouvelables abondantes telles que la géothermie/solaire sont souvent caractérisées par de petites exploitations. Par conséquent, les centrales électriques de petite taille et de taille moyenne ($O(10^1-10^4)$ kW) pourraient jouer un rôle clé pour ces sources d'énergie. Parmi les technologies disponibles pour la conversion à haute efficacité de la puissance thermique en électricité dans cette plage de capacité, les ORC ont montré des avantages significatifs [Verneau, 1978, Angelino et al., 1984] en termes de fiabilité et de rentabilité. Les ORCs ont donc suscité un intérêt considérable de la part des milieux industriels et universitaires, en particulier en raison de sa capacité à récupérer de l'énergie mécanique à partir de sources de chaleur de qualité inférieure.

Le cycle de puissance Rankine est un cycle thermodynamique fermé présent dans toutes les centrales à vapeur classiques. Dans les ORC, similaires aux cycles à vapeur Rankine, le fluide de travail (eau) est remplacé par un fluide organique caractérisé par un poids moléculaire élevé. Dans sa forme de base, un ORC est constitué de quatre composants (Figure 2): évaporateur, turbine, condenseur, pompe.

Le fluide organique est pompé dans l'évaporateur, qui exploite une source de chaleur de faible teneur: le liquide sous pression est converti en vapeur surchauffée à pression constante. La nature rétrograde des fluides organiques typiques utilisés pour les ORC atténue le processus de surchauffe, qui n'a pas une importance cruciale dans les cycles à vapeur de Rankine classiques. Une turbine permet de détendre la vapeur chaude en convertissant la chute d'enthalpie en énergie mécanique (de rotation), puis en électricité en utilisant un générateur couplé à la turbine. La vapeur entre alors dans un condenseur qui, par transfert thermique avec la source froide (air ambiant, lac, etc...), le convertit en un état liquide. Le liquide basse pression est finalement dirigé vers la pompe d'alimentation, augmentant sa pression et en fermant le cycle thermodynamique. Dans la plupart des cas, un régénérateur est utilisé pour récupérer l'énergie

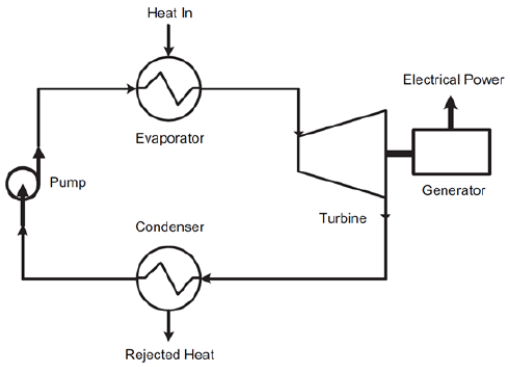

Figure 1 Illustration d'un ORC [Sauret and T Gu, 2014].

thermique de la vapeur sortant de la turbine. Les composés organiques permettent de convertir efficacement la chaleur à basse et moyenne température (à partir d'environ 90 °C) dans la plage de puissance faible à moyenne: leur chaleur de vaporisation, beaucoup plus faible que celui de l'eau offre un meilleur équilibre entre la trajectoire de chauffage du fluide de travail (organique) et celle de la source de chaleur qui refroidit (généralement de l'eau surchauffée ou huile), augmentant l'efficacité de la conversion [Karellas and Schuster, 2008, Larjola, 1995, Harinck, 2010].

Le bon choix du fluide organique par rapport à la température de la source de chaleur et à l'apport de chaleur entraînent une augmentation de la puissance de sortie ou des performances du cycle. Il est généralement choisi comme siloxane aromatique, fluorocarbure, fluorocarbone, hydrofluorocarbure ou chaîne droite [Curran, 1981, Angelino et al., 1984, Colonna, 1996, Angelino and Di Paliano, 1998]. La variété garantie par le large éventail de fluides organiques disponibles répond aux diverses exigences des dispositifs de conversion d'énergie thermique largement répandus [Macchi, 2017, Colonna et al., 2015]; ORC offre un grand potentiel d'utilisation de sources de chaleur externes durables, telles que l'énergie solaire, la géothermie, la biomasse ou même l'exploitation de chaleur perdue (WHR) (par exemple, centrales électriques en acier, camions). De telles sources présentent généralement des charges variables et, par conséquent, les conditions thermodynamiques à la sortie de la chaudière/entrée de la turbine subissent des variations importantes ; cette variation se combine également avec le changement saisonnier naturel de la température ambiante, qui pourrait modifier les conditions thermodynamiques du condenseur/sortie de turbine. Ces sources d'incertitude entraînent des différences considérables dans le fonctionnement de la turbine et, en particulier, une charge aérodynamique variable sur les cascades de la machine, réduisant potentiellement les performances de la turbine.

Une autre particularité du fluide organique a une incidence sur la conception de la turbine. D'une part, le processus d'expansion implique une faible diminution d'enthalpie spécifique, cette dernière étant inversement proportionnelle à la masse moléculaire élevée du fluide organique. Il permet l'adoption de turbines compactes et rentables composées d'un ou deux étages, sans tenir compte des problèmes liés à la vitesse de rotation élevée et aux pénalités d'efficacité qui en résultent [Angelino et al., 1984]. D'autre part, la combinaison de la faible vitesse du son et du taux d'expansion élevé par étage qui en résulte conduit généralement à des turbines transoniques ou supersoniques ORC, généralement soumises à de fortes ondes de choc et à des conditions d'écoulement bloquées. De plus, une partie du processus d'expansion peut se produire

à proximité immédiate de la courbe de vapeur saturée ou, dans certaines applications, à proximité du point critique. Dans ces conditions, la thermodynamique complexe caractérisant ce fluide de travail organique peut conduire à un comportement dynamique inhabituel du fluide, noté *gaz réel* [Wheeler and Ong, 2013], s'écartant de manière significative de celui d'un gaz parfait représenté par la loi de gaz parfait polytropique : la dépendance non idéale de la vitesse à la densité du fluide peut être observée lorsque le flux est soumis à des perturbations isentropiques [Cramer, 1991, Cramer and Best, 1991, Kluwick, 2004]. Cela est particulièrement vrai pour une classe de fluides connue sous le nom de *Bether-Zel'dovich-Thompson* (BZT) fluids [Bethe, 1998, Zeldovich, 1946, Thompson, 1971].

Par conséquent, des lois d'état (EOS) appropriées sont nécessaires pour décrire le comportement thermique et calorique d'un fluide, telles que l'EOS cubique suivant : *Soave-Redlich-Kwong* (SRK) [Soave, 1972] ou *Peng-Robinson-Stryjek-Vera* (PRSV) [Stryjek and Vera, 1986].

Les simulations fiable d'écoulement de gaz denses dans les solveurs de type Computational-Fluid-Dynamics (CFD) nécessitent des méthodes numériques pour la propagation d'incertitudes. Ils pourraient provenir soit de la forme mathématique de l'EOS choisie, soit des coefficients associés à l'EOS généralement étalonnés à partir des données expérimentales disponibles. Pour les fluides complexes, les données expérimentales précises sont difficiles à obtenir, ce qui complique en particulier l'estimation des propriétés des points critiques et des facteurs acentriques, couramment utilisés comme paramètres d'entrée pour l'EOS cubique. Certains travaux de quantification d'incertitude liés à l'EOS concernent des analyses de sensibilité de flux de gaz denses par rapport aux paramètres EOS incertains [Cinnella et al., 2011b], le calibrage bayésien lié à ces paramètres [Merle and Cinnella, 2015]. Des travaux récents ont étudié les incertitudes associés aux coefficients de l'EOS et de la forme du modèle (épistémique) au moyen d'une méthode d'inférence statistique [Merle and Cinnella, 2019].

Les cascades de turbines construites présentent inévitablement des écarts par rapport à la forme et à la taille prévues. Les *variabilités géométriques* indésirables résultent, par exemple, du processus de fabrication ou des opérations de finition. Comme souligné dans [Montomoli et al., 2015], les variations géométriques peuvent affecter les performances de la machine réelle. Des incertitudes géométriques sont présentes sur l'ensemble de la chaîne de conception et de fabrication, à commencer par la paramétrisation géométrique, qui s'étend aux étapes d'usinage individuelles, aux activités d'assemblage final de la turbomachine et même au fonctionnement de la machine. En effet, la production d'aubes de turbine ORC nécessite généralement la conversion d'un modèle géométrique paramétré (courbes de Bézier, Splines, par exemple) en données de type conception assistée par ordinateur (CAD) et ensuite en données CAM, entraînant des modifications de la représentation géométrique. L'étape de fabrication suivante nécessite généralement une série de processus différents tels que le fraisage, le moulage, le forgeage, le soudage, le pliage, induisant tous des déformations géométriques impactant la géométrie finale. Finalement, le fonctionnement de la turbine a également un effet néfaste sur les aubes car il entraîne une augmentation de la rugosité de la surface ainsi que des écoulements de fuite dans les joints à labyrinthe. En effet, la corrosion, l'impact des particules et l'encrassement sont à l'origine de la dégradation de surface. En dépit de l'idée généralement admise que la variabilité géométrique n'est pas souhaitable dans les turbomachines ORC, il existe peu d'informations détaillées sur son effet néfaste sur les performances des cascades.

Enfin, une des particularités des centrales ORC décentralisées de petite à moyenne envergure est la nécessité de fonctionner avec la disponibilité moyenne la plus élevée. Il représente le temps d'exploitation annuel et peut atteindre, pour les unités fiables, plus de 98%, avec seulement une semaine de maintenance prédictive par an. L'industrie tente généralement d'atteindre cet objectif en prenant des décisions critiques à partir de la conception mécanique afin de simplifier les problèmes d'ingénierie et d'obtenir une plus grande fiabilité du composant. Un exemple typique est le couplage direct entre le détendeur et le générateur évitant l'utilisation d'un réducteur, mais limitant généralement la vitesse de rotation du détendeur : il en résulte une réduction des fuites de fluide organique dans l'environnement, une réduction des pièces rotatives et un entretien réduit. En outre, une instrumentation appropriée du *Balance of Plant* (BOP), à savoir tous les composants nécessaires à l'installation de la centrale, y compris la tuyauterie, les vannes et connexion de contournement, jouent un rôle important dans la prévision de la maintenance. En effet, une analyse adéquate des mesures de pression et de température aux sections d'entrée et de sortie de chaque composant pourrait permettre de détecter des défaillances nécessitant une intervention humaine : température anormale d'un joint d'étanchéité défectueux, vibrations accrues ou propriétés détériorées du fluide organique indiquant un encrassement ou une contamination. De tels incidents peuvent avoir un effet néfaste sur l'efficacité à long terme de la machine. Dans ce contexte, la **prédiction d'événement rare** est alors un élément essentiel à intégrer au processus de conception.

Dans la conception actuelle des turbomachines, les méthodes de type *Fluid Shape Optimization* (FSO) sont couramment appliquées et ont récemment fait l'objet d'une amélioration significative, offrant la possibilité de traiter des problèmes complexes à un coût de calcul réduit [Pironneau, 1974]. Ces méthodologies jouent un rôle encore plus important dans le cas de technologies impliquant la Dynamique des fluides compressibles non idéale (NICFD), telles que les turbines ORC, pour lesquelles l'expérience de conception et les informations expérimentales sont limitées à de très rares cas. (voir [Spinelli et al., 2018] pour les toutes premières expériences sur NICFD dans des tuyères supersoniques). Au cours des cinq dernières années, des efforts de recherche concertés ont récemment été consacrés au développement de techniques FSO pour les applications NICFD, telles que celles pour les tuyères et les aubes de turbomachines, en utilisant des méthodes utisant le gradient ([Pini et al., 2015] [Vitale et al., 2017]) ou non ([Pasquale et al., 2013] [Rodriguez-Fernandez and Persico, 2015] [Persico, 2017]) ; une comparaison plus systématique entre ces deux classes d'optimisation, appliquée aux turbines ORC, est rapportée dans [Persico and Pini, 2017]. Dans ces études, des formulations déterministes du problème d'optimisation ont été la plupart du temps prises en compte, malgré la variabilité mentionnée ci-dessus dans les conditions de fonctionnement, la géométrie et les incertitudes liées aux paramètres de fluide.

–2 Optimisation Robuste de forme pour Turbomachines ORC : Challenges

L'importante augmentation de la puissance de calcul au cours des dernières décennies permet d'effectuer des simulations numériques complexes d'écoulements internes allant d'une cascade unique à toute la turbine, en utilisant une complexité de modélisation différente: solveurs Euler 2D, Calculs Navier–Stokes (RANS) 3D, simulations dynamiques telles que RANS instationaire, ou *Large Eddy Simulations* (LES).

À la suite d'études antérieures [Montomoli et al., 2015], certaines des principales limitations de la CFD des turbomachines peuvent être résumées comme suit:

- Les conditions de fonctionnement sont souvent inconnues à priori et comportent des conditions non uniformes et difficiles à déterminer. Des hypothèses raisonnables deviennent nécessaires et les étages de turbine conçus (cascades) doivent généralement répondre aux exigences aérodynamiques pour une large gamme de points de fonctionnement dans différentes conditions d'entrée / sortie.

- La différence entre la géométrie réelle et simulée peut être pertinente en raison d'erreurs de fabrication et de la dégradation en service. Cette différence doit être modélisée et prise en compte lors du processus de conception.

- La convergence de grille est un textit curse bien connu en CFD, et les turbomachines ne sont pas exemptées. Les études récentes cite alauzet2019numerical portent sur le calcul de l'erreur numérique résultant de la résolution de la grille à l'aide de méthodes sophistiquées d'adaptation du maillage.

- Le choix d'effectuer une simulation stable ou instable, par exemple dans le cas d'une interaction rotor / stator, peut avoir un impact important sur la précision de la simulation. Plus généralement, l'influence des effets instables doit être soigneusement évaluée si le processus de conception est uniquement fondé sur des simulations continues.

- Models Les incertitudes dans FSO sont principalement dues aux paramètres et à la forme du modèle. Des incertitudes sur les paramètres sont dues à l'étalonnage des coefficients de fermeture (EOS, turbulence) à l'aide de données expérimentales ou à des simulations de résolution d'échelle, tandis que les simulations sous forme de modèle résultent d'une insuffisance du modèle considéré (par exemple, modèle EOS, RANS). Par exemple, dans cite schmelzer2019estimation, un maximum d'estimations a posteriori des distributions postérieures des coefficients de fermeture RANS est étudié.

Par conséquent, la performance réelle d'une turbine (cascade) n'est pas déterministe par nature et devrait être décrite de manière idéale par des distributions de probabilité reflétant la dispersion en incertitudes géométriques, opérationnelles et de modélisation. Cette thèse est orientée vers le développement de méthodes numériques pour résoudre le problème d'*Optimisation sous incertitudes*, avec l'optimisation de la forme de la turbine ORC comme application cible. Cette rubrique est parfois appelée *Robust Engineering* bien que ce terme désigne une catégorie plus générale. Plus précisément, le présent travail de recherche vise à traiter des stratégies de conception

adaptées aux cascades de turbines ORC, en tenant compte des conditions de fonctionnement, des paramètres de fluide impliqués dans l'EOS décrivant le comportement du gaz dense et de la variabilité géométrique due à la fabrication. Dans la littérature, deux méthodes sont utilisées pour intégrer l'incertitude dans le cadre de l'optimisation, à savoir Optimisation Robuste (RO) et Optimisation de la conception basée sur la fiabilité (RBDO). Cette recherche porte sur deux aspects différents, *i.e.* Le calcul d'un événement rare pour l'optimisation de la conception basée sur la fiabilité et l'optimisation de la conception robuste. Dans ce qui suit, quelques défis pour ces deux problèmes sont illustrés.

Evènements rares et RBDO

L'objectif de RBDO est de concevoir sous contrainte de fiabilité (événements rares). Dans RBDO, la fiabilité est généralement mesurée par une *probabilité de défaillance*, qui doit rester inférieure à un seuil donné, généralement très faible. Une contrainte basée sur un quantile pourrait remplacer cette contrainte de probabilité de défaillance, tandis que le problème d'optimisation pourrait être soumis à plusieurs contraintes de fiabilité. Des formulations à objectifs multiples pourraient également être envisagées.

La principale difficulté de RBDO réside dans le fait qu'il faut estimer, à chaque itération de la formulation de RBDO, une faible probabilité d'échec ou un quantile. Ces estimations étant déjà difficiles, l'effort informatique est considérablement accru. Actuellement, les méthodes RBDO peuvent être classées en deux groupes, à savoir les algorithmes à deux niveaux (imbriqués) [Youn et al., 2003] et les algorithmes à boucle unique [Picheny et al., 2010c]. Comme son nom l'indique, les méthodes à deux niveaux comportent deux étapes: l'une correspondant à l'estimation d'événements rares, l'autre axée sur l'optimisation de la conception. Une méthode populaire appartenant à cette catégorie est la méthode *Reliability-Index Approach* RIA [Shi and Lin, 2016]; à chaque étape d'optimisation, l'estimation de la probabilité de défaillance est fondamentalement résolue en termes d'indices de fiabilité au moyen de la méthode bien connue *First Order Reliability Method* (FORM)[1] [Bourinet, 2018]. Ces méthodes souffrent généralement d'un faible taux de convergence, d'où un coût de calcul élevé. De plus, les résultats peuvent ne pas être optimaux, en particulier dans ls problèmes impliquant des contraintes probabilistes hautement non linéaires ou des modes de défaillance multiples. Pour faire face au nombre élevé d'évaluations du résolveur numérique, les méthodes à boucle unique sont devenues très populaires parmi les chercheurs, tentant de convertir la procédure à double boucle en une seule procédure. Une option consiste à convertir la contrainte probabiliste en une contrainte déterministe, puis à la remplacer par les conditions d'optimalité [Liang et al., 2008, Liang et al., 2008]. Bien qu'efficaces numériquement, ces méthodes donnent souvent des résultats erronés et peuvent conduire à des instabilités numériques. Une autre option fait appel au concept d'espace augmenté [Dubourg, 2011, Moustapha et al., 2016], basé sur l'utilisation de métamodèles, permettant l'approximation de la frontière (LSS) délimitant les designs défaillants des autres. Ils s'appuient sur des stratégies d'échantillonnage adaptatif conçues à l'origine pour l'estimation des probabilités de défaillance et des quantiles. La principale limitation de ces méthodes est

[1] ou *Second Order Reliability Method* (SORM), une fois que le point de défaillance le plus probable (MPFP) a été trouvé.

qu'elles ne conviennent pas aux événements extrêmes, *ie* associés à des seuils de probabilité d'échec (ou niveau de quantile) compris entre $0(10^{-5} - 10^{-9})$. Des méthodes efficaces appropriées pour le calcul des probabilités de défaillance faibles et des quantiles extrêmes, c'est-à-dire dont la stratégie adaptative est compatible avec les algorithmes RBDO sont donc considérées.

Optimisation Robuste

L'*Optimisation Robuste* (RO) consiste à minimiser l'influence des conditions environnementales incertaines sur les performances d'un système, *i.e.* cherchent à déterminer une conception insensible aux variations considérées. Une approche mono-objectif classique consiste, par exemple, à minimiser la moyenne (ou plus généralement une statistique sélectionnée) de la performance (fonction objectif scalaire). Les techniques d'optimisation robustes comportant une quantification explicite de l'incertitude posent des problèmes de dimensionnalité, en raison du grand nombre de calculs CFD nécessaires, qui déterminent finalement la faisabilité technique de la méthode. Les techniques de substitution sont principalement utilisées pour limiter le coût de calcul global ; voir par exemple [Keshavarzzadeh et al., 2017, Zhang et al., 2017] où la stratégie d'Optimisation approximative séquentielle (SAO) est illustrée. Une discussion sur l'intérêt d'utiliser des modèles de substitution pour une optimisation basée sur l'incertitude est présentée dans [Jin et al., 2003], où le Krigeage et plus généralement les techniques de Processus Gaussiens (GP) s'avèrent très prometteurs. Dans ce contexte, [LEE and PARK, 2006] propose une formulation basée sur la performance et la minimisation de la variance d'une quantité d'intérêt (QoI) ; la fonction de performance est approchée avec un modèle de krigeage dans l'espace couplé, et la méthode de Monte-Carlo est appliquée considérant le modèle à faible coût, permet de construire un deuxième métamodèle de krigeage sur les moments statistiques. Dans [Janusevskis and Le Riche, 2013], un modèle de stratégie de groupe est utilisé pour optimiser les performances moyennes, et cette optimisation est obtenue à l'aide de méthodes dites d'Optimization Bayesiennes. En ce qui concerne l'algorithme de minimisation, des techniques basées sur les GP, telles que *Efficient Global Optimization* (EGO) ont été utilisées massivement dans l'optimisation [Huang et al., 2006, Picheny et al., 2010a].

Même s'il est à présent établi et pleinement démontré, le RO visant à minimiser la moyenne d'une QoI pourrait souffrir d'un manque de contrôle de sa variabilité. Des formulations alternatives sont possibles pour améliorer le contrôle de la variabilité, en tenant compte de l'écart type de la QoI, par exemple en formulant la fonction objectif sous la forme $\mu \pm k\sigma$ ou Min σ s.t. $\mu < \mu_0$ par exemple, où μ, σ désignent respectivement la moyenne et l'écart type de la QoI. Cependant, ces méthodes souffrent du fait que les paramètres définis par l'utilisateur k, μ_0 ont un impact significatif sur la conception finale. De plus, l'inclusion explicite de l'écart type dans la fonction objectif induit une augmentation de la charge de calcul dans l'espace stochastique par rapport à la moyenne. Pour les problèmes liés aux ORC, une optimisation robuste multi-objectifs a été proposée à la fois sur la moyenne et sur l'écart type [Congedo et al., 2013a, Bufi et al., 2017, Bufi and Cinnella, 2017], et une approche multipoint a été proposée dans [Pini et al., 2014a].

–3 Contributions du Travail de Recherche

Ce manuscrit illustre les principales contributions accomplies pour relever certains des défis présentés dans la section précédente. La première partie est consacrée à la formulation et à l'évaluation de certains algorithmes d'estimation de faible probabilité de défaillance et de quantile extrême[2], proposant des stratégies d'échantillonnage adaptatif compatibles avec des méthodes RBDO existantes. Une application préliminaire de la méthode avec une turbine ORC de la méthode pour une faible probabilité de défaillance est également proposée.

La deuxième partie du manuscrit est consacrée à l'optimisation de la conception robuste et de la forme des turbines ORC. Premièrement, une analyse de sensibilité tenant compte de l'effet combiné des conditions de fonctionnement, des incertitudes géométriques et des incertitudes du modèle EOS sur une application de turbine ORC est présentée. Ensuite, un algorithme d'optimisation basée sur les quantiles est formulé et appliqué à la conception robuste d'un stator de turbine ORC.

Les principales contributions de cette thèse sont résumées ci-dessous.

Évènements Rares Deux méthodes d'estimation de probabilité de défaillance et une permettant d'estimer un petit quantile sont proposées, basées sur la modélisation de substitution de Kriging et des stratégies d'échantillonnage adaptatif, formulées dans l'espace standard. Cette classe de méthodes appartenant aux analyses de fiabilité et de risque concerne l'évaluation de la sécurité de systèmes d'ingénierie complexes. En fait, le domaine d'applications impliquant principalement des systèmes très dangereux est vaste, y compris les centrales chimiques et nucléaires, les dépôts de déchets radioactifs, la sécurité des structures ou l'évaluation de la conception de l'aérospatiale.

- **Estimation non-biasiée de très faible probabilité de défaillance**
  Ce premier algorithme combine trois contributions principales. Une nouvelle stratégie de raffinement séquentiel du métamodèle permet d'approcher avec précision la fonction de performance d'origine sans hypothèse restrictive sur le LSS, telle que la linéarité ou le nombre de modes de défaillance. En particulier, la stratégie de raffinement vise à affiner directement le substitut au voisinage du LSS (contrairement aux méthodes basées sur la simulation de sous-ensemble, par exemple). Un nouveau mélange gaussien Importance Sampling Density (ISD) permet d'estimer avec précision un très faible risque de défaillance dans le cas d'une fonction de performance d'analyse ou de métamodèle dans un nombre raisonnable d'évaluations, en alternative à la simulation de sous-ensembles. Enfin, un nouvel estimateur non biaisé basé sur l'échantillonnage d'importance et le contrôle varié inspiré de [Dubourg et al., 2013] permet, avec des simulations supplémentaires, de fournir une estimation non biaisée des petites probabilités de défaillance.

[2]Une attention particulière est accordée à leur adaptation aux probabilités de défaillance et au quantile de niveau $O(10^{-5} - 10^{-9})$.

- **Estimation de faibles probabilités de défaillance**
  Ce second algorithme est une extension de celui présenté dans [Echard et al., 2011] pour l'estimation de très faibles probabilités de défaillance, avec une stratégie de raffinement adaptative parallèle visant à estimer le LSS avec *directement*.

- **Estimation de quantile extrême**
  Cet algorithme permet l'estimation de quantiles extrêmes (niveau $\sim 10^{-5}$—10^{-9}) sans hypothèses restrictives sur le LSS, telles que la linéarité ou le nombre de modes de défaillance. Inspirée de [Echard et al., 2011], la stratégie de raffinement des substituts parallèles s'enrichit d'un niveau supplémentaire de parallélisation, également compatible avec l'algorithme de quantile séminal [Schöbi et al., 2016]. À la connaissance de l'auteur, aucune méthode de la littérature ouverte ne convient à un problème aussi complexe.

Optimisation Robuste appliquée à un stator de turbine ORC

- **Quantification d'Incertitude appliquée à un stator de turbine ORC**
  Parmi les premières études dans la littérature ouverte sur les systèmes ORC, l'application de techniques avancées de quantification d'incertitudes à l'analyse d'une cascade de turbine supersonique typique, comprenant une caractérisation détaillée des incertitudes géométriques, est considérée. Plusieurs sources d'incertitude sont prises en compte, liées aux tolérances géométriques de l'aube, aux conditions de fonctionnement et à certains paramètres du modèle thermodynamique. En outre, la méthode de calcul de la probabilité de défaillance faible, illustrée dans la partie précédente du manuscrit, est utilisée pour explorer un scénario de défaillance pour une turbine ORC.

- **Optimisation robuste à base de quantiles d'une cascade de turbine ORC**
  Une optimisation robuste de forme basée sur les quantiles sous contrainte probabiliste est développée en considérant une approche imbriquée et appliquée à la conception d'une cascade de turbine supersonique ORC. Les performances de l'algorithme proposé sont systématiquement comparées aux résultats d'un RO basée sur la moyenne.

–4 Aperçu du Manuscrit

Cette thèse est divisée en deux parties. La première partie porte sur les méthodes d'événements rares en tant que contributions à l'extension des méthodes RBDO adaptées aux événements extrêmes. La deuxième partie traite de la formulation des méthodes RO appliquées à la cascade ORC Turbine. Le premier chapitre est destiné à fournir des rappels mathématiques.

Chapitre 1 présente un ensemble d'outils mathématiques nécessaires à la compréhension de la thèse. Les principes généraux de la quantification de l'incertitude et de la théorie de la probabilité sont introduits de manière concise. Des détails sur la modélisation de substitution de Kriging sont ensuite présentés. Enfin, la propagation par

incertitude directe basée sur le krigeage, y compris l'estimation de statistiques ou d'indices de sensibilité, est illustrée. Ce chapitre ne présente aucune contribution originale.

Part A: Événements rares

Cette partie décrit les méthodes numériques appliquées à deux problèmes spécifiques liés à l'estimation des événements rares: la probabilité de défaillance faible et l'estimation du quantile extrême. Les méthodes développées sont spécialement conçues pour convenir dans le cas de *régions de défaillance multiples*, et restent applicables pour les probabilités de défaillance admissibles (ou niveau de quantile) comprises entre 10^{-2} et 10^{-9}, et caractérisé par une stratégie d'échantillonnage adaptatif *directe* du LSS. La fonction de performance est supposée être la sortie d'un code de simulation coûteux à évaluer. Par conséquent, seul un nombre raisonnable d'évaluations est possible (moins de quelques centaines).

Chapter II a pour but de présenter le cadre général des méthodes d'événements rares présentées dans la première partie du manuscrit, y compris des tests élémentaires académiques et des concepts généraux tels que Importance Sampling.

Chapter III vise à décrire une méthode pour le calcul non-biasé de petites probabilités d'échec. Un nouvel algorithme adapté à la probabilité de faible échec et des régions à défaillances multiples est proposé, ce qui permet à la fois de créer un métamodèle précis et de fournir une erreur cohérente sur le plan statistique. Une technique d'échantillonnage d'importance basée sur un mélange gaussien est proposée, permettant de réduire considérablement le coût de calcul lors de l'estimation d'une valeur de référence directement à partir du métamodèle.

Chapter IV présente une méthode facile à mettre en œuvre pour l'estimation efficace d'une très faible probabilité de défaillance, sur la base d'une stratégie de raffinement parallèle qui *directement* (contrairement à la simulation bayésienne de sous-ensembles [Bect et al., 2017]) vise à affiner le LSS.

Chapitre V est consacré à un cadre d'estimation de quantiles, des méthodes de krigeage. De la même manière que la stratégie présentée dans [Schöbi et al., 2016], la substitution est affinée de manière adaptative à l'aide du raffinement de remplissage parallèle fourni par la méthode d'estimation de la probabilité de défaillance développée au chapitre IV). Enfin, une approche de sélection multi-quantile permettant d'exploiter des architectures informatiques hautes performances d'un niveau supplémentaire est élaborée.

Part B: Méthodes d'optimisation robustes pour un stator de turbine ORC

La deuxième partie est centrée sur l'application d'une méthode originale de RO à la conception de forme d'une cascade de turbine supersonique ORC. En particulier, une analyse UQ tenant compte des paramètres opérationnels, des paramètres de fluide et des incertitudes géométriques (aléatoires) permet de donner un aperçu général de l'impact de multiples effets et constitue une étude préliminaire nécessaire pour le RO.

Chapitre VI introduit la configuration de turbine axiale, qui est un stator supersonique bien connu fonctionnant avec le siloxane MDM. Le cadre numérique comprenant notamment le solveur CFD, la paramétrisation, les outils de maillage et la modélisation de la variabilité géométrique est décrit.

Chapitre VII a pour objectif de présenter les résultats des méthodes efficaces de propagation d'incertitude basées sur des substituts appliquées à la cascade axiale de turbines supersoniques présentée dans le chapitre VI. L'impact des paramètres de fonctionnement, des fluides et des incertitudes géométriques sur différentes valeurs de QoI, telles que la pression totale ou le débit massique, est analysé et fournit une vue d'ensemble sur l'influence de multiples effets. Un scénario d'échec est également étudié en appliquant l'une des méthodes illustrées dans la première partie du manuscrit.

Chapter VIII est consacré à une formulation d'RO mono-objectif basée sur les quantiles appliquée à la conception du profil 2D du stator décrit, sous une contrainte probabiliste: la moyenne du débit massique est contraint. La comparaison avec l'optimisation déterministe contrainte et une approche RO classique, *i.e.* minimisant la moyenne de la fonction de performance soumise à la même contrainte, est illustrée.

Une compréhension approfondie du chapitre I n'est pas nécessaire, même s'il est essentiel de rappeler quelques résultats fondamentaux sur les prédicteurs de Kriging, leur application à la propagation d'incertitude directe et certains concepts probabilistes tels que Vecteurs aléatoires et Processus aléatoires. Bien que les parties A et B soient presque indépendantes, elles sont toutes deux destinées à être lues dans l'ordre chronologique, certaines sections présentant des concepts fondamentaux mentionnés dans les suivantes.

Introduction

–5 Context

In the energy industry, a renewed interest has arisen in decentralized power generation. Since abundant renewable sources such as geothermal/solar are often characterized by small exploitable power capacity for a single location, small-medium scale power plants ($O(10^1 - 10^4)$ kW) could consequently play a key role for such energy sources. Among available technologies for high-efficiency conversion of thermal power into electricity in this range of capacity, *Organic Rankine Cycles* (ORC) have shown significant advantages compared to steam Rankine Cycles [Verneau, 1978, Angelino et al., 1984] in terms of reliability and cost-effectiveness. ORC has therefore received considerable interest in both the industrial and academic community, in particular, due to its ability to recover mechanical energy from low-grade heat sources.

The Rankine power cycle is a closed thermodynamic cycle present in all conventional steam power plants. In ORCs, similar to steam Rankine Cycles, the working fluid (water) is replaced by an organic fluid characterized by high molecular weight. In its basic form, an ORC is constituted by four components (Figure 2): evaporator, turbine, condenser, pump.

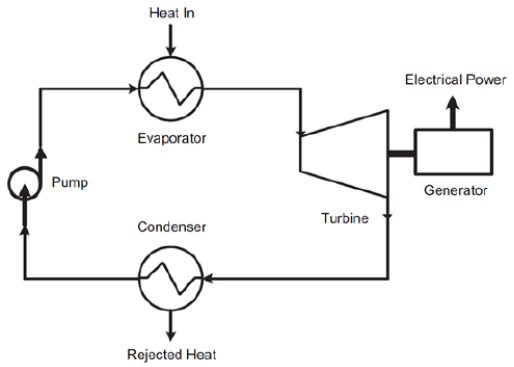

Figure 2 ORC illustration. Extracted from [Sauret and T Gu, 2014].

The organic fluid is pumped in the evaporator which exploits a low-grade heat source: the pressurized liquid is converted to superheated vapor at constant pressure. Note that the retrograde nature of typical organic fluids used for ORC alleviates the superheating process, which is instead of crucial importance in conventional Rankine steam cycles. A turbine (or expander) permits to expand the hot vapor, converting the enthalpy drop into mechanical (rotating) energy, further converted into electricity using a generator coupled to the turbine. The vapor then enters in a condenser, which, by thermal transfer with the cold source (e.g. ambient air, lake) converts it into a liquid state. The low-pressure liquid is finally directed to the feed pump, increasing its pressure and closing the thermodynamic cycle. In most cases, a regenerator is used to recover heat energy from the vapor leaving the turbine. Organic compounds permit to efficiently convert low-to-medium temperature heat (starting from approximately 90 °C) in the small to medium power range: their vaporization heat, much lower than the one from water offers a better balance between the heating trajectory of the working (organic) fluid and the cooling one of the heat source (typically superheated water or oil), increasing the conversion efficiency [Karellas and Schuster, 2008, Larjola, 1995, Harinck, 2010].

The proper selection of the organic fluid w.r.t. the heat source temperature and heat input results in increased power output or cycle performances. It is usually chosen as an aromatic siloxane, fluorocarbon, fluorocarbon, hydrofluorocarbon or a straight chain [Curran, 1981, Angelino et al., 1984, Colonna, 1996, Angelino and Di Paliano, 1998]. The variety guaranteed by the broad spectrum of available organic fluids matches with the diverse requirements of widely distributed thermal energy conversion devices [Macchi, 2017, Colonna et al., 2015]; ORC offers great potential to utilize external sustainable heat sources such as solar (thermal collectors), geothermal, biomass, or even exploitation of *Waste Heat Recovery* (WHR) (e.g. steel power plants, trucks). Such sources typically feature variable loads and, hence, the thermodynamic condition at the exit of the boiler/inlet of the turbine undergoes significant variations; such variation also combines with the natural seasonal change in ambient temperature, which might alter the thermodynamic conditions of the condenser/outlet of the turbine. These sources of **uncertainty** result in considerable differences in the turbine operation and, in particular, in a variable aerodynamic load on the cascades of the machine, potentially reducing the turbine performance.

Another peculiarity of the organic fluid impacts the turbine design. On the one hand, the expansion process entails a small specific enthalpy drop, the latter being inversely proportional to the high molecular weight of the organic fluid. It allows the adoption of cost-effective and compact turbines composed of one or two stages, without considering problems associated with high rotational speed and resulting penalties on efficiency [Angelino et al., 1984]. On the other hand, the combination of the low speed of sound and the resulting high expansion ratio per stage typically lead to transonic or supersonic ORC turbines, commonly subject to strong shock waves and chocked flow conditions. Additionally, part of the expansion process might occur in the close vicinity of the saturated vapor curve, or, in some applications, close to the critical point. In those conditions, the complex thermodynamics characterizing such organic working fluid may lead to unusual fluid dynamic behavior denoted as *real gas*[3]

[3] a.k.a. *dense gas* or *non-ideal gas*.

effects in the literature [Wheeler and Ong, 2013], deviating significantly from that of a perfect gas represented by the polytropic perfect gas law: non-ideal dependence of the speed of sound on the fluid density might be observed when the flow is submitted to isentropic perturbations [Cramer, 1991, Cramer and Best, 1991, Kluwick, 2004]. This is particularly true for a class of fluids known as the *Bether-Zel'dovich-Thompson* (BZT) fluids [Bethe, 1998, Zeldovich, 1946, Thompson, 1971]. Consequently, suitable so-called *Equations of State* (EOS) are necessary to describe the fluid thermal and caloric behavior, such as the following cubic EOS, *Soave-Redlich-Kwong* (SRK) [Soave, 1972] or *Peng-Robinson-Stryjek-Vera* (PRSV) [Stryjek and Vera, 1986]. *Reliable* simulations of dense gas flows in Computational-Fluid-Dynamics (CFD) solvers requires numerical methods for the propagation of **thermodynamic modeling uncertainties**. They might stem either from the mathematical form of the EOS chosen or from the closure coefficients associated to the EOS usually calibrated from available experimental data. For molecularly complex fluids, accurate experimental data are hardly available, complicating, in particular, the estimation of critical-point properties and acentric factors, commonly used as input parameters for cubic EOS. Some uncertainty quantification works related to EOS concern sensitivity analyses of dense gas flows w.r.t. uncertain EOS parameters [Cinnella et al., 2011b], Bayesian calibration related to those parameters [Merle and Cinnella, 2015]. Recent works investigated both EOS closure coefficient (parametric) and model-form (epistemic) uncertainties by means of a statistical inference methodology [Merle and Cinnella, 2019].

Finished/designed turbine cascade inevitably exhibit deviations from their intended shape and size. The associated undesirable *geometric variability* stems, for instance, from the manufacturing process or hand-finishing operations. As stressed out in [Montomoli et al., 2015], the geometrical variations can affect the performance of the real machine. Geometrical uncertainties are present for the entire design and manufacturing chain beginning with geometrical parametrization reaching over to the individual machining steps, to final assembly activities of the turbomachine and even to machine operation. Indeed, production of ORC turbine blades usually requires conversion from a parametrized geometrical model (e.g. Bézier curves, Splines) possibly to a *Computer-Aided Design* (CAD) data and further to a *Computer-Aided Manufacturing* (CAM) data, resulting in changes in the geometric representation. The following manufacturing step typically requires a sequence of different processes such as milling, casting, forging, welding, bending, all inducing relevant geometric deformations for the final geometry. Eventually, turbine operation has also a detrimental effect on the blades as it leads to an increase of surface roughness as well as leakage flows in labyrinth seals. Indeed, corrosion, particle impact and fouling are at the origin of surface degradation. Despite the generally accepted notion that **geometric variability** is undesirable in ORC turbomachinery, scarce detailed information is available about its detrimental effect on the cascades' performances.

Finally, one peculiarity of decentralized small-medium range ORC power plants is the necessity to operate with the highest *average availability*. It represents the annual time under operation per year and can reach, for reliable units, more than 98%, with only one week of predictive maintenance annually. The industry commonly attempts to attain this goal by making critical decisions from the mechanical design to simplify engineering challenges and obtain higher reliability in the component. One typical example is the direct coupling between the expander and the generator avoiding the use of a gearbox, but usually limiting the rotational speed of the expander: it results to re-

duced leakage of organic fluid into the external environments, less rotating parts and reduced maintenance. Additionally, proper instrumentation of the so-called *Balance of Plant* (BOP)[4], namely all the components required to complete the power plant installation including piping, valves and bypass connection, play a significant role in the prediction of maintenance. Indeed, an adequate analysis of pressure and temperature measurements at the inlet and outlet section of each component could permit to detect failure events requiring human intervention: abnormal temperature of a defective sealing, increased vibrations, or deteriorated properties of the organic fluid indicating fouling or oil contamination. Such failure events may have a detrimental effect on long-time efficiency of the machine. In this context, the **prediction of rare-event** is then an essential ingredient to integrate within the design process.

In present-day turbomachinery design, *Fluid-dynamic Shape Optimization* (FSO) methods are routinely applied and have recently undergone a significant improvement, offering the possibility to deal with complex problems at a reduced computational cost [Pironneau, 1974]. Those methodologies play an even more important role in the case of technologies entailing the *Non-Ideal Compressible Fluid Dynamics* (NICFD), such as ORC turbines, for which design experience and experimental information are limited to very few cases (see [Spinelli et al., 2018] for the very first experiments on NICFD in supersonic nozzles). In the last five years, concerted research efforts have been recently devoted to develop FSO techniques for NICFD applications, such as for nozzles and turbomachinery blades, using either gradient-based ([Pini et al., 2015] [Vitale et al., 2017] [Rubino et al., 2018]) or gradient-free algorithms ([Pasquale et al., 2013] [Rodriguez-Fernandez and Persico, 2015] [Persico, 2017]); a more systematic comparison between these two classes of optimization, when applied to ORC turbines, is reported in [Persico and Pini, 2017]. In such studies, deterministic formulations of the optimization problem have, most of the time, been considered, despite the variability mentioned above in operating conditions, geometry and uncertainties related to fluid parameters.

–6 Robust shape optimization for ORC Turbomachinery CFD: challenges

The tremendous increase in computational power over the last decades allows for complex numerical simulations of internal flows ranging from a single cascade up the entire turbine, using different modeling complexity: 2D Euler solvers, *Reynolds-averaged Navier–Stokes* (RANS) 3D simulations, dynamic simulations such as unsteady RANS, *Detached Eddy Simulation* (DES) or *Large Eddy Simulation* (LES). Besides, the computational power in combination with automated execution of simulations (e.g. scripting) allows for automated design optimization.

Following previous studies [Montomoli et al., 2015], some main limitations in turbomachinery CFD can be resumed as follows:

[4]The instrumentation is part of the BOP

- Operational conditions are often unknown a priori, and feature non-uniform conditions which are difficult to determine. Reasonable assumptions become necessary, and designed turbine stages (cascades) must typically fulfill aerodynamic requirements for a wide range of operating points with different inlet/outlet conditions.

- The difference between the real geometry and the simulated one can be relevant due to manufacturing errors and in-service degradation. This difference should be modeled and taken into account during the design process.

- Grid-convergence is a well-known *curse* in CFD, and turbomachinery is not exempted. Recent studies [Alauzet et al., 2019] focus on the computation of the numerical error stemming from the grid resolution by means of sophisticated mesh adaptation methods.

- The choice to perform steady or unsteady simulation, for example in the case of rotor/stator interaction can impact deeply the accuracy of the simulation. More generally, the influence of unsteady effects should be carefully assessed if the design process is uniquely based on steady simulations.

- Models Uncertainties in FSO are mainly due to parameters and model-form. Parameters uncertainties arises due to closure coefficients (EOS, turbulence) calibration using experimental data or scale-resolving simulations, while model-form ones result from inadequacy of the model of interest (e.g. EOS, RANS model). For instance, in [Schmelzer et al., 2019], a maximum a posteriori estimates of the posterior distributions of RANS closure coefficients is investigated.

Concerning the ORC turbine simulation particularly, some problematic aspects have required and require particular attention:

- The presence of a few experimental data has caused a greater difficulty in the validation of the physical models used to simulate the non-ideal fluids used for ORC turbines. A great effort has been made recently to generate a set of experimental data that can be used to validate thermodynamic models in conditions similar to those used in ORC turbines [Zocca et al., 2018, Spinelli et al., 2017].

- The experimental validation of the thermodynamic models is still to achieve for non-ideal flows, though some recent studies show that other sources of uncertainties could be in principle more important [Congedo et al., 2013b].

- The formulation of RANS turbulence models adapted to non-ideal flows is an important objective to achieve to improve the prediction of the non-ideal solvers [Sciacovelli et al., 2018]. This problem requires experimental data especially conceived for measuring turbulent flows. From a modeling point of view, a strong effort is underway to perform Direct Numerical Simulation of non-ideal flows [Sciacovelli et al., 2017].

As a matter of fact, the real performance of a turbine (cascade) is non-deterministic by nature and should be ideally described by probability distributions reflecting the scattering in geometry, operational and modeling uncertainties.

This thesis is oriented towards the development of numerical methods to tackle *Optimization under uncertainties* problem, with the shape optimization of ORC turbine as the target application. This topic is sometimes referred to as *Robust Engineering* although this term indicates a specific category of the former more general problem. More specifically, the present research work is intended to addressing design strategies suitable for ORC turbine cascades, accounting for operating conditions, fluid parameters involved in EOS describing dense gas behavior, and geometric variability due to manufacturing. In literature, two methodologies are used in order to incorporate uncertainty into the framework of optimization, namely *Robust Design Optimization*, a.k.a. *Robust Optimization* (RO) and *Reliability-Based Design Optimization* (RBDO). This research focuses on two different aspects, *i.e.* the computation of a rare event for reliability-based design optimization and the robust design optimization. In the following, some challenges for these two problems are illustrated.

Rare events and Reliability-Based Design Optimization

RBDO aim is to design for safety w.r.t. extreme (rare) events. In RBDO, the reliability is generally measured by a *failure probability*, which is constrained to be lower than a given threshold typically very small. A quantile-based one might replace the failure probability constraint while the optimization problem might be subject to several reliability constraints. Multi-objective formulations could also be considered.

The primary bottleneck of RBDO resides in the fact that one has to estimate, at each iteration of the RBDO formulation, a small failure probability or quantile. Those estimations being already challenging, the computational effort is significantly increased. Currently, RBDO methods can be classified in two groups, namely bi-level (a.k.a. nested) algorithms [Youn et al., 2003] and single-loop ones [Picheny et al., 2010c]. As suggested by the name, bi-level methods involve two stages: one corresponding to the rare event estimation, while the other focuses on the design optimization. One popular method belonging to this category is the *Reliability-Index Approach* (RIA) [Shi and Lin, 2016]; at each optimization step, the failure probability estimation is basically solved in terms of reliability indices by means of the well known *First-Order Reliability Method* (FORM)[5] [Bourinet, 2018]. Those methods usually suffer from low rate of convergence, hence a large computational cost. Additionally, results might not be optimal, specifically in problems involving highly non-linear probabilistic constraints or multiple failure modes. To tackle the high number of evaluations of the numerical solver, single-loop methods have become quite popular among researchers, attempting to convert the double loop procedure into a single one. One option consists in converting the probabilistic constraint into a deterministic one, and then replace it by optimality conditions [Liang et al., 2008, Liang et al., 2008]. Even though computationally efficient, such methods often yields erroneous results and can lead to numerical instabilities. Another option resorts to the concept of *augmented space* [Dubourg, 2011, Moustapha et al., 2016], where surrogate[6]-based methods avoiding restrictive assumptions such as the linearity of the so-called *Limit-State Surface* (LSF)[7], or the number of the *failure domains* are considered. They rely on *adaptive*

[5] or using *Second-Order Reliability Method* (SORM), once the so-called *Most Probable Failure Point* (MPFP) has been found.

[6] a.k.a. emulators of the physical model or metamodel

[7] The Limit-State Surface is loosely defined as the frontier between the *safe* and *failure* designs.

sampling strategies originally designed for the estimation of failure probabilities and quantiles. The main limitation of their methods is that they are not suitable for *extreme* events, *i.e.* associated to failure probability thresholds (or quantile level) in the range $O(10^{-5} - 10^{-9})$. Suitable efficient methods for the computation of small failure probability and extreme quantile, i.e. whose adaptive strategy is compatible with RBDO algorithms [Dubourg, 2011, Moustapha et al., 2016], might benefit to adapt the latter when involving extreme quantiles and small failure probabilities in the constraints, without considering restrictive assumptions on the LSS.

Robust Design Optimization

Robust Design Optimization or *Robust Optimization* (RO) seeks to minimize both the influence of the uncertain environmental conditions on the performance of a system and the performance *itself*, *i.e.* aims at finding a design insensitive to deviations from the nominal inputs. A classic mono-objective approach consists, e.g., in minimizing the mean (or more generally a selected statistics) of the fitness function. Robust optimization techniques featuring an explicit uncertainty quantification suffer from dimensionality issues, due to a large number of fluid-dynamic calculations required, which eventually determine the technical feasibility of the method. Surrogate-based techniques are primarily used to limit the overall computational cost; see for example [Keshavarzzadeh et al., 2017] or [Zhang et al., 2017], where a kriging-based *Sequential Approximate Optimization* (SAO) strategy is illustrated. A discussion over the interest in using surrogate models for uncertainty-based optimization is presented in [Jin et al., 2003], where Kriging and more generally *Gaussian Processes* (GP) techniques are shown to be very promising. In this context, [LEE and PARK, 2006] proposes formulation based on a target performance and variance minimization of a specific *Quantity of Interest* (QoI); the performance function is approximated with a kriging model in coupled space, and low-cost *Monte-Carlo Sampling* (MCS) on the model allows to build a second kriging metamodel on the statistical moments. In [Janusevskis and Le Riche, 2013], a GP model is used to perform mean performance optimization, and optimization is achieved through *Bayesian Optimization* (BO). Regarding the minimization algorithm, GP-based techniques such as the *Efficient Global Optimization* (EGO) have been massively used in optimization (see for example [Huang et al., 2006] or [Picheny et al., 2010a]).

Even though nowadays established and fully demonstrated, RO aimed at minimizing the mean of a QoI might suffer from a lack of control of its variability. Alternative formulations are possible to enhance the control of the variability, taking into account the QoI's standard deviation, for example by formulating the objective function as $\mu \pm k\sigma$, or Min σ s.t. $\mu < \mu_0$ for instance, where μ, σ denote the QoI's mean and standard deviation respectively. However, such methods suffer from the fact that the user-defined parameters k, μ_0 have a substantial impact on the final design. Moreover, including explicitly the standard deviation in the objective function induces an increase in the computation burden in the stochastic space with respect to the mean. For ORC-driven problems, essentially multi-objective robust optimization have been proposed on both the mean and the standard deviation [Congedo et al., 2013a, Bufi et al., 2017, Bufi and Cinnella, 2017], and a multi-point approach was proposed in [Pini et al., 2014a].

–7 Contributions of the Research Work

This manuscript illustrates the main contributions accomplished to tackle some of the challenges introduced in the previous section. The first part is devoted to the formulation and assessment of some algorithms for the estimation of small failure probability, and extreme quantile[8], the latter featuring adaptive sampling strategies compatible with existing RBDO methods. A preliminary ORC turbine application of the method for small failure probability is also illustrated.

The second part of the manuscript is devoted to robust design optimization and the shape optimization of ORC turbines. First, a sensitivity analysis taking into account the combined effect of operating conditions, geometric and model uncertainties on a ORC turbine application is presented. Then, an algorithm for quantile-based optimization is formulated and applied to the *Robust* design of an ORC Turbine nozzle.

The main contributions of this thesis are summarized in the following.

Rare Events Two methods for failure probability estimation and one permitting to estimate a small quantile are proposed, based on Kriging surrogate-modeling and adaptive sampling strategies, formulated in the standard space. This class of methods belonging to reliability and risk analyses are for the safety assessment of complex engineering systems. As a matter of fact, the field of applications mostly involving highly hazardous systems is broad, including chemical and nuclear power plants, radioactive waste repositories, structural safety or aerospace design assessment.

- **Unbiased estimation of small failure probability estimation**
  This first algorithm combines three main contributions. A new metamodel sequential refinement strategy permits to accurately approximate the original performance function without restrictive assumptions on the LSS such as linearity or number of failure modes. In particular, the refinement strategy aims at *directly* refine the surrogate in the vicinity of the so-called LSS (unlike Subset-Simulation based methods, e.g.). A new Gaussian mixture ISD permits the accurate estimation of very small failure probability in the case of analytical or metamodel performance function in a reasonable number of evaluations, as an alternative to Subset Simulation. Finally, a new unbiased estimator based on Importance Sampling and Control Variate inspired by [Dubourg et al., 2013] permits with additional simulations to provide an unbiased estimation of small failure probabilities.

- **Small failure probability estimation**
  This second algorithm is an extension of the one presented in [Echard et al., 2011] for the estimation of *small* failure probability analysis, featuring a parallel adaptive refinement strategy aiming at *directly* refine the LSS, and a Kriging based in-line bounds estimation.

- **Extreme quantile estimation**
  This algorithm permits the estimation of small quantiles (of level $\sim 10^{-5} - 10^{-9}$) without restrictive assumptions on the LSS, such as linearity or number of failure

[8] Particular attention is dedicated to making them suitable for failure probabilities and quantile of level in the range $O(10^{-5} - 10^{-9})$.

modes. Inspired from [Echard et al., 2011], the parallel surrogate refinement strategy is enriched with an additional level of parallelization, which is also compatible with the seminal quantile algorithm [Schöbi et al., 2016]. To the knowledge of the author, no method in the open literature is suitable for such challenging problem.

Robust design optimization methods applied to ORC Turbine Cascade

- **Uncertainty Quantification Analysis applied to ORC Turbine Cascade**
  Among the first studies in the open Literature on ORC power systems, the application of advanced Uncertainty Quantification techniques to the analysis of a typical supersonic turbine cascade, including a detailed characterization of the geometric uncertainties is investigated. Multiple sources of uncertainty are taken into account, related to the geometric tolerances of the blade, the operating conditions, and some parameters of the thermodynamic model. Furthermore, the method for computing small failure probability, illustrated in the previous part of the manuscript, is used to explore a failure scenario for an ORC turbine.

- **Quantile-based Robust Optimization of an ORC Turbine cascade**
  A quantile-based Robust shape optimization under probabilistic constraint is developed considering a nested approach and applied to the design of a supersonic ORC turbine cascade. The performances of the proposed algorithm are systematically compared to the results of a mean-based RO.

–8 Outline of the Manuscript

This thesis is divided into two parts. The first part focuses on Rare Events methods as contributions for the extension of RBDO methods suitable for extreme (rare) events. The second part deals with the formulation of RO methods applied to ORC Turbine cascade. The first Chapter is intended as providing a mathematical background.

Chapter 1 presents a set of mathematical tools necessary for the understanding of the thesis. General principles of Uncertainty Quantification and the theory of probability are concisely introduced. Details about Kriging surrogate-modeling are then presented. Finally, kriging-based forward uncertainty propagation, including the estimation of statistics or sensitivity indices, is illustrated. This chapter does not feature any original contribution.

Part A: Rare Events

This part aims at describing numerical methods applied in two specific problems related to rare event estimation: small failure probability and extreme quantile estimation. The methods developed are specifically designed to be suitable in the case of so-called *multiple failure regions*, to remain applicable for admissible failure probabilities (or quantile level) ranging from 10^{-2} to 10^{-9}, and characterized by a *direct* adaptive sampling strategy (*i.e.* aiming at *directly* refine the so-called Limit-State-Surface). The

performance function is assumed to be the output of an expensive to evaluate simulation code. Hence only a reasonable number of evaluations is possible (less than a few hundred).

Chapter II is intended to introduce the general framework of the rare events methods presented in the first part of the manuscript, including academic test-cases and general concepts such as Importance Sampling.

Chapter III aims at describing a method for the *unbiased* computation of small failure probabilities. A novel algorithm suitable for low-failure probability and multiple-failure regions is proposed, which permits to both build an accurate metamodel and provide a statistically consistent error. A Gaussian mixture-based importance sampling technique is proposed, permitting to drastically reduce the computational cost when estimating some reference values, or the failure probability directly from the metamodel.

Chapter IV presents an easy to implement method permitting to perform efficient estimation of very small failure probability, based on a parallel refinement strategy which *directly* (unlike Bayesian Subset Simulation [Bect et al., 2017]) aims at refining the LSS.

Chapter V is devoted to a Quantile Estimation framework, Kriging surrogate modeling based. Similarly to the strategy presented in [Schöbi et al., 2016], the surrogate is adaptively refined using the parallel infill refinement provided by the failure probability estimation method developed in Chapter IV). Finally, a multi-quantile selection approach allowing to exploit high-performance computing architectures one level further is elaborated.

Part B: Robust Optimization Methods for ORC Turbine Cascade

The second part is focused on the application of an original RO method to the Shape Design of a supersonic ORC Turbine cascade. In particular, a comprehensive *Uncertainty Quantification* (UQ) analysis accounting for operational, fluid parameters and geometric (aleatoric) uncertainties permits to provide a general overview over the impact of multiple effects and constitutes a preliminary study necessary for RO.

Chapter VI introduces the turbine configuration of interest, which is a well known axial-flow supersonic nozzle cascade operating with the siloxane MDM. The numerical framework including, in particular, the CFD solver, the parametrization, the mesh tools and the geometric variability modeling is described.

Chapter VII aims at presenting the outcomes of efficient surrogate-based uncertainty propagation methods performed on the axial supersonic turbine cascade introduced in Chapter VI. The impact of operational, fluid parameters and geometric uncertainties on different QoI such as the total pressure or the mass-flow rate is analyzed and provides a general overview over the influence of multiple effects. A failure scenario is also investigated, by applying one of the methods illustrated in the first part of the manuscript.

Chapter VIII is devoted to a quantile-based mono-objective RO formulation applied to the design of the 2D profile of a supersonic turbine cascade, under a probabilistic constraint: the mean mass-flow rate is constrained to be with a prescribed range. Comparison with constrained DO and a classical RO approach, *i.e.* minimizing the mean of the performance function subject to the same constraint, are illustrated.

A deep understanding of Chapter I is not necessary, even if it is essential to recall some fundamental results about Kriging predictors, their application to forward uncertainty propagation and some probabilistic concepts such as Random Vectors and Random Processes. Despite Part A and B are almost independent, both are intended to be read in chronological order as some sections feature fundamental concepts that are always being referred to in the subsequent ones.

I

Surrogate Modeling and Uncertainty Quantification

Overview *A set of mathematical tools used throughout this manuscript is presented in this chapter as well as general principles of Uncertainty Quantification. An introduction to the theory of probability concisely introduces classic concepts such as probability space, random vectors and random processes. Details about Kriging surrogate-modeling are then presented. Finally, forward uncertainty propagation techniques permitting in particular the estimation of statistics or sensitivity indices, considering an input random vector affected by aleatoric uncertainty are described.*

Contribution *This chapter does not provide any original contribution. It aims solely at proposing a mathematical background for the reading of the manuscript.*

Introduction

As the speed and power of computer systems continue to grow, computational engineering importance in our society grow in parallel. In particular, *Computational Fluid Dynamics* (CFD), a branch of computational physics aiming at predicting the behavior of fluids in a broad sense play a tremendous role. It is now routinely employed as a design tool in industry as it is in general a more cost-effective and less time-consuming approach than experiments that may be prohibitive. The question of *reliability* of CFD predictions to practical applications is however crucial and has led to focus on the *accuracy* of the predicted simulations by comparing it to experimental measurements [Oberkampf and Barone, 2006], in order to reduce and control modeling and numerical errors (e.g. thermodynamic model, discretization error).

Verification and Validation

This question has led to the subject of *Verification and Validation* (VV) [Mehta, 1991, Roache, 1997, Oberkampf and Trucano, 2002, Hanson, 1999]. The validation process addresses the quality and relevance of the physical model[1], while the verification process aims at determining if the computation model[2] represents the physical model with sufficient accuracy. The verification process, carried out prior to the validation [Babuska and Oden, 2004] involves the code verification (software) and the solution verification (*i.e.* an *a posteriori* error estimation) [Roy, 2005]. The validation process *corroborates* the accuracy of the verified computational model by direct comparison of specific *Quantity of Interest* (QoI) obtained by *experimental data* and predicted simulations [Babuska and Oden, 2004].

Uncertainty Quantification

Previous approaches [Glimm and Sharp, 1999, Stern et al., 2001, Iaccarino et al., 2011] reoriented the question of CFD reliability towards the following one: "How should *confidence* in CFD simulations be *quantitatively* assessed?". The perspective to CFD *uncertainty* in broader sense requires to question about a description of uncertainties, that are generally categorized in two categories.

Aleatory Uncertainty arises because of inherent natural, unpredictable variation in the performance of the system. Aleatory uncertainty is also known as statistical, irreducible, stochastic or variability uncertainty. The knowledge of experts cannot be expected to reduce aleatoric uncertainty although their knowledge may be useful in quantifying the uncertainty. Its randomness is generally modeled as a random vector fully parametrized by its *Probability Density Function* (PDF) in the continuous case, or its discrete counterpart for discrete variables.

[1] The physical model denotes the mathematical/PDE formulation consistent with a scientific theory representing the physical event of interest.

[2] The computational model is composed of both the numerical method (e.g. Finite Volumes/Elements) being the discretized version of the physical model, and the computer code implementing the latter.

Epistemic Uncertainty stems from a lack of knowledge about the behavior of the system that is conceptually resolvable. Epistemic uncertainty is also known as reducible or ignorance uncertainty. Therefore, it may, in principle, be eliminated or reduced with sufficient data, expert judgments, improved numerical approximations, or by refining models. Its randomness is generally represented as an *interval* or a PDF representing a *degree of belief* of the expert.

All stages of CFD predictions might be corrupted by such uncertainties. Uncertainties in the physical model result from mathematical formulations, abstractions, hence are by nature epistemic [Ferson et al., 2008]. Sources of uncertainty in the computational model affect the numerical approximation[3] or the inputs of the model[4].

Within a probabilistic framework modeling these uncertainties (e.g. *evidence theory* [Diaconis and Shafer, 1978], *probability* [Feller, 1958] or *fuzzy set* [Lootsma, 1997]), the initial fluid flow problem is governed by *Stochastic Partial Differential Equations* (SPDE) whose solution is a *Random Process*. From a practical point of view, it requires the following three successive steps:

- *Characterization* (i.e. modeling) of all sources of uncertainty
- *Propagation* of this uncertainty through the computational model
- *Quantification* of the uncertainty on meaningful quantities of interest

These three components constitute the so-called *Uncertainty Quantification* (UQ). An additional step consists in ranking sources of uncertainty by their influence on the solution variability, named *Sensitivity Analysis* (SA).

Three main classes of methods suitable to UQ in CFD is reported here, with an emphasis on the propagation and quantification steps:

- The *sampling* methods [Lootsma, 1996, Rubinstein and Kroese, 1996] include *Monte-Carlo* (MC) based methods which, despite their high robustness even for nonlinear problems, suffer from low convergence rate involving a prohibitive computational cost in most cases.
- The *perturbation*[5] methods [Kleiber and Hien, 1994, Jameson et al., 1998, Cacuci, 2003] take advantage of the computation of partial *derivatives* of the field variables w.r.t. the uncertain parameters, in order for instance to reduce the problem dimensionality or perform gradient-based sensitivity analysis.
- *Surrogate models* are approximate models of the expensive-to-evaluate model of interest, while being computationally cheap to evaluate. Once the surrogate model of the physical quantity of interest is considered accurate enough, it may be exploited at almost no cost by sampling methods for instance. Several methods exist such as linear least square [Trevor Hastie, 2009], polynomial approximations [Freeny, 1988, Draper, 1997] including Polynomial Chaos [Knio and Le Maitre, 2006], Multivariate Adaptive Regression Splines [Victoria

[3] Those sources include discretization errors, round-off errors due to finite precision arithmetic, iterative convergence errors, possibly coding errors.

[4] Modeling parameters, computational domain (geometry), boundary/initial conditions are model inputs that might affect the model.

[5] a.k.a. *sensitivity* or *adjoint* methods.

C. P. Chen and Shoemaker, 1999], *Radial Basis Functions* (RBF), *Artificial Neural Networks* (ANN) [by: Nicholas Lange, 1997], *Support Vector Regression* (SVR) [Bourinet, 2016] and Kriging (a.k.a. Gaussian Process Regression) [C. E. Rasmussen, 2006].

For a detailed review on Uncertainty Quantification methods, see [Ghanem et al., 2017]. In the sequel, and in particular in this section, emphasis will be placed on UQ methods based on Surrogate Models, more precisely Kriging. Its main advantage above aforementioned methods consists in its ability to provide a measure of the epistemic error associated with the prediction at unknown locations.

Section I–1 introduces general probabilistic concepts, Section I–2 describes Kriging surrogate-modeling. Finally, forward uncertainty propagation techniques permitting in particular the estimation of statistics or sensitivity indices, considering an input random vector affected by aleatoric uncertainty are described in Section I–3.

I–1 Probabilistic Concepts

Overview *The purpose of this section is to summarize some general concepts in probability theory used in the sequel.*

Probability Space Let $(\Omega, \mathcal{F}, \mathbb{P})$ denote a *Probability Space* associated with a random experiment, where:

- Ω is the *outcome space*, a.k.a. *event space* whose element ω is an outcome of the experiment.
- the σ-algebra $\mathcal{F}$ is a collection of events whose elements are subsets of Ω.
- $\mathbb{P}$ is a *probability measure* defined on elements of $\mathcal{F}$.

I–1.1 Random Variables

A real-valued random variable

$$\begin{aligned} Y : \ & \Omega \mapsto \mathbb{Y} \subseteq \mathbb{R} \\ & \omega \to Y(\omega) \end{aligned} \tag{I.1}$$

is a measurable function mapping the probability space $(\Omega, \mathcal{F}, \mathbb{P})$ in the measurable output space $\mathbb{Y}$. $y = Y(\omega)$ is denoted as a *realization* of the random variable Y associated to some event $\omega \in \Omega$.

The random variable Y induces a probability space $(\mathbb{Y}, \mathcal{B}(\mathbb{Y}), \mathbb{P}_Y)$. The induced probability measure $\mathbb{P}_Y$ is defined as:

$$\mathbb{P}_Y(S) = \mathbb{P}(\{\omega \in \Omega | Y(\omega) \in S\}), \ \forall S \in \mathcal{B}(\mathbb{Y}). \tag{I.2}$$

$\mathcal{B}(\mathbb{Y})$ denotes the so-called *Borel Algebra* (a.k.a. *Borel Field*) of $\mathbb{Y}$. Y is completely defined by its *Cumulative Density Function* (CDF):

$$F_Y(y) = \mathbb{P}_Y(Y \leq y), \tag{I.3}$$

or equivalently, by its *Probability Density Function* (PDF)[6] f_Y defined as the derivative of the CDF, satisfying:

$$\mathbb{P}_Y(Y \in [a,b]) = \int_{[a,b]} f_Y(y)dy, \ \forall [a,b] \subseteq \mathbb{Y} \tag{I.4}$$

$$f_Y(y) = \frac{dF_Y(y)}{dy}. \tag{I.5}$$

Denoting by $\mathbb{E}$ the *expectation operator* induced by the probability measure $\mathbb{P}_Y$, the mean value of the random variable Y is defined as:

$$\mu_Y = \mathbb{E}[Y] = \int_{\mathbb{Y}} y f_Y(y)dy, \tag{I.6}$$

while the moments (resp. central moments) of order $k > 1$ are defined as:

$$\mathbb{E}[Y^k] = \int_{\mathbb{Y}} y^k f_Y(y)dy \tag{I.7}$$

$$\mathbb{E}[(Y-\mu_Y)^k] = \int_{\mathbb{Y}} (y-\mu_Y)^k f_Y(y)dy \tag{I.8}$$

provided they exist. In particular, the central second-order moment $\sigma_Y^2 = \mathbb{V}[Y]$ is denoted as the *variance* and its square root the *standard deviation*. The so-called *Coefficient of Variation* (CoV) is defined as $\delta_Y \equiv \frac{\sigma_Y}{|\mu_Y|}$, provided $\mu_Y \neq 0$.

The covariance between two random variables X and Y is defined as:

$$\mathrm{Cov}(X,Y) = \mathbb{E}[(X - \mathbb{E}_X[X])(Y - \mathbb{E}_Y[Y])], \tag{I.9}$$

under existence. In Eq. I.9, $\mathbb{E}_X$ and $\mathbb{E}_Y$ refers to the expectation operator linked to the probability measure induced respectively by X and Y, while $\mathbb{E}$ is associated to the joint distribution of (X,Y). In particular:

$$\mathrm{Cov}(Y,Y) = \mathbb{V}[Y]. \tag{I.10}$$

Example: Univariate Gaussian A Gaussian random variable Y is denoted as

$$Y \sim \mathcal{N}(\mu_Y, \sigma_Y^2) \tag{I.11}$$

with $\sigma_Y > 0$. The standard Gaussian random variable is $\frac{Y-\mu_Y}{\sigma_Y} \sim \mathcal{N}(0,1)$, whose PDF ϕ and CDF Φ are defined as:

$$\phi(t) = \frac{1}{\sqrt{2\pi}} \exp\left(-\frac{t^2}{2}\right) \tag{I.12}$$

$$\Phi(t) = \int_{-\infty}^{t} \frac{1}{\sqrt{2\pi}} \exp\left(-\frac{\xi^2}{2}\right) d\xi, \ \forall t \in \mathbb{R}. \tag{I.13}$$

[6] In the manuscript, only continuous random variables admitting a PDF will be considered.

I–1.2 Random Vectors

A random vector

$$\begin{aligned} \boldsymbol{Y}: \ \Omega &\mapsto \mathbb{Y} \subseteq \mathbb{R}^d \\ \omega &\to \boldsymbol{Y}(\omega) \end{aligned} \tag{I.14}$$

is a measurable function mapping the probability space $(\Omega, \mathcal{F}, \mathbb{P})$ in the measurable d-dimensional output space $\mathbb{Y}$. The d components of $\boldsymbol{Y} = (Y_1, ..., Y_d)$ are random variables as defined in Subsection I–1.1. Continuous random vectors are fully defined either by their so-called *joint PDF* $f_{\boldsymbol{Y}}(\boldsymbol{y})$ or *joint CDF* $F_{\boldsymbol{Y}}(\boldsymbol{y})$.

The random vector $\boldsymbol{Y}$ induces a probability space $(\mathbb{Y}, \mathcal{B}(\mathbb{Y}), \mathbb{P}_{\boldsymbol{Y}})$. The induced probability measure $\mathbb{P}_Y$ is defined as:

$$\mathbb{P}_{\boldsymbol{Y}}(S) = \mathbb{P}(\{\omega \in \Omega | \boldsymbol{Y}(\omega) \in S\}), \ \forall S \in \mathcal{B}(\mathbb{Y}). \tag{I.15}$$

The mean value $\boldsymbol{\mu_Y}$ of the random vector $\boldsymbol{Y}$ is defined as

$$\boldsymbol{\mu_Y} = \mathbb{E}[\boldsymbol{Y}] = \int_{\mathbb{Y}} \boldsymbol{y} f_{\boldsymbol{Y}}(\boldsymbol{y}) d\boldsymbol{y}, \tag{I.16}$$

where $\mathbb{E}$ refers to the expectation operator induced by the probability measure $\mathbb{P}_{\boldsymbol{Y}}$.

The symmetric positive-definite covariance matrix of $\boldsymbol{Y}$ is defined as:

$$\boldsymbol{\Sigma} = \mathbb{E}[(\boldsymbol{Y} - \boldsymbol{\mu_Y})(\boldsymbol{Y} - \boldsymbol{\mu_Y})^T] \tag{I.17}$$

$$= \mathbb{E}[\boldsymbol{Y}\boldsymbol{Y}^T] - \mathbb{E}[\boldsymbol{Y}]\mathbb{E}[\boldsymbol{Y}]^T. \tag{I.18}$$

In particular:

$$\boldsymbol{\Sigma}^{(ij)} = \mathrm{Cov}(Y_i, Y_j). \tag{I.19}$$

Example: Multivariate Gaussian A d-dimensional Gaussian random vector $\boldsymbol{Y}$ is denoted as

$$\boldsymbol{Y} \sim \mathcal{N}_d(\boldsymbol{\mu_Y}, \boldsymbol{\Sigma_Y}), \tag{I.20}$$

with $\boldsymbol{\Sigma_Y} \in \mathbb{R}^{d \times d}$ and $\boldsymbol{\mu_Y} \in \mathbb{R}^d$ denoting respectively the symmetric positive definite covariance matrix and the mean of $\boldsymbol{Y}$. Its PDF $f_{\boldsymbol{Y}}$ is defined as:

$$f_{\boldsymbol{Y}}(\boldsymbol{y}) = \frac{1}{\sqrt{|\boldsymbol{\Sigma_Y}|(2\pi)^n}} \exp\left(-\frac{1}{2}(\boldsymbol{y}^T - \boldsymbol{\mu_Y})\boldsymbol{\Sigma_Y}^{-1}(\boldsymbol{y}^T - \boldsymbol{\mu_Y})\right), \tag{I.21}$$

$|\boldsymbol{\Sigma_Y}|$ referring to the determinant of the invertible matrix $\boldsymbol{\Sigma_Y}$. More details about Gaussian Vectors can be found [Dubourg, 2011], Appendix A.

I–1.3 Random Processes a.k.a. Random Fields

Given a probability space $(\Omega, \mathcal{F}, \mathbb{P})$, a continuous random process Y is defined as a collection of random variables[7] indexed by elements in a topological space $\mathbb{X} \subseteq \mathbb{R}^d$:

$$Y = \{Y(\boldsymbol{x}) : \Omega \mapsto \mathbb{R}, \ \boldsymbol{x} \in \mathbb{X}\}, \tag{I.22}$$

[7] Only real-valued random field $Y(\boldsymbol{x}, \omega) \in \mathbb{Y} \subseteq \mathbb{R}$ are considered in the sequel.

where, for $\boldsymbol{x} \in \mathbb{X}$, $Y(\boldsymbol{x})$ is a random variable (See Subsection I–1.1). Note that a random field is another term for stochastic process in modern mathematics, with some restriction on its index set: the underlying parameter is no longer a real or integer valued *time*.
Equivalently, it can be seen as an application mapping $\mathbb{X} \times (\Omega, \mathcal{F}, \mathbb{P})$ to the domain $\mathbb{Y}$:

$$\begin{aligned} Y : \ & \mathbb{X} \times \Omega \mapsto \mathbb{Y} \subseteq \mathbb{R} \\ & (\boldsymbol{x}, \omega) \to Y(\boldsymbol{x}, \omega) \end{aligned} \tag{I.23}$$

For $\omega_0 \in \Omega$, $y(\boldsymbol{x}) \equiv Y(\boldsymbol{x}, \omega_0)$ denotes a *realization* or *sample path* of the underlying random field, which is a function of $\boldsymbol{x} \in \mathbb{X}$.

Example: Gaussian Process A random field Y is said to be Gaussian if, for any $(\boldsymbol{x}_1, ..., \boldsymbol{x}_m) \in \mathbb{X}^m$, the random vector $(Y(\boldsymbol{x}_1), ..., Y(\boldsymbol{x}_m))$ is a m-dimensional Gaussian vector. A so-called Gaussian process (or field) is a second-order random process completely defined by its mean function $\mu : \mathbb{X} \mapsto \mathbb{Y}$ and its autocovariance function $C : \mathbb{X} \times \mathbb{X} \mapsto \mathbb{Y}$, defined by:

$$\mu(\boldsymbol{x}) \equiv \mathbb{E}[Y(\boldsymbol{x})] \tag{I.24}$$

$$C(\boldsymbol{x}, \boldsymbol{x}') \equiv \mathbb{E}[(Y(\boldsymbol{x}) - \mu(\boldsymbol{x}))(Y(\boldsymbol{x}') - \mu(\boldsymbol{x}'))], \ \forall \boldsymbol{x}, \ \boldsymbol{x}' \in \mathbb{X}. \tag{I.25}$$

Note that admissible autocovariance function C must be symmetric and semi-positive, namely:

$$C(\boldsymbol{x}, \boldsymbol{x}') = C(\boldsymbol{x}', \boldsymbol{x}), \ \forall \boldsymbol{x}, \ \boldsymbol{x}' \in \mathbb{X} \tag{I.26}$$

$$\sum_{i,j=1}^{k} \alpha_i \alpha_j C(\boldsymbol{x}_i, \boldsymbol{x}_j) \geq 0, \forall (\boldsymbol{x}_1, ..., \boldsymbol{x}_k) \in \mathbb{X}^k, \ (\alpha_1, ..., \alpha_k) \in \mathbb{R}^k. \tag{I.27}$$

In the sequel, only events which are outcomes in the Borel probability space $(\mathbb{Y}, \mathcal{B}(\mathbb{Y}), \mathbb{P}_Y)$, with $\mathbb{Y} \subseteq \mathbb{R}^d$, induced by some random vector/variable $\boldsymbol{Y}$ will be considered. For a sake of readability, except when explicitly highlighted, the expectation $\mathbb{E}$ and variance $\mathbb{V}$ operators refer to the induced probability measure $\mathbb{P}_Y$. In that framework, there will be no need to work within the so-called base space *or* underlying probability space $(\Omega, \mathcal{F}, \mathbb{P})$.

I–2 Kriging

Overview *In this section, general details about* Simple/Universal Kriging *in the noiseless cases are provided. In particular, predictors derivations, hyperparameter selection and implementation details are given.*

For comprehensive details about Kriging, the reader may refer to well-known references [Cressie, 1992] [Stein, 2012] [Santner et al., 2013] [Rasmussen and Williams, 2006]. More concise descriptions can be found in [Dubourg, 2011] [Bourinet, 2018] [Roustant et al., 2012].

The objective is to construct an approximation $\tilde{y}$ of a true (expensive to evaluate) unknown function $y : \mathbb{X} \subseteq \mathbb{R}^d \to \mathbb{Y} \subseteq \mathbb{R}$, based on a training set of size $n \in \mathbb{N}^*$ (a.k.a. *Design of Experiment* (DoE)) $\mathcal{T} = \{\boldsymbol{x}_i, y_i\}_{i \in [\![1,n]\!]}$, where $y_i = y(\boldsymbol{x}_i)$. In the framework of the probabilistic space $(\Omega, \mathcal{F}, \mathbb{P})$, the output of the deterministic computer experiment y is assumed to be a *realization* of a real-valued Gaussian process Y indexed over $\mathbb{X}$. The set of the observed outputs $\{y_i\}_i$ then appear as respective realizations of the random process $\{Y(\boldsymbol{x}_i)\}_i$. For $\boldsymbol{x} \in \mathbb{X}$, we assume $Y(\boldsymbol{x})$ of the form:

$$Y(\boldsymbol{x}) = \mu(\boldsymbol{x}) + Z(\boldsymbol{x}), \tag{I.28}$$

with $\mu(x)$ being the mean of $Y(\boldsymbol{x})$ and $Z(\cdot)$ being a zero mean stationary random process, fully characterized by its symmetric positive definite autocovariance function (a.k.a. covariance kernel) satisfying:

$$k(\boldsymbol{x}, \boldsymbol{x}') = \mathrm{Cov}[Z(\boldsymbol{x}), Z(\boldsymbol{x}')] = \mathbb{E}[Z(\boldsymbol{x})Z(\boldsymbol{x}')], \ \forall \boldsymbol{x}, \ \boldsymbol{x}'. \tag{I.29}$$

The specific case of a known mean function μ is equivalent to consider the Kriging formulation Equation I.30, applying the affine map $y \leftarrow y - \mu$, known as *Simple Kriging* (SK):

$$Y(\boldsymbol{x}) = Z(\boldsymbol{x}). \tag{I.30}$$

Assuming the mean μ as a linear combination of so-called *basis functions* leads to the so-called *Universal Kriging* (UK) formulation:

$$Y(\boldsymbol{x}) = \boldsymbol{f}(\boldsymbol{x})^T \boldsymbol{\beta} + Z(\boldsymbol{x}), \tag{I.31}$$

where $\boldsymbol{f} : \mathbb{X} \to \mathbb{R}^p$, $\boldsymbol{f}(\boldsymbol{x}) = (f_1(\boldsymbol{x}), ..., f_p(\boldsymbol{x}))$ is a map of $p \in \mathbb{N}^*$ user-defined basis functions and $\boldsymbol{\beta} \in \mathbb{R}^p$ is an unknown vector of weights to be determined. Note that the particular case of UK where $\boldsymbol{f}$ boils down to $\boldsymbol{x} \mapsto 1$ is known as *Ordinary Kriging* (OK), leading to:

$$Y(\boldsymbol{x}) = \beta_0 + Z(\boldsymbol{x}), \tag{I.32}$$

with $\beta_0 \in \mathbb{R}$ being the unknown constant trend.

I–2.1 Kriging Predictors

Considering a given $\boldsymbol{x} \in \mathbb{X}$ (untried location), the objective of Kriging, belonging to the more general Bayesian prediction methodology, is to derive a random predictor $\hat{Y}(\boldsymbol{x})$ of the unknown random process Y at $\boldsymbol{x}$. In particular, it is assumed that the vector gathering the observations $\boldsymbol{y} = (y_1, ..., y_n)$ and the unobserved $y(\boldsymbol{x})$ is a realization of a random vector according to a joint parametric distribution $F \in \mathcal{F}$. This class of distributions is restricted in this manuscript to multivariate Gaussian distribution due to its convenience, and the intrisic properties satisfied by the predictor are detailed in the following.

The so-called *Best Linear Unbiased Predictor* (BLUP) $\hat{Y}(\boldsymbol{x})$ is considered, satisfying the following properties:

- Linear: a vector $\boldsymbol{\lambda} \equiv \boldsymbol{\lambda}(\boldsymbol{x}) \in \mathbb{R}^n$ permits to write

$$\hat{Y}(\boldsymbol{x}) = \sum_{i=1}^{n} \lambda_i Y(\boldsymbol{x}_i) = \boldsymbol{\lambda}^T \boldsymbol{Y}, \tag{I.33}$$

where $\boldsymbol{Y} = (Y(\boldsymbol{x}_1), ..., Y(\boldsymbol{x}_n))$ is the vector of the unknown random process at the observation points $\boldsymbol{x}_i$, and $\boldsymbol{\lambda} \in \mathbb{R}^n$. Predictors may have any functional form w.r.t. observations $\boldsymbol{Y}$, although most practical applications reduce to linear predictors.

- Unbiasedness:
$$\mathbb{E}[\hat{Y}(\boldsymbol{x}) - Y(\boldsymbol{x})] = 0. \tag{I.34}$$

- Best (in the mean square sense): $\hat{Y}(\boldsymbol{x})$ minimizes the quadratic risk among all linear and unbiased predictors
$$\hat{Y}(\boldsymbol{x}) = \underset{\text{s.t. } \hat{Y}^*(\boldsymbol{x}) \text{ Linear and Unbiased}}{\text{Argmin}} \quad \mathbb{E}[(\hat{Y}^*(\boldsymbol{x}) - Y(\boldsymbol{x}))^2]. \tag{I.35}$$

The Kriging mean predictor is defined as:

$$\mu_{\hat{Y}}(\boldsymbol{x}) = \mathbb{E}[\hat{Y}(\boldsymbol{x})]. \tag{I.36}$$

The estimation of the *Mean Square Error* (MSE) a.k.a. the Kriging variance predictor yields:

$$\sigma^2_{\hat{Y}}(\boldsymbol{x}) = \mathbb{E}[(\hat{Y}(\boldsymbol{x}) - Y(\boldsymbol{x}))^2]. \tag{I.37}$$

while the surrogate $\tilde{y}(\boldsymbol{x})$ for $y(\boldsymbol{x})$ is simply taken as:

$$\tilde{y}(\boldsymbol{x}) = \mu(\boldsymbol{x}). \tag{I.38}$$

In the following, details permitting to derive the expression of the BLUP $\hat{Y}(\boldsymbol{x})$ are provided, distinguishing between the SK and UK cases. The corresponding mean and variance predictors are consequently given.

I–2.1.1 Simple Kriging Predictor

In the case of Simple Kriging (Eq I.30), the unbiasedness property is implicitly satisfied. Indeed,

$$\mathbb{E}[\hat{Y}(\boldsymbol{x}) - Y(\boldsymbol{x})] = \sum_{i=1}^{n} \lambda_i \mathbb{E}[Y(\boldsymbol{x}_i)] - \mathbb{E}[Y(\boldsymbol{x})] = 0, \tag{I.39}$$

by virtue of $\mathbb{E}[Y(\boldsymbol{x})] = \mathbb{E}[Z(\boldsymbol{x})] = 0$ for SK, and the linearity of the expectation operator.

The problem of finding $\hat{Y}(\boldsymbol{x})$ is equivalent to finding a vector $\boldsymbol{\lambda} \in \mathbb{R}^n$ solution of the following unconstrained optimization problem:

$$\begin{aligned} \boldsymbol{\lambda} &= \underset{\boldsymbol{\lambda}^* \in \mathbb{R}^n}{\text{Argmin}} \; J(\boldsymbol{\lambda}^*) \\ J(\boldsymbol{\lambda}^*) &= \mathbb{E}\left[\left(\sum_{i=1}^{n} \lambda_i^* Y(\boldsymbol{x}_i) - Y(\boldsymbol{x}) \right)^2 \right], \end{aligned} \tag{I.40}$$

J being the cost function to minimize.
Using the relation $\mathbb{E}[Y(\boldsymbol{x})Y(\boldsymbol{x}')] = \mathbb{E}[Z(\boldsymbol{x})Z(\boldsymbol{x}')] = k(\boldsymbol{x}, \boldsymbol{x}')$, J is re-written in matricial form:

$$J(\boldsymbol{\lambda}^*) = \sum_{i,j=1}^{n} \lambda_i^* \lambda_j^* k(\boldsymbol{x}_i, \boldsymbol{x}_j) - 2\sum_{i=1}^{n} \lambda_i^* k(\boldsymbol{x}_i, \boldsymbol{x}) + k(\boldsymbol{x}, \boldsymbol{x})$$
$$= \boldsymbol{\lambda}^{*^T} \boldsymbol{K} \boldsymbol{\lambda}^* - 2\boldsymbol{\lambda}^{*^T} \boldsymbol{k}(\boldsymbol{x}) + k(\boldsymbol{x}, \boldsymbol{x}), \tag{I.41}$$

where $\boldsymbol{K} = (k(\boldsymbol{x}_i, \boldsymbol{x}_j))_{i,j} \in \mathbb{R}^{n \times n}$ is the symmetric positive (definite under conditions on $(\boldsymbol{x}_i)_i$ and k) covariance matrix of the random variables $\{Y(\boldsymbol{x}_i)\}_i$ representing the *correlation* between the observed points. The covariance vector between the untried $\boldsymbol{x}$ and the observed points is denoted as $\boldsymbol{k}(\boldsymbol{x}) = (k(\boldsymbol{x}_i, \boldsymbol{x}))_i \in \mathbb{R}^n$. The first-order optimality condition reads

$$\nabla J(\boldsymbol{\lambda}) = 0$$
$$\iff 2\boldsymbol{K}\boldsymbol{\lambda} - 2\boldsymbol{k}(\boldsymbol{x}) = 0. \tag{I.42}$$

Assuming that all observed points are different, and using a positive definite kernel k, the matrix $\boldsymbol{K}$ is full rank, therefore invertible. The optimal weights read:

$$\boldsymbol{\lambda} = \boldsymbol{K}^{-1} \boldsymbol{k}(\boldsymbol{x}). \tag{I.43}$$

The BLUP $\hat{Y}(\boldsymbol{x})$ finally reads:

$$\hat{Y}(\boldsymbol{x}) = \boldsymbol{k}(\boldsymbol{x})^T \boldsymbol{K}^{-1} \boldsymbol{Y}. \tag{I.44}$$

By virtue of Eq. I.36, the SK mean predictor is written as:

$$\mu_{SK}(\boldsymbol{x}) = \boldsymbol{k}(\boldsymbol{x})^T \boldsymbol{K}^{-1} \boldsymbol{y}. \tag{I.45}$$

The SK variance predictor (Eq. I.37) reads:

$$\sigma_{SK}^2(\boldsymbol{x}) = J(\boldsymbol{\lambda})$$
$$= k(\boldsymbol{x}, \boldsymbol{x}) - \boldsymbol{k}(\boldsymbol{x})^T \boldsymbol{K}^{-1} \boldsymbol{k}(\boldsymbol{x}). \tag{I.46}$$

It's worth noting that the variance predictor $\sigma_{SK}^2(\boldsymbol{x})$ does not depend on the vector of observations $\boldsymbol{y}$.

I–2.1.2 Universal Kriging (Kriging with a trend)

Within that framework, the random process $Y(\boldsymbol{x})$ at un unknown location $\boldsymbol{x} \in \mathbb{X}$ is assumed to be the sum of two terms, respectively denoted as the *drift* (or trend) and *residual* $Z(\boldsymbol{x})$:

$$Y(\boldsymbol{x}) = \boldsymbol{f}(\boldsymbol{x})^T \boldsymbol{\beta} + Z(\boldsymbol{x}), \tag{I.47}$$

where $\boldsymbol{f}(\boldsymbol{x})^T \boldsymbol{\beta}$ is the unknown mean, and $Z(\boldsymbol{x})$ the null mean random process defined by its covariance kernel k Eq. I.29.

The following equalities consequently hold:

$$\mathbb{E}[Y(\boldsymbol{x})] = \boldsymbol{f}(\boldsymbol{x})^T \boldsymbol{\beta} \tag{I.48}$$
$$\mathbb{E}[(Y(\boldsymbol{x}) - \boldsymbol{f}(\boldsymbol{x})^T \boldsymbol{\beta})^2] = \mathbb{E}[Z(\boldsymbol{x})^2] = k(\boldsymbol{x}, \boldsymbol{x}). \tag{I.49}$$

Based on the derivation

$$\begin{aligned}\hat{Y}(\boldsymbol{x}) - Y(\boldsymbol{x}) &= \boldsymbol{\lambda}^T \boldsymbol{Y} - Y(\boldsymbol{x}) \\ &= \boldsymbol{\lambda}^T (\boldsymbol{F}\boldsymbol{\beta} + \boldsymbol{Z}) - (\boldsymbol{f}(\boldsymbol{x})^T \boldsymbol{\beta} + Z(\boldsymbol{x})) \\ &= \boldsymbol{\lambda}^T \boldsymbol{Z} - Z(\boldsymbol{x}) + (\boldsymbol{\lambda}^T \boldsymbol{F} - \boldsymbol{f}(\boldsymbol{x})^T)\boldsymbol{\beta}, \end{aligned} \tag{I.50}$$

with $\boldsymbol{F} = [\boldsymbol{f}(\boldsymbol{x}_1)^T, ..., \boldsymbol{f}(\boldsymbol{x}_n)^T] \in \mathbb{R}^{n \times p}$ and $\boldsymbol{Z} = (Z(\boldsymbol{x}_1), ..., Z(\boldsymbol{x}_n))$, the unbiasedness constraint of the BLUP $\hat{Y}(\boldsymbol{x})$ is obtained as

$$\begin{aligned} &\mathbb{E}[\hat{Y}(\boldsymbol{x}) - Y(\boldsymbol{x})] &&= 0 \\ \Leftrightarrow &\boldsymbol{\lambda}^T \mathbb{E}[\boldsymbol{Z}] - E[Z(\boldsymbol{x})] + (\boldsymbol{\lambda}^T \boldsymbol{F} - \boldsymbol{f}(\boldsymbol{x})^T)\boldsymbol{\beta} &&= 0 \\ \Leftrightarrow &\boldsymbol{F}^T \boldsymbol{\lambda} - \boldsymbol{f}(\boldsymbol{x}) &&= 0. \end{aligned} \tag{I.51}$$

The quadratic risk expression, under the unbiasedness constraint, reads the same expression as in the SK case Eq. I.41:

$$\begin{aligned}\mathbb{E}[(\hat{Y}(\boldsymbol{x}) - Y(\boldsymbol{x}))^2] &= \mathbb{E}[(\boldsymbol{\lambda}^T \boldsymbol{Z} - Z(\boldsymbol{x}) + \boldsymbol{\beta}^T (\boldsymbol{F}^T \boldsymbol{\lambda} - \boldsymbol{f}(\boldsymbol{x})))^2] \\ &= \mathbb{E}[(\boldsymbol{\lambda}^T \boldsymbol{Z} - Z(\boldsymbol{x}))^2]. \end{aligned} \tag{I.52}$$

The optimization problem consisting in finding the set of optimal weights $\boldsymbol{\lambda} \in \mathbb{R}$ then reads:

$$\boldsymbol{\lambda} = \underset{\boldsymbol{\lambda}^* \in \mathbb{R}^n \text{ s.t. } \boldsymbol{F}^T \boldsymbol{\lambda}^* - \boldsymbol{f}(\boldsymbol{x}) = 0}{\operatorname{Argmin}} J(\boldsymbol{\lambda}^*). \tag{I.53}$$

The Lagrange multiplier $\boldsymbol{\mu} \in \mathbb{R}^p$ is introduced to enforce the equality constraint. The optimization problem re-written in Lagrangian form reads:

$$\begin{aligned} \boldsymbol{\mu}, \boldsymbol{\lambda} &= \underset{(\boldsymbol{\mu}^*, \boldsymbol{\lambda}^*) \in \mathbb{R}^p \times \mathbb{R}^n}{\operatorname{Argmin}} L(\boldsymbol{\mu}^*, \boldsymbol{\lambda}^*) \\ L(\boldsymbol{\mu}^*, \boldsymbol{\lambda}^*) &= J(\boldsymbol{\lambda}^*) + \boldsymbol{\mu}^{*^T} (\boldsymbol{F}^T \boldsymbol{\lambda}^* - \boldsymbol{f}(\boldsymbol{x})). \end{aligned} \tag{I.54}$$

The first-order optimality conditions of this unconstrained optimization problem read:

$$\begin{aligned} \nabla_{\boldsymbol{\lambda}^*} L(\boldsymbol{\lambda}, \boldsymbol{\mu}) &= 2\boldsymbol{K}\boldsymbol{\lambda} - 2\boldsymbol{k}(\boldsymbol{x}) + \boldsymbol{F}\boldsymbol{\mu} &&= 0 \\ \nabla_{\boldsymbol{\mu}^*} L(\boldsymbol{\lambda}, \boldsymbol{\mu}) &= \boldsymbol{F}^T \boldsymbol{\lambda} - \boldsymbol{f}(\boldsymbol{x}) &&= 0, \end{aligned} \tag{I.55}$$

leading to the vector of optimal weights $\boldsymbol{\lambda}$:

$$\boldsymbol{\lambda} = \boldsymbol{K}^{-1}\boldsymbol{k}(\boldsymbol{x}) - \boldsymbol{K}^{-1}\boldsymbol{F}(\boldsymbol{F}^T \boldsymbol{K}^{-1} \boldsymbol{F})^{-1}(\boldsymbol{F}^T \boldsymbol{K}^{-1}\boldsymbol{k}(\boldsymbol{x}) - \boldsymbol{f}(\boldsymbol{x})). \tag{I.56}$$

Defining

$$\hat{\boldsymbol{\beta}} = (\boldsymbol{F}^T \boldsymbol{K}^{-1} \boldsymbol{F})^{-1} \boldsymbol{F}^T \boldsymbol{K}^{-1} \boldsymbol{y}, \tag{I.57}$$

the UK predictive mean $\mu_{UK}(\boldsymbol{x}) = \mathbb{E}[\boldsymbol{\lambda}^T \boldsymbol{Y}]$ reduces to:

$$\mu_{UK}(\boldsymbol{x}) = \boldsymbol{k}^T(\boldsymbol{x}) \boldsymbol{K}^{-1} (\boldsymbol{y} - \boldsymbol{F}\hat{\boldsymbol{\beta}}) + \boldsymbol{f}(\boldsymbol{x})^T \hat{\boldsymbol{\beta}}. \tag{I.58}$$

The UK predictive variance $\sigma^2_{UK}(\boldsymbol{x}) = \mathbb{E}[(\hat{Y}(\boldsymbol{x}) - Y(\boldsymbol{x}))^2]$ is written as:

$$\sigma^2_{UK}(\boldsymbol{x}) = k(\boldsymbol{x}, \boldsymbol{x}) - k^T(\boldsymbol{x}) \boldsymbol{K}^{-1} \boldsymbol{k}(\boldsymbol{x}) + u^T(\boldsymbol{x}) (\boldsymbol{F}^T \boldsymbol{K}^{-1} \boldsymbol{F})^{-1} u(\boldsymbol{x}), \tag{I.59}$$

with $u(\boldsymbol{x}) = \boldsymbol{F}^T \boldsymbol{K}^{-1} \boldsymbol{k}(\boldsymbol{x}) - \boldsymbol{f}(\boldsymbol{x})$.

I–2.2 Kriging Properties

We recall few properties verified in this framework where no additional noise is considered on the observations.

Exact Interpolator We first observe that

$$\begin{aligned} \boldsymbol{k}(\boldsymbol{x}_i)^T \boldsymbol{K}^{-1} \boldsymbol{Y} &= Y(\boldsymbol{x}_i) \\ \boldsymbol{k}(\boldsymbol{x}_i)^T \boldsymbol{K}^{-1} \boldsymbol{F} &= \boldsymbol{f}(\boldsymbol{x}_i)^T. \end{aligned} \tag{I.60}$$

It is then easy to show that for SK/UK:

$$\hat{Y}(\boldsymbol{x}_i) = Y(\boldsymbol{x}_i), \tag{I.61}$$

yielding to the Kriging interpolation property:

$$\mu_{\hat{Y}}(\boldsymbol{x}_i) = y_i. \tag{I.62}$$

Null Variance at observed points, is a natural consequence of Eq I.61:

$$\sigma^2_{\hat{Y}}(\boldsymbol{x}_i) = \mathbb{E}[(\hat{Y}(\boldsymbol{x}_i) - Y(\boldsymbol{x}_i))^2] = 0. \tag{I.63}$$

Gaussian Process Assumption As mentioned earlier, the Kriging prediction methodology does not require the Gaussian assumption for the underlying random process Y: only assumptions of square integrability[8] are required in the BLUP derivations. The Gaussian assumption is hence transmitted to the BLUP predictor $\hat{Y}(\boldsymbol{x})$ as a linear combination of $Y(\boldsymbol{x}_i)$. It leads to the following property of practical importance:

$$\hat{Y}(\boldsymbol{x}) = \mathcal{N}(\mu_{\hat{Y}}(\boldsymbol{x}), \sigma^2_{\hat{Y}}(\boldsymbol{x})). \tag{I.64}$$

This enables straightforward analytic calculations such as confidence intervals, with probability $1-\alpha$, $\alpha \in [0,1]$:

$$\hat{Y}(\boldsymbol{x}) \in [\mu_{\hat{Y}}(\boldsymbol{x}) - \Phi^{-1}\left(1-\frac{\alpha}{2}\right)\sigma_{\hat{Y}}(\boldsymbol{x}); \mu_{\hat{Y}}(\boldsymbol{x}) + \Phi^{-1}\left(1-\frac{\alpha}{2}\right)\sigma_{\hat{Y}}(\boldsymbol{x})], \text{ with probability } 1-\alpha, \tag{I.65}$$

or

$$\mathcal{P}(\hat{Y}(\boldsymbol{x}) \in [a,b]) = \Phi\left(\frac{a-\mu_{\hat{Y}}(\boldsymbol{x})}{\sigma_{\hat{Y}}(\boldsymbol{x})}\right)\left(1-\Phi\left(\frac{b-\mu_{\hat{Y}}(\boldsymbol{x})}{\sigma_{\hat{Y}}(\boldsymbol{x})}\right)\right), \tag{I.66}$$

with $a, b \in \mathbb{R}$, $\alpha \in [0,1]$ and $\mathcal{P}$ referring to the probability measure associated to the Gaussian random variable $\hat{Y}(\boldsymbol{x})$.

Noisy Data In cases where the true model y is characterized by a stochastic nature, the interpolation property is no longer required. The training set is then assumed to be composed of *noisy* observations modeled as:

$$y_i = y(\boldsymbol{x}_i) + \epsilon_i, \tag{I.67}$$

[8] or equivalently second-order statistics existence

$y(\boldsymbol{x})$ being the true output, where the noises ϵ_i are assumed to be independent zero-mean Gaussian random variables with a variance τ_i^2. In Kriging equations, the covariance matrix $\boldsymbol{K}$ is replaced by $\boldsymbol{K}+\Omega$, $\Omega = \mathrm{diag}(\tau_1^2, ..., \tau_n^2)$. The main consequences of such an assumption are the loss of the interpolation property, and the predictive variance does not vanish at the observation points. In the particular case where $\tau^2 = \tau_1^2 = ... = \tau_n^2$, the covariance matrix $\boldsymbol{K}$ is replaced by $\boldsymbol{K} + \tau^2\boldsymbol{I}$, corresponding to the assumption of a homogeneous level of noise.

I–2.3 Covariance Kernel

The choice of a covariance kernel k for a random process is of paramount importance for the accuracy of the predicted output. A usual approach consists in choosing a *stationary* (a.k.a. translation/shift-invariant) covariance kernel, defined in terms of the so-called *autocorrelation* function R:

$$k(\boldsymbol{x}, \boldsymbol{x}') = \sigma^2 R(\boldsymbol{x} - \boldsymbol{x}'),\ \forall x,\ x' \in \mathbb{X}, \tag{I.68}$$

where $\sigma^2 = k(\boldsymbol{x}, \boldsymbol{x})$ is the variance of the process.

The expressions of the Kriging mean and variance predictors re-written in terms of the autocorrelation function R and the variance of the process σ^2 are provided in the following.

Simple Kriging The SK mean and variance predictions rewrite as:

$$\begin{aligned} \mu_{SK}(\boldsymbol{x}) &= \boldsymbol{r}(\boldsymbol{x})^T \boldsymbol{R}^{-1} \boldsymbol{y} \\ \sigma_{SK}^2(\boldsymbol{x}) &= \sigma^2(1 - \boldsymbol{r}(\boldsymbol{x})^T \boldsymbol{R}^{-1} \boldsymbol{r}(\boldsymbol{x})), \end{aligned} \tag{I.69}$$

with $\boldsymbol{r}(\boldsymbol{x}) = (R(\boldsymbol{x} - \boldsymbol{x}_1), ..., R(\boldsymbol{x} - \boldsymbol{x}_n)) \in \mathbb{R}^n$, and $\boldsymbol{R}$ is the symmetric positive definite matrix defined by $\boldsymbol{R} = R(\boldsymbol{x}_i - \boldsymbol{x}_j)_{i,j} \in \mathbb{R}^{n \times n}$, since k is a covariance kernel satisfying the symmetric positive definite function property.

Universal Kriging The UK mean and variance read:

$$\mu_{UK}(\boldsymbol{x}) = \boldsymbol{r}(\boldsymbol{x})^T \boldsymbol{R}^{-1} (\boldsymbol{y} - \boldsymbol{F}\hat{\boldsymbol{\beta}}) + \boldsymbol{f}(\boldsymbol{x})^T \hat{\boldsymbol{\beta}} \tag{I.70}$$

$$\sigma_{UK}^2(\boldsymbol{x}) = \sigma^2(1 - r^T(\boldsymbol{x}) \boldsymbol{R}^{-1} \boldsymbol{r}(\boldsymbol{x}) + u^T(\boldsymbol{x})(\boldsymbol{F}^T \boldsymbol{R}^{-1} \boldsymbol{F})^{-1} u(\boldsymbol{x})), \tag{I.71}$$

with

$$\hat{\boldsymbol{\beta}} = (\boldsymbol{F}^T \boldsymbol{R}^{-1} \boldsymbol{F})^{-1} \boldsymbol{F}^T \boldsymbol{R}^{-1} y \tag{I.72}$$

$$u(\boldsymbol{x}) = \boldsymbol{F}^T \boldsymbol{R}^{-1} \boldsymbol{r}(\boldsymbol{x}) - \boldsymbol{f}(\boldsymbol{x}). \tag{I.73}$$

Two classes of stationary autocorrelation functions are commonly used in literature:

1. Isotropic (or radial), which only depends on the norm of $\boldsymbol{x} - \boldsymbol{x}'$ and not its direction:
$$R(\boldsymbol{x} - \boldsymbol{x}') = R(\| \boldsymbol{x} - \boldsymbol{x}' \|_2), \tag{I.74}$$
where $\| \cdot \|_2$ denotes the usual L_2-norm in $\mathbb{R}^d$.

2. Anisotropic (or separable): a tensor product of stationary univariate kernels is assumed.

$$R(\boldsymbol{x}-\boldsymbol{x}^{'})=\prod_{i=1}^{d}R_i(x_i-x_j^{'}), \tag{I.75}$$

given $\boldsymbol{x}$, $\boldsymbol{x}^{'}\in\mathbb{X}$. In the present manuscript, only anisotropic kernels are considered.

A list of popular autocorrelation functions is given below, depending on $\boldsymbol{\theta}\in\mathbb{R}^{d}_{*,+}$ denoting the vector of *lengthscales* (a.k.a. *scales parameters*) to be determined.

The exponential autocorrelation function The anisotropic exponential autocorrelation function is defined as:

$$R(\boldsymbol{x}-\boldsymbol{x}^{'},\boldsymbol{\theta})=\prod_{i=1}^{d}\exp\left(-\frac{|x_i-x_i^{'}|}{\theta_i}\right). \tag{I.76}$$

Random processes sample paths (function of $\boldsymbol{x}\in\mathbb{X}$) associated to this autocorrelation function are $\mathcal{C}^0$: *continuous* and *nowhere differentiable*.

The squared exponential autocorrelation function (a.k.a. Gaussian RBF) The anisotropic squared exponential autocorrelation function (a.k.a. Gaussian Radial Basis Function) is defined as:

$$R(\boldsymbol{x}-\boldsymbol{x}^{'},\boldsymbol{\theta})=\prod_{i=1}^{d}\exp\left(-\frac{|x_i-x_i^{'}|^2}{2\theta_i^2}\right). \tag{I.77}$$

Random processes sample paths (function of $\boldsymbol{x}\in\mathbb{X}$) associated to the Gaussian RBF autocorrelation function are *infinitely differentiable*.

Matérn $\nu=\frac{3}{2}$ autocorrelation function The anisotropic Matérn $\nu=\frac{3}{2}$ autocorrelation function, belonging to the general family of *Matérn* functions (not detailed here) is defined as:

$$R(\boldsymbol{x}-\boldsymbol{x}^{'},\boldsymbol{\theta})=\prod_{i=1}^{d}\exp\left(-\frac{\sqrt{3}|x_i-x_i^{'}|}{\theta_i}\right)\left(1+\frac{\sqrt{3}|x_i-x_i^{'}|}{\theta_i}\right). \tag{I.78}$$

Random processes sample paths (function of $\boldsymbol{x}\in\mathbb{X}$) associated to the Matérn $\nu=\frac{3}{2}$ autocorrelation function are *once differentiable*.

Matérn $\nu=\frac{5}{2}$ autocorrelation function The anisotropic Matérn $\nu=\frac{5}{2}$ autocorrelation function is defined as:

$$R(\boldsymbol{x}-\boldsymbol{x}^{'},\boldsymbol{\theta})=\prod_{i=1}^{d}\exp\left(-\frac{\sqrt{5}|x_i-x_i^{'}|}{\theta_i}\right)\left(1+\frac{\sqrt{5}|x_i-x_i^{'}|}{\theta_i}+\frac{5|x_i-x_i^{'}|^2}{3\theta_i^2}\right). \tag{I.79}$$

Random processes sample paths (function of $\boldsymbol{x}\in\mathbb{X}$) associated to the Matérn $\nu=\frac{5}{2}$ autocorrelation function are *twice differentiable*.

I–2.4 Hyperparameters Selection

The Kriging predictors SK/UK Equations I.69 I.71 are given considering the following quantities known, denoted in the literature as the *hyperparameters*:

- σ^2, the process variance;
- $\boldsymbol{\theta}$, through the correlation matrix $\boldsymbol{R}$;
- $\boldsymbol{\beta} \in \mathbb{R}^p$, the weights associated to the basis functions for UK.

We discuss here a procedure to fit them. In the following, the dependency between $\boldsymbol{R}$ and $\boldsymbol{\theta}$ is explicitly highlighted by expressing the correlation matrix as $\boldsymbol{R}(\boldsymbol{\theta})$.

Two classic approaches are used in literature:

- *Maximum Likelihood Estimation* (MLE);
- *Cross-Validation* (CV).

I–2.4.1 Maximum Likelihood Estimation

Given a set of data assumed to be distributed according to some mathematical model, MLE consists in maximizing the PDF associated to the random process. The presentation is restricted to noise-free Kriging (see [Roustant et al., 2012], Appendix A for noisy Kriging).

Simple Kriging Observations are assumed to be distributed satisfying $\boldsymbol{Y} \sim \mathcal{N}(0, \sigma^2 \boldsymbol{R}(\boldsymbol{\theta}))$. The so-called *likelihood* of the observations writes:

$$\mathcal{L}(\boldsymbol{y}|\sigma^2, \boldsymbol{\theta}) = \frac{1}{\sqrt{|\boldsymbol{R}(\boldsymbol{\theta})|(2\pi\sigma^2)^n}} \exp\left(-\frac{1}{2\sigma^2}\boldsymbol{y}^T \boldsymbol{R}(\boldsymbol{\theta})^{-1}\boldsymbol{y}\right), \tag{I.80}$$

where $|\boldsymbol{R}(\boldsymbol{\theta})|$ denotes the determinant of $\boldsymbol{R}(\boldsymbol{\theta})$. The optimal $\widehat{\sigma}^2$ and $\hat{\boldsymbol{\theta}}$ are then obtained by maximizing the likelihood, or equivalently, its natural logarithm (a.k.a. log-likelihood):

$$\widehat{\sigma}^2,\ \hat{\boldsymbol{\theta}} = \underset{\sigma^2, \boldsymbol{\theta}}{\text{Argmax}}\, \text{Log}\, \mathcal{L}(\boldsymbol{y}|\sigma^2, \boldsymbol{\theta}). \tag{I.81}$$

$$\text{Log}\, \mathcal{L}(\boldsymbol{y}|\sigma^2, \boldsymbol{\theta}) = -\frac{1}{2}\ln|\boldsymbol{R}(\boldsymbol{\theta})| - \frac{n}{2}\ln(\sigma^2) - \frac{n}{2}\ln(2\pi) - \frac{1}{2\sigma^2}\boldsymbol{y}^T \boldsymbol{R}(\boldsymbol{\theta})^{-1}\boldsymbol{y}. \tag{I.82}$$

The first-order optimality conditions imply:

$$\frac{\partial \text{Log}\, \mathcal{L}(\boldsymbol{y}|\widehat{\sigma}^2, \boldsymbol{\theta})}{\partial \sigma^2} = 0. \tag{I.83}$$

It further leads to the optimal variance process, depending on $\boldsymbol{\theta}$:

$$\widehat{\sigma}^2(\boldsymbol{\theta}) = \frac{1}{n}\boldsymbol{y}^T \boldsymbol{R}(\boldsymbol{\theta})^{-1}\boldsymbol{y}. \tag{I.84}$$

Plugging Eq. I.84 into Eq. I.82 leads to a new expression depending on $\boldsymbol{\theta}$ only:

$$\text{Log}\,\mathcal{L}(\boldsymbol{y}|\widehat{\sigma}^2(\boldsymbol{\theta}),\boldsymbol{\theta}) = -\frac{n}{2}\ln\Psi(\boldsymbol{\theta}) - \frac{n}{2}(\ln(2\pi)+1), \tag{I.85}$$

where the so-called *reduced likelihood* $\Psi(\boldsymbol{\theta})$ is defined as

$$\Psi(\boldsymbol{\theta}) = \widehat{\sigma}^2(\boldsymbol{\theta})|\boldsymbol{R}(\boldsymbol{\theta})|^{\frac{1}{n}}. \tag{I.86}$$

The maximum likelihood estimate $\hat{\boldsymbol{\theta}}$ is consequently the following global optimizer:

$$\hat{\boldsymbol{\theta}} = \underset{\boldsymbol{\theta}}{\text{Argmin}}\,\Psi(\boldsymbol{\theta}). \tag{I.87}$$

Universal Kriging Observations are assumed to be distributed satisfying $\boldsymbol{Y} \sim \mathcal{N}_n(\boldsymbol{f}(\boldsymbol{x})\boldsymbol{\beta}^T, \sigma^2\boldsymbol{R}(\boldsymbol{\theta}))$, so the the likelihood $\mathcal{L}(\boldsymbol{y}|\sigma^2,\boldsymbol{\theta},\boldsymbol{\beta})$ of the observations writes:

$$\mathcal{L}(\boldsymbol{y}|\sigma^2,\boldsymbol{\theta},\boldsymbol{\beta}) = \frac{1}{\sqrt{|\boldsymbol{R}(\boldsymbol{\theta})|(2\pi\sigma^2)^n}}\exp(-\frac{1}{2\sigma^2}(\boldsymbol{y}-\boldsymbol{F}\boldsymbol{\beta})^T\boldsymbol{R}(\boldsymbol{\theta})^{-1}(\boldsymbol{y}-\boldsymbol{F}\boldsymbol{\beta})). \tag{I.88}$$

The first-order optimality conditions applied to the log-likelihood imply

$$\frac{\partial\,\text{Log}\,\mathcal{L}(\boldsymbol{y}|\widehat{\sigma}^2,\boldsymbol{\theta},\hat{\boldsymbol{\beta}})}{\partial\sigma^2} = 0 \tag{I.89}$$

$$\nabla_{\boldsymbol{\beta}}\text{Log}\,\mathcal{L}(\boldsymbol{y}|\widehat{\sigma}^2,\boldsymbol{\theta},\hat{\boldsymbol{\beta}}) = 0. \tag{I.90}$$

It yields the maximum likelihood estimate $\hat{\boldsymbol{\beta}}$ and $\widehat{\sigma}^2$ known as *general least square estimates* depending both on $\boldsymbol{\theta}$:

$$\hat{\boldsymbol{\beta}}(\boldsymbol{\theta}) = (\boldsymbol{F}^T\boldsymbol{R}(\boldsymbol{\theta})^{-1}\boldsymbol{F})^{-1}\boldsymbol{F}^T\boldsymbol{R}(\boldsymbol{\theta})^{-1}\boldsymbol{y} \tag{I.91}$$

$$\widehat{\sigma}^2(\boldsymbol{\theta}) = \frac{1}{n}(\boldsymbol{y}-\boldsymbol{F}\hat{\boldsymbol{\beta}}(\boldsymbol{\theta}))^T\boldsymbol{R}(\boldsymbol{\theta})^{-1}(\boldsymbol{y}-\boldsymbol{F}\hat{\boldsymbol{\beta}}(\boldsymbol{\theta})). \tag{I.92}$$

Note that the expression Eq. I.91 corresponds to the one used to calculate the UK predictive mean (Eq. I.57).

The maximum likelihood estimate $\boldsymbol{\theta}$ is then obtained solving Eq. I.87, similarly to the SK case.

Solving efficiently Eq. I.87 is a central issue in Kriging: the correlation matrix $\boldsymbol{R}(\boldsymbol{\theta})$ is known to suffer from ill-conditioning for several values of $\boldsymbol{\theta}$, while the reduced likelihood Ψ is highly multimodal [Marrel et al., 2008, Lophaven et al., 2002]. Several methods usually combining gradient-free and/or gradient-based (e.g. BFGS) optimization methods have been implemented and discussed in literature. [Han et al., 2010] uses a modified DIRECT algorithm, [GPy, 2012] resorts to a gradient-based method (BFGS) while [Marelli and Sudret, 2014] combines stochastic optimization (genetic algorithms) to identify promising regions and BFGS.

In [Marrel et al., 2008], the authors emphasize that the problem is particularly ill-posed when both the Gaussian RBF and a dense dataset $\mathcal{T}$ in $\mathbb{X}$ are used: the unavoidable noise in observations $\boldsymbol{y}$ combined with the infinite differentiability assumed

by this autocorrelation choice raises numerical inconsistencies. [Vazquez, 2005] recommends the use of Matérn autocorrelation function allowing to control the finite regularity of the experiment through the choice of ν. In the sequel, the Matérn $\nu = \frac{5}{2}$ autocovariance function is used, except when explicitly mentioned.

I–2.4.2 Cross-Validation

Alternatively, cross-validation can be used, using the so-called *Leave-One-Out* (LOO) exact prediction (see [Dubrule, 1983]). For given σ^2, $\boldsymbol{\theta}$, the following matrix B is considered:

Simple Kriging

$$B = \left[\sigma^2 \boldsymbol{R}(\boldsymbol{\theta})\right]^{-1}. \tag{I.93}$$

Universal Kriging

$$B = \begin{bmatrix} \sigma^2 \boldsymbol{R}(\boldsymbol{\theta}) & \boldsymbol{F} \\ \boldsymbol{F}^T & 0 \end{bmatrix}^{-1}. \tag{I.94}$$

If a nugget effect is considered, $\sigma^2 \boldsymbol{R}(\boldsymbol{\theta})$ is replaced by $\sigma^2 \boldsymbol{R}(\boldsymbol{\theta}) + \tau^2 I$. The so-called LOO predictions at the observation point $\boldsymbol{x}_i$ are:

$$\begin{aligned} \mu_{-i} &= -\sum_{j \neq i} \frac{B_{ij}}{B_{ii}} y_j \\ \sigma_{-i} &= \frac{1}{B_{ii}}. \end{aligned} \tag{I.95}$$

More precisely, μ_{-i} and σ_{-i} are respectively the Kriging predictive mean and variance at the observed location $\boldsymbol{x}_i$ considering *the hyperparameters* σ^2 *and* $\boldsymbol{\theta}$, built from the reduced dataset $\mathcal{T}_{-i} = \mathcal{T} \backslash \{\boldsymbol{x}_i, y_i\}$

It permits to estimate a meaningful coefficient of determination valid even for an interpolating model such as the Kriging predictor:

$$Q^2 = 1 - \frac{1}{n} \sum_{i=1}^{n} \left(\frac{\mu_{-i} - y_i}{\sigma_{-i}} \right)^2. \tag{I.96}$$

The higher is Q^2, the better is the predictor, with $Q^2 \leq 1$.

Maximum likelihood estimates are used in the sequel. CV however enables a posteriori tools to analyze the quality of the Kriging surrogate at negligible cost.

I–2.5 Implementation Details

We provide here implementation details, following some recommendations in [Han et al., 2010, Lophaven et al., 2002]. The training set is normalized so $\boldsymbol{x}_i \in [-1, 1]^d$ and $y_i \in [-1, 1]$.

The robustness of the Cholesky decomposition of the correlation matrix $R = LL^T$, with L lower-triangular matrix, depends on its condition number (see [Lophaven et al., 2002] for details), and might fail for ill-conditioned correlation matrix (numerically non positive definite matrix). To resort to this issue, a small noise is added to the diagonal:

$$LL^T = R + \gamma I, \tag{I.97}$$

with $\gamma = (10^3 + n)\epsilon_M$, $\epsilon_M = 2.22 \times 10^{-16}$ working in double precision. It is strictly equivalent to consider a homogeneous noise of variance $\tau^2 = \frac{\gamma}{\sigma^2}$. It implies that the interpolation and the vanishing variance properties at observed points are lost. For ease of implementation, a gradient free method (CMA, [Nikolaus Hansen, 2018]) is used to fit the lengthscale $\boldsymbol{\theta}$, minimizing the reduced likelihood Eq. I.87. As mentioned in [Lophaven et al., 2002], there is no need to tune exactly the hyperparameters.
The lengthscale $\boldsymbol{\theta}$ is sought in $[2d_{min}, 20d_{max}]^d$, with d_{min}, d_{max} defined by:

$$\begin{aligned} d_{min} &= \underset{i,j \in [\![1,n]\!]}{\text{Min}} \| \boldsymbol{x}_i - \boldsymbol{x}_j \|_2 \\ d_{max} &= \underset{i,j \in [\![1,n]\!]}{\text{Max}} \| \boldsymbol{x}_i - \boldsymbol{x}_j \|_2 . \end{aligned} \tag{I.98}$$

I–3 Surrogate-based Uncertainty Quantification

Overview *Forward uncertainty propagation methods permitting in particular the estimation of statistics or sensitivity indices, considering an input random vector affected by aleatoric uncertainty are described: they combine Monte-Carlo sampling and Kriging in the case of a real-valued output.* Principal Component Analysis *(PCA) is additionally used for high dimensional output.*

Note In the manuscript, only Forward Uncertainty Propagation of models depending on input whose source is characterized by Aleatoric uncertainties and modeled as a random vector fully parametrized by its PDF will be considered.
The probability measure $\mathcal{P}$ is dedicated to the *epistemic uncertainty* associated to the Kriging predictor (Eq. I.64), while the probability measure $\mathbb{P}$ is considered w.r.t. to the input random vector (defined by its PDF) characterized by *aleatoric uncertainties*.

In the following, the output of the computer model is referred to as the *Quantity of Interest* (QoI). The aleatoric uncertainty source is modeled as a random vector $\boldsymbol{X}$ completely defined by its PDF $f_{\boldsymbol{X}}$. Its induced probability space is denoted as $(\mathbb{X}, \mathcal{B}(\mathbb{X}), \mathbb{P})$, with $\mathbb{X} \subseteq \mathbb{R}^d$.

I–3.1 Forward Uncertainty Propagation for a scalar QoI

A basic description about the methods for the evaluation of some statistics of $Y = G(\boldsymbol{X})$, and its so-called *Sobol Indices* (SI) based on the well-known *ANalysis Of VAriance* (ANOVA) technique [Tang et al., 2015] is provided.

Note that in practice, the generic model G is replaced by a Kriging-based surrogate model (see Section I–2 for details) $\tilde{G}$, built based on *Latin Hypercube Sampling* (LHS) evaluations [Helton and Davis, 2003].

I–3.1.1 UQ Surrogated-based: Scalar Statistics Evaluation

In this Subsection, the generic real-valued random variable $Y = G(\boldsymbol{X})$ is considered, where G is a scalar (deterministic) response function representing the QoI associated to a physical model depending on a vector in $\mathbb{X}$:

$$\begin{aligned} G: \mathbb{X} \subseteq \mathbb{R}^d &\mapsto \mathbb{Y} \subseteq \mathbb{R} \\ \boldsymbol{x} &\to G(\boldsymbol{x}). \end{aligned} \tag{I.99}$$

The following statistics of Y are considered: mean $\mu_Y = \mathbb{E}_Y[Y] = \mathbb{E}[G(\boldsymbol{X})]$, standard deviation $\sigma_Y = \mathbb{V}_Y^{\frac{1}{2}}(Y) = \mathbb{V}^{\frac{1}{2}}(G(\boldsymbol{X}))$ and α-quantile $= q_\alpha^Y$, with $\mathbb{E}_Y$ and $\mathbb{V}_Y$ denoting respectively the expectation and variance operators induced by the random variable Y. We recall below their definition. The expectation μ_Y of Y is defined as:

$$\mathbb{E}_Y[Y] = \mathbb{E}[G(\boldsymbol{X})] = \int_{\mathbb{X}} G(\boldsymbol{x}) f_X(\boldsymbol{x}) d\boldsymbol{x}. \tag{I.100}$$

The so-called variance $\mathbb{V}_Y[Y]$ of Y is defined as:

$$\mathbb{V}_Y[Y] = \mathbb{E}_Y[Y^2] - \mathbb{E}_Y[Y]^2. \tag{I.101}$$

For $\alpha \in [0,1]$, the α-quantile, is defined by:

$$q_\alpha^Y = \inf\{q \in \mathbb{R}\, s.t.\ \ \mathbb{P}_Y(Y < q) \leqslant \alpha\}, \tag{I.102}$$

with $\mathbb{P}_Y$ referring to the probability measure induced by Y. Note the following equality $\mathbb{P}_Y(Y < q) = \mathbb{P}(G(\boldsymbol{X}) < q)$.

The Coefficient of Variation defined by $\delta_Y = \dfrac{\mathbb{V}_Y[Y]^{\frac{1}{2}}}{|\mathbb{E}_Y[Y]|}$ is also used to quantify the normalized variability of Y, provided $\mathbb{E}_Y[Y] \neq 0$.

Corresponding empirical estimators, based on Monte-Carlo sampling and Kriging surrogate-modeling of G, are computed with the following algorithm:

- Build a DoE (LHS) and run the expensive model G to evaluate each sample, yielding: $\{\boldsymbol{x}_j, G(\boldsymbol{x}_j)\}_{j \in [\![1, N_{LHS}]\!]}$, with N_{LHS} moderate.
- Build a surrogate (Kriging) from the DoE: $\tilde{Y} \equiv \tilde{G} : \mathbb{X} \mapsto \mathbb{Y}$
- Sample a large MC set: $\{\boldsymbol{x}_k\}_{k \in [\![1, N_{MC}]\!]}$, with $N_{MC} \sim O(10^{6-8})$.
- Compute the MC empirical statistics $\hat{\mu}_{\tilde{Y}}$, $\hat{\sigma}^2_{\tilde{Y}}$ and $\hat{q}_\alpha^{\tilde{Y}}$ based on the surrogate $\tilde{G}$ using Equations I.103, considering the set $\{\tilde{Y}(\boldsymbol{x}_k)\}_k$ sorted:

$$\begin{aligned} \hat{\mu}_{\tilde{Y}} &= \frac{1}{N_{MC}} \sum_{k=1}^{N_{MC}} \tilde{Y}(\boldsymbol{x}_k) \\ \hat{\sigma}^2_{\tilde{Y}} &= \frac{1}{N_{MC}} \sum_{k=1}^{N_{MC}} (\tilde{Y}(\boldsymbol{x}_k) - \hat{\mu}_{\tilde{Y}})^2 \\ \hat{q}_\alpha^{\tilde{Y}} &= \tilde{Y}(\boldsymbol{x}_{\lceil \alpha N_{MC} \rceil}), \end{aligned} \tag{I.103}$$

$\lceil \cdot \rceil$ denoting the ceiling function.

I–3.1.2 ANOVA: Sobol Indices

Variance-based sensitivity indices are common tools in the analysis of complex physical phenomena. More precisely, we are interested in the total SI [Saltelli et al., 2004, Sobol, 2001].

The variance decomposition of the response can be written as follows:

$$\mathbb{V}(Y) = \sum_{u \subseteq U} \sigma_u^2(\boldsymbol{X}_u), \tag{I.104}$$

where $U = (1, 2, ..., d)$ is the set of random variables indexes, $u \subseteq U$ a partition of U and σ_u^2 is the variance introduced by interactions of random variables $\boldsymbol{X}_u \subseteq \boldsymbol{X}_U$. The associated sensitivity measure of $\boldsymbol{X}_u$ is written as the correlation ratio:

$$S_u = \frac{\mathbb{V}(\mathbb{E}[Y|\boldsymbol{X}_u])}{\mathbb{V}(Y)} = \frac{\sum_{v \leqslant u} \sigma_v^2}{\mathbb{V}(Y)}. \tag{I.105}$$

For a single variable X_i, the first order SI S_i is given by:

$$S_i = \frac{\mathbb{V}(\mathbb{E}[Y|X_i])}{\mathbb{V}(Y)}. \tag{I.106}$$

It quantifies the contribution to the global variance $\mathbb{V}(Y)$ of the main effect of X_i varying alone, but averaged over variations in other input parameters.
The total order SI S_{T_i} is defined by:

$$S_i^T = \frac{\mathbb{E}[\mathbb{V}(Y|\boldsymbol{X}_{(i)})]}{\mathbb{V}(Y)} = 1 - \frac{\mathbb{V}(\mathbb{E}[Y|\boldsymbol{X}_{(i)}])}{\mathbb{V}(Y)}, \tag{I.107}$$

where the $\boldsymbol{X}_{(i)}$ notation indicates the set of all variables except X_i. It measures the contribution to $\mathbb{V}(Y)$ of X_i caused by its interactions with all other input variables.

The first and total SI satisfy the following properties:

$$\sum_i^d S_i = 1 \tag{I.108}$$

$$\sum_i^d S_i^T \geqslant 1. \tag{I.109}$$

The SI are estimated using a Monte-Carlo algorithm [Sobol, 2001], using the surrogate $\tilde{Y}$ as built above.

I–3.2 UQ methods for High Dimensional QoI

Let us consider the generic random variable $\boldsymbol{Y} = \boldsymbol{G}(\boldsymbol{X})$ where

$$\begin{aligned} \boldsymbol{G} : \ \mathbb{X} \subseteq \mathbb{R}^d &\mapsto \mathbb{Y} \subseteq \mathbb{R}^n \\ \boldsymbol{x} &\to \boldsymbol{G}(\boldsymbol{x}) \end{aligned} \tag{I.110}$$

is a multidimensional function defined on $\mathbb{X}$, and $\boldsymbol{X}$ is a random vector characterized by its PDF $f_{\boldsymbol{X}}$. We are interested in the evaluation of the statistics of $\boldsymbol{Y}$. The scalar method described in Subsection I–3.1 is not tractable in practice, since it would require to build n Kriging surrogates, with n possibly large ($n \sim O(10^{3-6})$). In the

following, we describe a stochastic method combining a PCA (Principal Component Analysis) decomposition to reduce the dimension space n, surrogate modeling and MC sampling. The idea merely consists, first, in building a *Kriging-PCA* surrogate for the high-dimensional output function $\boldsymbol{G}$, $\tilde{\boldsymbol{G}} : \mathbb{X} \to \mathbb{Y}$. A forward uncertainty analysis is then performed on the surrogate, similarly to Subsection I–3.1. Since a MC+Kriging analysis has to be performed independently on the n components of $\boldsymbol{G}$, the process might be computationally expensive and possibly prohibitive, even if the component-wise surrogates $\boldsymbol{x} \to \tilde{\boldsymbol{G}}(\boldsymbol{x})^{(i)}$ are already built. However, it is, within this framework, the only way to estimate quantiles or sensitivity indices. Taking advantage of the linearity of the expectation operator, it is possible, though, to estimate in an efficient manner both the mean $\mathbb{E}[\boldsymbol{Y}]$ and the variances $\mathbb{V}[Y_i]$, where Y_i denotes the i-th component of the random vector $\boldsymbol{Y}$. The method is summarized below:

1. Build a *Kriging-PCA* surrogate of $\boldsymbol{G}$, $\tilde{\boldsymbol{G}} : \mathbb{X} \to \mathbb{Y}$
   (a) Set an *initial DOE*: Data generation using LHS.
   (b) *PCA*: compute the eigenmodes, and select the most energetic ones.
   (c) *Build a surrogate* of each scalar coefficient in the reduced basis.
2. Perform the UQ analysis on $\tilde{\boldsymbol{Y}} \equiv \tilde{\boldsymbol{G}}(\boldsymbol{X})$
   (a) Basic Method: independent scalar UQ propagation on $\tilde{Y}_i$
   (b) Efficient Method: $\mathbb{E}[\tilde{\boldsymbol{Y}}]$ and variances $\mathbb{V}[\tilde{Y}_i]$

I–3.2.1 Kriging-PCA Surrogate

Initial DOE N_{LHS} samples using LHS are generated, then stored in the mean subtracted data matrix $\mathcal{Y} = [\boldsymbol{G}(\boldsymbol{x}_i)^{(j)} - \boldsymbol{\mu}_{\boldsymbol{G}}^{(j)}]_{ij} \in \mathbb{R}^{N_{LHS} \times n}$. $\boldsymbol{G}(\boldsymbol{x}_i) = (\boldsymbol{G}(\boldsymbol{x}_i)^1, ..., \boldsymbol{G}(\boldsymbol{x}_i)^n) \in \mathbb{R}^n$ denotes the i-th sample. $\boldsymbol{\mu}_{\boldsymbol{G}} \in \mathbb{R}^n$ denotes the data empirical mean, defined as $\boldsymbol{\mu}_{\boldsymbol{G}}^{(j)} = \dfrac{1}{N_{LHS}} \sum_{k=1}^{N_{LHS}} \boldsymbol{G}(\boldsymbol{x}_i)^{(j)}$. Mean subtraction is an integral part of the solution towards finding a principal component basis minimizing the data approximation mean square error [Miranda et al., 2008].

2) PCA and modes selection The semi-definite positive empirical covariance matrix is built:

$$C = \frac{\mathcal{Y}^T \mathcal{Y}}{N_{LHS} - 1}. \tag{I.111}$$

$C \in \mathbb{R}^{n \times n}$ is then decomposed into an orthogonal basis of eigenvectors:

$$C = V \Lambda V^T, \tag{I.112}$$

where $\boldsymbol{V} = (\boldsymbol{v}_1, ..., \boldsymbol{v}_n)$ is an orthogonal matrix, its columns satisfying:

$$\boldsymbol{v}_i^T \boldsymbol{v}_j = \delta_{ij}, \tag{I.113}$$

and $\Lambda = diag(\lambda_1, ..., \lambda_n)$ is a diagonal matrix where the positive eigenvalues are sorted in decreasing order. The decay of the eigenvalues (or modes) permits to truncate the expansion. The normalized cumulative energy from the first p modes is defined as

$$E(p) = \frac{\sum_{i=1}^{p} \lambda_i}{\sum_{i=1}^{n} \lambda_i}. \tag{I.114}$$

It is used to select the l most energetic modes, up to a threshold value ϵ (e.g. $\epsilon = 99\%$) driving the expansion accuracy:

$$l = \text{Min}\{k \in \mathbb{N}^* \text{ s.t. } E(k) < \epsilon\}. \tag{I.115}$$

Note that in the cases of interest, $N_{LHS} < n$, so the covariance matrix C has a rank N_{LHS} at maximum hence $l \leq N_{LHS}$. The l eigenvectors $\{\boldsymbol{v}_k\}_{k\in[\![1,l]\!]}$ with $\boldsymbol{v}_k \in \mathbb{R}^n$ are set as basis vectors: the vector solution $\boldsymbol{G}(\boldsymbol{x})$ at an unknown location $\boldsymbol{x}$ is sought in the form

$$\boldsymbol{G}(\boldsymbol{x}) - \boldsymbol{\mu}_{\boldsymbol{G}} = \sum_{i=1}^{l} h_i(\boldsymbol{x})\boldsymbol{v}_i, \tag{I.116}$$

where $h_i(\boldsymbol{x})$ denote the scalar coefficients in the reduced basis, which need to be approximated by a surrogate. In particular, h_i satisfies:

$$h_i(\boldsymbol{x}) = \boldsymbol{v}_i^T(\boldsymbol{G}(\boldsymbol{x}) - \mu_G), \ \forall i \in [\![1,l]\!], \ \forall \boldsymbol{x} \in \mathbb{X}, \tag{I.117}$$

by virtue of Eq. I.113.

Build a surrogate For each $i \in [\![1,l]\!]$, the DoE $\{\boldsymbol{x}_k, \boldsymbol{v}_i^T(\boldsymbol{G}(\boldsymbol{x}_k) - \mu_G)\}_{k\in[\![1,N_{LHS}]\!]}$ is used to build a surrogate $\tilde{h}_i : \mathbb{X} \mapsto \mathbb{R}$ for h_i. A surrogate for $\boldsymbol{G}$ consequently reads

$$\tilde{\boldsymbol{G}}(\boldsymbol{x}) = \boldsymbol{\mu}_{\boldsymbol{G}} + \sum_{i=1}^{l} \tilde{h}_i(\boldsymbol{x})\boldsymbol{v}_i. \tag{I.118}$$

The UQ analysis is then performed on the surrogate random vector $\tilde{\boldsymbol{Y}} \equiv \tilde{\boldsymbol{G}}(\boldsymbol{X})$.

I–3.2.2 UQ on the surrogate random vector $\tilde{Y}$

Basic Method: independent scalar UQ propagation on $\tilde{Y}_i$ Based on MC samples, the scalar approach derived in Subsection I–3.1 is applied independently to each component $Y_i \equiv \boldsymbol{G}(\boldsymbol{X})^{(i)}$. Although based on surrogates already built, this approach might be computationally expensive when n is very large.

Efficient Method: $\mathbb{E}[\tilde{Y}]$ and variances $\mathbb{V}[\tilde{Y}_i]$ To address the issue raised in the previous paragraph when only the first and second-order statistics are of interest, another MC-based approach is used. From the linearity of the operator $\mathbb{E}$, we obtain:

$$\boldsymbol{\mu}_{\tilde{\boldsymbol{Y}}} = \mathbb{E}[\tilde{\boldsymbol{G}}(\boldsymbol{X})] = \boldsymbol{\mu}_{\boldsymbol{G}} + \sum_{i=1}^{l} \mu_{\tilde{h}_i}\boldsymbol{v}_i, \tag{I.119}$$

where $\mu_{\tilde{h}_i} = \mathbb{E}[\tilde{h}_i(\boldsymbol{X})]$ denotes the mean of the real-valued random variable $\tilde{h}_i(\boldsymbol{X})$.

The marginal variances (or diagonal of the covariance matrix) of $\tilde{\boldsymbol{Y}} = \boldsymbol{G}(\boldsymbol{X})$ is derived by component $j \in [\![1,n]\!]$:

$$\begin{aligned}\mathbb{V}[\tilde{\boldsymbol{G}}(\boldsymbol{X})^{(j)}] &= \mathbb{V}\left[\sum_{i=1}^{l} \tilde{h}_i(\boldsymbol{X})\boldsymbol{v}_i^{(j)}\right] \\ &= \sum_{i=1}^{l} \boldsymbol{v}_i^{(j)}\boldsymbol{v}_i^{(j)}\sigma_{\tilde{h}_i}^2 + 2\sum_{i=1}^{n}\sum_{k=i+1}^{n} \boldsymbol{v}_i^{(j)}\boldsymbol{v}_k^{(j)}\tilde{\rho}_{ik},\end{aligned} \tag{I.120}$$

where $\sigma^2_{\tilde{h}_i} = \mathbb{V}[\tilde{h}_i(\boldsymbol{X})]$ and $\tilde{\rho}_{ik} = \mathbb{E}[\tilde{h}_i(\boldsymbol{X})\tilde{h}_k(\boldsymbol{X})] - \mu_{\tilde{h}_i}\mu_{\tilde{h}_k}$ denote respectively the variance of $\tilde{h}_i$ and the covariance between $\tilde{h}_i$ and $\tilde{h}_k$. This derivation (Equation I.120) takes into account that the coefficients $\tilde{h}_i$ can be correlated.

$\mu_{\tilde{h}_i}$, $\sigma^2_{\tilde{h}_i}$, $\tilde{\rho}_{ik}$ are evaluated numerically by means of MC on the metamodels $\tilde{h}_i$ so the mean (resp. marginal variances) of $\boldsymbol{G}(\boldsymbol{X})$ are easily reconstructed using Equation I.119 (resp. Equation I.120).

Computational aspects Note that in practice, the eigendecomposition $(\Lambda, \boldsymbol{V})$ is not obtained by evaluating the covariance matrix C and then perform the diagonalization as suggested by Equation I.112. Indeed, $C \in \mathbb{R}^{n\times n}$ can be very large and ill-conditioned since $\text{cond}(C) = \text{cond}(\mathcal{Y})^2$.
A Singular Value Decomposition (SVD) on the mean subtracted data matrix $\mathcal{Y}$ is preferred, yielding

$$\mathcal{Y} = \boldsymbol{U}\Sigma\boldsymbol{V}^T. \tag{I.121}$$

$\boldsymbol{U} \in \mathbb{R}^{N_{LHS}\times N_{LHS}}$ is an orthonormal matrix with the property $\boldsymbol{U}^T\boldsymbol{U} = I_{N_{LHS}}$. $\Sigma \in \mathbb{R}^{N_{LHS}\times n}$ is a *diagonal matrix* of eigenvalues $\{\sigma_k\}_k$. Equation I.121 is justified by

$$\begin{aligned} C &= \frac{(\boldsymbol{U}\Sigma\boldsymbol{V}^T)^T\boldsymbol{U}\Sigma\boldsymbol{V}^T}{N_{LHS}-1} \\ &= \boldsymbol{V}\frac{\Sigma^T\Sigma}{N_{LHS}-1}\boldsymbol{V}^T. \end{aligned} \tag{I.122}$$

Equation I.122 also shows the underlying relation between eigenvalues of matrices C and $\mathcal{Y}$:

$$\lambda_i = \frac{\sigma_i^2}{N_{LHS}-1}. \tag{I.123}$$

Part A

Rare Events: Failure Probability and Quantile Estimation

Overview *This part aims at describing numerical methods applied in two specific problems related to rare event estimation:*

- *Failure Probability (a.k.a. Risk Analysis):*

$$\mathbb{P}(G(\boldsymbol{X}) < u) = \bullet \tag{I.124}$$

- *Quantile Estimation:*

$$\mathbb{P}(G(\boldsymbol{X}) < \bullet) = \alpha \tag{I.125}$$

where $G : \mathbb{X} \subseteq \mathbb{R}^d \mapsto \mathbb{Y} \subseteq \mathbb{R}$ denotes an expensive to evaluate deterministic function characterized by a limited budget. The methods developed are specifically designed to be suitable in the case of so-called multiple failure regions *and extreme (rare) events ($\alpha \sim O(10^{-6} - 10^{-10})$).*

Contribution *Two methods for failure probability estimation (MetaAL-OIS, eAK-MCS) and one permitting to estimate a small quantile (QeAK-MCS) are proposed. They constitute the basis of three journal articles (1 published, 2 submitted):*

1. *N. Razaaly, P.M. Congedo, Novel Algorithm using Active Metamodel Learning and Importance Sampling: application to multiple failure regions of low probability, Journal of Computational Physics, Volume 368, Pages 92-114, 2018.*
2. *N. Razaaly, P.M. Congedo, Extension of AK-MCS for the efficient computation of very small failure probabilities, Reliability Engineering and System Safety, Submitted January 2019.*
3. *N. Razaaly, P.M. Congedo, A Efficient Kriging-Based Extreme Quantile Estimation suitable for expensive performance function., International Journal of Numerical Methods in Engineering, Submitted March 2019.*

Outline

The outline of the first part of the manuscript is the following. Chapter II presents a review of reliability analysis methods and a general framework containing different concepts at the basis of the three proposed methods. In Chapter III, the first method, named *Metamodel-based combining Active Learning and quasi-Optimal Importance Sampling* (MetaAL-OIS), for the *unbiased* estimation of failure probabilities is presented. In Chapter IV, the second method, named *extreme Active Kriging-Monte Carlo Sampling* (eAK-MCS), for the estimation of failure probabilities is described, equipped with a parallel refinement strategy inherited from [Schöbi et al., 2016]. In Chapter V, the method *Quantile extreme Active Kriging-Monte Carlo Sampling* (QeAK-MCS) permits the estimation of extreme quantiles ($\alpha < 10^{-5}$), adapting eAK-MCS for quantile estimation similarly to [Schöbi et al., 2016]. The original parallel surrogate refinement strategy is enriched with an additional level of parallelization, which is also suitable with the seminal quantile algorithm [Schöbi et al., 2016].

II

General Framework of Reliability Analysis Methods

Overview *This chapter is intended to introduce the general framework of the rare events methods presented in the first part of the manuscript.*

Outline

This chapter is organized as follows. Section II–1 introduces the scope and field of application of the original methods described in the sequel. Section II–2 reviews state-of-the-art methodologies in reliability analysis emphasizing direct (*i.e.* using directly the performance function) and surrogate-based methods. The general framework used in the first part of the manuscript is finally reported.

II–1 Introduction

II–1.1 Problem Definition

The scope of the methods proposed in this part is restricted to *time-invariant* a.k.a. *static* simulation problems characterized by a *deterministic* scalar performance function, in which time is not an explicit variable, and repeated model calls to the same input provide the very same output response. Let us define

$$\begin{aligned} J : \mathcal{D}_J \subseteq \mathbb{R}^d &\mapsto \mathbb{R} \\ \boldsymbol{y} &\to J(\boldsymbol{y}), \end{aligned} \tag{II.1}$$

the *performance function* a.k.a. *Limit-State Function* (LSF) defined in the so-called *physical space* $\mathcal{D}_J$, representing the scalar output of a computationally expensive numerical model, hence associated to a limited number of evaluations N_{budget} ($N_{\text{budget}} = O(10^{2-3})$). Let

$$\boldsymbol{Y} : \Omega \mapsto \mathbb{Y} \subseteq \mathcal{D}_J \subseteq \mathbb{R}^d \tag{II.2}$$

be a random variable representing the uncertain scalar parameters input, defined by its joint continuous PDF $f_{\boldsymbol{Y}}$. The reliability analysis problem consists in the estimation of the failure probability p_f defined by:

$$p_f = \mathbb{P}_{\boldsymbol{Y}}(J(\boldsymbol{Y}) < u), \tag{II.3}$$

where $\mathbb{P}_{\boldsymbol{Y}}$ refers to the probability measure induced by $\boldsymbol{Y}$. In the sequel, it is considered that a so-called *isoprobabilistic transformation* $T : \mathbb{Y} \mapsto \mathbb{R}^d$ satisfies:

$$\boldsymbol{X} = T(\boldsymbol{Y}) \Leftrightarrow \boldsymbol{Y} = T^{-1}(\boldsymbol{X}) \tag{II.4}$$

where $\boldsymbol{X} \sim \mathcal{N}_d(0, I_d)$ is the d-dimensional standard Gaussian vector (also referred to as the *standard normal space*). Its joint PDF $f_{\boldsymbol{X}}$ is defined by

$$f_{\boldsymbol{X}}(\boldsymbol{x}) = \frac{1}{(2\pi)^{\frac{d}{2}}} \exp\left(-\frac{\boldsymbol{x}^T\boldsymbol{x}}{2}\right). \tag{II.5}$$

The *normalized* LSF G

$$\begin{aligned} G : \mathbb{R}^d &\mapsto \mathbb{R} \\ \boldsymbol{x} &\to G(\boldsymbol{x}) = (J \circ T^{-1})(\boldsymbol{x}) \end{aligned} \tag{II.6}$$

consequently permits to reformulate the reliability problem (Eq. II.3) in the standard space as:

$$p_f = \mathbb{P}(G(\boldsymbol{X}) < u) = \mathbb{E}[\mathbb{1}_{G<u}(\boldsymbol{X})] = \int_{\mathbb{R}^d} \mathbb{1}_{G<u}(\boldsymbol{x}) f_{\boldsymbol{X}}(\boldsymbol{x}) d\boldsymbol{x}, \tag{II.7}$$

where $\mathbb{P}$ and $\mathbb{E}$ denote resp. the probability measure and expectation operators induced by $\boldsymbol{X}$, and $\mathbb{1}$ the indicator function.

The second problem of interest consisting in the estimation of the quantile $q \in \mathbb{R}$ associated to a level of probability $\alpha \in]0, 1[$ reads:

$$\mathbb{P}(G(\boldsymbol{X}) < q) = \alpha, \tag{II.8}$$

which can be seen as an inverse problem w.r.t. Eq. II.7. Note that it is assumed without loss of generality that $\alpha \sim 0$. Indeed, if $\alpha \sim 1$, Problem II.8 is simply re-written as $\mathbb{P}(-G(\boldsymbol{X}) < q^*) = \alpha^*$, with $\alpha^* = 1-\alpha$, and the quantile sought is obtained as $q = -q^*$.

This reformulation in the standard space, although presenting clear advantages such as the normalized uncorrelated input variability, depends strongly on the assumption of the complete knowledge of the joint PDF f_Y and the existence of the isoprobabilistic transform T.

Limit-State Surface Let us now introduce the following definitions:

- The set $\{\boldsymbol{x} \in \mathbb{R}^d \; s.t. \; G(\boldsymbol{x}) < u\}$ is defined as the *failure region* or *failure domain*.
- The set $\{\boldsymbol{x} \in \mathbb{R}^d \; s.t. \; G(\boldsymbol{x}) > u\}$ is defined as the *safe region* or *safe domain*.
- The set $\{\boldsymbol{x} \in \mathbb{R}^d \; s.t. \; G(\boldsymbol{x}) = u\}$ is defined as the performance function *failure branch* or its *Limit State Surface* (LSS).

In case these sets are not connected, they are referred to as *regions*, *modes* or *branches*, respectively. The indication function $\mathbb{1}$ transforming the integration problem (Eq. II.7) into a classification problem consists in identifying accurately the failure and safe domains: it is hence sufficient to approximate the LSS to accurately estimate the associated failure probability.

Remark The algorithms *proposed* to solve those problems rely primarily on the construction of Kriging surrogate model to approximate the LSF G and adaptive refinement strategies permitting to increase the accuracy of the latter surrogate in the region of interest. Particular attention has been devoted for those proposed algorithms to be suitable to cases characterized by extreme events ($\alpha, p_f \sim \mathrm{O}(10^{-2} - 10^{-9})$) and multiple failure regions. Additionally, those refinement algorithms are said *direct* as they provide samples aiming at *directly* refine the LSS[1].

II–1.2 Field of Application

The problem of tail probability estimation (Eq. II.7) arises naturally in several domains such as risk analysis. For those applications, the final goal is to obtain an estimation of the failure probability in order to assess the reliability of a design. The proposed algorithms, likewise some other surrogate-based methods in the literature (e.g. [Schöbi et al., 2016, Lelièvre et al., 2018]), embeds a *direct*[1] adaptive refinement strategy: at each iteration, candidate sample points are selected aiming at refining the LSS, based of the current knowledge brought by the Kriging surrogate of the LSF G. The remarkable feature makes this class of algorithms of particular interest for reliability-derived problems where a rare event estimation is part of a more extended framework. *Reliability-Based Design Optimization* (RBDO) as presented in [Moustapha et al., 2016] belong to this set: a reliability analysis [Echard et al., 2011] based refinement strategy is used as a tool in the global framework. The three algorithms proposed in this part

[1]The refinement algorithm BSS [Bect et al., 2017] does not satisfy this property, since intermediate LSS are iteratively refined.

are developed so their refinement strategy could be afterwards isolated and used as a tool for RBDO or *Robust Optimization* (RO) methods.

The three algorithms developed being suitable to deal with multiple failure regions and extreme rare events make their *direct* refinement strategy tool very promising for such RBDO or RDO methods.

The following example, taken from [Fenrich and Alonso, 2017], can be used to illustrate the need for such RBDO methods. It merely consists in solving an optimization problem in the form:

$$\begin{aligned} \text{Minimize} \quad & \mathbb{E}[f(\boldsymbol{x}, \boldsymbol{\xi})] \\ \text{s.t.} \quad & \mathbb{P}[G_k(\boldsymbol{x}, \boldsymbol{\xi}) < 0] = 10^{-7}, \ \forall k \in [\![1, n_c]\!] \\ & \boldsymbol{x} \in \Omega, \end{aligned} \tag{II.9}$$

where the mean of the objective function f has to be minimized s.t. n_c failure probabilities associated to the LSF G_k have to be lower than 10^{-7}, the design vector $\boldsymbol{x} \in \Omega$ belonging to the design space Ω, and $\mathbb{P}$, $\mathbb{E}$ denoting resp. the probability measure and expectation operator induced by the random vector $\boldsymbol{\xi}$. Due to the complexity of the problem, the authors chose to relax the initial probabilistic constraints so the failure probabilities only have to be lower than 10^{-2}[Fenrich and Alonso, 2017]. Those remarks motivate the development of suitable methods allowing to adapt RBDO schemes to tackle such issues.

In the context of reliability analysis, the assumption of the perfect knowledge of the input distribution in the physical space $\boldsymbol{Y}$, or the possibility to *exactly* recast it in the standard space, is very unlikely. In [Chabridon et al., 2017], the impact of aleatoric uncertainty in the input distribution is studied, performing a reliability analysis in a context of uncertainties affecting probability distribution parameters. This approach seems to be of interest, and it is shown that such uncertainties inherent to some parameters of the input distribution might have a non-negligible impact on the estimated failure probability, which is then considered a random variable. It is worth noting that the CPU efficiency and field of applicability of the underlying surrogate-based approach selected (e.g. eAK-MCS, AK-MCS) is at the core of their effectiveness. Those facts further motivate the need for such independent *direct* refinement strategies. The algorithm *Quantile extreme Active Kriging-Monte Carlo Sampling* (QeAK-MCS) alleviates the problem of the quantile estimation within the hypotheses detailed in Subsection II–1.1, amonsgt which:

1. The induced failure probability problem might be subject to multiple failure regions, namely, the LSS defined as $\{\boldsymbol{x} \in \mathbb{R}^d \ s.t. \ G(\boldsymbol{x}) = q\}$, where $q \in \mathbb{R}$ is the unknown quantile, might be composed of several failure branches.

2. The level of quantile α might be *extreme*, say $\alpha \in [10^{-5}, 10^{-9}]$. For such low levels, the only method able to alleviate the point 1 ([Schöbi et al., 2016]) would fail.

To the best of the knowledge of the author, only [Schöbi et al., 2016] can deal with assumption 1, while no methods can deal with both assumptions.

II–2 Review of Existing Methods

Risk analysis methods can roughly be decomposed in two classes. A first family of method denoted as *Direct Methods* or *Sampling Methods* make only use of the performance function G. Classic considerations raised by the crude *Monte-Carlo Sampling* (MCS) are presented in Subsubsection II–2.1.1. *Importance Sampling* (IS) techniques [Rubinstein, 1981], [Fishman, 1996] aim at reducing the so-called *variance estimator*[2] in order to reduce the number of evaluations of the performance function, for a given target error. The success of the method relies on a prudent choice of the importance sampling density. IS is described within the general framework of the proposed methods in Subsubsection II–2.1.4. *First-Order Reliability Method* (FORM) and *Second-Order Reliability Method* (SORM) are based on the concept of so-called *Most Probable Failure Point* (MPFP), and provide a generally biased estimation of the failure probability under restrictive assumptions on the LSS. They are introduced in Subsubsection II–2.1.2. *Cross-Entropy* (CE) and *Subset Simulation* (SS) methods are presented in Subsubsection II–2.1.3

Surrogate-based methods are part of the latter. In substance, the original performance function G is replaced by a surrogate model orders of magnitude cheaper to evaluate, on which generally methods of the former family are used. They are presented in Subsection II–2.2. A comprehensive introduction to reliability analysis methods can be found in [Bourinet, 2018].

II–2.1 Direct Methods

II–2.1.1 Monte-Carlo Sampling

Monte-Carlo Sampling (MCS) method permits to estimate the failure probability (Eq. II.7) using the following estimator:

$$\hat{p}_f = \mathbb{E}[\mathbb{1}_{G<0}(\boldsymbol{X})] = \frac{1}{N_{MC}} \sum_{i=1}^{N_{MC}} \mathbb{1}_{G<0}(\boldsymbol{x}^{(i)}), \tag{II.10}$$

where $\{\boldsymbol{x}^{(1)}, ..., \boldsymbol{x}^{(N_{MC})}\}$ is a set of N_{MC} independent samples drawn from the random vector $\boldsymbol{X}$. This estimator is asymptotically unbiased and convergent. Its variance $\mathbb{V}[\hat{p}_f]$ reads:

$$\sigma_f^2 = \frac{p_f - p_f^2}{N_{MC}}, \tag{II.11}$$

leading to its variance estimator

$$\hat{\sigma}_f^2 = \frac{\hat{p}_f - \hat{p}_f^2}{N_{MC}}. \tag{II.12}$$

The accuracy of the estimate is measured using its CoV

$$\hat{\delta}_f = \frac{\hat{\sigma}_f}{\hat{p}_f} = \sqrt{\frac{1 - \hat{p}_f}{\hat{p}_f N_{MC}}}, \tag{II.13}$$

[2]The variance estimator quantifies the accuracy of the failure probability estimation

provided $\hat{p}_f \neq 0$. It illustrates its low convergence rate $\propto N_{MC}^{-\frac{1}{2}}$. If a target error of $\hat{\delta}_f < 10^{-\Delta}$ is aimed, a failure probability as low as $p_f = 10^{-\gamma}$ would require a number of samples of $N_{MC} \approx 10^{2\Delta+\gamma}$. This is illustrated in Table II.1. If a surrogate for the LSF G (orders of magnitude cheaper to evaluate than G) is considered, an accurate reliability analysis (target CoV $\delta < 0.1\%$) would require $\sim 10^{15}$ surrogate evaluations for an underlying failure probability $p_f = 10^{-9}$. Generally computationally expensive in practice, such calculation might also lead to RAM issues according to the implementation.

δ	p_f	N_{MC}
1%	10^{-5}	10^{9}
	10^{-9}	10^{13}
0.1%	10^{-5}	10^{11}
	10^{-9}	10^{15}

Table II.1 MCS computational cost: number of MCS evaluations (N_{MC}) as a function of the target CoV δ and the true failure probability p_f.

II–2.1.2 MPFP based methods: FORM/SORM

MPFP The so-called *Most Probable Failure Point* (MPFP) or *design point* $\boldsymbol{x}^* \in \mathbb{R}^d$ associated to the LSS $\{\boldsymbol{x} \in \mathbb{R}^d \; s.t. \; G(\boldsymbol{x}) = u\}$ is defined as the point in the failure domain with the largest PDF value, in the standard space. Equivalently, it can be defined as the closest point to the origin, belonging to the LSS. It is the supposedly unique solution of the following quadratic optimization under non-linear constraint:

$$\boldsymbol{x}^* = \underset{\boldsymbol{x}\in\mathbb{R}^d \text{ s.t. } G(\boldsymbol{x})=u}{\text{Argmin}} \; \| \boldsymbol{x} \|_2 \, . \tag{II.14}$$

The so-called *Hasofer-Lind* reliability index is defined as:

$$\beta = \| \boldsymbol{x}^* \|_2 \, . \tag{II.15}$$

The constrained optimization Eq. II.14 is generally solved by means of a gradient-based optimization method, such as *Sequential Quadratic Programming* (SQP), or *Hasofer-Lind-Rackwitz-Fiessler* (HLRF) algorithm [Hasofer and Lind, 1974]. They require the evaluation of the gradient of the LSF G w.r.t. the input vector at each iteration step, by means of finite differences in most cases.

FORM FORM consists in approximating the LSF G by it linear approximation around the MPFP $\boldsymbol{x}^*$ in the integral Eq. II.7:

$$G^{FORM}(\boldsymbol{x}) - u = \nabla G(\boldsymbol{x}^*)^T (\boldsymbol{x} - \boldsymbol{x}^*), \tag{II.16}$$

since $G(\boldsymbol{x}^*) = u$.

The approximate failure probability consequently reads:

$$p_f^{FORM} = \mathbb{E}[\mathbb{1}_{G^{FORM}<u}(\boldsymbol{X})], \tag{II.17}$$

with $\boldsymbol{X} \sim \mathcal{N}_d(0, I_d)$. This integral can be written in closed-form

$$p_f^{FORM} = \Phi(-\beta), \tag{II.18}$$

Φ denoting the standard univariate Gaussian CDF. This approximation of the failure probability is under the assumption of an *unique* MPFP $\boldsymbol{x}^*$ and a linear LSS: it may indeed be corrupted with a large bias w.r.t. the true p_f.

SORM SORM assumes twice differentiability of the LSF G in the neighborhood of the MPFP $\boldsymbol{x}^*$ found. The LSF is then approximated by its second order Taylor expansion around $\boldsymbol{x}^*$:

$$G^{SORM}(\boldsymbol{x}) - u = \nabla G(\boldsymbol{x}^*)^T(\boldsymbol{x} - \boldsymbol{x}^*) + \frac{1}{2}(\boldsymbol{x} - \boldsymbol{x}^*)^T \nabla^2 G(\boldsymbol{x}^*)(\boldsymbol{x} - \boldsymbol{x}^*), \tag{II.19}$$

since $G(\boldsymbol{x}^*) = u$, $\nabla^2 G(\boldsymbol{x}^*)$ denotes the $\mathbb{R}^{d\times d}$ *Hessian* matrix of G at the MPFP $\boldsymbol{x}^*$. The SORM-approximate failure probability reads:

$$p_f^{SORM} = \mathbb{E}[\mathbb{1}_{G^{SORM}<u}(\boldsymbol{X})]. \tag{II.20}$$

Several expressions permit to approximate accurately and at a negligible computational cost ([Breitung, 1984] [Tvedt, 1989]) this integral. The CPU overhead w.r.t. FORM, after the MPFP has been found is due to the evaluation of the hessian matrix, requiring $\frac{d(d+1)}{2}$ LSF evaluations, by means of finite differences.

The case of multiple MPFPs (several failure regions) is partially addressed in [Der Kiureghian and Dakessian, 1998]: the MPFP search is repeated with a modified LSF, which permits the search outside the zone where previous MPFPs have been found. Corresponding modification in FORM/SORM expressions of the approximated failure probability are then prescribed.

II–2.1.3 Subset Simulation

The main idea of *Subset Simulation* (SS) [Au and Beck, 2001] is to consider a small probability of a rare event E as a product of larger probabilities of nested intermediate events E_i, $i \in [\![1, m]\!]$: $E = E_m \subset \ldots \subset E_1$. The sought failure probability consequently reads:

$$\begin{aligned} p_f &= \mathbb{P}(E_m) \\ &= \mathbb{P}(E_m|E_{m-1})\mathbb{P}(E_{m-1}) \\ &= \mathbb{P}(E_m|E_{m-1})\ldots\mathbb{P}(E_2|E_1)\mathbb{P}(E_1) \\ &= \prod_{i=1}^{m} p_i, \end{aligned} \tag{II.21}$$

with $p_1 = \mathbb{P}(E_1)$, and $p_i = \mathbb{P}(E_i|E_{i-1})$ for $i > 1$. p_f results as the product of m larger probability (easier to evaluate with classic sampling methods). The wisely-chosen intermediate levels u_i, with $u_m = u$ and $u_m < \cdots < u_1$, permit to define the intermediate events as

$$E_i = \{\omega \in \Omega \text{ s.t. } G(\boldsymbol{X}(\omega)) < u_i\}, \tag{II.22}$$

Ω referring to the *outcome space* of the underlying probability space. The intermediate probabilities p_i are defined as:

$$p_1 = \mathbb{P}(G(\boldsymbol{X}) < u_1) = \mathbb{E}[\mathbb{1}_{G<u_1}(\boldsymbol{X})] \tag{II.23}$$

$$p_i = \mathbb{P}(G(\boldsymbol{X}) < u_i | G(\boldsymbol{X}) < u_{i-1}) = \mathbb{E}_{E_{i-1}}[\mathbb{1}_{G<u_i}(\boldsymbol{X})], \tag{II.24}$$

for $i > 1$. $\mathbb{E}_{E_{i-1}}$ denotes the expectation operator induced by the random vector fully defined by the conditional PDF

$$f_{\boldsymbol{X}}(\boldsymbol{x}|E_{i-1}) = \frac{f_{\boldsymbol{X}}(\boldsymbol{x})\mathbb{1}_{G<u_{i-1}}(\boldsymbol{x})}{\mathbb{E}[\mathbb{1}_{G<u_{i-1}}(\boldsymbol{X})]}. \tag{II.25}$$

The estimation of p_i, $i > 1$ requires a numerical method to sample according to the conditional PDF $f_{\boldsymbol{X}}(\bullet|E_{i-1})$ such as acceptance-rejection, *Markov Chain Monte Carlo* (MCMC) [Metropolis et al., 1953] or *Sequential Monte Carlo* (SMC) [Bect et al., 2017] [Del Moral et al., 2006]. The intermediate levels u_i are selected so the estimates $\hat{p}_i$, for $i \in [\![1, m-1]\!]$ equal a prescribed probability level p_0, chosen in the *optimal range* [0.1,0.3] [Zuev et al., 2012].

II–2.1.4 Importance Sampling

The IS method is one of the most well-known variance reduction techniques used for assessing small failure probabilities. The idea consists in drawing samples following another distribution than the original in order to populate more frequently the failure domain: the failure probability estimate is then obtained as a weighted average of these draws. The general theory of IS is first presented, while examples of IS densities are then discussed, introducing as well Cross-Entropy methods in the context of failure probability estimation.

General Theory The following generic computation is considered:

$$p_g = \mathbb{E}[g(\boldsymbol{X})], \tag{II.26}$$

where $\boldsymbol{X} \sim \mathcal{N}_d(0, \boldsymbol{I}_d)$, $g : \mathcal{D}_{\boldsymbol{X}} = \mathbb{R}^d \mapsto \mathbb{R}$ refers for instance to $\boldsymbol{x} \to \mathbb{1}_{G<u}(\boldsymbol{x})$ or $\boldsymbol{x} \to \mathbb{1}_{\mu_{\hat{G}}+k\sigma_{\hat{G}}<\boldsymbol{u}}(\boldsymbol{x})$, with $\hat{G}(\boldsymbol{x}) = \mathcal{N}(\mu_{\hat{G}}(\boldsymbol{x}), \sigma^2_{\hat{G}}(\boldsymbol{x}))$ denoting the underlying Gaussian predictor of the Kriging surrogate $\tilde{G}$ of G at the location $\boldsymbol{x}$.

Let h be a proposal PDF[3], assumed to dominate $gf_{\boldsymbol{X}}$ in the absolutely continuous sense:

$$\forall \boldsymbol{x} \in \mathcal{D}_{\boldsymbol{X}}, \;\; h(\boldsymbol{x}) = 0 \implies g(\boldsymbol{x})f_{\boldsymbol{X}}(\boldsymbol{x}) = 0. \tag{II.27}$$

Then, p_g may be rewritten as follows:

$$p_g = \int_{\mathbb{R}^d} g(\boldsymbol{x})\frac{f_{\boldsymbol{X}}(\boldsymbol{x})}{h(\boldsymbol{x})}h(\boldsymbol{x})d\boldsymbol{x} = \mathbb{E}_h\left[g(\boldsymbol{X})\frac{f_{\boldsymbol{X}}(\boldsymbol{X})}{h(\boldsymbol{X})}\right], \tag{II.28}$$

$\mathbb{E}_h$ referring to the expectation operator induced by the ISD h.

It easily leads to the *importance sampling estimator*:

[3] a.k.a. biasing/instrumental PDF or *Importance Sampling Density* (ISD)

$$\hat{p}_g = \frac{1}{N}\sum_{i=1}^{N} g(\boldsymbol{x}^{(i)})\frac{f_X(\boldsymbol{x}^{(i)})}{h(\boldsymbol{x}^{(i)})}, \tag{II.29}$$

where $\boldsymbol{x}^{(1)}, ..., \boldsymbol{x}^{(N)} \overset{\text{iid}}{\sim} h$. This estimator is unbiased and its accuracy is measured by means of its variance estimator:

$$\hat{\sigma}_g^2 = \frac{1}{N-1}\left(\frac{1}{N}\sum_{i=1}^{N} g(\boldsymbol{x}^{(i)})^2\frac{f_X(\boldsymbol{x}^{(i)})^2}{h(\boldsymbol{x}^{(i)})^2} - \hat{p}_g^2\right). \tag{II.30}$$

The corresponding CoV reads:

$$\hat{\delta}_g = \frac{\hat{\sigma}_g}{\hat{p}_g}. \tag{II.31}$$

provided $\hat{p}_g \neq 0$. The $(k-\sigma)$-IS confidence interval bounds $\hat{p}_{g,min}$ and $\hat{p}_{g,max}$ are given by:

$$\begin{aligned} \hat{p}_{g,min} &= \hat{p}_g - k\hat{\sigma}_g \\ \hat{p}_{g,max} &= \hat{p}_g + k\hat{\sigma}_g. \end{aligned} \tag{II.32}$$

The accuracy of the approximation given by IS critically depends on the choice of the ISD h.

It can be shown that the estimator's variance is zero (optimality of the IS estimator) when the instrumental PDF is chosen as the theoretically optimal importance PDF defined by:

$$h_g^*(\mathbf{x}) = \frac{|g(\mathbf{x})|f_{\mathbf{X}}(\mathbf{x})}{\mathbb{E}[|g(\boldsymbol{X})|]}. \tag{II.33}$$

However, this PDF involves the unknown $\mathbb{E}[|g(\boldsymbol{X})|]$ in its denominator, so it is not implementable in practice. A good ISD h should have the following properties:

- h dominates $gf_{\mathbf{X}}$.
- $h(\mathbf{x})$ should be close to be proportional to $g(\mathbf{x})f_{\mathbf{X}}(\mathbf{x})$.
- It should be easy to sample from h.

In the specific case of $g = \mathbb{1}_{G<u}$, the optimal ISD reads:

$$h_G^*(\mathbf{x}) = \frac{\mathbb{1}_{G<u}(\mathbf{x})f_{\mathbf{X}}(\mathbf{x})}{p_f}. \tag{II.34}$$

Examples of ISD A classic choice of the ISD in the FORM/SORM context (in the standard space) consists simply in considering the original distribution centered in the supposedly unique MPFP $\boldsymbol{x}^*$ already found:

$$h(\boldsymbol{x}) = f_{\boldsymbol{X}}(\boldsymbol{x} - \boldsymbol{x}^*). \tag{II.35}$$

If several MPFPs $\boldsymbol{x}_i^*$ are identified, mixtures of multivariate standard Gaussian PDF can also be considered:

$$h(\boldsymbol{x}) = \frac{1}{m}\sum_{i=1}^{m} f_{\boldsymbol{X}}(\boldsymbol{x} - \boldsymbol{x}_i^*). \tag{II.36}$$

In other works, *adaptive Importance Sampling* methods consist in adjusting the ISD iteratively [Bucher, 1988] [Au and Beck, 1999] [Morio, 2012].

Cross-Entropy In the context of the estimation of failure probability, CE methods consider that the ISD h belongs to some parametrized family:

$$h \in \{h(\bullet, \boldsymbol{q}), \boldsymbol{q} \in \mathcal{Q} \subset \mathbb{R}^m\}. \tag{II.37}$$

The objective is finding a vector $\boldsymbol{q}^*$ such that $h(\bullet, \boldsymbol{q}^*)$ is as close as possible to the optimal ISD h_G^*, w.r.t. a given measure. The so-called *Kullback-Leibler* (KL) *divergence* (or *distance*) [Kullback and Leibler, 1951] is considered; for f, g two PDF, the KL distance between f and g reads

$$\mathcal{D}_{KL}(f, g) = \int_{\mathbb{R}^d} f(\boldsymbol{x}) \text{Log}\left(\frac{f(\boldsymbol{x})}{g(\boldsymbol{x})}\right) d\boldsymbol{x}, \tag{II.38}$$

under the assumption that $g(\boldsymbol{x}) = 0 \implies f(\boldsymbol{x}) = 0$ (absolute continuity). Therefore, the optimal parameter $\boldsymbol{q}^*$ leading to the minimal KL distance between $h(\bullet, \boldsymbol{q}^*)$ and h_G^* is the solution of the minimization problem:

$$\boldsymbol{q}^* = \underset{\boldsymbol{q} \in \mathcal{Q}}{\text{Argmin}} \int_{\mathbb{R}^d} h_G^*(\boldsymbol{x}) \text{Log}\left(\frac{h_G^*(\boldsymbol{x})}{h(\boldsymbol{x}, \boldsymbol{q})}\right) d\boldsymbol{x}, \tag{II.39}$$

or equivalently:

$$\boldsymbol{q}^* = \underset{\boldsymbol{q} \in \mathcal{Q}}{\text{Argmax}} \int_{\mathbb{R}^d} h_G^*(\boldsymbol{x}) \text{Log}\left(h(\boldsymbol{x}, \boldsymbol{q})\right) d\boldsymbol{x}. \tag{II.40}$$

For the case of the estimation of the failure probability estimation ($g = \mathbb{1}_{G<u}$), $\boldsymbol{q}^*$ reads:

$$\begin{aligned} \boldsymbol{q}^* &= \underset{\boldsymbol{q} \in \mathcal{Q}}{\text{Argmax}} \int_{\mathbb{R}^d} \mathbb{1}_{G<u}(\boldsymbol{x}) \text{Log}\left(h(\boldsymbol{x}, \boldsymbol{q})\right) f_X(\boldsymbol{x}) d\boldsymbol{x} \\ &= \underset{\boldsymbol{q} \in \mathcal{Q}}{\text{Argmax}}\, \mathbb{E}[\mathbb{1}_{G<u}(\boldsymbol{X}) \text{Log}\left(h(\boldsymbol{X}, \boldsymbol{q})\right)]. \end{aligned} \tag{II.41}$$

II–2.2 Surrogate-based methods

Surrogate[4]-based methods rely on the approximation of the original costly-to-evaluate LSF G by a metamodel, which is orders of magnitude faster to evaluate. The approximate model can be used in conjunction with sampling methods, to improve the latter or to correct the potential bias due to the surrogate model.

Polynomial response surfaces used as surrogate for the LSF first appear in the literature in [Faravelli, 1989], inspiring different works in the nineties [Bucher and Bourgund, 1990, Enevoldsen and Sørensen, 1993, Rajashekhar and Ellingwood, 1993]: a quadratic polynomial is built in the neighborhood of an *supposedly unique* MPFP. To alleviate the possible severely biased estimation due to the latter assumption, least-squares polynomial regression are adopted in [Most and Bucher, 2008] [Proppe, 2008] [Kang et al., 2010]. Other approaches based on *Artificial Neural Network* (ANN) [Papadrakakis and Lagaros, 2002] [Hurtado and Alvarez, 2000] [Elhewy et al., 2006] [Cardoso et al., 2008] [Papadopoulos et al., 2012], in most cases combine the training of the *Multilayer Perceptron* (with one or several layers) and MCS or SS. Since the failure probability estimation can be seen as a binary classification problem where the two

[4] a.k.a. response surface, metamodel or approximate model

classes correspond to the safe or failure domain, *Support Vector Machines* (SVM) are investigated in [Deheeger and Lemaire, 2006] [Most, 2007] [Basudhar et al., 2008]. The LSF might also be considered from a regression viewpoint (not only the binary but the real value returned by the LSF is accounted for) [Pai and Hong, 2006, Dai et al., 2012, Bourinet, 2016], using support vector regression. Kriging-based methods including [Bichon et al., 2005, Kaymaz, 2005, Ranjan et al., 2008, Bichon et al., 2008, Picheny et al., 2010b, Bect et al., 2012] retain in particular our interest. Note that in such metamodel-based approaches, MCS (AK-MCS [Echard et al., 2011]) or IS techniques (AK-IS [Echard et al., 2013], MetaAK-IS^2 [Cadini et al., 2014], KAIS [Zhao et al., 2015]) or even SS (AK-SS [Huang et al., 2016]) are used directly on the surrogate.

In particular, the so-called *Active learning reliability method combining Kriging and Monte Carlo Simulation* (AK-MCS) is presented in [Echard et al., 2011]. The Kriging surrogate replacing the LSF J in the *physical space* is iteratively refined using the popular *U-function* to select samples among MC samples.

Assessing a relatively low probability ($p_f < 10^{-5}$) with this method remains an issue though, due to the very large number of MC samples involved. One important limitation of metamodel-based approaches lies in the complexity to keep the approximation error under control.

In order to cure this issue, [Dubourg et al., 2013] proposed to resort to a kriging-based surrogate model to approximate the optimal importance density. The so-called meta-IS [Dubourg et al., 2013] algorithm allows to obtain a new estimator of the failure probability as the product of a term given by a standard MC estimation based on the Kriging approximation, and a correction factor computed by means of a IS technique applied to the original performance function. Nevertheless, in [Cadini et al., 2015], they identified an apparent unbalanced effort between the estimation of the correction factor and the refinement of the metamodel itself.

To evaluate small failure probabilities ($p_f < 10^{-5}$) that would need more memory than available RAM with standard AK-MCS, the so-called AK-MCSi [Lelièvre et al., 2018] proposes to split the large MC population into several populations of smaller sizes and thus to perform sequential MC simulations. The authors also introduce a multi-point enrichment strategy similar to AK-MCS [Schöbi et al., 2016] and an original stopping criterion suitable when the probability of failure is MCS-based. However, in cases of very small failure probability, the method still requires a considerable number of metamodel evaluations (as in AK-MCS).

Among metamodel-based methods suitable for very small failure probability, the BSS [Bect et al., 2017] adaptively improves the surrogate accuracy corresponding to intermediate thresholds to avoid failure domains, combining SS and a sequential Bayesian approach [Bect et al., 2012].

II–3 General Framework

This section aims at describing the general concepts at the basis of the three proposed algorithms presented in this Part.

II–3.1 Isoprobabilistic Transformation

A central idea in the present Part consists in rewriting the failure probability and quantile definitions in the standard space. A diffeomorphism[5] referred to as an *isoprobabilistic transform*

$$\begin{aligned} T : \mathbb{Y} &\mapsto \mathbb{R}^d \\ \boldsymbol{y} &\to \boldsymbol{x} = T(\boldsymbol{y}) \end{aligned} \tag{II.42}$$

is constructed. Consequently, the following equalities hold:

$$\boldsymbol{X} = T^{-1}(\boldsymbol{Y}) \Leftrightarrow \boldsymbol{Y} = T(\boldsymbol{X}). \tag{II.43}$$

According to the available knowledge of the *physical* random vector $\boldsymbol{Y}$, several approaches are considered.

Independent Random Inputs The specific case of statistical independence between all the components is presented hereafter. It is assumed that the marginal distributions of $\boldsymbol{Y}$ are known through their CDFs F_{Y_i}. To build T, each component Y_i is first mapped into a uniform random variable $V_i \sim \mathcal{U}[0,1]$ using its CDF F_{Y_i}. The latter is then mapped into a standard normal variable X_i using the inverse CDF Φ^{-1} of the univariate standard normal distribution.

$$\begin{aligned} T :& \mathbb{Y} \mapsto \mathbb{R}^d \\ \boldsymbol{y} = (y_1, \ldots, y_d) \to & \qquad \boldsymbol{x} = \left(\Phi^{-1}(F_{Y_1}(y_1)), \ldots, \Phi^{-1}(F_{Y_d}(y_d))\right) \end{aligned} \tag{II.44}$$

Nataf Transform It is again assumed that the marginal distributions of $\boldsymbol{Y}$ are known through their CDFs F_{Y_i}, without the independence assumption though. Measures of dependence such as *copulas* [Nelson, 1999] might be used to represent the complementary information needed to define the joint CDF of $\boldsymbol{Y}$, in addition to the information provided by its marginals. The Nataf transformation [Nataf, 1962] [Lebrun and Dutfoy, 2009] can be considered, in particular, in the framework of copulas, or when the correlation matrix is known.

Rosenblatt Tranform The random vector $\boldsymbol{Y}$ is assumed to be known throught its full joint CDF $F_{\boldsymbol{Y}}$. The Rosenblatt is used to define T:

$$\begin{aligned} T :& \mathbb{Y} \mapsto \mathbb{R}^d \\ \boldsymbol{y} = (y_1, \ldots, y_d) &\to \boldsymbol{x} = (x_1, \ldots, x_d) \end{aligned} \tag{II.45}$$

where $\boldsymbol{x}$ can be defined as[6]

$$\begin{aligned} x_1 &= \Phi^{-1}\left(F_{Y_1}(y_1)\right) \\ x_2 &= \Phi^{-1}\left(F_{Y_2|Y_1}(y_2|y_1)\right) \\ &\ldots \\ x_d &= \Phi^{-1}\left(F_{Y_d|Y_1,\ldots,Y_{d-1}}(y_d|y_1, \ldots, y_{d-1})\right) \end{aligned} \tag{II.46}$$

Note that this expression requires the knowledge of the conditional CDFs.

[5] T is a bijection with T and T^{-1} continuously-differentiable.

[6] $d!$ choices can be made due to the variable ordering in the conditional expressions.

II–3.2 Initial DoE

An initial design of size $n_0 = 5d$ [Bect et al., 2017, Dubourg, 2011, Dubourg et al., 2013] is generated as described in [Bect et al., 2017], for the initialization of the surrogate of the LSF $\tilde{G}$.

A compact subset $\mathbb{X}_0 = \prod_{i=1}^{d}[q_\epsilon^i, q_{1-\epsilon}^i]$ is constructed, where q_ϵ^i and $q_{1-\epsilon}^i$ are respectively the quantiles of order ϵ and $1-\epsilon$ of the i^{th} input variable. Working in the standard space, $\mathbb{X}_0$ reads $[\Phi(\epsilon), \Phi(-\epsilon)]^d$. A LHS design on $[0,1]^d$ of size n_0 (criterion *maximin* here) is then scaled to $\mathbb{X}_0$ using an affine map. Such a sampling in the standard space is built in order to explore regions characterized by low density, from the initialization step.

II–3.3 Kriging Surrogate Model

In the context of failure probability or quantile estimation, a Kriging metamodel for G (Eq. I.124-II.8) is used.

It requires the generation of a DoE, denoted here by $\mathcal{X} = \{\boldsymbol{x}_1, ..., \boldsymbol{x}_m\}$, belonging to the support $\mathcal{D}_{\boldsymbol{x}} = \mathbb{R}^d$ of $\boldsymbol{X}$ (see Subsection II–3.2 for the initial DoE generation).

A Kriging surrogate $\hat{G}$ is built (Section I–2 for details), its BLUP predictor $\hat{G}(\boldsymbol{x})$ at an unknown location $\boldsymbol{x}$ satisfying:

$$\hat{G}(\boldsymbol{x}) = \mathcal{N}(\mu_{\hat{G}}(\boldsymbol{x}), \sigma^2_{\hat{G}}(\boldsymbol{x})) \tag{II.47}$$

G is assumed to be a sample path of the Gaussian Process $\hat{G}$. The metamodel of the original performance function is denoted by:

$$\tilde{G}(\boldsymbol{x}) = \mu_{\hat{G}}(\boldsymbol{x}).$$

In cases where an isoprobabilistic transform T is used to recast the *physical* problem into the *standard* one, it might be recommended to build a surrogate in the *physical* space first, namely for $J : \boldsymbol{y} \to J(\boldsymbol{y})$. It yields:

$$\tilde{G}(\boldsymbol{x}) = \mu_{\hat{G}}(\boldsymbol{x}) = \mu_{\hat{J}}(\boldsymbol{y}) \tag{II.48}$$

$$\sigma_{\hat{G}}(\boldsymbol{x}) = \sigma_{\hat{J}}(\boldsymbol{y}), \tag{II.49}$$

where $\boldsymbol{y} = T^{-1}(\boldsymbol{x})$.

II–3.4 Gaussian ISD Tuning: $\mathcal{N}(0, \gamma^2 I_d)$

In the following, ISD belonging to the family of centered isotropic multivariate Gaussian $\mathcal{N}(0, \gamma^2 I_d)$ are considered, parametrized by a scalar $\gamma \geq 1$. γ is tuned using the strategy described hereafter, based on CoV reduction considerations. The following failure probabilities are considered, based on the knowledge of the Kriging surrogate of G:

$$p_{\tilde{f}} = \mathbb{E}[\mathbb{1}_{\mu_{\hat{G}} < u}(\boldsymbol{X})] \tag{II.50}$$

$$p_{\tilde{f}}^{(k)+} = \mathbb{E}[\mathbb{1}_{\mu_{\hat{G}} + k\sigma_{\hat{G}} < u}(\boldsymbol{X})]. \tag{II.51}$$

A suitable choice for γ is expected to minimize the CoV when estimating the *predicted* failure probability $p_{\tilde{f}}$ with IS using the ISD $f_{\mathcal{N}(0,\gamma^2 I_d)}$. Based on this assumption, the following heuristic strategy is proposed to tune γ. For a fixed number of samples

N_γ, the functions $\mathrm{CoV}(\gamma)$ and $\mathrm{CoV}^+(\gamma)$ are defined on the range $[\gamma_{min}, \gamma_{max}]$ as the CoV obtained evaluating $p_{\tilde{f}}$, respectively $p_{\tilde{f}}^{(k)+}$, using the IS method (Section III–2.2) with $f_{\mathcal{N}(0,\gamma I_d)}$ as the ISD. Note that for a given metamodel and γ, those quantities may not be defined since $p_{\tilde{f}}$ or $p_{\tilde{f}}^{(k)+}$ might be null. The chosen value γ^*, is selected as the argument minimizing $\mathrm{CoV}(\gamma)$, if exists, otherwise as the one minimizing $\mathrm{CoV}^+(\gamma)$. If the latter does not exist, it is set to a default value γ_0.

Since only a gross estimation of γ is necessary, the following Monte-Carlo based algorithm for its selection is proposed:

1. Generate n_γ samples $\{\gamma_i\}_i$ uniformly in $[\gamma_{min}, \gamma_{max}]$.
2. For each i, evaluate: $\mathrm{CoV}(\gamma_i)$ and $\mathrm{CoV}^+(\gamma_i)$ (under existence)
3. Under existence, set $\gamma^* = \arg\min_i \mathrm{CoV}(\gamma_i)$.
4. Otherwise, under existence, set $\gamma^* = \arg\min_i \mathrm{CoV}^+(\gamma_i)$.
5. Otherwise, set $\gamma^* = \gamma_0$ (Default Value)

This operation requires $N_\gamma n_\gamma$ metamodel evaluations, and is performed anytime the metamodel is updated.

II–3.5 Test-Cases used for the assessment

Below is provided with a list of test-cases, used as benchmarks for the methods presented in Part A, for either failure probabilities (MetaAL-OIS, eAK-MCS) or extreme quantile estimation (QeAK-MCS). Test-cases described in Subsubsections II–3.5.1 II–3.5.3 II–3.5.5 II–3.5.6 are used in the scope of extreme quantile estimation, the latter seen as an inverse problem w.r.t. to the reliability analysis one. Indeed, the reference failure probability is viewed as the input quantile level, while the threshold value is considered as the sought quantile. This approach is adopted since designing accurately an extreme quantile test-case is a complex task, not solved in the sequel.

II–3.5.1 Single Failure Region 2D

A first 2D example is taken from [Echard et al., 2013] [Cadini et al., 2014]. This example is characterized by a low failure probability ($p_f \sim 3 \times 10^{-5}$), a very smooth (non-linear) limit state and a single failure region. The performance function in the standard space reads:

$$G(x_1, x_2) = \frac{1}{2}(x_1 - 2)^2 - \frac{3}{2}(x_2 - 5)^3 - 3, \tag{II.52}$$

where $X_1, X_2 \sim \mathcal{N}(0,1)$. The probability of failure reads $p_f = \mathbb{P}(G(\boldsymbol{X}) < 0)$. The reference value is estimated as 2.874×10^{-5} with a CoV of 0.03% using IS with a Gaussian mixture ISD [Razaaly and Congedo, 2018] based on 10^7 samples, reported in Table II.2.

Figure II.1 reports 2D contours and the LSS associated to the threshold $u = 0$.

Table II.2 Reference values for Single Failure Region 2D.

$p_f = \mathbb{P}(G(\boldsymbol{X}) < 0)^a$	CoV	N	MetaAL-OIS (Chapter III)	eAK-MCS (Chapter IV)	QeAK-MCS (Chapter V)
2.874×10^{-5}	0.04%	10^7	Subsection III–4.1	Section III–4	Subsection V–4.1

[a] Reference: IS with a Gaussian mixture as ISD [Razaaly and Congedo, 2018], 50 independent runs.

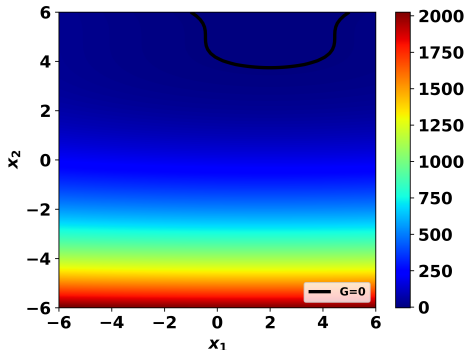

Figure II.1 Single Failure Region 2D performance function (Eq. II.52): Contours and LSS ($u = 0$).

II–3.5.2 Two failure regions 2D

This example deals with a case of two non-connected failure regions, featuring failure probabilities lying from around 3×10^{-3} to 9×10^{-7}, according to the selected parameter c in Equation II.53. The performance function [Cadini et al., 2014, Au and Beck, 1999, Dubourg et al., 2013] in the standard space reads:

$$G(x_1, x_2) = \min \left\{ \begin{array}{c} c - 1 - x_2 + e^{\frac{-x_1^2}{10}} + (\frac{x_1}{5})^4 \\ \frac{c^2}{2} - x_1 \cdot x_2 \end{array} \right\}, \tag{II.53}$$

where x_1, x_2 are the realizations of two independent standard Gaussian random variables. The three MPFPs are located at $\boldsymbol{u}_1^* = (0, c)$, $\boldsymbol{u}_2^* = (\frac{c}{\sqrt{2}}, \frac{c}{\sqrt{2}})$ and $\boldsymbol{u}_3^* = (-\frac{c}{\sqrt{2}}, -\frac{c}{\sqrt{2}})$, with the first two MPFPs belonging to the same failure region.

Au and Beck [Au and Beck, 1999] focused on the two first design points and apparently omitted the third one without much consequence on the results they present though [Dubourg et al., 2013].

We consider here three cases, with $c = 3, 4, 5$, respectively, the associated reference failure probabilities reported in Table II.3.

Table II.3 Reference values for Two Failure Regions 2D.

c	$p_f = \mathbb{P}(G(\boldsymbol{X}) < 0)^a$	CoV	N	MetaAL-OIS (Chapter III)	eAK-MCS (Chapter IV)	QeAK-MCS (Chapter V)
3	3.47×10^{-3}	0.10%	1.3×10^6	Subsection III–4.2	-	-
4	8.99×10^{-5}	0.10%	1.6×10^6	Subsection III–4.2	-	-
5	8.97×10^{-7}	0.10%	1.8×10^6	Subsection III–4.2	-	-

[a] Reference: IS with a Gaussian mixture as ISD [Razaaly and Congedo, 2018].

Figure II.2 reports 2D contours and the LSSs associated to the threshold $u = 0$ and the parameter c successively equal to 3, 4, 5.

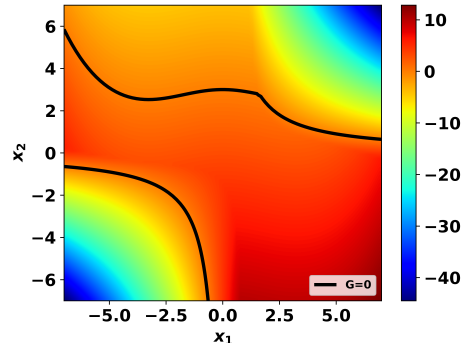

(a) $c = 3$

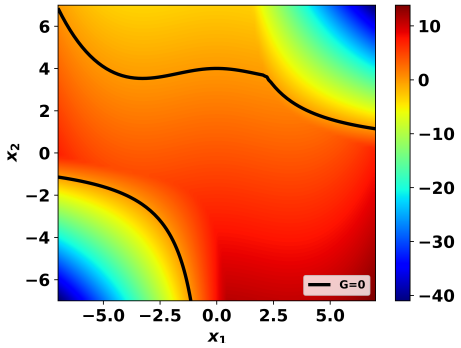

(b) $c = 4$

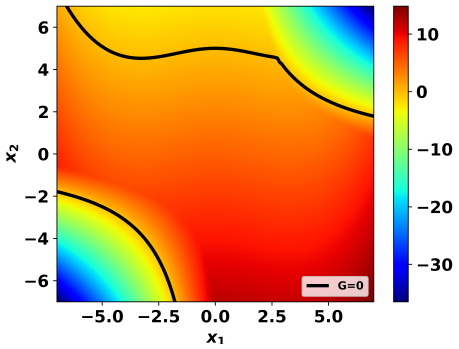

(c) $c = 5$

Figure II.2 Two Failure Regions 2D performance function (Eq. II.53): (a) $c = 3$, (b) $c = 4$, (c) $c = 5$.

II–3.5.3 Four-branch series system 2D

This example is a classical structural reliability test case [Cadini et al., 2014, Dubourg et al., 2013, Bect et al., 2017]. The performance function is defined as:

$$G(x_1, x_2) = \min \left\{ \begin{array}{c} 3 + \frac{(x_1 - x_2)^2}{10} - \frac{x_1 + x_2}{\sqrt{2}} \\ 3 + \frac{(x_1 - x_2)^2}{10} + \frac{x_1 + x_2}{\sqrt{2}} \\ x_1 - x_2 + \frac{7}{\sqrt{2}} \\ -(x_1 - x_2) + \frac{7}{\sqrt{2}} \end{array} \right\}, \tag{II.54}$$

and $X_1, X_2 \sim \mathcal{N}(0, 1)$.

In [Bect et al., 2017], the threshold is modified to make p_f smaller. The objective is to estimate $p_f = \mathbb{P}(G(\boldsymbol{X}) \leq u)$. For $u = -4$, the value of p_f is $p_f \sim 5.596 \times 10^{-9}$, with a CoV of about 0.04% [Bect et al., 2017], based on 100 runs of Subset Simulation with sample size 10^7. Reference failure probabilities are reported in Table II.4.

Figure II.3 reports 2D contours and the LSS associated to the threshold $u = 0$ and $u = -4$.

Table II.4 Reference values the Four-branch series system 2D.

u	$p_f = \mathbb{P}(G(\boldsymbol{X}) < u)$	CoV	N	MetaAL-OIS (Chapter III)	eAK-MCS (Chapter IV)	QeAK-MCS (Chapter V)
0	2.22×10^{-3}	0.10%	$2.0 \times 10^{6,a}$	Subsection III–4.3	-	-
-4	5.596×10^{-9}	0.04%	$10^{7,b}$	-	Section III–4	Subsection V–4.2

[a] Reference: IS with a Gaussian mixture as ISD [Razaaly and Congedo, 2018], based on 50 independent runs.

[b] Reference: SS [Bect et al., 2017], 100 independent runs.

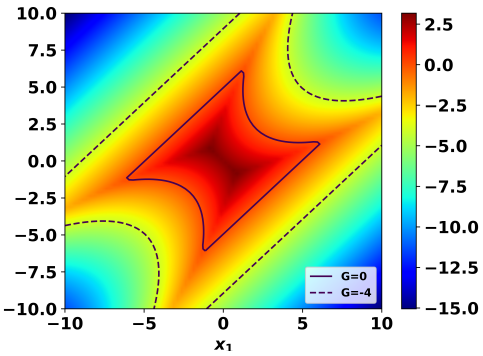

Figure II.3 Four-branch series system 2D performance function (Eq. II.54): Contours and LSSs.

II–3.5.4 Analytic "tricky" example with multiple failure regions: modified Rastrigin function

This test-case deals with a highly non-linear function involving non-convex and non-connected domains of failure (*i.e.* "*scattered gaps of failure*").

This case study is chosen because, in many works of literature, it represents a challenging test for the algorithms, due to the very complex failure domain made up of several disconnected regions, and despite the relatively large failure probability and close failure domains. The performance function [Cadini et al., 2014] [Dubourg et al., 2013] in the standard space reads:

$$G(x_1, x_2) = 10 - \sum_{i=1}^{2} (x_i^2 - 5\cos(2\pi x_i)) \tag{II.55}$$

where x_1, x_2 are the realizations of two independent standard Gaussian random variables. Reference failure probability is reported in Table II.5.

Table II.5 Reference values for the modified Rastrigin 2D case.

$p_f = \mathbb{P}(G(\boldsymbol{X}) < u)^a$	CoV	N	MetaAL-OIS (Chapter III)	eAK-MCS (Chapter IV)	QeAK-MCS (Chapter V)
7.29×10^{-2}	0.10%	$1.3 \times 10^{6,a}$	Subsection III–4.4	-	-

[a] Reference: IS with a Gaussian mixture as ISD [Razaaly and Congedo, 2018].

Figure II.4 reports 2D contours and the LSS associated to the threshold $u = 0$.

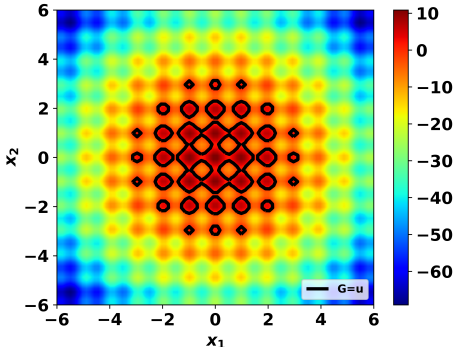

Figure II.4 Modified Rastrigin case 2D performance function (Eq. II.55): Contour and LSS.

II–3.5.5 Deviation of a Cantilever Beam 2D

This example is taken from [Bect et al., 2017]. A cantilever beam, with a rectangular cross-section is subjected to an uniform load. The deflection of the tip of the beam reads:

$$f(x_1, x_2) = \frac{3L^4 x_1}{2E x_2^3}, \tag{II.56}$$

with $L = 6$, $E = 2.6 \times 10^4$, X_1 and X_2 are assumed independent, with $X_i \sim \mathcal{N}(\mu_i, \sigma_i^2)$, $\mu_1 = 10^{-3}$, $\sigma_1 = 0.2\mu_1$, $\mu_2 = 0.3$ and $\sigma_2 = 0.1\mu_2$. The failure probability reads $p_f = \mathbb{P}(-f(\boldsymbol{X}) < -\frac{L}{325})$. The reference value is $p_f \sim 3.937 \times 10^{-6}$, with a CoV of about 0.03% [Bect et al., 2017], based on 100 runs of Subset Simulation with sample size 10^7, as reported in Table II.6.

Table II.6 Reference values: Deflection of a Cantilever Beam 2D

$p_f = \mathbb{P}(-f(\boldsymbol{X}) < -\frac{L}{325})^a$	CoV	N	MetaAL-OIS (Chapter III)	eAK-MCS (Chapter IV)	QeAK-MCS (Chapter V)
3.937×10^{-6}	0.04%	$10^{7,a}$	-	Section III–4	Subsection V–4.3

[a] Reference: SS [Bect et al., 2017], 100 independent runs.

Figure II.5 reports 2D contours and the LSS associated to the level $\{\boldsymbol{x} \in \mathbb{R}^2 \text{ s.t. } f(\boldsymbol{x}) = \frac{L}{325}\}$.

II–3.5.6 Response of a Nonlinear Oscillator 6D

This example deals with a non-linear undamped single degree of freedom system as reported in Figure II.6. This problem is selected because it presents a moderate number of random variables and is a classic benchmark in the literature [Echard et al., 2011, Echard et al., 2013, Bect et al., 2017].

The performance function is given as follows:

$$G(C_1, C_2, m, r, t_1, F_1) = 3r - \left| \frac{2F_1}{m\omega_0^2} sin\left(\frac{\omega_0 t_1}{2}\right) \right|, \tag{II.57}$$

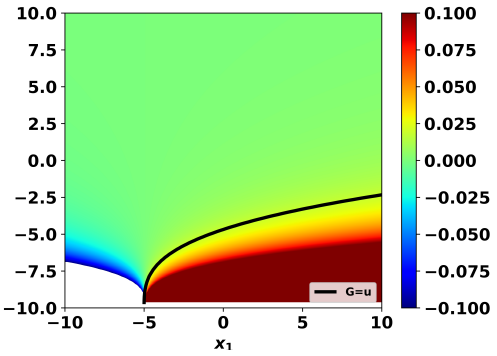

Figure II.5 Deviation of a Cantilever Beam 2D performance function: Contours and LSS associated to the level $\{\boldsymbol{x} \in \mathbb{R}^2 \text{ s.t. } \{f(\boldsymbol{x}) = \frac{L}{325}\}$.

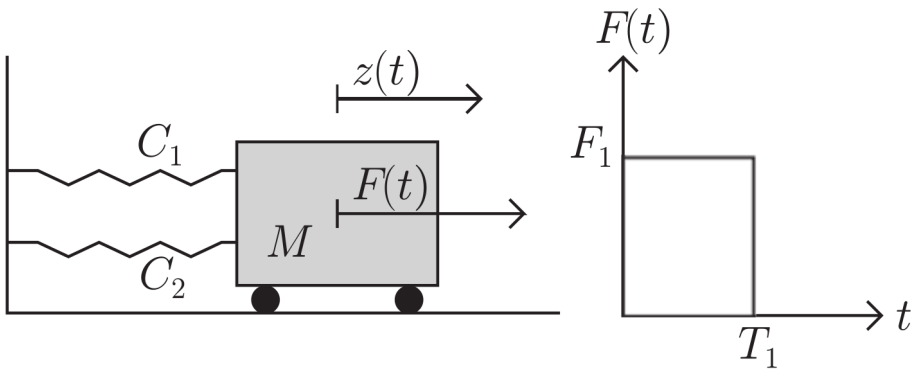

Figure II.6 Non-linear undamped single degree of freedom oscillator (Extracted from [Echard et al., 2013]).

with $\omega_0 = \sqrt{\frac{C_1 + C_2}{m}}$[7]. The six random variables (assumed independent) are listed in Table II.8.

The difficulty here comes from the relatively high dimension of the problem. The random variable $F_1 \sim N(1, 0.2^2)$ is defined in the original formulation in [Echard et al., 2011] with a failure probability $p_f \sim 3 \times 10^{-2}$. In [Bect et al., 2017], the variability of F_1 is modified w.r.t. [Echard et al., 2011] in order to make the failure probability $p_f = \mathbb{P}(G(\boldsymbol{X}) < 0)$ smaller ($p_f \sim 1.514 \times 10^{-8}$), as reported in Table **??**.

F_1	$p_f = \mathbb{P}(G(\boldsymbol{X}) < u)$	CoV	N	MetaAL-OIS (Chapter III)	eAK-MCS (Chapter IV)	QeAK-MCS (Chapter V)
$F_1 \sim N(1, 0.2^2)$ [Echard et al., 2011]	2.856×10^{-2}	0.10%	$2.9 \times 10^{6,a}$	Subsection III–4.5	-	-
$F_1 \sim N(0.45, 0.075^2)$ [Bect et al., 2017]	1.514×10^{-8}	0.04%	$10^{7,b}$	-	Section III–4	Subsection V–4.4

Table II.7 Reference values: Non-Linear Oscillator 6D.

[a] Reference: IS with a Gaussian mixture as ISD [Razaaly and Congedo, 2018].

[b] Reference: SS [Bect et al., 2017], 100 independent runs.

[7] $C_1 + C_2$ could be treated as an univariate Gaussian random variable. For sake of comparison, the problem formulation [Bect et al., 2017] remains unchanged.

Variable[a]	P.D.F.	Mean	Standard Deviation
m	Normal	1	0.05
C_1	Normal	1	0.1
C_2	Normal	0.1	0.01
r	Normal	0.5	0.05
F_1 [Echard et al., 2011]	Normal	1	0.2
F_1 [Bect et al., 2017]	Normal	0.45	0.075
t_1	Normal	1	0.2

Table II.8 Random Variables of the Non-Linear Oscillator 6D. Variability for F_1 is indicated twice, according to the version used (original [Echard et al., 2011] or modified [Bect et al., 2017].

[a] Variables are independent

III

Novel algorithm using Active Metamodel Learning and Importance Sampling: Application to multiple failure regions of low probability

Overview *A novel algorithm suitable for low-failure probability and multiple-failure regions, permitting to both building an accurate metamodel and to provide a statistically consistent error is proposed. Two unbiased estimators (including the one proposed in [Dubourg et al., 2013]) permit, by exploiting an ISD approximating the optimal one considering the Kriging surrogate knowledge, to provide an unbiased estimator at a low computational cost. Additionally, a Gaussian mixture-based importance sampling technique is proposed, permitting to drastically reduce the computational cost when estimating some reference values, or the failure probability directly from the metamodel. Several numerical examples are carried out, showing the very good performances of the proposed method with respect to the state-of-the-art in terms of accuracy and computational cost.*

III–1 Introduction

The problem of interest consists in providing an unbiased estimation of the following probability of failure re-written in the standard space:

$$p_f = \mathbb{P}(G(\mathbf{X}) < 0) = \mathbb{E}[\mathbb{1}_{G<0}(\mathbf{X})] = \int_{\mathbb{R}^n} \mathbb{1}_{G<0}(\mathbf{x}) f_{\mathbf{X}}(\mathbf{x}) d\mathbf{x}. \tag{III.1}$$

where $\mathbf{X} \sim \mathcal{N}(0, I_n)$, and G is the LSF in the standard space. For a sake of simplicity of the notation, the critical value is nullified without loss of generality (w.r.t. to Eq. II.7): $u = 0$.

The novel approach named *Metamodel-based combining Active Learning and quasi-Optimal Importance Sampling* (MetaAL-OIS), permits to explore all the failure regions simultaneously at a very low computational cost. It is based on the learning function used in AK-MCS [Echard et al., 2011], the K-Means clustering algorithm [MacQueen, 1967], and a MCMC sampling method. The metamodel proposed here focuses the refinement efforts on the limit state performance function. It is designed to fit with multiple failure regions, and very low probability. The method is characterized by the main following features: i) a parameter is used to avoid points clustering and also permits to implicitly control the refinement cost; ii) For multiple failure regions, which could be also non-connected, the failure branches are refined back and forth during the process; iii) An importance sampling procedure can be carried out in order to obtain an unbiased estimator of the failure probability; iv) The metamodel can be used in order to obtain an estimation of the failure probability; v) Refinement efforts are concentrated on the limit-state function.

The second contribution of the proposed method is the use of a quasi-optimal Importance Sampling Density (ISD) ([Dubourg et al., 2013]) built from the metamodel, in order to obtain an unbiased estimation of p_f (see Section III–3.2). The notation *quasi-optimal* is used since a perfect knowledge of the failure region (and then of the optimal density) is not possible in practice [Dubourg et al., 2013]. Two different estimators are considered in this case. One [Dubourg et al., 2013] involves the product of two terms: namely one obtained by sampling the *surrogate* performance function, and the other one being a corrector factor computed from the *original* performance function. The second one combines a Control Variate technique with Importance Sampling, permitting to obtain another unbiased estimator, using the same performance function evaluations. Then, it is possible to select the best estimator *a posteriori* without any further computations.

An additional contribution is also the formulation of a method permitting to *significantly* reduce the computational time (compared to MCS) in order to compute a failure probability directly from the metamodel, especially when the failure probability is expected to be very low. AK-IS [Echard et al., 2013], KAIS [Zhao et al., 2015] and AK-SS [Huang et al., 2016] have proposed similar approaches. The idea here is to mimic the quasi-optimal ISD (Importance Sampling Density) behavior with a Gaussian mixture law. This Gaussian mixture density thus serves as the ISD in the IS method, in order to reduce dramatically the number of metamodel calls, when computing the failure probability from the metamodel. The same method can be applied to the original performance function, for example in analytic cases, in order to compute accurate reference values.

This presentation is organized as follows. First, some general definitions concerning Gaussian Processes (GP) and IS theory are recalled in Section III–2. The new algorithm proposed in this study is illustrated in Section III–3. In particular, the metamodel adaptive refinement and the quasi-optimal IS strategy are described in Subsubsection III–3.1 and III–3.3, respectively. Section III–4 illustrates several numerical examples in order to assess the accuracy and efficiency of the MetaAL-OIS method.

III–2 General concepts

In this section, some general concepts useful in order to illustrate the MetaAL-OIS are introduced. Indeed, the first step of the proposed algorithm, is to build a metamodel $\tilde{G}$ of the original performance function: i) The metamodel is initialized with Latin Hypercube Sampling (LHS) points, and a Gaussian Process (GP) is used to define the surrogate $\tilde{G}$; ii) a refinement strategy based on Markov Chain Monte Carlo (MCMC) sampling is performed.

Then, once the metamodel is accurately refined on the surrogate limit-state region $\{\tilde{G}(\mathbf{x}) = 0\}$, an IS method is extensively used for the computation of different quantities using different Importance Sampling Densities (ISD). Finally, the unbiased estimation computation is carried out by using a multimodal MCMC technique aimed at sampling points drawn from the quasi-optimal ISD.

III–2.1 Probabilistic classification using Gaussian Processes

A Kriging surrogate (see Section I–2) is built from a DoE $\mathcal{X} = \{(\mathbf{x}_i, G(\mathbf{x}_i)\}_{i\in 1,m}$. Its BLUE $\hat{G}(\boldsymbol{x})$ at an unknown location $\boldsymbol{x}$ satisfies:

$$\hat{G}(\mathbf{x}) \sim \mathcal{N}(\mu_{\hat{G}(\mathbf{x})}, \sigma^2_{\hat{G}(\mathbf{x})}),$$

while the surrogate $\tilde{G}$ for the LSF G reads $\tilde{G}(\mathbf{x}) = \mu_{\hat{G}(\mathbf{x})}$.

The *probabilistic classification function* [Dubourg et al., 2013] is introduced:

$$\pi(\mathbf{x}) = \mathcal{P}[\hat{G}(\mathbf{x}) \leq 0], \tag{III.2}$$

where the probability measure $\mathcal{P}[\cdot]$ refers to the Gaussian nature of the GP predictor $\hat{G}(\mathbf{x})$. The function $\pi(\mathbf{x})$ rewrites as follows:

$$\pi(\mathbf{x}) = \phi\left(\frac{0 - \mu_{\hat{G}(\mathbf{x})}}{\sigma_{\hat{G}(\mathbf{x})}}\right), \text{ if } \mathbf{x} \notin \mathcal{X}, \tag{III.3}$$

where ϕ denotes the *cumulative density function* (CDF) of the one-dimensional standard normal law. Concerning the points of the experimental design for which the prediction variance is equal to zero, the above function reads

$$\pi(\mathbf{x}) = \begin{cases} 1 & \text{if } \mathbf{x} \in \mathcal{X},\ G(\mathbf{x}) \leq 0 \\ 0 & \text{if } \mathbf{x} \in \mathcal{X},\ G(\mathbf{x}) > 0. \end{cases} \tag{III.4}$$

It may be interpreted as the probability that the predictor $\hat{G}(\mathbf{x})$ is negative with respect to the epistemic uncertainty. Note that π can be used as a surrogate for $\mathbb{1}_{G<0}$.

III–2.2 Surrogate-based Importance sampling

The expression of the optimal ISD for the computation of the failure probability (Eq. V.1) is recalled:

$$h_G^*(\mathbf{x}) = \frac{\mathbb{1}_{G<0}(\mathbf{x}) f_{\mathbf{X}}(\mathbf{x})}{p_f}. \tag{III.5}$$

In this case, $\pi(\mathbf{x})$ is used as a surrogate for $\mathbb{1}_{G<0}(\mathbf{x})$. In order to ensure that the resulting quasi-optimal ISD h_π^* is a PDF, a constant $p_\pi = \int_{\mathbb{R}^n} \pi(\mathbf{x}) f_{\mathbf{X}}(\mathbf{x}) d\mathbf{x} = \mathbb{E}[\pi(\mathbf{X})]$ has to be computed, so h_π^* reads:

$$h_\pi^*(\mathbf{x}) = \frac{\pi(\mathbf{x}) f_{\mathbf{X}}(\mathbf{x})}{p_\pi}. \tag{III.6}$$

Note that using $\mathbb{1}_{\tilde{G}<0}(\mathbf{x})$ as a surrogate for $\mathbb{1}_{G<0}(\mathbf{x})$ is tempting, leading to the following ISD $h_{\tilde{G}}^*$:

$$h_{\tilde{G}}^*(\mathbf{x}) = \frac{\mathbb{1}_{\tilde{G}<0}(\mathbf{x}) f_{\mathbf{X}}(\mathbf{x})}{p_{\tilde{f}}}. \tag{III.7}$$

where $p_{\tilde{f}} = \mathbb{E}[\mathbb{1}_{\tilde{G}<0}(\mathbf{X})]$. However, the condition $\mathbb{1}_{\tilde{G}<0}(\mathbf{x}) f_{\mathbf{X}}(\mathbf{x}) = 0 \implies \mathbb{1}_{G<0}(\mathbf{x}) f_{\mathbf{X}}(\mathbf{x}) = 0$ can not be ensured, so a bias may occur. In this sense, $h_\pi^*(\mathbf{x})$ is a robust quasi-optimal ISD and does not induce a bias in the final estimation. The p_π estimation is illustrated in Subsection III–3.2.

III–2.3 MCMC Metropolis-Hastings sampling

In order to sample points according to a given target PDF $p(\boldsymbol{x})$, it is resorted to a MCMC Metropolis-Hastings algorithm (see algorithm III.1).

Algorithm III.1 Metropolis-Hastings sampler

Input: *Seed* $\boldsymbol{x}^{(0)}$ s.t. $p(\boldsymbol{x}^{(0)}) > 0$, Proposal PDF q, $N \in \mathbb{N}$
Output: $\{\boldsymbol{x}^{(i)}\}_{i \in [\![1,N]\!]} \sim p$

$i = 0$ **while** $i < N$ **do**
  Propose a new candidate $\boldsymbol{x}^* \sim q(\cdot|\boldsymbol{x}^{(i)})$
  $r^{(i+1)} = \min(1; \frac{p(\boldsymbol{x}^*) q(\boldsymbol{x}^{(i)}|\boldsymbol{x}^*)}{p(\boldsymbol{x}^{(i)}) q(\boldsymbol{x}^*|\boldsymbol{x}^{(i)})})$
  Sample $u \sim \mathcal{U}[0,1]$
  if $u < r^{(i+1)}$ **then**
    Accept $\boldsymbol{x}^*$. $\boldsymbol{x}^{(i+1)} \leftarrow \boldsymbol{x}^*$
  else
    Reject $\boldsymbol{x}^*$. $\boldsymbol{x}^{(i+1)} \leftarrow \boldsymbol{x}^{(i)}$
  $i \leftarrow i + 1$

Note that it is only required to compute $p(\boldsymbol{x})$ within a multiplicative constant. When dealing with an unimodal pdf p, it is resorted to the modified Metropolis-Hasting sampler proposed in [Au and Beck, 2001]. It requires a new parameter, referred in the following as α_{MCMC}. The new candidate computation step is replaced by $\boldsymbol{x}^* \sim \mathcal{U}[\boldsymbol{x}^{(i)} - \alpha_{MCMC}, \boldsymbol{x}^{(i)} + \alpha_{MCMC}]$. This proposal PDF q being symmetrical, the new acceptance probability reads $r^{(i+1)} = \min(1; \frac{p(\boldsymbol{x}^*)}{p(\boldsymbol{x}^{(i)})})$. It is suggested in [Au and Beck, 2001] to

take $\alpha_{MCMC} = 1$.
When dealing with a multimodal proposal PDF p, a multimodal Proposal PDF q is used as a mixture of Gaussian law, depending of the current position of the chain. The mixture of Gaussian law's parameters' computations are detailed in the Subsection III–3.2 and it is considered that p contains at maximum M modes. Finally, the algorithm III.2 is used, which is inspired from [Au and Beck, 2001]. Note that $c \sim \mathcal{D}(\alpha)$ refers $\mathcal{D}(\alpha_1, ..., \alpha_M)$ defined by $\mathbb{P}(c = j) = \alpha_j$, for $j \in [\![1, M]\!]$. For $k \in [\![1, M]\!]$, $\boldsymbol{e_k}$ is the square matrix defined by $\boldsymbol{e_k} = [\delta_{kj}]_{i,j \in [\![1,M]\!]}$, δ denoting the Kronecker function, so it is null except on the k^{th} column where it is 1.
Also, for $z = (c, \boldsymbol{\mu})$ and $\tilde{z} = (\tilde{c}, \tilde{\boldsymbol{\mu}})$, the following equality holds:

$$q(z|\tilde{z}) = \alpha_c f_{\mathcal{N}(\tilde{\mu}_c, \Sigma_c)}(\mu_c), \tag{III.8}$$

where $f_{\mathcal{N}(\mu,\Sigma)}$ refers to the multivariate Gaussian PDF with mean μ and covariance Σ.

Algorithm III.2 Multimodal Metropolis-Hastings sampler

Input: $(\Sigma_1, ..., \Sigma_M)$ a set of $(d \times d)$ covariance matrices
$\alpha = (\alpha_1, ..., \alpha_M) \in [0, 1]^M$ a set of weights such $\sum_{k=1}^{M} \alpha_k = 1$
$\boldsymbol{\mu}^{(0)} = (\mu_1^{(0)}, ..., \mu_M^{(0)}) \in \mathbb{R}^{d \times M}$ s.t. $\forall k \in [\![1, M]\!],\ p(\mu_k^{(0)}) > 0$
$c^{(0)} \sim \mathcal{D}(\alpha)$
$z^{(0)} = (c^{(0)}, \boldsymbol{\mu}^{(0)})$
$\boldsymbol{x}^{(0)} = \mu_{c^{(0)}}^{(0)}$
$N \in \mathbb{N}$
Output: $\{\boldsymbol{x}^{(i)}\}_{i \in [\![1,N]\!]} \sim p$
$i = 0$ **while** $i < N$ **do**
  Propose a new candidate $z^* = (c^*, \boldsymbol{\mu}^*) \sim q(\cdot|z^{(i)})$:
    $c^* \sim \mathcal{D}(\alpha)$
    $\mu_{c^*}^* \sim \mathcal{N}(\mu_{c^*}^{(i)}, \Sigma_{c^*})$
    $\boldsymbol{\mu}^* = \boldsymbol{\mu}^{(i)} + \boldsymbol{e_{c^*}}(\mu_{c^*}^* - \mu_{c^*}^{(i)})$
    $z^* = (c^*, \boldsymbol{\mu}^*)$
    $\boldsymbol{x}^* = \mu_{c^*}^*$
  $r^{(i+1)} = \min(1; \frac{p(\boldsymbol{x}^*) q(z^{(i)}|z^*)}{p(\boldsymbol{x}^{(i)}) q(z^*|z^{(i)})})$
  Sample $u \sim \mathcal{U}[0, 1]$
  if $u < r^{(i+1)}$ **then**
    Accept z^*: $z^{(i+1)} \leftarrow z^*$
      $\boldsymbol{x}^{(i+1)} \leftarrow \boldsymbol{x}^*$
  else
    Reject z^*. $z^{(i+1)} \leftarrow z^{(i)}$
      $\boldsymbol{x}^{(i+1)} \leftarrow \boldsymbol{x}^{(i)}$
  $i \leftarrow i + 1$

III–3 The MetaAL-OIS algorithm

In this Section, the method proposed, *i.e.* the MetaAL-OIS algorithm is described. A general sketch of the algorithm is given in Figure III.2. The first step consists in building a metamodel refined on the limit-state region, which is described in Subsection

III–3.1 and Figure III.1. This step is divided in two main parts: i) Building the metamodel from an initial sampling (LHS); ii) Refining iteratively the metamodel in the failure region.

Secondly, a Gaussian mixture ISD is used to compute a primary estimation of the probability of failure, based only on the metamodel:

$$\hat{p}_{\tilde{f}} = \mathbb{E}[\mathbb{1}_{\tilde{G}<0}(\boldsymbol{X})] \tag{III.9}$$

$$\hat{p}_{\pi} = \mathbb{E}[\pi(\boldsymbol{X})]. \tag{III.10}$$

This method is particularly fit for very low failure probabilities, where MCS method would involve a very large number of metamodel evaluations. A sharp estimation based on the metamodel is then available with a reasonable number of metamodel evaluations. This is illustrated in Subsection III–3.2. Third, in order to provide an unbiased estimation of p_f at a low computational cost, two estimators, described in Subsection III–3.3, are computed: the first one is directly taken from MetaIS [Cadini et al., 2014] algorithm, and the second uses both Control Variate method and IS. They both use the same points drawn from the multimodal MCMC sampler (see algorithm III.2) with the ISD $h^*_{\pi}(\boldsymbol{x})$. The original performance function G is evaluated at those points, and the two estimators are computed. So, an *a posteriori* analysis of their respective variance estimator leads the user to select the best estimation. If the target coefficient of variation δ_{target} is not reached, new points are sampled, and the estimators are updated. Otherwise, the algorithm stops, and the estimator associated to the lowest coefficient of variation is returned. Finally, Subsection V–3.4 is devoted to a description about the parameters tuning of the proposed algorithm.

III–3.1 Metamodel Refinement Strategy

A new metamodel refinement strategy is here proposed. In order to show the main features of this algorithm, let us introduce first the definition of the learning function U [Cadini et al., 2015] associated to $\tilde{G}$. For a given $\boldsymbol{x}$, $U(\boldsymbol{x})$ is defined as

$$U(\boldsymbol{x}) = \frac{|\mu_{\hat{G}}(\boldsymbol{x})|}{\sigma_{\hat{G}}(\boldsymbol{x})}. \tag{III.11}$$

In this definition, $\Phi(U(\boldsymbol{x}))$ is the probability that $\boldsymbol{x}$ is correctly classified by the predictor, where Φ refers to the CDF of the standard Gaussian random variable. For a given set of points $\mathcal{X}$, $\boldsymbol{x}_0$, defined as follows

$$\boldsymbol{x}_0 = \underset{\boldsymbol{x}\in\mathcal{X}}{\arg\min}\ U(\boldsymbol{x}), \tag{III.12}$$

indicates the point where the classification is the most uncertain among $\mathcal{X}$. In AK-MCS [Echard et al., 2011], the DoE is iteratively enriched at the point $\boldsymbol{x}_0$ by minimizing the learning function U (see Eq. III.12) searching in a Monte Carlo population. The stopping criterion is $U(\boldsymbol{x}_0) \geqslant 2$, meaning that the sample, whose group is the most uncertain, displays a probability being correctly classified of at least $\Phi(2) = 97.7\%$. Though, this method has several drawbacks. When the limit state $G(\boldsymbol{x}) = 0$ has different branches, the learning function U usually focuses on one of them first. Once the metamodel is accurate enough in this region, the learning criterion goes to another branch and carries on. If the refinement procedure is stopped, for instance because the

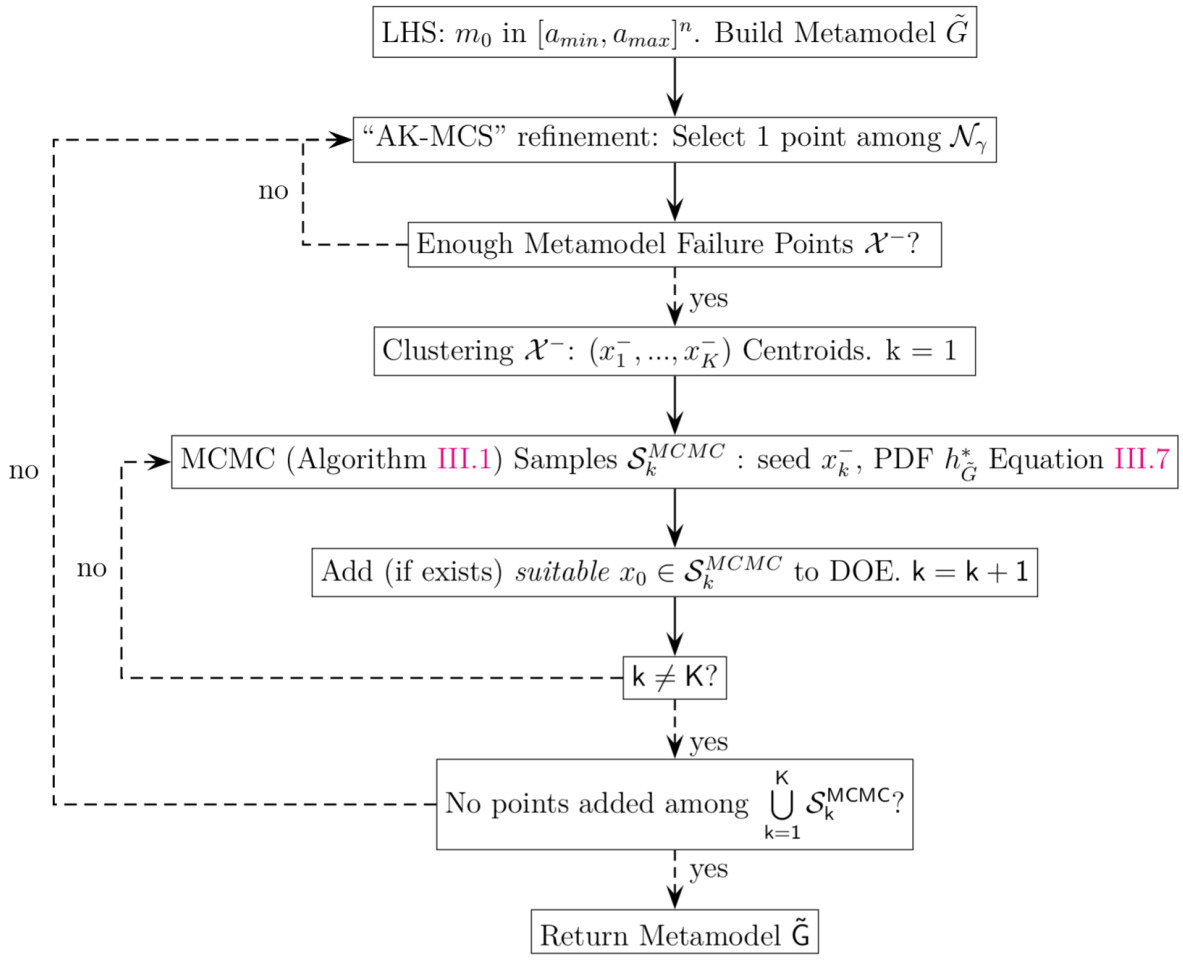

Figure III.1 MetaAL-OIS: Metamodel Refinement.

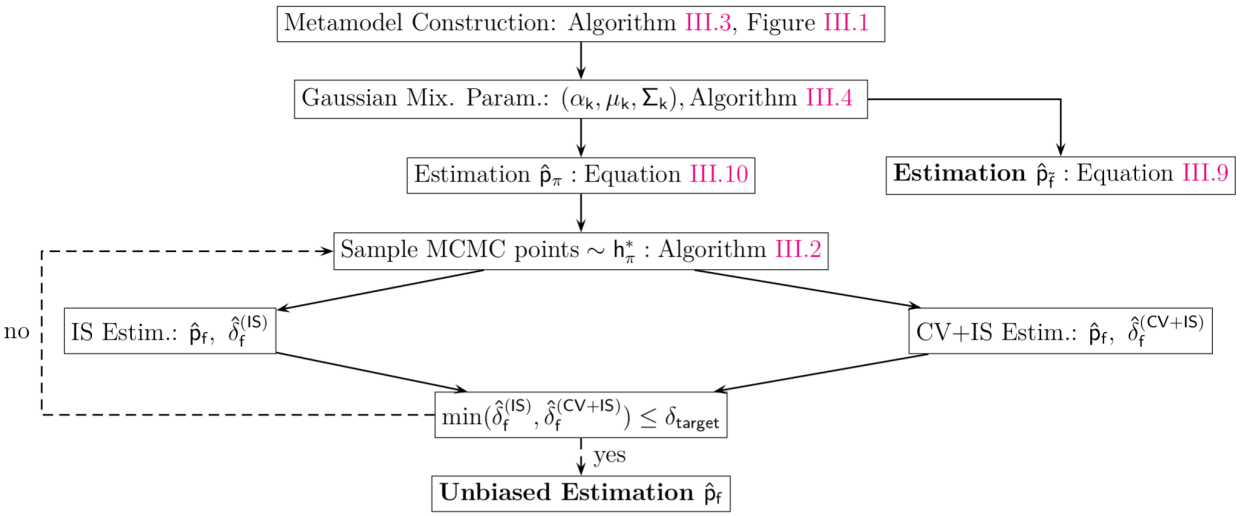

Figure III.2 MetaAL-OIS: Algorithm.

DOE is too large, the metamodel can be accurately refined in some failure branches

and too coarse on some others. Moreover, it can lead to clusters of points so numerical instabilities can arise during the metamodel building.

For these reasons, it is resorted to a new learning function,
$\mathcal{L}_U(\mathcal{X}, d_{min}, r_{max}, U_{max}, \mathcal{X}_{DOE})$:
It returns either a set containing a new point $\{\boldsymbol{x}_0\} \in \mathcal{X}$, or $\varnothing$. The algorithm has the following steps :

1. Compute the subset $\mathcal{Y} \subseteq \mathcal{X}$ such that $\forall \boldsymbol{y} \in \mathcal{Y}$:
   - $\min_{\boldsymbol{z} \in \mathcal{X}_{DOE}} \|\boldsymbol{y} - \boldsymbol{z}\| > d_{min}$,
   - $\|\boldsymbol{y}\| \leqslant r_{max}$
2. In $\mathcal{Y}$, select the point (if $\mathcal{Y}$ is not empty) minimizing the learning function U: $\boldsymbol{x}_0 = \arg\min_{\boldsymbol{y} \in \mathcal{Y}} U(\boldsymbol{y})$.
3. If $\mathcal{Y}$ is empty, or $U(\boldsymbol{x}_0) > U_{max}$, return $\varnothing$. Otherwise return $\{\boldsymbol{x}_0\}$.

Note that $\mathcal{X}_{DOE}$ represents the current set of DoE, $\mathcal{Y}$ contains points which satisfy geometrical conditions prescribing a minimal distance between the DoE candidates and the current ones. Moreover, candidates which are too far from the center $0_{\mathbb{R}^d}$ are discarded.
Minimizing the learning function U on $\mathcal{Y}$ permits to find the point among $\mathcal{Y}$ having the highest probability of being misclassified by the GP predictor. Returning only points $\boldsymbol{x}_0$ such that $U(x_0) \leq U_{max}$ ensures that points too accurately predicted are not considered as D.o.E candidates.

The parameter d_{min} represents the minimal distance between two elements of the DoE in the standard space. A proper choice of this parameter could permit to avoid a clustering of points of the DoE and to increase numerical stability when building the metamodel. In the following, $d_{min} = 0.5$ is fixed.
As in [Echard et al., 2011], it is suggested to take $U_{max} = 2$. In this way, accepted DoE candidates are correctly classified by the predictor with a probability higher than 97.7%. Considering a higher value of this parameter could increase both the global number of samples constituting the DoE and the metamodel accuracy.
The refinement algorithm for the metamodel construction relies then on the following steps:

1. *Initial DOE and metamodel definition*: A number m_0 of samples generated by means of a Latin Hypercube Sampling (LHS) in $[a_{min}, a_{max}]^n$. Build the metamodel $\tilde{G}$. If p_f is expected to be very low, so the failure regions should be more distant from the standard space center, the size of the hypercube box should be increased. This is further discussed in Subsubsection V–3.4. Set i = 1.
2. "*AK-MCS*" *Step*: Sample a quite large population $\mathcal{N}_\gamma = \{\boldsymbol{x}_\gamma^{(1)}, ..., \boldsymbol{x}_\gamma^{(N_\gamma)}\}$ constituted by independent samples drawn from $\mathcal{N}(0, \gamma I_d)$. Update the D.o.E with $\boldsymbol{x}_0 \in \mathcal{N}_\gamma$, obtained by minimizing the learning function U. Note that $x_0 = \mathcal{L}_U(\mathcal{N}_\gamma, d_{min}, r_{max}, U_{max}, \mathcal{X}_{DOE})$. Update $\tilde{G}$. If $\#\{\text{D.o.E.}\} \geqslant N_{DOE}^{MAX}$, stop the metamodel refinement algorithm. This step is aimed to capture all failure regions, with a relatively low number of samples, mimicking the AK-MCS algorithm. Go to step 3.

3. *Classification*:
   Compute $\mathcal{X}^- = \{\boldsymbol{x} \in \mathcal{N}_\gamma : \mu_{\hat{G}(\boldsymbol{x})} \leq 0\}$. If $\#\{\mathcal{X}^-\} < K$, go step 2, step 4 otherwise.

4. *Seed Selection*: Use k-Means [MacQueen, 1967] clustering algorithm on the set $\mathcal{X}^-$. Its K clusters centroids are considered: $(\boldsymbol{x}_1^-, ..., \boldsymbol{x}_K^-)$. Set $k = 1$.

5. *Unimodal MCMC Sampling*: Sample a set of N_{MCMC} points $\mathcal{S}_k^{MCMC}$ drawn from the PDF $h^*_{\tilde{G}}$ using the MCMC Metropolis-Hastings sampler (Algorithm III.1), with the seed initialized at $\boldsymbol{x}_k^-$.

6. *Enrich DoE at step k*: Update the metamodel at $\tilde{\boldsymbol{x}}_k^- = \mathcal{L}_U(\mathcal{S}_k^{MCMC}, d_{min}, r_{max}, U_{max}, \mathcal{X}_{DOE})$; if $\#\{\text{D.o.E.}\} \geqslant N_{DOE}^{MAX}$, stop the metamodel refinement algorithm.

7. *Stopping criterion:* If $k \neq K$, set $k = k + 1$ and loop back to step 5.
   If $k = K$ and $\bigcup_{k=1}^{K} \{\tilde{x}_k^-\} = \varnothing$, stop the metamodel refinement algorithm.
   If $i = N_{loop}^{MAX}$, stop the metamodel refinement algorithm.
   Otherwise, set $i = i + 1$ and loop back to step 2.

Globally, the metamodel refinement strategy can be resumed under the Algorithm III.3.

Algorithm III.3 Metamodel Refinement Algorithm

Input: m_0, N_{loop}^{MAX}, K

Output: Metamodel $\tilde{G}$

Sample m_0 LHS points in $[a_{min}, a_{max}]^d$. Build $\tilde{G}$.
for $i_{loop} = 1,\ N_{loop}^{MAX}$ **do**
  Set $\mathcal{X}^- = \varnothing$
  while $\#\{D.o.E.\} < N_{DOE}^{MAX}$ *and* $\#\{\mathcal{X}^-\} < K$ **do**
    Sample $\mathcal{N}_\gamma$, select $x_0 \in \mathcal{N}_\gamma$, update $\tilde{G}$ and $\mathcal{X}^-$.
  Run k-Means algorithm on $\mathcal{X}^-$ and find $(\boldsymbol{x}_1^-, ..., \boldsymbol{x}_K^-)$.
  for $k = 1,\ K$ **do**
    Sample $\mathcal{S}_k^{MCMC}$ using MCMC: the target PDF is $h^*_{\tilde{G}}$, the seed is x_k^-.
    Select (if exists) $\boldsymbol{x}_0 \in \mathcal{S}_k^{MCMC}$; Update $\tilde{G}$.
  if *No points added among* $\bigcup_{k=1}^{K} \mathcal{S}_k^{MCMC}$ **then**
    Return $\tilde{G}$.
  Return $\tilde{G}$.

Concerning the possibility to exploit parallelism to accelerate the algorithm, note that the first step of the metamodel building (LHS) can be fully parallelized. By contrast, the metamodel refinement strategy presented in this study is sequential. The unbiased estimation step can be *almost* fully parallelized: in practice, this estimation is either driven by a maximal budget evaluation, in which case the step is fully parallelizable; or driven by a CoV target. In the latter case, the unbiased estimation should be updated "iteratively", after parallelized evaluations of sampling sets of a given size (depending on power availability).

III–3.2 Importance Sampling on the metamodel: Gaussian mixture ISD

In this Subsubsection, the method used to compute p_π and $p_{\tilde{f}}$, starting with a refined metamodel $\tilde{G}$ is described. The p_π and $p_{\tilde{f}}$ values are computed using Importance Sampling, the instrumental PDF $h_{\mathcal{N}}$ being chosen as a mixture of Gaussians as follows:

$$h_{\mathcal{N}}(\boldsymbol{x}) = \sum_{k=1}^{K^{IS}} \alpha_k^{IS} f_{\mathcal{N}(\mu_k^{IS}, \Sigma_k^{IS})}(\boldsymbol{x}), \tag{III.13}$$

where $\alpha_k^{IS} \in [0,1]$ are weights such that $\sum_{k=1}^{K^{IS}} \alpha_k^{IS} = 1$, $f_{\mathcal{N}(\mu_k^{IS}, \Sigma_k^{IS})}$ denotes the PDF of the Gaussian vector centered in $\mu_k^{IS} \in \mathbb{R}^n$ with a covariance matrix $\Sigma_k^{IS} \in \mathbb{R}^{n \times n}$.

Note that a suitable estimation of $\{\alpha_k^{IS},\ \mu_k^{IS}, \Sigma_k\}_k$ is the key of the efficiency of this method, resumed in Algorithm III.4. In a nutshell, failure points $\mathcal{X}^-$ are sampled using step 5 of Algorithm III.3 and classified in K^{init} groups. Centroids of these groups are iteratively used as the seed of the unimodal MCMC sampler, in order to sample points following the quasi-optimal ISD h_π^*, in *all failure regions*.
These samples are again classified in K^{IS} groups, from which the empirical weight, mean and covariance are estimated and used as the Gaussian mixture parameters.

Algorithm III.4 Empirical estimation of $\{\alpha_k^{IS},\ \mu_k^{IS}, \Sigma_k\}_k$

Input: $K^{init}, K^{IS}, \tilde{G}$
Output: $\{\alpha_k^{IS},\ \mu_k^{IS}, \Sigma_k\}_{k \in [\![1, K^{IS}]\!]}$

22 Sample failure points $\mathcal{X}^-$ according to $\tilde{G}$.
Run k-Means algorithm on $\mathcal{X}^-$ and find the centroids $(x_1^-, ..., x_{K^{init}}^-)$.

23 **for** $k = 1,\ K^{init}$ **do**

24 Sample $\mathcal{S}_k^{MCMC}$ using MCMC: the target PDF is h_π^*, the seed is x_k^-.

25 Run k-Means algorithm on $\bigcup_{k=1}^{K} \mathcal{S}_k^{MCMC}$ so it is classified in K^{IS} sets $(\mathcal{S}_1^{IS}, ..., \mathcal{S}_{K^{IS}}^{IS})$.
$\forall k \in [\![1, K^{IS}]\!]$, μ_k^{IS} and Σ_k are defined respectively as the empirical mean and the empirical covariance of $\mathcal{S}_k^{IS}$. α_k^{IS} is defined as the empirical weight $\dfrac{\#\mathcal{S}_k^{IS}}{\#\bigcup_{k=1}^{K^{IS}} \mathcal{S}_k^{IS}}$.

Using this IS method is not necessary when the estimated failure probability is relatively high. Though, even in the case of very low failure probabilities, it is possible to have sharp estimations of those quantities with a reasonable number of metamodel evaluations. The idea behind this IS technique, is to mimic the quasi-optimal multimodal ISD in order to decrease the required number of samples, with a Gaussian mixture density which does not require any unknown parameters.

The resulting computations provide the estimations of $\hat{p}_\pi$ and $\hat{p}_{\tilde{f}}$, the corresponding variance estimations $\hat{\sigma}^2_{p_\pi}$ and $\hat{\sigma}^2_{p_{\tilde{f}}}$ and the coefficients of variation $\hat{\delta}_{p_\pi}$ and $\hat{\delta}_{p_{\tilde{f}}}$. The $\hat{p}_{\tilde{f}}$ value can be used as a good estimation of p_f, but an error bound cannot be provided. However, it is in practice a very good estimation.

This IS procedure, aimed to provide the estimation of $\hat{p}_{\tilde{f}}$ based on a sampling technique applied to the metamodel, shares the same objective of the following metamodel-based methods, once the metamodel is refined: AK-IS, KAIS, MetaAK-IS^2, AK-SS. It aims to decrease the number of metamodel evaluations when the expected failure probability is very low.

III–3.3 Importance Sampling on the performance function: quasi-optimal ISD

In order to have a statistically consistent error for $\hat{p}_f$, the instrumental PDF $h^*_\pi(\boldsymbol{x}) = \dfrac{\pi(x) f_X(\boldsymbol{x})}{p_\pi}$ is used, and two estimators based on this quasi-optimal ISD are considered.

III–3.3.1 Importance Sampling Estimator

This estimator is the one used in the second step of the metaIS [Dubourg et al., 2013]. The failure probability is re-written as:

$$\begin{aligned} p_f &= \int_{\mathbb{R}^n} \mathbb{1}_{G<0}(\boldsymbol{x}) \frac{f_X(\boldsymbol{x})}{h^*_\pi(\boldsymbol{x})} h^*_\pi(\boldsymbol{x}) d\boldsymbol{x} \\ &= p_\pi \int_{\mathbb{R}^n} \frac{\mathbb{1}_{G<0}(\boldsymbol{x})}{\pi(\boldsymbol{x})} h^*_\pi(\boldsymbol{x}) d\boldsymbol{x} \\ p_f &= p_\pi \alpha_\pi, \end{aligned} \tag{III.14}$$

where $\alpha_\pi = \mathbb{E}_{h^*_\pi}\left[\frac{\mathbb{1}_{G<0}(\boldsymbol{X})}{\pi(\boldsymbol{X})}\right]$ is a correction factor. Its estimator $\hat{\alpha}_\pi$ is evaluated using the importance sampling method described in Subsection III–2.2, with the instrumental PDF h^*_π, regardless of the constant p_π. The points are sampled using the multimodal MCMC Metropolis Hastings sampler, initializing the seed and the covariances by using the empirical quantities $\{\alpha_k^{IS}, \mu_k^{IS}, \Sigma_k\}_k$. The variance estimator $\hat{\sigma}^2_{\alpha_\pi}$ and the coefficient of variation $\hat{\delta}_{\alpha_\pi}$ are also estimated (Eq. II.30).
A first unbiased estimator of p_f, as referred in the following to $\hat{p}_f$, provided by IS, reads

$$\hat{p}_f = \hat{p}_\pi \hat{\alpha}_\pi. \tag{III.15}$$

Its variance estimator reads

$$\begin{aligned} \hat{\sigma}^2_f &= \mathbb{E}[\hat{p}^2_\pi \hat{\alpha}^2_\pi] - \hat{p}^2_f \\ &= \mathbb{E}[\hat{p}^2_\pi]\mathbb{E}[\hat{\alpha}^2_\pi] - \hat{p}^2_\pi \hat{\alpha}^2_\pi \\ &= (\hat{\sigma}^2_{p_\pi} + \hat{p}^2_\pi)(\hat{\sigma}^2_{\alpha_\pi} + \hat{\alpha}^2_\pi) - \hat{p}^2_\pi \hat{\alpha}^2_\pi \\ \hat{\sigma}^2_f &= \hat{\sigma}^2_{p_\pi} \hat{\sigma}^2_{\alpha_\pi} + \hat{\sigma}^2_{p_\pi} \hat{\alpha}^2_\pi + \hat{p}^2_\pi \hat{\sigma}^2_{\alpha_\pi}, \end{aligned} \tag{III.16}$$

III–3.3.2 Control Variate/Importance Sampling estimator

A novel estimator based on a combination between Control Variate and IS methods is presented. The failure probability is re-written as:

$$p_f = \mathbb{E}[\mathbb{1}_{\tilde{G}<0}(\boldsymbol{X})] + \int_{\mathbb{R}^n} \{\mathbb{1}_{G<0}(\boldsymbol{x}) - \mathbb{1}_{\tilde{G}<0}(\boldsymbol{x})\} \frac{f_X(\boldsymbol{x})}{h_\pi^*(\boldsymbol{x})} h_\pi^*(\boldsymbol{x}) d\boldsymbol{x}$$
$$= p_{\tilde{f}} + p_\pi \eta_\pi, \tag{III.17}$$

where $\eta_\pi = \mathbb{E}_{h_\pi^*}\left[\frac{\mathbb{1}_{G<0}(\boldsymbol{x}) - \mathbb{1}_{\tilde{G}<0}(\boldsymbol{x})}{\pi(\boldsymbol{x})}\right]$.
Its estimator $\hat{\eta}_\pi$ is evaluated using the importance sampling method described in Subsection III–2.2, with the instrumental PDF h_π^*, similarly to the estimation of $\hat{\alpha}_\pi$. The variance estimator $\hat{\sigma}^2_{\eta_\pi}$ and the coefficient of variation $\hat{\delta}_{\eta_\pi}$ are also given in a similar pattern. Let set $\epsilon_\pi = p_\pi \eta_\pi$. The idea is to compute accurate estimations of $p_{\tilde{f}}$ and p_π using only metamodel evaluations. A correction constant ϵ_π is then computed using performance evaluations in order to obtain a unbiased estimation of p_f. An unbiased estimator of ϵ_π is given by

$$\hat{\epsilon}_\pi = \hat{p}_\pi \hat{\eta}_\pi. \tag{III.18}$$

Its variance estimator is given by

$$\hat{\sigma}^2_{\epsilon_\pi} = \hat{\sigma}^2_{p_\pi} \hat{\sigma}^2_{\eta_\pi} + \hat{\sigma}^2_{p_\pi} \hat{\eta}^2_\pi + \hat{p}^2_\pi \hat{\sigma}^2_{\eta_\pi}. \tag{III.19}$$

An unbiased estimator of p_f, referred in the following as $\hat{p}_f$ and provided by CV+IS, reads

$$\hat{p}_f = \hat{p}_{\tilde{G}} + \hat{\epsilon}_\pi, \tag{III.20}$$

where its variance estimator is

$$\hat{\sigma}^2_f = \hat{\sigma}^2_{p_{\tilde{f}}} + \hat{\sigma}^2_{\epsilon_\pi}, \tag{III.21}$$

and its coefficient of variation is defined by:

$$\hat{\delta}^2_f = \frac{\hat{\sigma}^2_f}{\hat{p}^2_f}. \tag{III.22}$$

Since the points required for the estimation of η_π and α_π are the same, it is possible during this step to compute with the same points two unbiased estimators (IS and CV+IS) for p_f, and then select the one that returns the lowest coefficient of variation.

III–3.4 Parameters tuning

In this Subsection, general recommendations are provided for the choice of parameters used in Subsections III–3.1 III–3.2 III–3.3, which are resumed in Table V.1.

Concerning the MCMC parameters (N^{min}_{MCMC}, t_{MCMC}), multimodal MCMC Algorithm III.2 is used in Subsection III–3.3 to sample from the quasi-optimal ISD in order to compute the unbiased estimation. To avoid correlations between samples [Dubourg et al., 2013], the so-called *burn-in* and *thinning* procedures are used. The first N^{min}_{MCMC}

samples are eliminated. One sample every t_{MCMC} states of the chain is retained (say $N_{MCMC}^{min} = 10^4$ [Cadini et al., 2015] and $t_{MCMC} = 10$ [Dubourg et al., 2013]).

Besides, for the metamodel refinement strategy (Algorithm III.3) and the estimation of Gaussian mixture ISD parameters (Algorithm III.4), the MCMC sampling Algorithm III.1 is used, where correlations between samples have a low impact. The value of the parameters N_{MCMC}^{min}, t_{MCMC} can be decreased to reduce the computational burden. Running MCMC is moderately costly, since it only involves metamodel evaluations (although the cost can be relevant when increasing N_{MCMC}^{min} and t_{MCMC}).

For the number of clusters (K^{init}, K^{IS}, K), it is suggested to select $K^{init} = K^{IS} = K$, where K is the maximum number of expected failure regions, based on the experience of the user with respect to the problem of interest.

The parameters related to the DOE size (N_{DOE}^{MAX}, N_{loop}^{MAX}) should be selected based on a maximal computational budget available.

The choice of the initial sampling size m_0 can be selected by using $m_0 = 5n$, n being the stochastic space dimension.

The parameters a_{min}, a_{max}, r_{max} represent *how far* from the standard space's center, the performance function G should be evaluated. The following settings are suggested:

$$\begin{aligned} \beta &= -a_{min} = a_{max} = r_{max}, \\ p_f^{MIN} &= \Phi(-\beta), \end{aligned} \tag{III.23}$$

where β represents the Hasofer-Lind's reliability index used in FORM estimation [Ditlevsen, 1979], associated to p_f^{MIN}, a lower bound for the expected failure probability p_f.

In the metamodel refinement strategy (Algorithm III.3) and the computation of the Gaussian mixture ISD parameters (Algorithm III.4), N_γ samples drawn from $\mathcal{N}(0, \gamma I_d)$ are required. Higher values of γ should permit to have samples more distant from the standard space center, with a reasonable value for N_γ, say 10^6.

A heuristic method to select γ is based on the computation of $p_{\tilde{f}}$ using IS with a PDF equal to $f_{\mathcal{N}(0,\gamma I_d)}$, where the objective is to minimize the associated CoV estimator, denoted as $\hat{\delta}_{\tilde{G},\gamma}$. Based on this heuristic, the optimal choice γ^* reads

$$\gamma^* = \arg\min_{\gamma} \hat{\delta}_{\tilde{G},\gamma}. \tag{III.24}$$

Since only a gross estimation of γ is necessary, the following Monte-Carlo based algorithm is proposed[1]:

1. Generate $\{\gamma_i\}_i$ uniformly in $[1, 9]$.
2. Compute $p_{\tilde{f}}$ and the associated CoV estimator $\hat{\delta}_{\tilde{G},\gamma_i}$ using IS with N_γ samples drawn from a PDF equal to $f_{\mathcal{N}(0,\gamma_i I_d)}$. It involves N_γ metamodel evaluations for each $\hat{\delta}_{\tilde{G},\gamma_i}$ estimation.
3. Select $\gamma^* = \arg\min_{\gamma_i} \hat{\delta}_{\tilde{G},\gamma_i}$

[1] Classic unconstrained derivative-free optimization methods could also be used.

N_{MCMC}^{min}	t_{MCMC}	K	m_0	a_{min}	r_{max}	a_{max}	N_γ	γ
10^4	10	5	$5n$	$-\beta$	β	β (Eq III.23)	10^6	γ^* (Eq III.24)

Table III.1 Tuning Parameters

III–4 Numerical results

In this Section, several numerical examples introduced in Subsection II–3.5 are treated in order to illustrate the efficiency of the proposed method. The recommended tuning parameters described in Table V.1 are systematically used, except if explicitly mentioned. The proposed method is compared to those ones providing an unbiased estimation and to others including metamodel-based construction, where only an estimation of the failure probability based on the metamodel is provided. Comparisons in terms of accuracy and computational costs are illustrated on resuming tables. In particular, the first part of the tables shows the p_f estimation and associated errors based only on the metamodel, including the number of calls done on the performance function in order to construct the metamodel. For computing $p_{\tilde{f}}$, the current practice consists in using Monte Carlo Sampling (MCS) directly on the metamodel. In this study, it is shown how to use IS (see Subsection III–3.2) with the Gaussian mixture density as the ISD in order to obtain a sharp estimation of $p_{\tilde{f}}$ in a reasonable number of metamodel calls. The second part of the tables shows the results based on the unbiased methods, including the total number of calls done on the performance function. Moreover, in order to assess the method, results are compared to a reference value, provided by MCS. Its variance estimation provides a $3-\sigma$ prediction interval in which the true failure probability p_f should lie. When p_f is very low, since a very large number of MCS points are necessary, this $3-\sigma$ interval should still be quite large. In order to reduce it, and to obtain a more precise $3-\sigma$ prediction interval, the IS method mentioned in Subsection III–3.2 using a Gaussian mixture density as the ISD to compute the reference value very accurately is again handled, until the associated coefficient of variation is below 0.10%. This method is labeled with *Perf + IS* in the tables.
In the papers where comparisons are provided, as for instance in [Cadini et al., 2014] [Echard et al., 2011] [Echard et al., 2013], methods returning an unbiased failure probability estimation aim generally a CoV target of 5%. In the following cases, this accuracy is most of the time attained (once the metamodel is built), by computing the unbiased estimators with only the first two hundred (200) performance calls. As a consequence, results for a CoV target of 1% are shown.

III–4.1 Single failure region 2D

The 2D analytic example taken from [Echard et al., 2013] [Cadini et al., 2014] characterized by a low failure probability ($p_f \sim 3 \times 10^{-5}$), a very smooth limit state and a single failure region, and introduced in Subsubsection II–3.5.1 is first considered.

Figure III.3 illustrates how well the limit-state branch is approximated by the metamodel. Nine points are adaptively added, in order to fit the limit-state branch. The quasi-optimal ISD h_π^* seems to accurately approximate the optimal ISD h_f^*, and $\pi(\boldsymbol{x})$, to be an accurate surrogate for $\mathbb{1}_{\tilde{G}<0}(\boldsymbol{x})$. In Table III.2, we compare the results with those ones reported in [Cadini et al., 2014], based on the following methods: Crude

MC, FORM, FORM+IS, AK-IS, MetaAK-IS^2. MetaAL-OIS method, based only on $\tilde{G}$, returns a very good result, with a number of calls similar to the other metamodel-based methods, though with a much lower CoV, *i.e.* $\hat{\delta}_{p_{\tilde{f}}}$. Indeed, applying the IS method described in Subsection III–3.2 using a Gaussian mixture density as the ISD, it is possible to have a very accurate estimation of $p_{\tilde{f}}$ in less than 10^7 metamodel calls. This remark applies systematically to each test-case presented in this Section III–4. Concerning the unbiased estimation, a reference solution is computed again using a Gaussian mixture density as the ISD (labeled as Perf+IS in the table). In this case, a coefficient of variation of 0.10% is attained on the computation of a low probability $p_f = 2.87 \times 10^{-5}$ in only 1.05×10^6 evaluations. To reach the same accuracy, Crude MC method would require around 3×10^{10} evaluations. As a consequence, the 3-σ interval for Perf+IS is narrower than the one for Crude MC method, with a lower number of evaluations. Then, it should be more accurate. Again, this behavior is observed for each test-case presented in this Section. With the method proposed in this study, i.e. MetaAL-OIS, only two hundred additional points are necessary in order to obtain an unbiased p_f estimation. Indeed, in this case, the metamodel is so well refined that the CV+IS estimator gives exactly the estimator $\hat{p}_f$. It means that the estimation of the correction constant $\hat{\epsilon}$ is zero: among the two hundred samples drawn, no one lies between the two limit-state $\{\tilde{G}(\boldsymbol{x}) = 0\}$ and $\{G(\boldsymbol{x}) = 0\}$. We outline that the attained accuracy is very high: $\hat{\delta}_f = 0.10\%$. We can note that the IS estimator, for the same two hundred additional points, returns an unbiased estimation with $\hat{\delta}_f = 1.31\%$ which is already very low, but anyway greater than the one obtained with the CV+IS estimator. Note that the computation of the $3-\sigma$ interval is obviously coherent with the result of $\hat{\delta}_f$. Note also that the results obtained with MetaAL-OIS are coherent with the reference solution (Perf+IS), presented earlier. In FORM method, the Most Probable failure Point (MPP) is evaluated, assuming the case of a single failure region, so an estimation of p_f is returned assuming that G is locally linear. As it can be observed, the solution is wrong. In FORM+IS method, the standard Gaussian distribution is shifted to this MPP and used as the ISD of an Importance Sampling method, so it is possible to obtain an unbiased estimation of p_f, but usually at a high computational cost. Finally, in this case involving a one failure region characterized by a low probability, MetaAL-OIS is fully satisfactory, providing an accurate metamodel at a low cost, and a highly accurate unbiased failure probability estimation with only two hundred additional points.

	Metamodel-based Estimation				Unbiased Estimation			
Method	$\tilde{N}_{calls}$	$\hat{p}_{\tilde{G}}$	$\hat{\delta}_{p_{\tilde{f}}}$	$3-\hat{\sigma}_{p_{\tilde{f}}}$ Interval	N_{calls}	$\hat{p}_f$	$\hat{\delta}_f$	$3-\hat{\sigma}_f$ Interval
Crude MC					5×10^7	2.85×10^{-5}	2.64%	$[2.62, 3.08] \times 10^{-5}$
Perf + IS					1.05×10^6	2.87×10^{-5}	0.10%	$[2.86, 2.89] \times 10^{-5}$
FORM					19	4.21×10^{-7}		
FORM + IS					$19 + 10^4$	2.86×10^{-5}	2.39%	$[2.66, 2.95] \times 10^{-5}$
AK-IS	26	2.86×10^{-5}	2.39%	$[2.65, 3.07] \times 10^{-5}$				
MetaAK-IS^2	28	2.87×10^{-5}	2.39%	$[2.66, 3.08] \times 10^{-5}$				
MetaAL-OIS	**19**	$\mathbf{2.87 \times 10^{-5}}$	**0.10%**	$\mathbf{[2.86, 2.88] \times 10^{-5}}$	**19 + 200**	$\mathbf{2.87 \times 10^{-5}}$	**0.10%**	$\mathbf{[2.86, 2.88] \times 10^{-5}}$
MetaAL-OIS(IS)					19 + 200	2.81×10^{-5}	1.31%	$[2.70, 2.93] \times 10^{-5}$
MetaAL-OIS(CV+IS)					19 + 200	2.87×10^{-5}	0.10%	$[2.86, 2.88] \times 10^{-5}$

Table III.2 Comparison of the performances of the MetaAL-OIS with several algorithms of literature[Cadini et al., 2014]: Single Failure Region 2D.

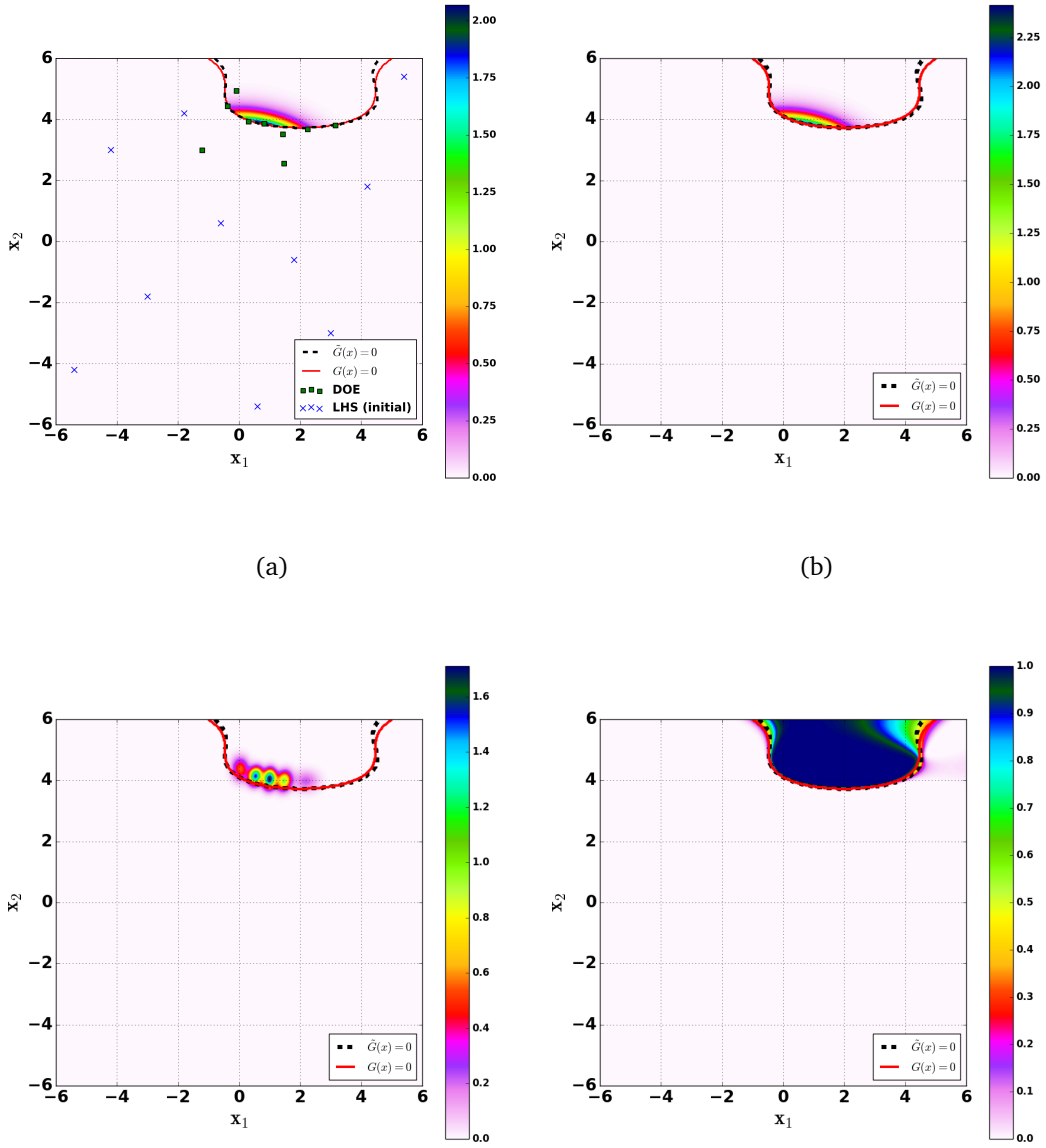

(a) (b)

(c) (d)

Figure III.3 Single Failure Region 2D: Metamodel limit-state $\{\tilde{G}(\boldsymbol{x})=0\}$ (dashed black line), Exact limit-state $\{G(\boldsymbol{x})=0\}$ (red line). (a) Contour of quasi-optimal density h^*_π, LHS points (blue crosses), DOE adaptively added (green square). (b) Optimal Density function h^*_G contour. (c) Gaussian Mixture Density contour $h_{\mathcal{N}}$. (d) π function contour.

III–4.2 Two Failure Regions 2D

This example deals with a case of two non-connected failure regions, featuring failure probabilities lying from around 3×10^{-3} to 9×10^{-7}, according to the selected parameter c in Equation II.53.

We consider here three cases, with $c=3,4,5$, as introduced in Subsubsection II–3.5.2. Note that for $c=5$, the case is challenging because it involves two non-connected failure regions and a very low failure probability. Concerning the parameters tuning, it is unchanged for $c=3$. We set $r_{max}=7$, $a_{min}=-6$ and $a_{max}=6$

for $c = 4$. For the $c = 5$ case, we set $r_{max} = 8$, $a_{min} = -7$ and $a_{max} = 7$. The results in Table III.3, are compared to those one reported in [Cadini et al., 2014] based on Crude MC, FORM, Subset, Au and Beck, Meta-IS and MetaAK-IS^2 methods. As it can be observed, MetaAL-OIS behaves systematically much better than the other metamodel-based method available for this example (Meta-IS^2) for each c. In fact, the parameter $\hat{\delta}_{p_{\tilde{f}}}$ is much lower with much less points for building the metamodel. Indeed, the result is always very close to the reference value, computed with *Perf+IS* (considered as the reference in this study). Concerning the computation of the unbiased estimation, it can be noted that the CV+IS and IS unbiased estimators return similar CoV. For $c = 3, 4, 5$, the CV+IS unbiased estimator is the one providing the lowest CoV, at 1% for 524, 722 and 580 total performance calls, respectively. Note that these results are systematically better than the ones given by Meta-IS, which provides a 5% CoV with 644 total performance calls for $c = 3, 4$, and with 2940 calls for $c = 5$. With $c = 3$ ($c = 4$), consider also that CV+IS estimator returns a $\hat{p}_f = 3.37 \times 10^{-3}$ ($\hat{p}_f = 8.87 \times 10^{-5}$) with a CoV of 2.4% (4.2%) for only 244 (268) total performance calls. Note also that the result provided by MetaAL-OIS, is always very close to the reference value, computed with *Perf+IS* (considered as the reference in this study), and involving much less points for building the metamodel. We note that the bias in the result given by the IS estimator is quite high for $c = 5$, so the $3-\sigma$ interval prediction do not contain the *reference* value p_f. In general, the CV+IS estimator is more robust, even if sometimes the estimated error $\hat{p}_f$ is higher than the one provided by IS. This example suggests that the user should always check the $3-\sigma$ interval prediction returned by both estimator, and select the one provided by CV+IS if those intervals are very different. With the IS method mentioned in III–3.2 using a Gaussian mixture density as the ISD, a coefficient of variation of 0.10% is reached on the computation of the low probability (for $c = 5$) $p_{\tilde{f}} = 9.03 \times 10^{-7}$ in only 9.45×10^6 metamodel evaluations. To reach the same accuracy, MCS method would require around 10^{12} metamodel evaluations. Figures III.4 (resp. III.5) illustrates the limit-state branch and the approximation with the metamodel for $c = 3$ (resp. $c = 5$). The metamodel captures very well the failure branches. The optimal ISD $h^*_{\tilde{f}}$ seems to be very well approximated by the quasi-optimal ISD h^*_{π}. The Gaussian mixture ISD mimics well the behaviour of the quasi-optimal ISD, involving a non-zero density mostly in the failure region, and covering the true limit-state region. Then, $\pi(\boldsymbol{x})$ is a good surrogate of $\mathbb{1}_{G<0}(\boldsymbol{x})$ except in too distant regions, which are not interesting since characterized by a too low density. Finally, it is worth noting that in this test-case the MetaAL-OIS features better performances than any of the other methods considered here.

III–4.3 Four-branch series system 2D

Let us consider now a test-case with four failure regions [Cadini et al., 2014, Dubourg et al., 2013], characterized by two MPFPs and four failure domains as introduced in Subsubsection II–3.5.3 ($u = 0$). The results in Table V.3, are compared to those ones reported in [Echard et al., 2011][Cadini et al., 2014] based on the following methods: crude MC, FORM, DS, Subset, SMART, MetaAK-IS^2 and AK-MCS+U. Compared with the other metamodel-based methods available for this example (MetaAK-IS^2 and AK-MCS+U), it seems that MetaAL-OIS features the best performances, in terms of CoV and global number of calls. Moreover, the result is always very close to the reference value, involving less training points for building the metamodel. In this case, the IS unbiased estimator returns the lowest CoV: 1% for 575 total performance calls.

	Metamodel-based Estimation				Unbiased Estimation			
Method	N_{calls}	$\hat{p}_{\hat{G}}$	$\hat{\delta}_{p_{\hat{f}}}$	$3-\hat{\sigma}_{p_{\hat{f}}}$ Interval	N_{calls}	$\hat{p}_f$	$\hat{\delta}_f$	$3-\hat{\sigma}_f$ Interval
c = 3								
Crude MC					$120,000$	3.35×10^{-3}	$<5\%$	$\subseteq[2.85,3.85]\times10^{-3}$
Perf + IS					1.3×10^{6}	3.47×10^{-3}	0.10%	$[3.47,3.49]\times10^{-3}$
FORM					7	1.35×10^{-3}		
Subset					$300,000$	3.48×10^{-3}	$<3\%$	$\subseteq[3.17,3.80]\times10^{-3}$
Au and Beck					600	2.47×10^{-3}	8%	$[1.88,3.06]\times10^{-3}$
Meta-IS					$44+600$	3.54×10^{-3}	$<5\%$	$\subseteq[3.00,4.07]\times10^{-3}$
MetaAK-IS^2	117	3.47×10^{-3}	$<5\%$	$\subseteq[2.94,3.99]\times10^{-3}$				
MetaAL-OIS	**44**	$\mathbf{3.53\times10^{-3}}$	**0.10%**	$\mathbf{[3.52,3.54]\times10^{-3}}$	$\mathbf{44+480}$	$\mathbf{3.46\times10^{-5}}$	**1.00%**	$\mathbf{[3.35,3.56]\times10^{-5}}$
MetaAL-OIS (IS)					$44+480$	3.52×10^{-3}	1.02%	$[3.41,3.63]\times10^{-3}$
MetaAL-OIS (CV+IS)					$44+480$	3.46×10^{-3}	1.00%	$[3.35,3.56]\times10^{-3}$
c = 4								
Crude MC					$4,620,000$	8.68×10^{-5}	$<5\%$	$\subseteq[7.38,9.98]\times10^{-5}$
Perf + IS					1.6×10^{6}	8.99×10^{-5}	0.10%	$[8.97,9.02]\times10^{-5}$
FORM					7	3.17×10^{-5}		
Subset					$500,000$	8.34×10^{-5}	$<4\%$	$\subseteq[7.34,9.34]\times10^{-5}$
Au and Beck					600	6.51×10^{-5}	10%	$[4.56,8.46]\times10^{-5}$
Meta-IS					$64+600$	8.60×10^{-5}	$<5\%$	$\subseteq[7.31,9.89]\times10^{-5}$
MetaAK-IS^2	118	8.49×10^{-5}	$<5\%$	$\subseteq[7.22,9.76]\times10^{-5}$				
MetaAL-OIS	**68**	$\mathbf{8.86\times10^{-5}}$	**0.10%**	$\mathbf{[8.83,8.89]\times10^{-5}}$	$\mathbf{68+722}$	$\mathbf{8.92\times10^{-5}}$	**1.00%**	$\mathbf{[8.65,9.19]\times10^{-5}}$
MetaAL-OIS (IS)					$68+722$	8.92×10^{-5}	1.00%	$[8.65,9.19]\times10^{-5}$
MetaAL-OIS (CV+IS)					$68+722$	8.88×10^{-5}	1.17%	$[8.57,9.19]\times10^{-5}$
c = 5								
Crude MC					$422,110,000$	9.48×10^{-7}	$<5\%$	$\subseteq[8.06,11.9]\times10^{-7}$
Perf + IS					1.8×10^{6}	8.97×10^{-7}	0.10%	$[8.95,9.00]\times10^{-7}$
FORM					7	2.87×10^{-7}		
Subset					$700,000$	6.55×10^{-7}	$<5\%$	$\subseteq[5.57,7.53]\times10^{-7}$
Au and Beck					600	6.54×10^{-7}	12%	$[4.19,8.90]\times10^{-7}$
Meta-IS			$<5\%$		$40+2900$	9.17×10^{-7}	$<5\%$	$\subseteq[7.80,10.5]\times10^{-7}$
MetaAK-IS^2	236	8.16×10^{-7}	$<5\%$	$\subseteq[6.94,9.38]\times10^{-7}$				
MetaAL-OIS	**84**	$\mathbf{9.03\times10^{-7}}$	**0.10%**	$\mathbf{[9.00,9.05]\times10^{-7}}$	$\mathbf{84+496}$	$\mathbf{8.91\times10^{-7}}$	**1.00%**	$\mathbf{[8.64,9.18]\times10^{-7}}$
MetaAL-OIS (IS)					$84+496$	9.61×10^{-7}	1.28%	$[9.24,9.98]\times10^{-7}$
MetaAL-OIS (CV+IS)					$84+496$	8.91×10^{-7}	1.00%	$[8.64,9.18]\times10^{-7}$

Table III.3 Comparison of the performances of the MetaAL-OIS with several algorithms of literature[Cadini et al., 2014]: Two Failure Regions 2D.

Consider that with 269 total performance calls, it gives a $\hat{p}_f = 2.17\times10^{-3}$ with a CoV of only 3.1%. Finally, note that MetaAL-OIS provides the best unbiased estimation with respect to the other methods considered here. The capability of the metamodel to capture the limit-state region is illustrated in Figure III.6. The parameters K, K^{IS}, K^{init} are fixed at 5, which is higher than the true number of failure regions. We note that the Gaussian mixture ISD has five centers, of which two are located in one branch. Again, the surrogate π is well approximated except for distant regions characterized by negligible densities. The DOE used for the metamodel is well focused on the failure branches. The optimal ISD h_f^* seems to be very well approximated by the quasi-optimal ISD h_π^*.

	Metamodel-based Estimation				Unbiased Estimation			
Method	N_{calls}	$\hat{p}_{\hat{G}}$	$\hat{\delta}_{p_{\hat{f}}}$	$3-\hat{\sigma}_{p_{\hat{f}}}$ Interval	N_{calls}	$\hat{p}_f$	$\hat{\delta}_f$	$3-\hat{\sigma}_f$ Interval
Crude MC					$781,016$	2.24×10^{-3}	2.23%	$[2.09,2.39]\times10^{-3}$
Perf + IS					2×10^{6}	2.22×10^{-3}	0.10%	$[2.21,2.23]\times10^{-3}$
FORM					7	1.35×10^{-3}		
DS					1800	2.22×10^{-3}		
Subset					$600,000$	2.22×10^{-3}	1.5%	$[2.12,2.32]\times10^{-3}$
SMART					1035	2.21×10^{-3}		
MetaAK-IS^2	138	2.22×10^{-3}	1.7%	$[2.11,2.33]\times10^{-3}$				
AK-MCS+U	96	2.23×10^{-3}						
MetaAL-OIS	**69**	$\mathbf{2.21\times10^{-3}}$	**0.10%**	$\mathbf{[2.20,2.22]\times10^{-3}}$	$\mathbf{69+506}$	$\mathbf{2.21\times10^{-3}}$	**1.00%**	$\mathbf{[2.15,2.23]\times10^{-3}}$
MetaAL-OIS (IS)					$69+506$	2.21×10^{-3}	1.00%	$[2.15,2.23]\times10^{-3}$
MetaAL-OIS (CV+IS)					$69+506$	2.21×10^{-3}	1.22%	$[2.13,2.29]\times10^{-3}$

Table III.4 Comparison of the performances of the MetaAL-OIS with several algorithms of literature[Cadini et al., 2014]: Four-Branch seried 2D ($u=0$).

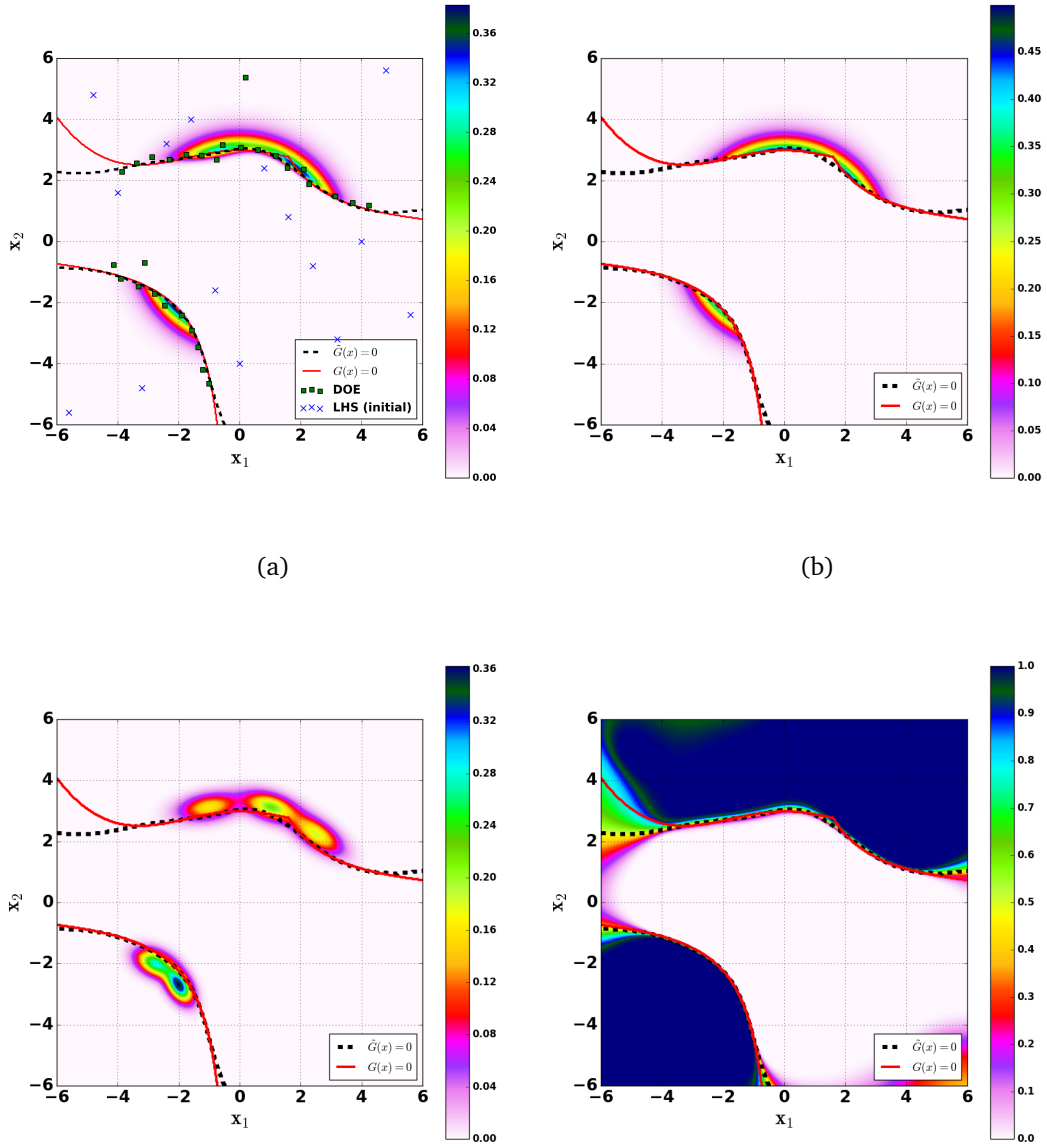

(a) (b)

(c) (d)

Figure III.4 Two Failure Regions 2D - $c = 3$: Metamodel limit-state $\{\tilde{G}(\boldsymbol{x}) = 0\}$ (dashed black line), Exact limit-state $\{G(\boldsymbol{x}) = 0\}$ (red line). (a) Contour of quasi-optimal density h^*_π, LHS points (blue crosses), DOE adaptively added (green square). (b) Optimal Density function h^*_G contour. (c) Gaussian Mixture Density contour $h_{\mathcal{N}}$. (d) π function contour.

III–4.4 2D analytic "tricky" example with multiple failure regions: modified Rastrigin function

This test-case deals with a highly non-linear function involving non-convex and non-connected domains of failure (*i.e.* "*scattered gaps of failure*"), introduced in section III–4.4. This example is tricky because of the numerous number of failure regions. However, they are close to each other, and the failure probability is relatively high. In this test-case, the tuning parameters K, K^{IS} and K^{init} are fixed at 50. Table III.5

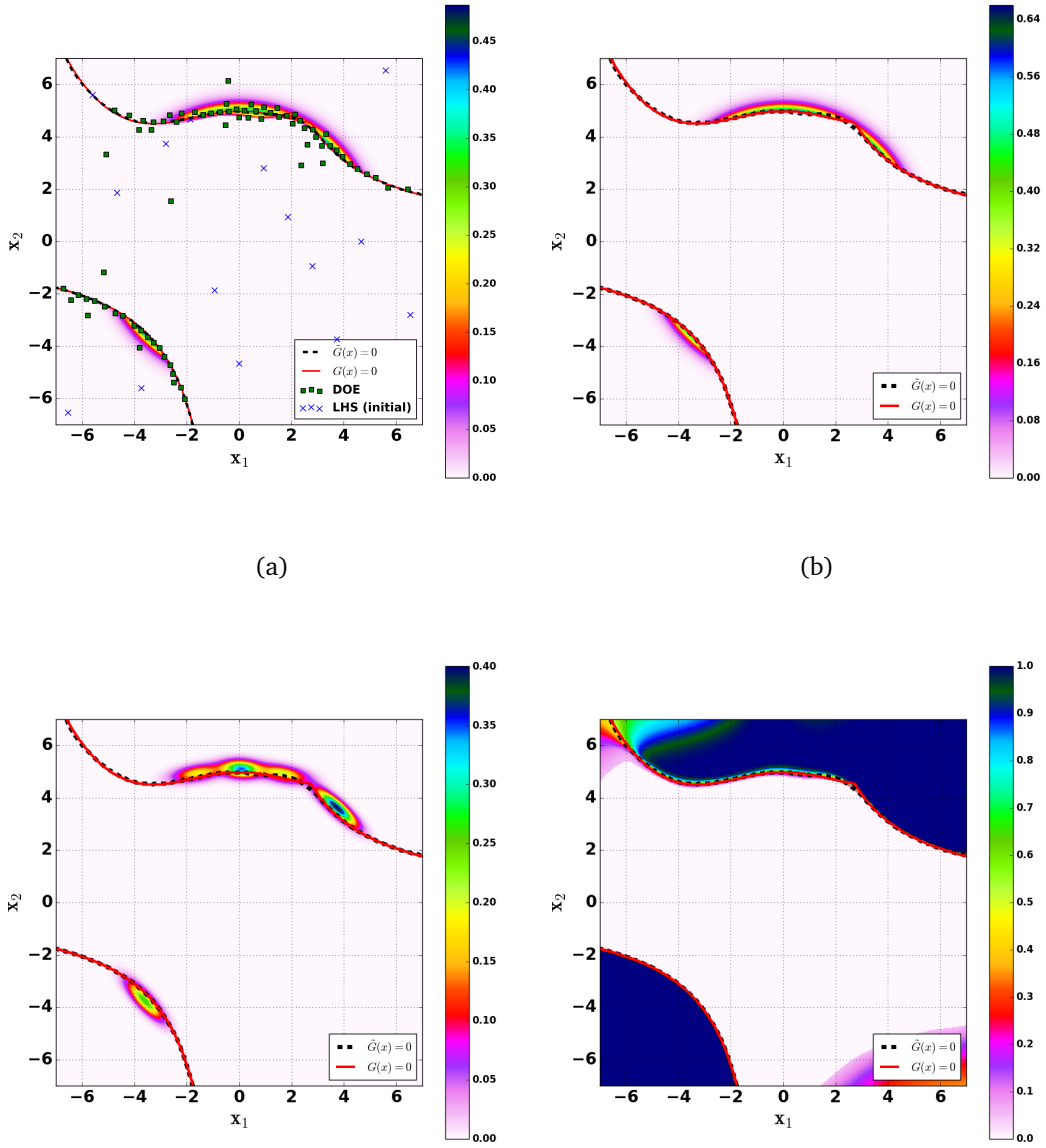

(a) (b)

(c) (d)

Figure III.5 Two Failure Regions 2D - $c = 5$: Metamodel limit-state $\{\tilde{G}(\boldsymbol{x}) = 0\}$ (dashed black line), Exact limit-state $\{G(\boldsymbol{x}) = 0\}$ (red line). (a) Contour of quasi-optimal density h^*_π, LHS points (blue crosses), DOE adaptively added (green square). (b) Optimal Density function h^*_G contour. (c) Gaussian Mixture Density contour $h_{\mathcal{N}}$. (d) π function contour.

illustrates the comparison between MetaAL-OIS and the methods reported in [Cadini et al., 2014]: crude MC, FORM, AK-MCS and MetaAK-IS^2. It can be observed that MetaAL-OIS behaves better than the other metamodel-based methods available for this example (MetaAK-IS^2 and AK-MCS). In fact, a lower CoV is associated to a lower number of functional evaluation as well. Moreover, the result is very close to the

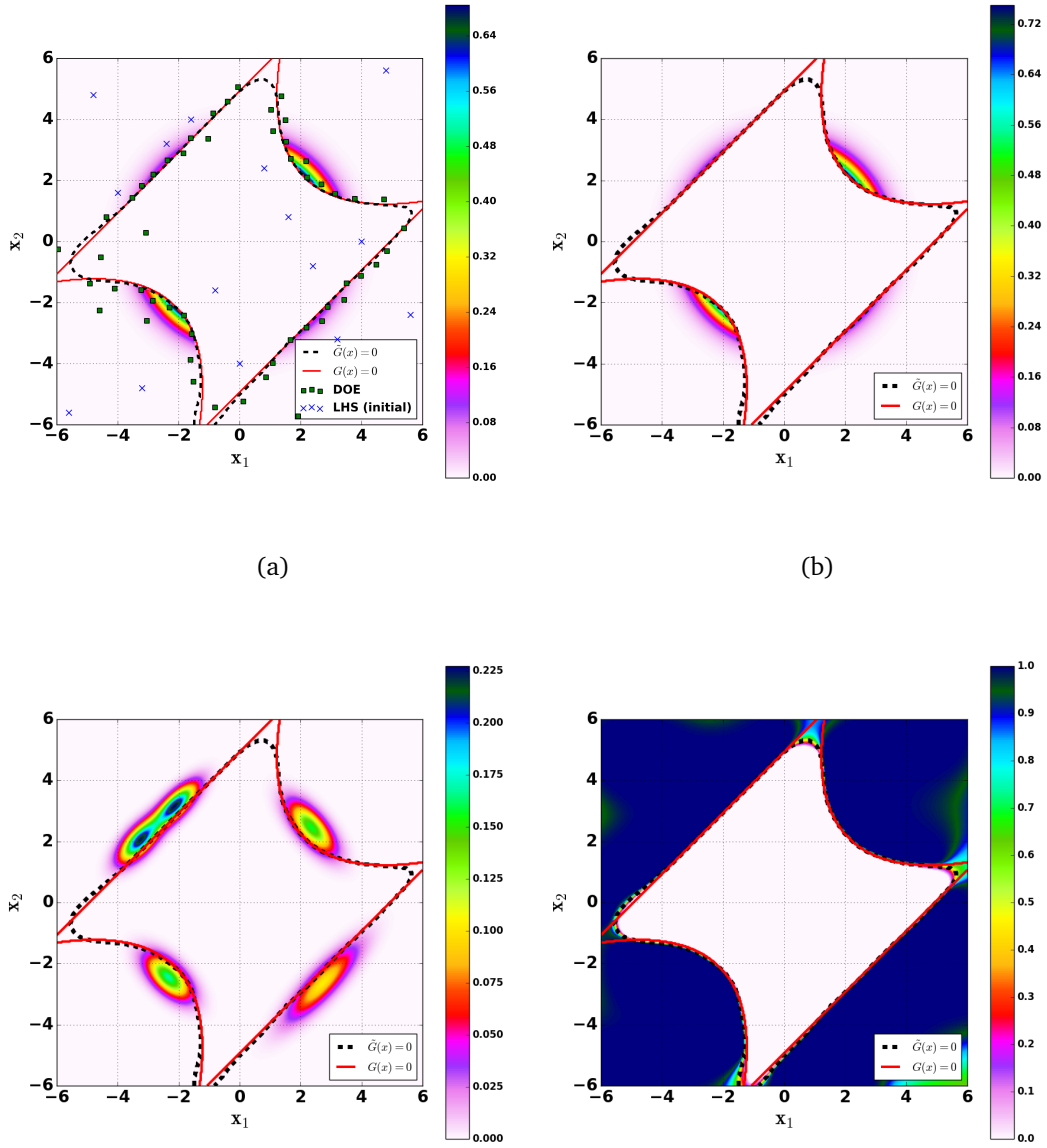

(a) (b)

(c) (d)

Figure III.6 Four-Branch seried 2D ($u = 0$): Metamodel limit-state $\{\tilde{G}(\boldsymbol{x}) = 0\}$ (dashed black line), Exact limit-state $\{G(\boldsymbol{x}) = 0\}$ (red line). (a) Contour of quasi-optimal density h^*_π, LHS points (blue crosses), DOE adaptively added (green square). (b) Optimal Density function h^*_G contour. (c) Gaussian Mixture Density contour $h_{\mathcal{N}}$. (d) π function contour.

reference value. In this case, the CV+IS unbiased estimator returns the lowest CoV, *i.e.* 0.10% for 351 total performance calls, while the IS estimator features a worse performance (*i.e.* 2.15% for the same 351 calls).

As done in the other test-cases, we then compare the limit-state region and the metamodel behavior (see Figure III.7). Also in this challenging case, very good performances are observed. In particular, the metamodel is able to capture and represent several domains of failure.

	Metamodel-based Estimation				Unbiased Estimation			
Method	N_{calls}	$\hat{p}_{\tilde{G}}$	$\hat{\delta}_{p_f}$	$3-\hat{\sigma}_{p_f}$ Interval	N_{calls}	$\hat{p}_f$	$\hat{\delta}_f$	$3-\hat{\sigma}_f$ Interval
Crude MC [Cadini et al., 2014]					25,000	7.43×10^{-2}	2.23%	$[6.93,7.93]\times10^{-2}$
Perf + IS					1.3×10^{6}	7.29×10^{-2}	0.10%	$[7.27,7.32]\times10^{-2}$
FORM					20	6.83×10^{-6}		
AK-MCS	391	7.43×10^{-2}	2.23%	$[6.93,7.93]\times10^{-2}$				
MetaAK-IS^2	480	7.35×10^{-2}	2.5%	$[6.80,7.90]\times10^{-2}$				
MetaAL-OIS	**151**	$\mathbf{7.31\times10^{-2}}$	**0.10%**	$\mathbf{[7.28,7.33]\times10^{-2}}$	**151 + 200**	$\mathbf{7.31\times10^{-2}}$	**0.10%**	$\mathbf{[7.28,7.33]\times10^{-2}}$
MetaAL-OIS (IS)					151 + 200	7.11×10^{-2}	2.15%	$[6.65,7.57]\times10^{-2}$
MetaAL-OIS (CV+IS)					151 + 200	7.31×10^{-2}	0.10%	$[7.28,7.33]\times10^{-2}$

Table III.5 Comparison of the performances of the MetaAL-OIS with several algorithms of literature[Cadini et al., 2014]: Modified Rastrigin function.

III–4.5 Response of a non-linear Oscillator 6D

This test-case is a problem with six random variables in the physical space. The performance function is smooth with respect to the considered inputs. It consists of a non-linear undamped single degree of freedom system [Echard et al., 2011], as introduced in section II–3.5.6. The difficulty here comes from the relatively high dimension of the problem, adding to the fact that the input variable belong to the physical space. The proposed approach MetaAL-OIS is compared to MCS and other metamodels based methods [Echard et al., 2011]; only the ones that returned a fairly good estimation of p_f are mentioned. Note that C.O.V are not available in [Echard et al., 2011] for the computation associated to $p_{\tilde{f}}$, estimated with metamodel-based methods, so not quoted in Table III.6. MetaAL-OIS metamodel requires 70 performance evaluations, which is slightly more than for the AK-MCS+EFF (only 45), with a very good accuracy. In fact, the CoV is 0.10% for MetaAL-OIS metamodel, which is very low. Finally, performances of the MetaAL-OIS method seem very good also in this case, even if a proper comparison can not be done since only partial data about the performances of the other methods are available. Concerning the unbiased estimation, note that only 228 additional evaluations lead to a sharp unbiased estimation with $\hat{\delta}_f = 1\%$. Again, MetaAL-OIS gives very satisfactory results with respect to other methods, for a low computational effort.

	Metamodel-based Estimation		Unbiased Estimation			
Method	N_{calls}	$\hat{p}_{\tilde{G}}$	N_{calls}	$\hat{p}_f$	$\hat{\delta}_f$	$3-\hat{\sigma}_f$ Interval
MCS			70,000	2.834×10^{-2}	2.2%	$[2.647,3.021]\times10^{-2}$
Perf + IS			2.9×10^{6}	2.856×10^{-2}	0.10%	$[2.846,2.865]\times10^{-2}$
AK-MCS+U	58	2.834×10^{-2}				
AK-MCS+EFF	45	2.851×10^{-2}				
DS + Neural Network	86	2.8×10^{-2}				
Importance Sampling (IS)			6144	2.7×10^{-2}		
IS + Response Surface	109	2.5×10^{-2}				
IS + Spline	67	2.7×10^{-2}				
IS + Neural Network	68	3.1×10^{-2}				
MetaAL-OIS	**70**	$\mathbf{2.847\times10^{-2}}$	**70 + 228**	$\mathbf{2.848\times10^{-2}}$	**1.00%**	$\mathbf{[2.763,2.934]\times10^{-2}}$
MetaAL-OIS (IS)			70 + 228	2.848×10^{-2}	1.00%	$[2.763,2.934]\times10^{-2}$
MetaAL-OIS (CV+IS)			70 + 228	2.880×10^{-2}	1.16%	$[2.781,2.981]\times10^{-2}$

Table III.6 Comparison of the performances of the MetaAL-OIS with several algorithms of literature[Echard et al., 2011]: Non-Linear Oscillator 6D.

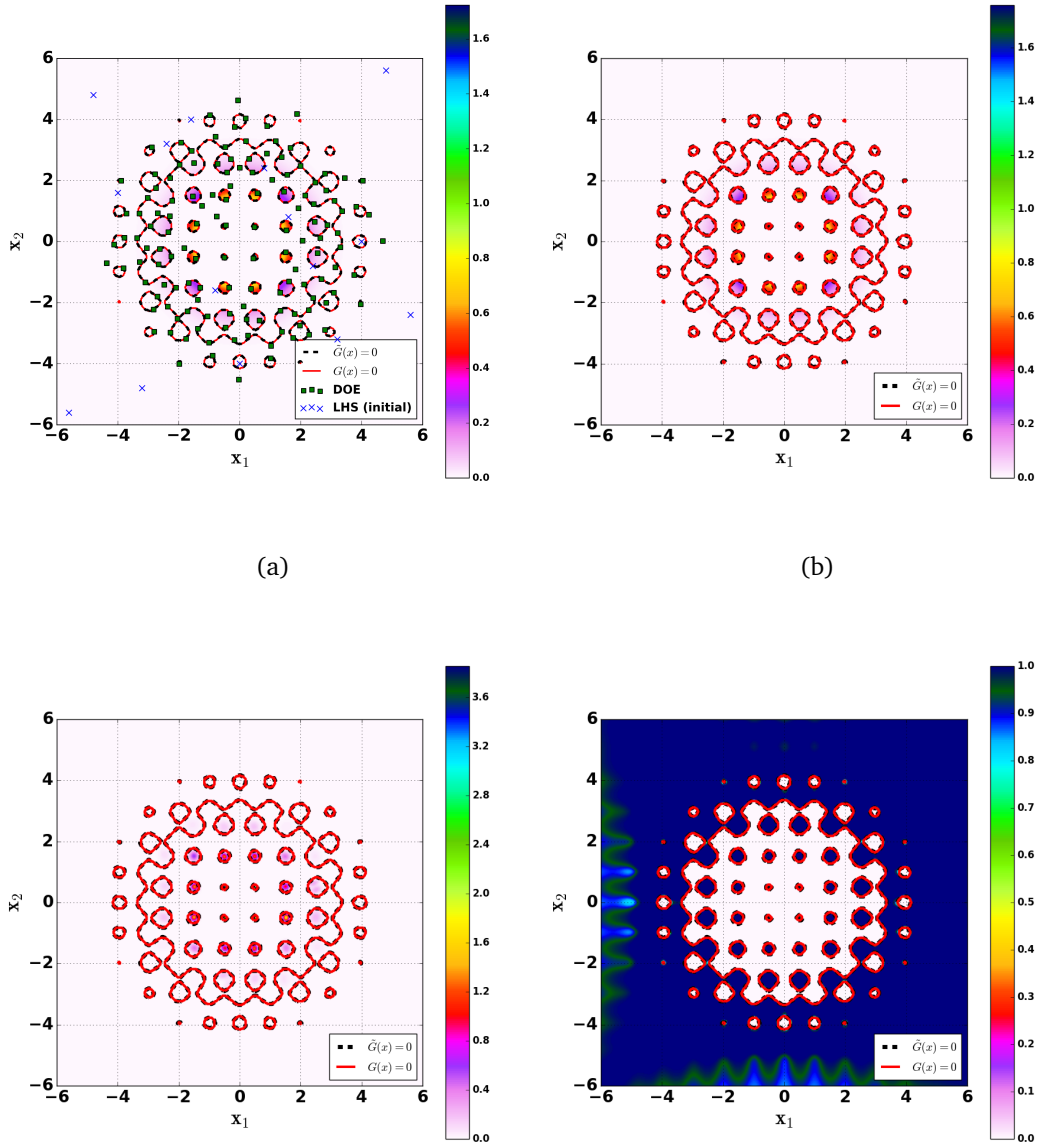

(a) (b)

(c) (d)

Figure III.7 Modified Rastrigin function: Metamodel limit-state $\{\tilde{G}(\boldsymbol{x}) = 0\}$ (dashed black line), Exact limit-state $\{G(\boldsymbol{x}) = 0\}$ (red line). (a) Contour of quasi-optimal density h^*_π, LHS points (blue crosses), DOE adaptively added (green square). (b) Optimal Density function h^*_G contour. (c) Gaussian Mixture Density contour $h_{\mathcal{N}}$. (d) π function contour.

III–5 Conclusion

In this Chapter, we have proposed a metamodel-based method for the computation of tail probabilities, suitable for very low probability and/or multiple failure regions, also able to return an accurate unbiased estimation of the failure probability with few additional performance function calls. In particular, we have proposed a significant improvement of the Meta-IS algorithm developed by Dubourg [Dubourg et al., 2013].

The main improvement is obtained by modifying the metamodel construction, suitable for multiple failure regions and very low failure probability. Moreover, we have also described and assessed a method allowing to reduce significantly the number of metamodel calls, when estimating the failure probability from the metamodel (which can be very large if p_f is very low), with respect to MCS. Indeed, the metamodel construction and the Gaussian mixture IS method can be an accurate and a general alternative to AK-MCS, MetaAK-IS^2, KAIS and AK-SS. In fact, it provides a surrogate-based analysis, using the metamodel instead of the original limit-state function, dealing with multiple failure regions and low probability.

Additionally, to obtain an unbiased failure estimation, we have used directly the second part of the Meta-IS [Dubourg et al., 2013], involving MCMC sampling, and proposed another unbiased estimator. It is slightly different and does not induce additional computations. In some cases, it can further significantly reduce the number of performance function calls. Among methods returning an unbiased estimation, we have shown MetaAL-OIS permits a lower computational cost for a better accuracy.

The proposed method has been tested until 6 uncertainties. We expect that this could be efficient for even higher (moderate) dimensions, but in this case maybe a more efficient MCMC algorithm should be considered.

We have shown the ability of the method to deal with very low probability and multiple failure regions by performing several test-cases. The construction of the metamodel requires in general significantly less computational calls than other metamodel-based methods, and preserves the global accuracy.

IV

Extension of AK-MCS for the efficient computation of very small failure probabilities

Overview *This Chapter presents an* extreme *version of AK-MCS [Schöbi et al., 2016] for the computation of very small failure probabilities (say* $\sim 10^{-5} - 10^{-9}$*),* *named* extreme Active Kriging-Monte Carlo Sampling *(eAK-MCS). It consists mainly of reformulating the MCS-based samples generation and failure probability estimation. Indeed a centered uncorrelated Gaussian distribution, whose standard deviation is iteratively tuned, is used to generate the samples and its distribution is selected as the so-called biasing distribution of the IS method to estimate the failure probability on the surrogate. It indeed reduces the number of samples that would be not tractable with a MCS-based method in the case of very small failure probability. Note however that unlike AK-MCS [Schöbi et al., 2016], the proposed method requires to work in the standard space, resorting if necessary to an isoprobabilistic transformation.*

IV–1 Introduction

The problem of estimating a probability of failure p_f is considered, defined as the volume of the excursion set of a complex (*e.g.* output of an expensive-to-run finite element model) scalar performance function J below a given threshold, under a probability measure that can be recast as a multivariate standard Gaussian law using an isoprobabilistic transformation. We propose a method able to deal with cases characterized by multiple failure regions, possibly very small failure probability p_f (say $\sim 10^{-5} - 10^{-9}$), and when the number of evaluations of J is limited. The present work is an extension of the popular Kriging-based active learning algorithm known as AK-MCS, as presented by Schobi and Sudret (2016), permitting to deal with very low failure probabilities. The key idea merely consists in replacing the Monte-Carlo sampling, used in the original formulation to propose candidates and evaluate the failure probability, by a centered isotropic Gaussian sampling in the standard space, whose standard deviation is iteratively tuned. This *extreme* AK-MCS (eAK-MCS) inherits its former multi-point enrichment algorithm allowing to add several points in parallel in each iteration and, due to the Gaussian nature of the surrogate, to estimate a failure probability range at each iteration step.

To evaluate failure probabilities that would need more memory than available RAM with standard AK-MCS, the so-called AK-MCSi [Lelièvre et al., 2018] proposes to split the large MC population into several populations of smaller sizes and thus to perform sequential MC simulation. It also introduces a multipoint enrichment strategy similar to AK-MCS [Schöbi et al., 2016] and an original stopping criterion suitable when the probability of failure is MCS-based. However, in cases of very small failure probability, the method still requires a considerable number of metamodel evaluations (as in AK-MCS), with a rather significant coefficient of variation, which is partially cured by the method proposed in this study, *i.e.* eAK-MCS. Note that both AK-MCSi and eAK-MCS aims at refining *directly* the so-called *Limit State Surface*, while, among metamodel-based methods suitable for very small failure probability, the BSS [Bect et al., 2017] adaptively improves the surrogate accuracy corresponding to intermediate thresholds to avoid failure domains. Numerical experiments conducted with *unfavorable* initial Design of Experiment suggests the ability of the proposed method, to detect failure

domains. One compelling advantage of eAK-MCS over BSS lies in the fact that AK-MCS (more specifically, its refinement strategy) has been adapted to other fields [Lelièvre et al., 2018] such as quantile estimation [Schöbi et al., 2016] and (quantile-based) optimization under uncertainty [Moustapha et al., 2016]. As a consequence, eAK-MCS could enable the adaptation of those methodologies associated to very small probabilities.

The failure probability problem consists in estimating p_f defined as:

$$p_f = \mathbb{P}(G(\boldsymbol{X}) \leq u) = \mathbb{E}[\mathbb{1}_{G<u}(\boldsymbol{X})] = \int_{\mathbb{R}^d} \mathbb{1}_{G<u}(\boldsymbol{x}) f_{\boldsymbol{X}}(\boldsymbol{x}) d\boldsymbol{x}, \tag{IV.1}$$

where $\boldsymbol{X} \sim \mathcal{N}(0, I_d)$ is the standard normal random vector of $\mathbb{R}^d$, described by its PDF $f_{\mathcal{N}(0,I_d)}$. $\mathbb{1}_{G<u}$ being the indicator function such that $\mathbb{1}_{G<u} = 1$ for $G < u$ and $\mathbb{1}_{G<u} = 0$ otherwise.

The presentation is structured as follows. In Section IV–2, the proposed algorithm, i.e. *extended* AK-MCS (eAK-MCS), is described. Numerical experiments illustrating the method are presented in Section IV–3 to illustrate its efficiency. Conclusions are finally drawn in Section IV–4.

IV–2 The eAK-MCS Algorithm

The eAK-MCS algorithm aims at building a Kriging-based surrogate, refining it iteratively in the LSS $\{G(\boldsymbol{x}) = u\}$, and estimating the *predicted* failure probability $\hat{p}_{\tilde{f}}$ as an approximation of p_f.

The main steps can be summarized as follows (similarly to AK-MCS [Schöbi et al., 2016]):

1. *Initial DoE*: An experimental design $\mathcal{X}$ is generated by Latin-Hypercube Sampling (LHS) (See Subsubsection II–3.2).
2. *Metamodel Update*: The exact response $\mathcal{Y}$ of the exact performance function G is carried out on $\mathcal{X}$. The metamodel is calibrated based on $\{\mathcal{X}, \mathcal{Y}\}$ (See Subsection II–3.3), using Kriging (Section I–2). The key parameter γ is then automatically tuned (See Subsection II–3.4).
3. *Candidates*: A set of N_C candidate points $\mathcal{S}$ is generated (See Subsection IV–2.2).
4. *Selection Step*: The *selection step* determines the sample(s) $\boldsymbol{x}^*$ to be added to the experimental design: $\mathcal{X} \leftarrow \{\mathcal{X}, \boldsymbol{x}^*\}$ (See Subsection IV–2.3).
5. *Stopping Criterion*: If a stopping criterion is satisfied (See Subsection V–3.3), the enrichment stops. The failure probability is estimated using IS on the metamodel. Otherwise the algorithm goes back to step 3.

W.r.t. the AK-MCS algorithm as presented in [Schöbi et al., 2016], the fundamental difference lies in the generation of candidate points (Step 3) and is the main contribution of the method. The candidate selection procedure and the stopping criterion, described respectively in Step 4 and 7 are inspired mainly from [Schöbi et al., 2016] but slightly modified and suggested here to improve the efficiency of the proposed algorithm. Finally, in Subsection IV–2.5, some typical values for the tuning parameters are indicated.

IV–2.1 Model Accuracy

A Kriging surrogate of G is built (see Section I–2 and Subsection II–3.2). Taking into account for the prediction uncertainty in the Kriging model, we define [Schöbi et al., 2016, Dubourg, 2011] the lower $\{\boldsymbol{x} \in \mathbb{R}^d : \mu_{\hat{G}}(\boldsymbol{x}) - k\sigma_{\hat{G}}(\boldsymbol{x}) = u\}$ and upper $\{\boldsymbol{x} \in \mathbb{R}^d : \mu_{\hat{G}}(\boldsymbol{x}) + k\sigma_{\hat{G}}(\boldsymbol{x}) = u\}$ boundaries of the *predicted* LSS $\{\boldsymbol{x} \in \mathbb{R}^d : \mu_{\hat{G}}(\boldsymbol{x}) = u\}$, where k sets the confidence level, (typically $1.96 = \Phi(97.5\%)$). Analogously, the lower and upper bounds, and *predicted* failure domains are defined as:

$$\begin{aligned} \mathcal{D}_f^{(k)-} &= \{\boldsymbol{x} \in \mathbb{R}^d : \mu_{\hat{G}}(\boldsymbol{x}) + k\sigma_{\hat{G}}(\boldsymbol{x}) < u\} \\ \mathcal{D}_f^{(k)+} &= \{\boldsymbol{x} \in \mathbb{R}^d : \mu_{\hat{G}}(\boldsymbol{x}) - k\sigma_{\hat{G}}(\boldsymbol{x}) < u\} \\ \mathcal{D}_f^{0} &= \{\boldsymbol{x} \in \mathbb{R}^d : \mu_{\hat{G}}(\boldsymbol{x}) < u\}, \end{aligned} \tag{IV.2}$$

with $\mathcal{D}_f^{(k)-} \subset \mathcal{D}_f^{0} \subset \mathcal{D}_f^{(k)+}$. The *predicted* failure probability $p_{\tilde{f}}$ and its lower and upper bounds, resp. $p_{\tilde{f}}^{(k)-}$ and $p_{\tilde{f}}^{(k)+}$ are defined as:

$$\begin{aligned} p_{\tilde{f}}^{(k)-} &= \mathbb{P}(\mu_{\hat{G}}(\boldsymbol{X}) + k\sigma_{\hat{G}}(\boldsymbol{X}) < u) &&= \mathbb{E}[\mathbb{1}_{\mu_{\hat{G}}+k\sigma_{\hat{G}}<u}(\boldsymbol{X})] \\ p_{\tilde{f}}^{(k)+} &= \mathbb{P}(\mu_{\hat{G}}(\boldsymbol{X}) - k\sigma_{\hat{G}}(\boldsymbol{X}) < u) &&= \mathbb{E}[\mathbb{1}_{\mu_{\hat{G}}-k\sigma_{\hat{G}}<u}(\boldsymbol{X})] \\ p_{\tilde{f}} &= \mathbb{P}(\mu_{\hat{G}}(\boldsymbol{X}) < u) &&= \mathbb{E}[\mathbb{1}_{\mu_{\hat{G}}<u}(\boldsymbol{X})]. \end{aligned} \tag{IV.3}$$

The so-called *Limit State Margin* (LSM) $\mathbb{M}_f^{(k)} = \mathcal{D}_f^{(k)+} \backslash \mathcal{D}_f^{(k)-}$ [Schöbi et al., 2016, Dubourg, 2011] is a natural region where to focus the design enrichment. In the following, for a given set of samples $S = \{\boldsymbol{x}_1, ..., \boldsymbol{x}_N\}$, $S^{(k)} = S \cap \mathbb{M}_f^{(k)}$ denotes samples in S belonging to the LSM $\mathbb{M}_f^{(k)}$, containing points of interest for enrichment among S, since they should lie close to the true limit state surface. Note that $S^{(k)}$ can be empty for a given set S.

IV–2.2 Candidates Generation

Using MC samples as candidates points as in the original AK-MCS algorithm [Echard et al., 2011, Schöbi et al., 2016] is not suitable when p_f is very small: possibly only a few of them would lie in the LSM $\mathbb{M}_f^{(k)}$. To tackle this issue, samples are generated from the centered uncorrelated multivariate Gaussian $\mathcal{N}(0, \gamma^2 I_d)$, where the choice of $\gamma \geqslant 1$ is discussed in Subsection II–3.4. Too *distant* samples from the center are discarded. This step is summarized below (Algorithm IV.1).

Algorithm IV.1 Candidates Generation

Input: N_C, r_{max}, p, γ
Output: Set $\mathcal{S}$ of N_C samples

Generation of pN_C samples $\{\boldsymbol{x}_1, ..., \boldsymbol{x}_{pN_C}\} \overset{\text{iid}}{\sim} \mathcal{N}(0, \gamma^2 I_d)$.
Discard Distant samples: $I = \{i \in [1, pN_C] \text{ s.t. } \|\boldsymbol{x}_i\|_2 < r_{max}\} = \{i_1, ..., i_{|I|}\}$ with $i_k < i_{k+1}$ and $|I| \geqslant N_C$. (If not, increase p).
Candidate: $\mathcal{S} = \{\boldsymbol{x}_{i_1}, ..., \boldsymbol{x}_{i_{N_C}}\}$.

IV–2.3 DoE Selection

Considering a set $\mathcal{S}$ of candidate points as described in Algorithm IV.1, we follow a strategy very similar to [Schöbi et al., 2016] to select the point(s) to be added to the DoE.

IV–2.3.1 Single Sample Selection: Single eAK-MCS

Due to the underlying Gaussian nature of the metamodel, to each sample $\boldsymbol{x} \in \mathbb{R}^d$ corresponds the so-called probability of misclassification $P_m(\boldsymbol{x})$ defined as the non-zero probability that the Gaussian predictor $\hat{G}(\boldsymbol{x}) > u$ (safe) while the prediction mean $\mu_{\hat{G}}(\boldsymbol{x}) < u$ (failure) or viceversa. It can be written as [Bect et al., 2012]:

$$P_m(\boldsymbol{x}) = \Phi\left(-\frac{|\mu_{\hat{G}}(\boldsymbol{x}) - u|}{\sigma_{\hat{G}}(\boldsymbol{x})}\right). \tag{IV.4}$$

The so-called U-function U is then defined as the *reliability index* linked to the probability of misclassification P_m [Cadini et al., 2015, Echard et al., 2011, Schöbi et al., 2016]:

$$U(\boldsymbol{x}) = \frac{|\mu_{\hat{G}}(\boldsymbol{x}) - u|}{\sigma_{\hat{G}}(\boldsymbol{x})}. \tag{IV.5}$$

Similarly to AK-MCS, the sample used to enrich the DoE among the candidates $\mathcal{S}$ is the one minimizing the U-function, thus maximizing its probability of being misclassified:

$$\boldsymbol{x}^* = \arg\min_{\boldsymbol{x}\in\mathcal{S}} U(\boldsymbol{x}) = \arg\max_{\boldsymbol{x}\in\mathcal{S}} P_m(\boldsymbol{x}). \tag{IV.6}$$

IV–2.3.2 Multiple Sample Selection

If parallel computing is available, and $(K+1)$ samples can be added simultaneously to the DoE, the following strategy is proposed, largely inspired from [Schöbi et al., 2016]:

1. One sample $\boldsymbol{x}_0^*$ is selected among $\mathcal{S}$ following the single eAK-MCS selection (Eq. IV.6).

2. K samples $(\boldsymbol{x}_1^*, ..., \boldsymbol{x}_K^*)$ are simultaneously selected among the margin set $\mathcal{S}^{(k)}$ belonging to the LSM $\mathbb{M}_f^{(k)}$, using a clustering technique [Schöbi et al., 2016] detailed hereafter for a sake of clarity. If this method returns only $K_1 < K$ samples ($K_1 = 0$ possibly), then the very same method is applied to the extended set $\mathcal{S}$ to provide the remaining $K - K_1$ samples.

3. To avoid samples too close to each other (for preventing metamodel training issues), a filtering procedure is performed on the selected samples $\mathcal{X}^* = (\boldsymbol{x}_0^*, ..., \boldsymbol{x}_K^*)$, removing too close points: if $\|\boldsymbol{x}_i^* - \boldsymbol{x}_j^*\|_2 < TOL$, $\boldsymbol{x}_j^*$ is discarded from $\mathcal{X}^*$, TOL being an user-defined parameter.

Weighted K-means Algorithm Let $\mathcal{A} = (\boldsymbol{x}_1, ..., \boldsymbol{x}_P)$ denote a sample set, that can be either $\mathcal{S}$ or $\mathcal{S}^{(k)}$. In step 2, a weighted K-means clustering algorithm is used [Zaki et al., 2014] for accounting for the importance of the samples in $\mathcal{A}$. The weights are set to the probability of misclassification (Eq. V.27) of each sample $\boldsymbol{x} \in \mathcal{A}$, bounded on $[0, 0.5]$ by definition. The K samples are then selected as the clusters' centroids. More specifically, this clustering technique aims at minimizing the total cluster variance defined as:

$$V_{\mathcal{A}} = \sum_{j=1}^{K} \sum_{l \backslash i_l = j} \|\boldsymbol{x}_j^* - \boldsymbol{x}_l\|_2, \tag{IV.7}$$

where $i_l = \underset{j \in [\![1,K]\!]}{\arg\min} \|\boldsymbol{x}_j^* - \boldsymbol{x}_l\|_2$, indicates the index of the closest centroid $\boldsymbol{x}_{i_l}^*$ to a sample $\boldsymbol{x}_l$. $\{\boldsymbol{x}_j^*\}_j$ denote the K weigthed centroids defined as

$$\boldsymbol{x}_j^* = \frac{1}{\sum\limits_{l \backslash i_l = j} \omega_l} \sum_{l \backslash i_l = j} \omega_l \boldsymbol{x}_l, \tag{IV.8}$$

where $\omega_l = P_m(\boldsymbol{x}_l)$ [Schöbi et al., 2016] is the weight associated to the sample $\boldsymbol{x}_l$. Note that in AKMCSi [Lelièvre et al., 2018], the chosen weights are $\omega_l = \dfrac{1}{U^2(\boldsymbol{x}_l)}$, with $\boldsymbol{x} \to \dfrac{1}{U^2(\boldsymbol{x})}$ and $\boldsymbol{x} \to P_m(\boldsymbol{x})$ having the same monoticity.

Setting $\omega_l = 1$ for all samples leads to the definition of the regular centroids, and by extension, to the regular K-means algorithm. The weighted K-means algorithm is summarized in Algorithm IV.2.

Remark The set of candidate points $S^{(k)}$ belonging to the LSM $\mathcal{M}^{(k)}$ can contain less than K samples, possibly being empty. This fact explains why a point in S maximizing the U-function is also selected.

Algorithm IV.2 Weighted K-means Algorithm [Schöbi et al., 2016].

Input: samples $\mathcal{A} = (\boldsymbol{x}_1, ..., \boldsymbol{x}_P)$, TOL, $NMAX$, P_m, K
Output: K centroids $(\boldsymbol{x}_1^*, ..., \boldsymbol{x}_K^*)$

27 If $P < K$, return $\mathcal{A}$.
Centroids Initialization $\mathcal{C}^{(0)} = (\boldsymbol{x}_1^{(0)}, ..., \boldsymbol{x}_K^{(0)})$: Regular K-means (or Random).
n=0 ; err=1 ;
while $n < NMAX$ *and* $err > TOL$ **do**
28 $n \leftarrow n + 1$
Assign a cluster i_l to each sample $\boldsymbol{x}_l$: $\forall l \in [1, P]$, $i_l = \underset{j \in [\![1,K]\!]}{\arg\min} \|\boldsymbol{x}_j^* - \boldsymbol{x}_l\|_2$
Update Weigthed centroids $\mathcal{C}^{(n)}$: Equation IV.8.
Update Error: $err = \sum\limits_{j=1}^{K} \|\boldsymbol{x}_j^{(n)} - \boldsymbol{x}_j^{(n-1)}\|_2$
29 Return $\mathcal{C}^{(n)}$

Illustrative example To showcase the process of selecting multiple additional samples, we consider the four-branch series example introduced in Subsubsection II–3.5.3, *i.e.* a 2D test-case characterized by two MPFPs and four failure regions, with a $p_f \sim 5.596 \times 10^{-9}$ and initialized with a DoE of size 10. The process of selecting $K+1=8$ samples (resp. $K+1=64$) is illustrated in Figure IV.1 (resp. Figure IV.2).

In Figures IV.1 (a) and IV.2 (a), the small black dots indicate the candidate points S among which a single point minimizing the U-function is selected (purple diamond). The candidates points of $S^{(k)}$ belonging to the LSM $\mathcal{M}^{(k)}$ and extracted from S are indicated in small black dots in Figures IV.1 (b) and IV.2 (b), where selected samples (weighted centroids from the clustering technique Algorithm IV.2) are indicated in red squares. The set $S^{(k)}$ contains less points focused on the LSM (*exploitation*), while the point selected among the set S has an *exploratory* role.

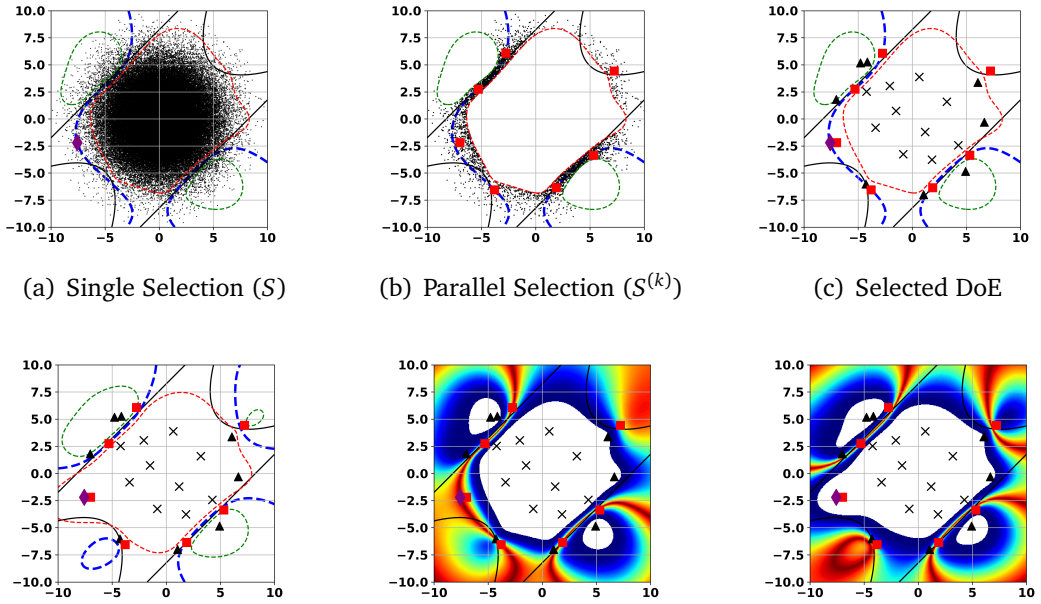

(a) Single Selection (S) (b) Parallel Selection ($S^{(k)}$) (c) Selected DoE

(d) Metamodel Updated (e) Selected DoE(P_m) (f) Metamodel Updated(P_m)

Figure IV.1 Illustration of the parallel refinement strategy: Selection of $K+1=8$ samples. Four-branch series system 2D (Subsubsection II–3.5.3).
LSS: The true LSS $\{G(\boldsymbol{x})=u\}$ is indicated by a black line, the *predicted* LSS $\{\mu_{\hat{G}}(\boldsymbol{x})=u\}$ by a dashed blue line, the lower LSS $\{\mu_{\hat{G}}(\boldsymbol{x})-k\sigma_{\hat{G}}(\boldsymbol{x})=u\}$ by a red dashed line and the upper LSS $\{\mu_{\hat{G}}(\boldsymbol{x})+k\sigma_{\hat{G}}(\boldsymbol{x})=u\}$ by a green dashed line.
DoE: The initial DoE is indicated by grey crosses, the current DoE by black triangles, the point selected with single eAK-MCS by a purple diamond and selected points with weighted K-means by red squares.
Contours of the probability of misclassification P_m are indicated in white when lower than 10^{-4}. Blue and red correspond respectively to 10^{-4} and 1.

IV–2.4 Stopping Criterion

The stopping criterion adopted in this study is the same as the one proposed in [Schöbi et al., 2016], focusing on the accuracy of the quantity of interest, consequently on the upper and lower bounds of the failure probability:

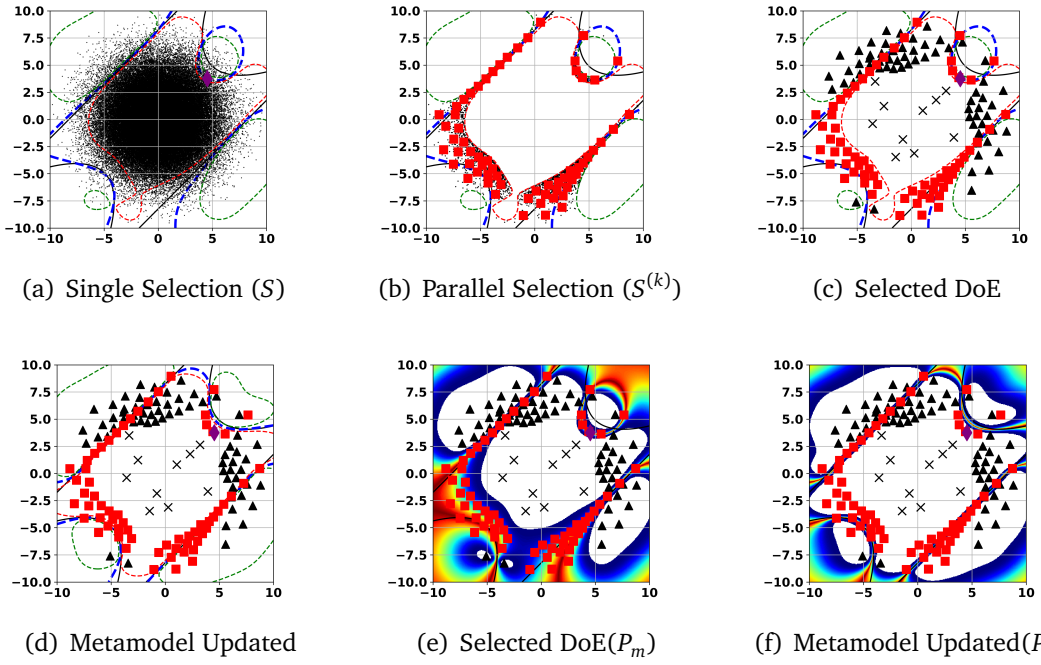

(a) Single Selection (S) (b) Parallel Selection ($S^{(k)}$) (c) Selected DoE

(d) Metamodel Updated (e) Selected DoE(P_m) (f) Metamodel Updated(P_m)

Figure IV.2 Illustration of the parallel refinement strategy: Selection of $K+1=64$ samples. Four-branch series system 2D (Subsubsection II–3.5.3). Legend settings in Figure IV.1.

$$\text{Basic: } \frac{\hat{p}_{\tilde{f}}^{(\tilde{k})+} - \hat{p}_{\tilde{f}}^{(\tilde{k})-}}{\hat{p}_{\tilde{f}}} < \epsilon_{p_{\tilde{f}}}, \tag{IV.9}$$

for two consecutive iteration steps, where $p_{\tilde{f}}$, $p_{\tilde{f}}^{(\tilde{k})+}$ and $p_{\tilde{f}}^{(\tilde{k})-}$ are estimated using IS based on the ISD $f_{\mathcal{N}(0,\gamma^{*2}I_d)}$ with N_γ^{IS} samples. Those estimations can be performed with another ISD, such as the Gaussian mixture as introduced in Section III–3.2. However, it seems that in high dimension and for very small failure probabilities, the IS efficiency is reduced involving estimates subject to larger CoVs, otherwise speaking, larger $(\alpha-\sigma)$-IS confidence intervals.

Modified versions of the *basic* stopping criterion (Eq. V.29) reads:

$$\text{Conservative: } \frac{\hat{p}_{\tilde{f},max}^{(\tilde{k})+} - \hat{p}_{\tilde{f},min}^{(\tilde{k})-}}{p_{\tilde{f}}} < \epsilon_{p_{\tilde{f}}}. \tag{IV.10}$$

$$\text{Fast: } \frac{\hat{p}_{\tilde{f},min}^{(\tilde{k})+} - \hat{p}_{\tilde{f},max}^{(\tilde{k})-}}{p_{\tilde{f}}} < \epsilon_{p_{\tilde{f}}}. \tag{IV.11}$$

Note also that the value of k depends on the level of accuracy required and might be different from the one used in the process of generating candidate points selection (via LSM $\mathbb{M}_f^{(k)}$) or when tuning γ, for which we would recommend a large value (say $k=3$). A lower value denoted as $\tilde{k}$ is used when evaluating the stopping criterion.

IV–2.5 eAK-MCS numerical settings

The tuning parameters mentioned in the method section are summarized in Table V.1 with their suggested value, used in the numerical experiments (except when explicitly mentioned). The stopping criterion selected is systematically *Fast* (Eq. IV.11).

$\tilde{k}$	k	n_0	ϵ	r_{max}	N_C	γ_0	γ_{min}	γ_{max}	N_γ	n_γ	N_γ^{IS}
1	3	$5d$	10^{-5}	$\lvert\Phi(10^{-20})\rvert \approx 9.2$	10^6	2.5	1	5	10^5	15	10^7
p	d_{min}	$K+1$	TOL	$NMAX$	α	$\epsilon_{p_{\tilde{f}}}$					
5	10^{-4}	8	10^{-4}	100	2	5%					

Table IV.1 Tuning Parameters

IV–3 Numerical experiments

In this Section, the capabilities of the algorithm is showcased through its application to several test-cases. Only cases involving $p_f \sim 10^{-5} - 10^{-9}$ are considered here, to showcase the suitability of the proposed algorithm to deal with very small failure probabilities (unlike AK-MCS). Comparison of eAK-MCS with examples suitable for AK-MCS are not presented for the sake of brevity, since similar performances would be obtained considering AK-MCS [Schöbi et al., 2016] with ordinary Kriging. Reference values are estimated either with Subset Simulation (from [Bect et al., 2017]) or using IS with a Gaussian mixture ISD Section III–3.2. Three 2D and one 6D examples are studied. They are introduced in Subsection II–3.5. A first study consists of the assessment of the eAK-MCS algorithm with the parallel refinement strategy, with $K+1=8$ samples being iteratively added to the DoE. Results are compared against literature when available, in particular BSS [Bect et al., 2017] and AK-MCSi [Lelièvre et al., 2018], in Subsection IV–3.1.

In Subsection IV–3.2, a second study is performed using the single refinement strategy, with an *unfavorable* DoE focused in the center of the standard space, to investigate the capability of eAK-MCS to detect failure regions, even when the initial surrogate does not.

IV–3.1 Basic Study: $K+1=8$

In this section, we have studied the four test cases listed in Subsection II–3.5 considering $K+1=8$ samples added at each iteration of the refinement procedure. To assess the statistical significance of the proposed method (due to its stochastic nature), each test case is studied based on 50 independent runs. The number of calls N_{calls} to the performance function, the number of iterations N_{iter}, the estimation of the failure probability $\hat{p}_f$, and the final relative $\epsilon_{p_f}^{rel}$ error, a.k.a. relative absolute bias $\epsilon_{p_f}^{rel} = \dfrac{|\hat{p}_{\tilde{f}} - p_f^{ref}|}{p_f^{ref}}$ are consequently random variable illustrated by their empirical average. The initial DoE is supposed to be evaluated in one iteration. Note that in the context of multiple independent runs, the CoV of $\hat{p}_{\tilde{f}}$ estimated from realizations of $\hat{p}_{\tilde{f}}$ (which is different from the IS-based CoV estimation (Equation II.31) for a single

run), is an indicator of the robustness of the method. The lowest is the CoV, the more likely the method will return an estimation $\hat{p}_{\tilde{f}}$ close to its asymptotic average. It is then dependent of the metamodel accuracy at the end of the refinement algorithm (or equivalently the DoE), and the IS-based CoV estimation (Equation II.31).

The tuning parameters are the ones provided in Table V.1. For each case, figures showing the average relative absolute bias $\epsilon_{p_f}^{rel}$, and the average estimate $\hat{p}_{\tilde{f}}$ as a function of the number of performance function calls are provided, where additional samples are added even after the stopping criterion is met, for a sake of illustration. The parallel strategy refinement might propose strictly less than $K+1=8$ samples, depending on the current metamodel accuracy. For two-dimensional examples, we have also provided an illustration of the final DoE and the refined metamodel, when the convergence criterion is satisfied, based on a single run. Whenever it is possible, results also are compared against other methods in the literature. The Four-Branch series 2D, the Cantilever Beam 2D and the non-linear Oscillator 6D are compared against BSS as reported in [Bect et al., 2017], based on 100 independent runs, for different accuracy settings (see [Bect et al., 2017] for details) and a *single* enrichment strategy. It explains the vast range of CoV and $\epsilon_{p_f}^{rel}$ for those cases estimated with BSS.

IV–3.1.1 Single Failure Region 2D (Subsubsection II–3.5.1)

This single failure region example is introduced in Subsubsection II–3.5.1. In Table V.2, we compare the results with the ones reported in [Cadini et al., 2014], against the following methods: Crude MC, FORM, FORM+IS, AK-IS, MetaAK-IS^2, based on single runs. The proposed algorithm performs well w.r.t. other metamodel based methods (AK-IS, MetaAK-IS^2) with reasonable accuracy, concerning the number of performance function calls, while it outperforms them regarding the number of iterations, as expected. An illustration is provided in Figure V.5(a), showing the refined metamodel for a single run. The DoE selected at the last iteration are well clustered around the True LSS. The True LSS is correctly estimated by the predicted LSS, the latter matching the upper/lower LSS. This is further illustrated in the failure probability history Figure V.5 (c) where the $2-\sigma$ confidence interval of $\hat{p}_{\tilde{f}}$ rapidly merges and converges to the reference value. After 4 iterations, the average absolute relative bias $\epsilon_{p_f}^{rel}$ is below 1%. The low CoV $\sim 1\%$ quantifies the high robustness of the method for this test-case.

The original function being a third order polynomial easily captured by the metamodel, this example is rather simple since also characterized by a single failure region. The low value of $\epsilon_{p_f}^{rel}$ can be explained by both the excellent quality of the surrogate, and the high IS efficiency for this case.

IV–3.1.2 Four-branch series system 2D (Subsubsection II–3.5.3, $u=-4$)

This benchmark example characterized by two MPFPs, four failure domains and a very small failure probability ($\sim 5.6\times10^{-9}$) is introduced in Subsubsection II–3.5.3 ($u=-4$). The results are presented in Table V.3 and Figure V.6. eAK-MCS stops after ~ 62 calls (~ 8 iterations) on average, while BSS uses between 50 and 80 calls. The CoV is small, 1.57%, and the accuracy satisfactory, with an average relative error of 1.20%. As seen in Figure V.6 (a), the True LSS is well estimated by the predicted LSS in the region characterized by high density of input distribution, where the ability of the surrogate to classify samples into the safe/unsafe domain is the most sensitive.

Table IV.2 Results of the Single Failure Region 2D with the parallel strategy ($K+1=8$).

Method	N_{calls}	N_{iter}	$\hat{p}_f$	CoV	$\epsilon_{p_f}^{rel}$
Reference[a]	10^7	-	2.874×10^{-5}	0.03%	0
FORM[b]	19	10	4.21×10^{-7}	-	98.5%
FORM + IS[b]	$19+10^4$	$10+10^4$	2.86×10^{-5}	2.39%	0.48%
AK-IS[b]	26	17	2.86×10^{-5}	2.39%	0.48%
MetaAK-IS^2 [b]	28	19	2.87×10^{-5}	2.39%	0.14%
eAK-MCS[c]	26.5	3.1	2.851×10^{-5}	1.02%	1.01%

[a] IS with a Gaussian mixture as ISD (Section III–3.2).

[b] Reproduced from [Cadini et al., 2014], single run, single refinement strategy.

[c] Initial DoE size: 10. K+1=8 samples iteratively added. Based on 50 independent runs.

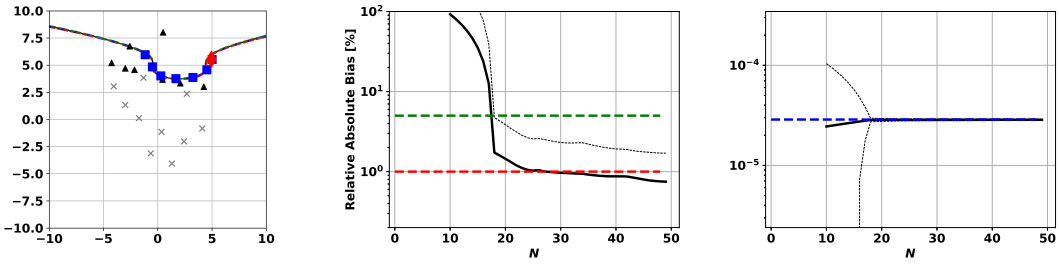

(a) Metamodel (b) Relative Absolute Bias History (c) $\hat{p}_f$ History

Figure IV.3 Results of the Single Failure Region 2D with the parallel strategy ($K+1=8$).
(a) Legend Settings in Figure IV.1.
(b) Green and red thick dashed lines indicate respectively 5% and 1% relative error. The y-axis is logarithmic. The average relative absolute bias and the associated $2-\sigma$ confidence intervall are represented respectively in black thick line and black thin dashed lines.
(c) The average *predicted* failure probability $\hat{p}_{\tilde{f}}$ and the associated $2-\sigma$ confidence intervall are represented respectively in black thick line and black thin dashed lines.

Note also that in that zone, the upper/lower predicted LSS match the predicted LSS, indicating high predictability and the presence of DoE clustered in that zone. Figures V.6 (b) (c) illustrate the average relative absolute bias and the failure probability history respectively as a function of the number of performance calls. One can note that after, 26 function calls (3 iterations), the average predicted failure probability $\hat{p}_{\tilde{f}}$ is already of the same order of magnitude of the reference value, and the convergence is then rather fast, with an average absolute relative bias lower that 1% after $\sim$ 70 function calls ($\sim$8 iterations).

IV–3.1.3 Deviation of a Cantilever Beam 2D (Subsubsection II–3.5.5)

This two-dimensional example is characterized by a single failure region, with $p_f \sim 4\times 10^{-6}$ and introduced in Subsubsection II–3.5.5. The results are presented in Table V.4 and Figure V.7. The eAK-MCS algorithm stops after $\sim$ 41 calls in average, significantly

Table IV.3 Results of the Four-branch series system 2D with the parallel strategy ($K+1=8$).

Method	N_{calls}	N_{iter}	$\hat{p}_f$	CoV	$\epsilon_{p_f}^{rel}$
Reference[a]	10^7	-	5.596×10^{-9}	0.04%	0
BSS [Bect et al., 2017]	$\sim 50-80$	$\sim 41-71$	-	$\sim 0.5-0.01$	$\sim 0.01-5\%$
eAK-MCS[b]	61.9	7.5	5.579×10^{-9}	1.57%	1.20%

[a] Based on 100 independent runs, for different accuracy settings and a single refinement strategy. [Bect et al., 2017].

[b] Initial DoE size: 10. K+1=8 samples iteratively added. Based on 50 independent runs.

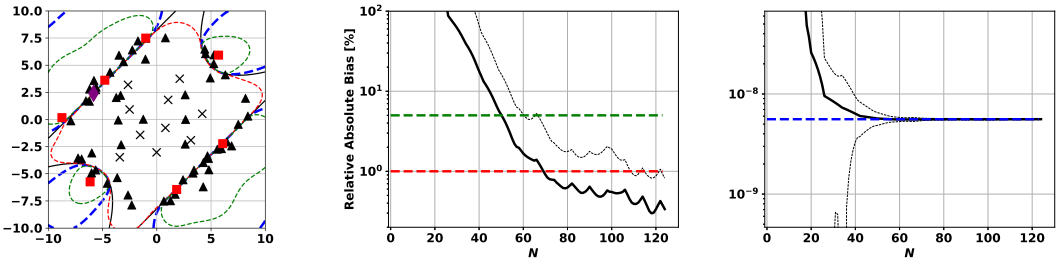

(a) Metamodel (b) Relative Absolute Bias History. (c) $\hat{p}_f$ History

Figure IV.4 Results of the Four-branch series system 2D with the parallel strategy ($K+1=8$). Legend settings in Figure V.5.

larger than for BSS (~ 25), but still with fewer iterations (~ 5 against ~ 15). Figure V.7 (b) shows that the average relative absolute bias is below 1% after around 48 calls. For the sake of illustration, we have truncated the history to 50 calls. Indeed, for few runs characterized by very accurate metamodels, the enrichment algorithm proposes candidates that are too close to the existing DoE to be accepted, and the algorithm stops.

The CoV is small, 2% and the accuracy is satisfactory, with an average relative error lower of 1.21%. It can be noticed that the surrogate detects spurious predicted LSS during the refinement step, which explains the additional computational burden. For the single run illustrated Figure V.7 (a), a second artificial failure region is finally so far from the origin (center of the standard space distribution) that it has no impact on the estimated failure probability. This behavior results from the choice of the surrogate itself. Using a suitable trend (here null) or choosing another covariance kernel should address this behavior.

IV–3.1.4 Response of a Nonlinear Oscillator 6D (Subsubsection II–3.5.6)

The results for this six-dimensional example (introduced Subsubsection II–3.5.6) characterized by $p_f \sim 1.5 \times 10^{-8}$ are presented in Table V.5 and Figure V.8. They are compared against BSS [Bect et al., 2017] and AK-MCSi [Lelièvre et al., 2018] (single run and sequential enrichment strategy). eAK-MCS requires on average ~ 45 calls, significantly less than AK-MCSi, similarly to BSS for the less costly settings, but with a meager number of iterations (~ 3). Note however that for the most expensive ones, BSS would require in average 180 calls. The robustness and accuracy for this higher

Table IV.4 Results of the Deviation of a Cantilever Beam 2D with the parallel strategy ($K+1=8$).

Method	N_{calls}	N_{iter}	$\hat{p}_f$	CoV	$\epsilon_{p_f}^{rel}$
Reference[a]	10^7	-	3.937×10^{-6}	0.03%	0
BSS [Bect et al., 2017]	$\sim 22-25$	$\sim 13-16$	-	$\sim 0.5-0.01$	$\sim 0.1-5\%$
eAK-MCS[b]	41.2	4.9	3.949×10^{-6}	2.07%	1.21%

[a] Based on 100 independent runs, for different accuracy settings and a single refinement strategy. [Bect et al., 2017].

[b] Initial DoE size: 10. K+1=8 samples iteratively added. Based on 50 independent runs.

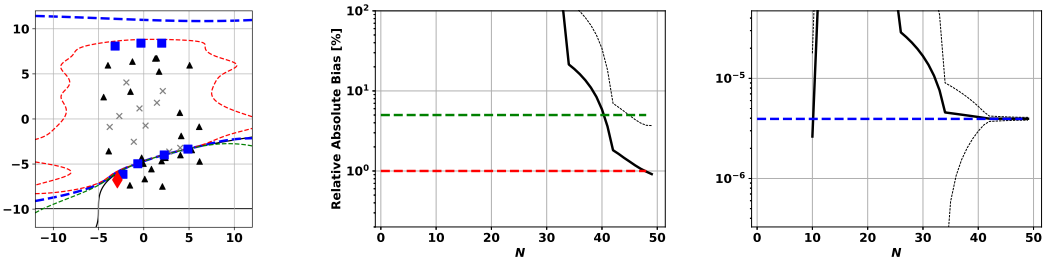

(a) Metamodel

(b) Relative Absolute Bias History.

(c) $\hat{p}_f$ History

Figure IV.5 Results of the Deviation of a Cantilever Beam 2D with the parallel strategy ($K+1=8$). Legend settings in Figure V.5.

dimensional test case are rather low (CoV $\sim$ 8.3%, average relative error $\sim$ 8.9%) compared to previous two-dimensional test-cases but still satisfactory considering the low computational cost.

This inaccuracy stems mainly from the *average* efficiency of the IS (with the ISD $\mathcal{N}(0, \gamma^2 I_d)$) to reduce the variance in this higher dimensional case. Indeed, the CoV of the IS estimation of $\hat{p}_{\tilde{f}}$ is in average $\sim$ 2.25 % (while below 0.5% for the two-dimensional cases), and is entirely independent of the quality of the surrogate (or the DoE). The second reason is the choice of the stopping criterion (*Fast*, Eq. IV.11) which is likely to stop prematurely, especially here with significant IS confidence intervals. Figure V.8 (a) show that the average relative error reaches around 2% after $\sim$ 75 calls and then oscillates to stay between $\sim$ 1.5% and 2.5%, confirming respectively that the algorithm stopped prematurely, and that the IS estimation is not accurate enough to provide an average relative error lower than 1%. The quality of the refinement algorithm itself (or equivalently, of the surrogate) is further confirmed in Figure V.8 (b) indicating that the reference value is however contained in the noise associated to the IS CoV. Resorting this issue and obtaining a more accurate estimation of the failure probability associated to the refined *surrogate* could require another sampling technique, which could be directly used on the surrogate as a post-processing, such as Subset Sampling or IS with a Gaussian Mixture ISD (Section III–3.2).

Table IV.5 Results of Response of a Nonlinear Oscillator 6D with the parallel strategy ($K+1=8$).

Method	N_{calls}	N_{iter}	$\hat{p}_f$	CoV	$\epsilon_{p_f}^{rel}$
Reference[a]	10^7	-	1.514×10^{-8}	0.04%	0
BSS [Bect et al., 2017]	$\sim 45-180$	$\sim 36-171$	-	$\sim 0.5-0.01\%$	$\sim 0.01-10$
AK-MCSi[b] [Lelièvre et al., 2018]	77	68	1.44×10^{-8}	$< 5\%$	3.4%
eAK-MCS[c]	44.7	2.8	1.633×10^{-8}	8.35%	8.91%

[a] Based on 100 independent runs, for different accuracy settings and a single refinement strategy. [Bect et al., 2017].

[b] Single Refinement Strategy [Lelièvre et al., 2018]

[c] Initial DoE size: 10. K+1=8 samples iteratively added. Based on 50 independent runs.

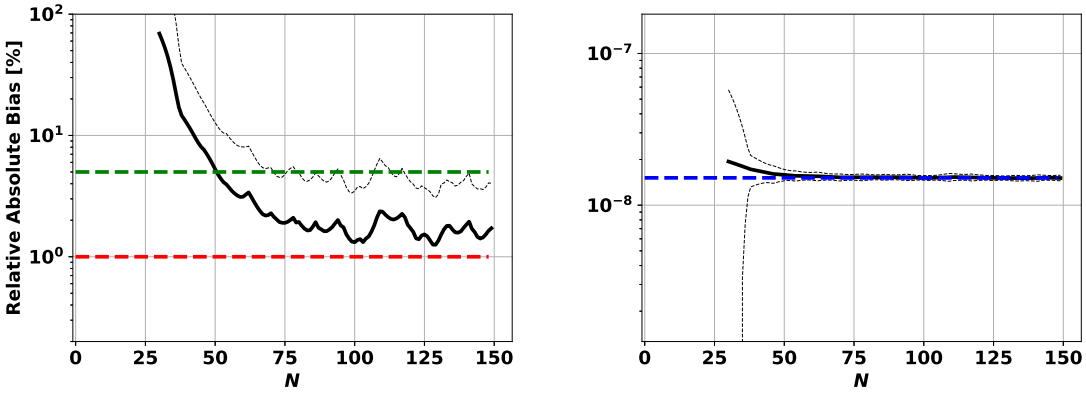

(a) Relative Absolute Bias History

(b) $\hat{p}_f$ History

Figure IV.6 Results of Response of a Nonlinear Oscillator 6D with the parallel strategy ($K+1=8$). Legend settings in Figure V.5.

IV–3.2 Single sample eAK-MCS Study: $K+1=1$

In this Subsection, we showcase the capability of the present method to detect all failure regions, even starting with a *unfavorable* initial DoE, namely *too* focused on the center of the standard space, corresponding to an ϵ rather big ($\epsilon = 10^{-2}$, against $\epsilon = 10^{-5}$ in default numerical settings). The single eAKMCS is used with no parallel refinement. The simple Single Failure 2D example is not considered for the sake of brevity. For each case, figures showing the relative absolute bias $\epsilon_{p_f}^{rel}$, and the estimates $\hat{p}_{\tilde{f}}^{(\tilde{k})+}$, $\hat{p}_{\tilde{f}}^{(\tilde{k})-}$ and $\hat{p}_{\tilde{f}}$ as a function of the number of performance function calls are provided. For two-dimensional examples, an illustration of the metamodel refinement detecting failure domains is also given.

IV–3.2.1 Four-branch series system 2D (Subsubsection II–3.5.3, $u=-4$)

Figures IV.7 (a), (b), (c) and (d) show that all the four failure domains are detected after respectively 11, 28, 56 and 100 calls of the original model. It illustrates a *behavior* discussed in the original AK-MCS version [Echard et al., 2011], namely that

the single refinement strategy tends to focus on each failure branch individually then *explore* other branches when sufficiently refined. Even though the initial DoE is very *unfavorable*, all failure domains are successfully detected.

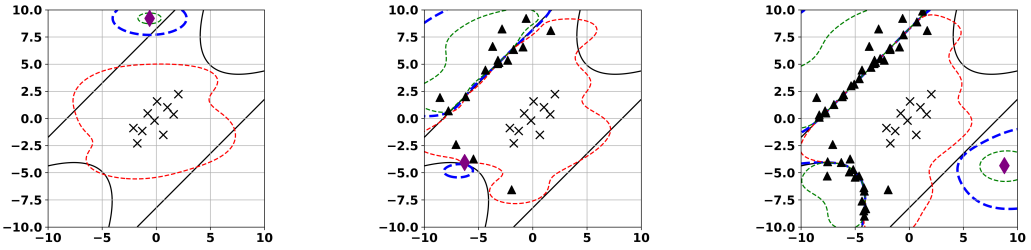

(a) First Failure Zone: $N = 11$. (b) Second Failure Zone: $N = 28$. (c) Third Failure Zone: $N = 56$.

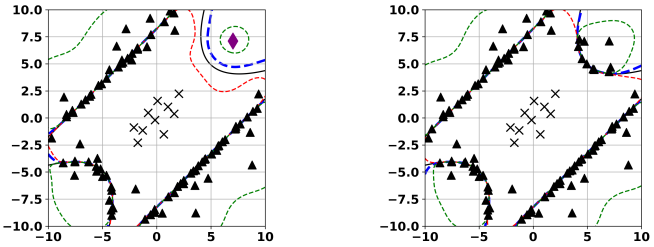

(d) Fourth Failure Zone: $N = 100$. (e) Final: $N = 112$.

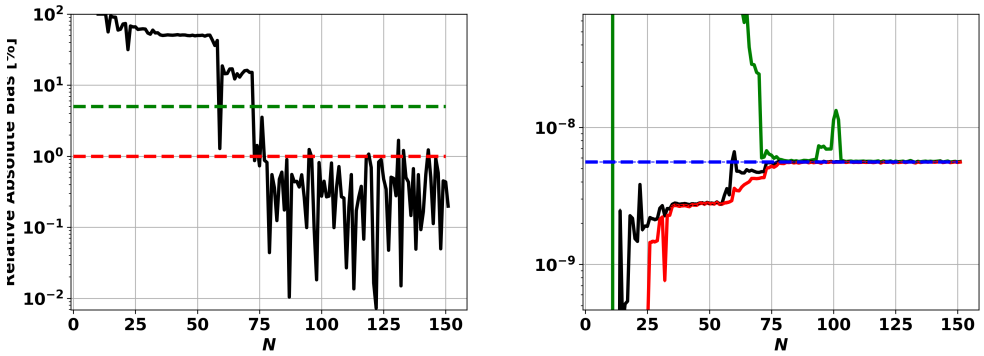

(f) Relative Absolute Bias History. (g) $\hat{p}_f$ History

Figure IV.7 Results of the Four-branch series system 2D with the single refinement strategy. Legend settings in Figure V.5 (a-f).
(g) The *predicted* failure probability $\hat{p}_{\tilde{f}}$, its lower and upper bounds $\hat{p}_{\tilde{f}}^{(\tilde{k})-}$, $\hat{p}_{\tilde{f}}^{(\tilde{k})+}$ are indicated respectively in black, red and green thick lines. Their associated $(\alpha-\sigma)$-IS confidence interval are indicated in thin dashed lines (not visible for small CoV).

IV–3.2.2 Deviation of a Cantilever Beam 2D (Subsubsection II–3.5.5)

Figure IV.8 (a) shows that the failure domain is detected after 14 performance function evaluations. The final metamodel is obtained iteratively with a total of 23 function calls, the same order of magnitude of function required for BSS (with iterative refinement). Note the strange convergence of the failure probability history, for which

we can notice that the reference value is globally not contained within the estimated failure probability range: it indicates again a lack of predictability of the surrogate whose trend/covariance kernel might be more carefully chosen and some hints about the robustness of the method.

eAK-MCS performance is satisfactory with this simple example, even though the failure probability is very low.

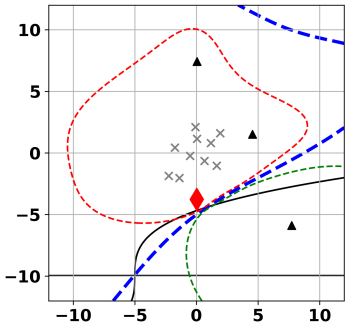

(a) First Failure Zone: $N = 14$.

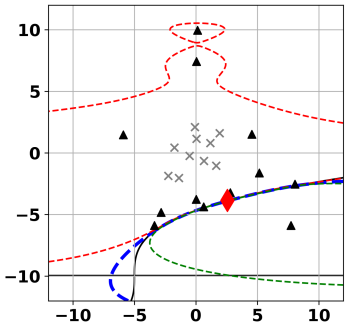

(b) Final: $N = 23$.

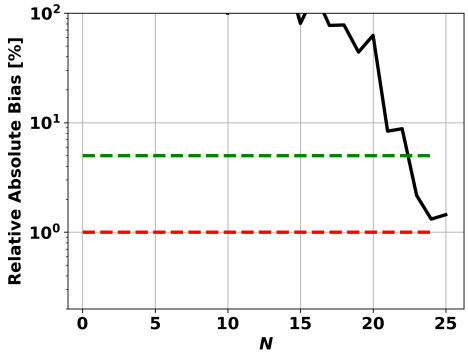

(c) Relative Absolute Bias History.

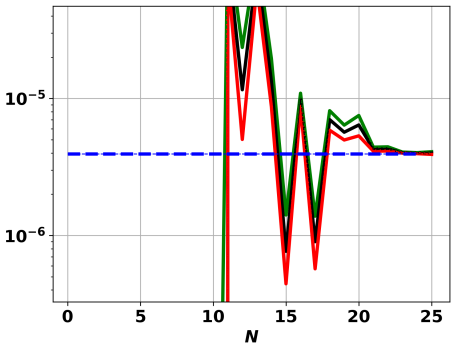

(d) $\hat{p}_f$ History

Figure IV.8 Results of the Deviation of a Cantilever Beam 2D with the single refinement strategy. Legend settings in Figure IV.7.

IV–3.2.3 Response of a Nonlinear Oscillator 6D (Subsubsection II–3.5.6)

The Absolute Relative Bias history represented in Figure IV.9 (a) shows that the relative error is below 5% after around 35-50 performance calls, corresponding to around 5-20 refinement steps. Note the oscillatory behavior of the relative absolute bias. Those oscillations stem from the large CoV associated with the IS failure probability estimation, similarly to the study of the very same case with the parallel strategy and *standard* initial DoE. Again, Figure IV.9 (b) shows that the reference value lies between the confidence interval of $\hat{p}_{\tilde{f}}$. It illustrates the capability of eAK-MCS, in this example, to detect failure regions even when under *unfavorable* initial DoE.

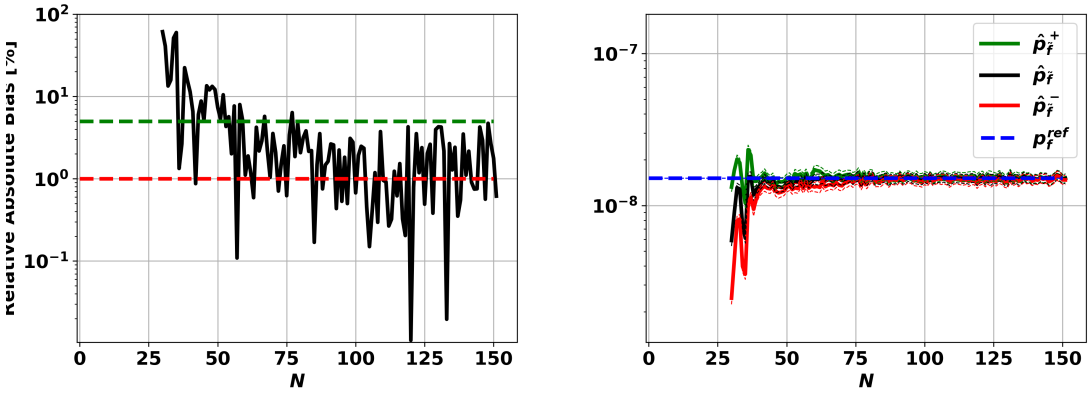

(a) Relative Absolute Bias History.

(b) $\hat{p}_f$ History

Figure IV.9 Results of Response of a Nonlinear Oscillator 6D with the single refinement strategy. Legend settings in Figure IV.7.

IV–4 Conclusion

An extension of AK-MCS as presented in [Schöbi et al., 2016] to make it suitable for very low failure probabilities is proposed. It uses a centered uncorrelated Gaussian distribution to sample candidate points and use the IS method to estimate p_f. A procedure is proposed to tune its standard deviation adaptively, based on variance reduction. Moreover, the original multipoint refinement strategy inherited from [Schöbi et al., 2016] is slightly modified, enabling the use of available high-performance computing resources. The performance of the proposed algorithm is assessed and illustrated through some benchmark analytical functions, showcasing very satisfactory performances, in less than 100 evaluations of the original model. Unlike AK-MCS, eAK-MCS requires to recast the problem in standard space. eAK-MCS, like most surrogate-based procedures, is a victim of the curse of dimensionality, and its efficiency is closely linked to the surrogate's ability to fit the original model. eAK-MCS is globally robust to the choice of the tuning parameters (Table V.1), which provide excellent results for a broad range of cases, including the ones presented in this work. However, the most sensitive parameters would be the ones related to the stopping criterion. In the context of reliability assessment, it has finally not an enormous impact since the user can stop at anytime the refinement, modify some parameters and re-run the procedure without losing any information.

The efficiency of eAK-MCS, concerning both the number of performance function calls and accuracy, seems to be of the same order of magnitude of BSS, which is to the best of the author' knowledge, one of the most efficient methods for assessing very small failure probabilities. While BSS seems to provide a more robust estimation than eAK-MCS, it requires, apparently, meticulous tuning of the parameters, and the user should wait for the refinement to reach the last threshold to have an estimate of the failure probability. Otherwise, in eAK-MCS, this estimation is available at any iteration of the algorithm. Additionally, eAK-MCS is more straightforward to implement w.r.t. BSS, with a clear parallelization strategy.

Studies with *unfavorable* initial DoE shows the ability of eAK-MCS to detect multiple failure domains, even if, unlike BSS, it aims at refining directly the *Limit-State Surface* $\{G(\boldsymbol{X}) = u\}$. This latter feature could be exploited in AK-MCS based derived methods such as quantile estimation [Schöbi et al., 2016] or in RBDO algorithms [Moustapha et al., 2016] where the refinement algorithm for a LSS of the form $\{G(\boldsymbol{x}) = u\}$ is part of more extensive procedure. It makes eAK-MCS particularly attractive, so the adaptation of the mentioned algorithms for LSS associated with small failure probability could be facilitated. The adaptation of the algorithm [Schöbi et al., 2016] for very small quantile estimation using eAK-MCS is presented in Chapter V.

V

Efficient Estimation of Extreme Quantiles using Adaptive Kriging and Importance Sampling

Overview *This Chapter presents a method permitting the estimation of extreme quantiles*[a]*, named* Quantile extreme Active Kriging-Monte Carlo Sampling *(QeAK-MCS) and inspired from [Schöbi et al., 2016]. This Kriging-based approach adapts the refined strategy provided by the reliability analysis algorithm named eAK-MCS (Chapter IV), enabling accurate quantile estimations in a reasonable number of calls to the performance function*[b]*. Direct use of Monte-Carlo simulation even on the surrogate model being too expensive, the key idea consists in using an Importance Sampling method based on an isotropic centered Gaussian with large Standard deviation permitting a cheap estimation of the quantiles on the surrogate. The original parallel surrogate refinement strategy is renriched with an additional level of parallelization, the latter being also compatible with the seminal quantile estimation algorithm [Schöbi et al., 2016].*

[a] Associated to levels in the range $O(10^{-9})$.
[b] Assumed to be the output of an expensive to evaluate simulation tool.

V–1 Introduction

Quantile estimation is of fundamental importance in statistics as well as in design applications [Law et al., 1991], the main challenge being the large required number of evaluations of the expensive performance function. Variance reduction techniques such as Importance Sampling [Glynn, 1996], correlation-induction [Avramidis and Wilson, 1998] and control variate [Hsu and Nelson, 1990] [Hesterberg and Nelson, 1998] have been proposed and implemented. The number of observations required is however large, especially when dealing with small quantiles.

The problem of interest consists in the estimation of the quantile $q \in \mathbb{R}$ associated to a level of probability $\alpha \in]0,1[$, with $\alpha \sim 0$:

$$\alpha = \mathbb{P}(G(\boldsymbol{X}) < q) = \mathbb{E}[\mathbb{1}_{G<q}(\boldsymbol{X})] = \int_{\mathbb{R}^d} \mathbb{1}_{G<q}(\boldsymbol{x}) f_{\boldsymbol{X}}(\boldsymbol{x}) d\boldsymbol{x}. \tag{V.1}$$

with $\boldsymbol{X} \sim \mathcal{N}(0, I_d)$ denoting the standard d-dimensional Gaussian vector, described by its PDF $f_{\mathcal{N}(0,I_d)}$ and G the LSF.

The problem of the quantile estimation is closely linked to the one of estimating a failure probability α, where the model response G is associated to the critical value q. A typical approach for estimating the latter (Eq. V.1) consists in resorting to a direct MC scheme. Its estimator reads

$$\hat{\alpha} = \mathbb{E}_{\boldsymbol{X}}[\mathbb{1}_{G<q}(\boldsymbol{X})] = \frac{1}{N} \sum_{i=1}^{N} \mathbb{1}_{G<q}(\boldsymbol{x}_i), \tag{V.2}$$

where $(\boldsymbol{x}_1, ..., \boldsymbol{x}_N) \overset{\text{iid}}{\sim} \boldsymbol{X}$. This estimator is asymptotically unbiased and convergent. Its variance estimator reads:

$$\hat{\sigma}^2_{\hat{\alpha}} = \frac{\hat{\alpha} - \hat{\alpha}^2}{N}. \tag{V.3}$$

The accuracy of the estimate can then be measured directly with the theoretical coefficient of variation (CoV):

$$\hat{\delta}_{\hat{\alpha}} = \frac{\hat{\sigma}_{\hat{\alpha}}}{\hat{\alpha}} = \sqrt{\frac{1-\hat{\alpha}}{\hat{\alpha} N}}. \tag{V.4}$$

A MC-based estimator of the quantile reads:

$$\hat{q} = G(\boldsymbol{x}_{\lfloor \alpha N \rfloor}) \tag{V.5}$$

after having re-ordered the set $\{G(\boldsymbol{x}_1), ..., G(\boldsymbol{x}_N)\}$ in ascending order. Its accuracy is strongly linked to the number of MC samples N and the quantile level α. It is quantified by the CoV of the estimation of the associated failure probability $\mathbb{P}(G(\boldsymbol{X}) < \hat{q})$, whose value is approximated by $\delta = \sqrt{\frac{1-\alpha}{\alpha N}}$. Consequently, if a target error of $\delta < 1\%$ is aimed, a quantile of level 10^{-9} would require a number of simulation $N \sim \frac{1}{\alpha \delta^2} \sim 10^{13}$ yielding a prohibitive computational cost for industrial cases, and likely very expensive even considering a surrogate model for G.

We propose here a methodology to estimate a small quantile where the LSF G is assumed to be an expensive to evaluate function and written in the standard space.

[Schöbi et al., 2016] proposed to formulate the problem of the estimation of failure probability and quantile in an unified way, based on the popular AK-MCS [Echard et al., 2011] algorithm, originally developed for the estimation of failure probability. A Gaussian-Process [Rasmussen and Williams, 2006] based surrogate (Polynomial Chaos Kriging in [Schöbi et al., 2016]) of the LSF G is adaptively refined until a convergence criterion depending on the surrogate accuracy is met. More precisely, the refinement algorithm based on AK-MCS permits to select a batch of samples added to the DoE, where the threshold value is the quantile estimated from a Monte-Carlo population and the surrogate. When dealing with quantile of small level, such surrogate-based approach becomes untractable due to the prohibitive large size of the Monte-Carlo population that needs to be evaluated with the surrogate itself, required to obtain a satisfactory evaluation of the quantile. The same comment applies for the computation of small failure probability, where AK-MCS [Schöbi et al., 2016] [Echard et al., 2011] becomes unaffordably tractable. eAK-MCS (Chapter IV) extends AK-MCS for very small failure probability, inheriting for similar refinement strategy and general properties. It requires though to map the input random vector to the standard space. An Importance Sampling (IS) whose Density (ISD) is an isotropic centered Gaussian with large standard deviation permits to satisfactorily estimate a small quantile with a tractable number of surrogate evaluations. Similarly to AK-MCS based quantile estimation [Schöbi et al., 2016], the adaptive refinement algorithm eAK-MCS is used to adaptively refine the surrogate for a threshold equal to the estimated quantile. Finally, a multi-quantile selection approach allowing to exploit high-performance computing architectures one level further is presented. We illustrate the performances of the proposed method on several two and six-dimensional cases. Accurate results are obtained in less than 100 runs of J.

This Chapter is organized as follows. Section V–2 presents an IS-based quantile estimation scheme. Section V–3 describes the QeAK-MCS algorithm. Numerical experiments illustrating the QeAK-MCS method are reported in Section V–4. Conclusions are drawn in Section V–5.

V–2 Importance Sampling based Quantile estimation

The QeAK-MCS algorithm is based on two main ingredients, described hereafter: Importance Sampling using the ISD $\mathcal{N}(0, \gamma^2 I_d)$, and an IS-based quantile estimator.

Importance Sampling

The accuracy of the approximation given by IS critically depends on the choice of the ISD h. In this work, the ISD is chosen as $\mathcal{N}(0, \gamma^2 I_d)$ where $\gamma \geqslant 1$ is a parameter which is defined using a rule of thumb as discussed in Subsection V–3.4. Note that a Gaussian mixture ISD with suitable empirical parameters might be used (Section III–3.2), but those empirical parameters would depend on the critical threshold u, which is unknown in the context of quantile estimation.

Quantile Estimation

At each step of QeAK-MCS, several estimations of quantiles based on the surrogate model $\tilde{G}$ are required. When α is very small ($\alpha < 10^{-5}$), an accurate estimation using the MC approach becomes expensive, possible unfeasible, even using surrogate evaluations. To alleviate this issue, the IS procedure using $h = f_{\mathcal{N}(0,\gamma^2 I_d)}$ as the ISD is preferred. We consider the generic problem of estimating the quantile q of level $\alpha \in]0,1[$ associated to a scalar function g (e.g. $g(\boldsymbol{x}) = \mu_{\hat{G}}(\boldsymbol{x})$):

$$\alpha = \mathbb{P}(g(\boldsymbol{X}) < q). \tag{V.6}$$

A set of N samples $(\boldsymbol{x}_1, ..., \boldsymbol{x}_N) \overset{\text{iid}}{\sim} f_{\mathcal{N}(0,\gamma^2 I_d)}$ is generated.

The IS estimator (Eq. II.29) permits to implicitly formulate an estimation of $\hat{q}$:

$$\hat{q} = \text{Argmin}\left\{q \in \mathbb{R} \text{ s.t. } \frac{1}{N}\sum_{i=1}^{N} \mathbb{1}_{g<q}(\boldsymbol{x}_i)\frac{f_X(\boldsymbol{x}_i)}{h(\boldsymbol{x}_i)} > \alpha\right\}. \tag{V.7}$$

The sample set is re-ordered so $(g(\boldsymbol{x}_1), ..., g(\boldsymbol{x}_N))$ is sorted in ascending order. Note that the ISD $h = f_{\mathcal{N}(0,\gamma^2 I_d)}$ does not depend of $\hat{q}$. The implicit estimation of $\hat{q}$ is re-written as:

$$\alpha = \sum_{i=1}^{N} \mathbb{1}_{g<\hat{q}}(\boldsymbol{x}_i) y_i, \tag{V.8}$$

where $y_i = \frac{f_X(\boldsymbol{x}_i)}{N h(\boldsymbol{x}_i)}$. c_i is defined as: $\forall i \in [\![1, N]\!]$,

$$c_i = \sum_{j=1}^{i} y_i. \tag{V.9}$$

It's then easy to show that $\exists! l \in [\![1, N-1]\!]$ s.t.

$c_l \leq \alpha < c_{l+1}$, if $c_1 \leq \alpha < c_N$. A simple estimator of $\hat{q}$ would then simply read:

$$\begin{aligned}
\hat{q} &= g(\boldsymbol{x}_1), \text{ if } \alpha < c_1 && \text{(V.10)}\\
&= g(\boldsymbol{x}_N), \text{ if } \alpha \geq c_N && \text{(V.11)}\\
&= g(\boldsymbol{x}_l), \text{ if } c_{l-1} \leq \alpha < c_l,\ l \in [\![2, N]\!]. && \text{(V.12)}
\end{aligned}$$

In order to slightly improve the accuracy of this quantile estimator, a linear interpolation[1] is performed:

$$\hat{q} = g(\boldsymbol{x}_k) + (\alpha - c_k)\frac{g(\boldsymbol{x}_{k+1}) - g(\boldsymbol{x}_k)}{c_{k+1} - c_k}, \tag{V.13}$$

with

$$\begin{aligned}
k &= 1, \text{ if } \alpha < c_1 && \text{(V.14)}\\
&= N-1, \text{ if } \alpha \geq c_N && \text{(V.15)}\\
&= l, \text{ if } c_1 \leq \alpha < c_N. && \text{(V.16)}
\end{aligned}$$

[1] This step can be replaced by a higher order (e.g. quadratic) interpolation. Numerical experiments do not suggest its relevance.

Due to numerical robustness considerations, the linear estimator (Eq. V.13) is replaced by the simple estimator (Eq. V.12) if $|c_{k+1} - c_k| < 10^{-14}$. This IS based quantile estimation is the key of the extension of eAK-MCS for extreme quantile estimation, since it allows one to significantly decrease the CPU cost associated to the estimation of an extreme quantile, even based on a surrogate model.

V–3 The QeAK-MCS Algorithm

In this Section, we describe the QeAK-MCS algorithm, aiming at building a GP-based surrogate of G, refining it iteratively considering the estimated quantile as the critical value of the associated failure probability estimation.

The main steps can be summarized as follows (similarly to the AK-MCS based quantile estimation [Schöbi et al., 2016]):

1. *Initial DoE*: An experimental design $\mathcal{X}$ is generated by Latin-Hypercube Sampling (LHS) (See Subsection II–3.2).
2. *IS Population*: A set of N sample points $\mathcal{S} = (\boldsymbol{x}_1, ..., \boldsymbol{x}_N) \overset{\text{iid}}{\sim} f_{\mathcal{N}(0,\gamma^2 I_d)}$ is generated.
3. *Metamodel Update*: The exact response $\mathcal{Y}$ of the exact performance function G is carried out on $\mathcal{X}$. The metamodel is calibrated based on $\{\mathcal{X}, \mathcal{Y}\}$.
4. *Critical Values/Quantiles Selection*: A set of K_q quantiles $(\hat{q}_1, ..., \hat{q}_{K_q})$ is selected based on the surrogate information (See Subsection V–3.1).
5. *eAK-MCS based Samples Selection*: for each $\hat{q}_l$, $l \in [\![1, K_q]\!]$, K_p samples $(\boldsymbol{x}_1^l, ..., \boldsymbol{x}_{K_p}^l)$ are selected following the refinement step of the algorithm eAK-MCS, for the failure probability $\mathbb{P}(G(\boldsymbol{X}) < \hat{q}_l)$.
6. *Filtering Procedure and Surrogate Update*: An a posteriori filtering procedure is performed on the selected samples $\mathcal{X}^* = \{\boldsymbol{x}_j^l\}_{j \in [\![1,K_q]\!],\ l \in]\!]1,K_p]\!]}$, removing too close points: for a, b distinct samples of $\mathcal{X}^*$, if $\|a - b\|_2 < TOL$, a is discarded from $\mathcal{X}^*$. It permits to avoid samples too close to each other (preventing metamodel training issues). The selected samples $\mathcal{X}^*$ is added to the experimental design $\mathcal{X}$, and Step 3 is applied.
7. *Stopping Criterion*: If a stopping criterion is satisfied (See Subsection V–3.3), the enrichment stops. Otherwise the algorithm goes back to step 4.

V–3.1 Critical Values/Quantiles Selection

At each step of the refinement algorithm, K_q quantiles are proposed, to serve afterwards as critical values for the eAK-MCS refinement algorithm.

First, the surrogate based quantile $\hat{q}$ is estimated using IS (Eq. V.13):

$$\alpha = \mathbb{P}(\mu_{\hat{G}}(\boldsymbol{X}) < \hat{q}). \tag{V.17}$$

Note that if $K_q = 1$, the selecting quantile is simply $\hat{q}$. Bounds $\hat{q}^-, \hat{q}^+$ of the quantile estimate $\hat{q}$ are derived using the surrogate Gaussian nature, in particular the predictive standard deviation estimator:

$$\alpha = \mathbb{P}(\mu_{\hat{G}}(\boldsymbol{X}) + k\sigma_{\hat{G}}(\boldsymbol{X}) < \hat{q}^+) \tag{V.18}$$
$$\alpha = \mathbb{P}(\mu_{\hat{G}}(\boldsymbol{X}) - k\sigma_{\hat{G}}(\boldsymbol{X}) < \hat{q}^-), \tag{V.19}$$

where k sets the confidence level.

Linear Selection The approach followed in this study consists in choosing linearly K_q quantiles in $[\hat{q}^-, \hat{q}^+]$. $\forall l \in [\![1, K_q]\!]$:

$$\hat{q}_l = \hat{q}^- + (l-1)\frac{\hat{q}^+ - \hat{q}^-}{K_q - 1}. \tag{V.20}$$

Two other approaches can be considered. Based on the experience of the author, there is no clear advantage of one selection criterion than another.

Linear–α Selection Similar linear selection is conducted, considering the surrogate-based bounds α^-, α^+ associated to the failure probability with $\hat{q}$ as critical value, calculated using the IS estimator for failure probability (Eq. II.29):

$$\alpha^- = \mathbb{P}(\mu_{\hat{G}}(\boldsymbol{X}) + k\sigma_{\hat{G}}(\boldsymbol{X}) < \hat{q}) \tag{V.21}$$
$$\alpha^+ = \mathbb{P}(\mu_{\hat{G}}(\boldsymbol{X}) - k\sigma_{\hat{G}}(\boldsymbol{X}) < \hat{q}). \tag{V.22}$$

Correspondingly, K_q quantiles defined based on level linearly selected in $[\alpha^-, \alpha^+]$ are chosen. $\forall l \in [\![1, K_q]\!]$:

$$\alpha_l = \alpha^- + (l-1)\frac{\alpha^+ - \alpha^-}{K_q - 1} \tag{V.23}$$
$$\alpha_l = \mathbb{P}(\mu_{\hat{G}}(\boldsymbol{X}) < \hat{q}_l). \tag{V.24}$$

Linear–k Selection Here, a linear discretization of the range $[-k, k]$ defined by the parameter k setting the confidence interval is chosen. It yields:

$$k_l = -k + (l-1)\frac{2k}{K_q - 1} \tag{V.25}$$
$$\alpha_l = \mathbb{P}(\mu_{\hat{G}}(\boldsymbol{X}) + k_l\sigma_{\hat{G}}(\boldsymbol{X}) < \hat{q})\alpha_l \qquad = \mathbb{P}(\mu_{\hat{G}}(\boldsymbol{X}) < \hat{q}_l),\ , \forall l \in [\![1, K_q]\!]. \tag{V.26}$$

In order to always include $\hat{q}$ in the selection, the following replacement is performed once $(\hat{q}_1, ..., \hat{q}_{K_q})$ is selected.
If K_q is odd, $\hat{q}_{\frac{K_q+1}{2}} = \hat{q}$.
If K_q is even, $\hat{q}_{\frac{K_q}{2}}$ or (random selection) $\hat{q}_{\frac{K_q}{2}+1}$ is set to $\hat{q}$.

V–3.2 eAK-MCS Selection

A summary of the basics of the refinement selection of eAK-MCS (see Chapter IV) is provided, given a critical value u, selecting K_p samples for the refinement of the performance function G. For each sample $\boldsymbol{x} \in \mathbb{R}^d$, the so-called probability of misclassification $P_m(\boldsymbol{x})$ is defined as [Bect et al., 2012]:

$$P_m^u(\boldsymbol{x}) = \Phi\Big(-\frac{|\mu_{\hat{G}}(\boldsymbol{x}) - u|}{\sigma_{\hat{G}}(\boldsymbol{x})}\Big). \tag{V.27}$$

The popular U-function associated to the level u [Cadini et al., 2015, Echard et al., 2011, Schöbi et al., 2016] is defined as:

$$U^u(\boldsymbol{x}) = \frac{|\mu_{\hat{G}}(\boldsymbol{x}) - u|}{\sigma_{\hat{G}}(\boldsymbol{x})}. \tag{V.28}$$

1. 1 sample $\boldsymbol{x}_0^*$ is selected among $\mathcal{S}$ following the single eAK-MCS selection: $\boldsymbol{x}^* = \underset{\boldsymbol{x}\in\mathcal{S}}{\arg\min}\, U^u(\boldsymbol{x})$.

2. $K_q - 1$ samples $(\boldsymbol{x}_1^*, ..., \boldsymbol{x}_{K_q-1}^*)$ are simultaneously selected among the set $\mathbb{M}^{\bar{k}}(u) = \{\boldsymbol{x} \in \mathcal{Q} :\ \mu_{\hat{G}}(\boldsymbol{x}) + \bar{k}\sigma_{\hat{G}}(\boldsymbol{x}) < u \text{ and } \mu_{\hat{G}}(\boldsymbol{x}) - \bar{k}\sigma_{\hat{G}}(\boldsymbol{x}) < u\}$, using a weighted K-means clustering technique, where the weights are chosen as $P_m^u(\boldsymbol{x})$ for each sample $\boldsymbol{x} \in \mathbb{M}^{\bar{k}}(u)$. If this method returns only $K_1 < K_q - 1$ samples ($K_1 = 0$ possibly), then the very same method is applied to the full IS population $\mathcal{S}$ to provide the remaining $K_q - 1 - K_1$ samples.

V–3.3 Stopping Criterion

The stopping criterion adopted is the same as the one proposed in [Schöbi et al., 2016], focusing on the accuracy of the quantity of interest, consequently on the upper and lower bounds of the quantile:

$$\frac{\hat{q}^+ - \hat{q}^-}{q_{ref}} < \epsilon, \tag{V.29}$$

for two consecutive iteration steps, where the quantiles bounds are estimated by:

$$\alpha = \mathbb{P}(\mu_{\hat{G}}(\boldsymbol{X}) + \tilde{k}\sigma_{\hat{G}}(\boldsymbol{X}) < \hat{q}^+) \tag{V.30}$$

$$\alpha = \mathbb{P}(\mu_{\hat{G}}(\boldsymbol{X}) - \tilde{k}\sigma_{\hat{G}}(\boldsymbol{X}) < \hat{q}^-), \tag{V.31}$$

the parameter $\tilde{k}$ setting the confidence interval for the stopping criterion. Note that $\tilde{k}$ is in practice different from k used in the selection of quantiles, and $\bar{k}$ used for the selection of samples in Subsection V–3.2. q_{ref} is a positive scalar value permitting to normalize the quantile. In industrial cases, experts are likely to be able to provide such normalization constant. In the analytical benchmark functions studied here, such constant is replaced by the standard deviation of the performance function σ_G, evaluated beforehand with MCS. It is suggested in [Schöbi et al., 2016] to replace q_{ref} by the surrogate-based estimation of the standard deviation of the performance function $\sigma_{\mu_{\hat{G}}}$. According to the author experience, this approach can be misleading since at a given iteration step, the standard deviation might be highly inaccurate and severely overestimated, leading the refinement algorithm to stop prematurely.

V–3.4 Quantile eAK-MCS numerical settings

The tuning parameters mentioned in the method subsection are summarized in Table V.1 with their suggested value, used in the numerical experiments (except when explicitly mentioned).

The level α being fixed, the choice of the tuning the parameter γ has a much lower impact on the efficiency than in the eAK-MCS. A less elaborate tuning method only based on α is sufficient to obtain satisfactory results. If $\alpha > 10^{-3}$, a MC-based method is enough to obtain an accurate quantile (CoV of 1%) with a reasonable number of samples (10^7), so $\gamma = 1$ is fine. A linear law in $\log_{10}(\alpha)$ is chosen, assuming that if $\alpha = 10^{-9}$, $\gamma = 2.5$ permits satisfactory results. The rule of thumb for tuning γ is then:

$$\gamma = \max(1, \frac{1}{4}(1 - \log_{10}\alpha)) \tag{V.32}$$

$\tilde{k}$	k	$\bar{k}$	n_0	ϵ	d_{min}	K_q	K_p	TOL	ϵ	γ	N
1	3	2	$5d$	10^{-5}	$\lvert\Phi(10^{-20})\rvert \approx 9.2$	3	3	10^{-4}	5%	Eq. V.32	10^7

Table V.1 Tuning Parameters

V–3.5 Illustrative Example

To showcase the process of selecting multiple additional samples, we consider the four-branch series example introduced in Subsubsection II–3.5.3 (with $\mathbb{P}(G(X) < -4) \sim 5 \times 10^{-9}$), *i.e.* a 2D test-case characterized by two MPFPs and four failure regions, initialized with a DoE of size 10. The process of selecting $K = K_q K_p = 18$ samples is illustrated. At each step, $K_q = 3$ quantiles $(\hat{q}_1, \hat{q}_2, \hat{q}_3)$ are estimated. Note that $(\hat{q}_1 = \hat{q}^-, \hat{q}_2 = \hat{q}, \hat{q}_3 = \hat{q}^+)$, for $K_q = 3$. $K_p = 6$ samples are then selected using the eAK-MCS refinement considering $\hat{q}_i$ as the critical value, as shown in Figures V.1, V.2 and V.3 corresponding to $i = 1$, $i = 2$ and $i = 3$, respectively. For a sake of illustration, the second refinement step is shown, starting from a DoE composed of the initial DoE, and the samples added to the experimental design after the first refinement step. The size of the IS population is set here to $N = 10^5$.

Figures V.4 (a) (b) illustrate the DoE refinement step respectively before and after the metamodel update. Figure V.4 (c) represents the surrogate levels associated $\hat{q}_1$, $\hat{q}_2$ and $\hat{q}_3$.

V–4 Numerical experiments

In this Section, the capabilities of the algorithm is illustrated through its application to several test-cases. Only cases involving $\alpha \sim 10^{-5} - 10^{-9}$ are considered here, to showcase the suitability of the proposed algorithm to deal with extreme quantiles. Comparison of QeAK-MCS with examples suitable for AK-MCS are not presented for a sake of brevity since, performing similarly as would do AK-MCS [Schöbi et al., 2016] with ordinary Kriging. Very accurate estimation of a quantile on an analytical function is still a complex task, to the best of the knowledge of the author. To alleviate this issue, test-cases available in the literature in the context of very small failure probability

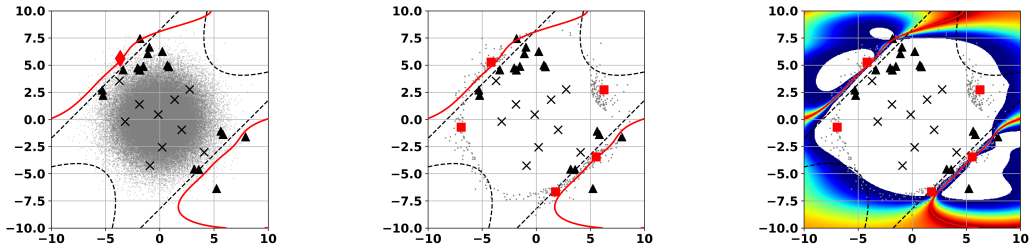

(a) Selection among $\mathcal{S}$ (b) Selection among $\mathbb{M}^{\bar{k}}(\hat{q}_1)$ (c) $P_m^{\hat{q}_1}$ Contours

Figure V.1 Refinement Illustration for $\hat{q}_1 = \hat{q}^- = -4.84$. Black crosses and triangles represent respectively the initial DoE, and the selected DoE at the first refinement step. The dashed black line represents the level $G = q$ based on the true performance function G and the exact quantile $q = -4$, the red line represents the level $\mu_{\hat{G}} = \hat{q}_1$ based on the surrogate. The diamond (a)(c) represent the selected point among the IS population $\mathcal{S}$ in grey dots (a). The squares (b)(c) represent the points selected among $\mathbb{M}^{\bar{k}}(\hat{q}_1)$ in grey dots (b), with $\bar{k} = 2$. In (c), the contours of the probability of misclassification w.r.t. the critical level $\hat{q}_1$, where blue ~ 0 and red ~ 1. For a sake of clarity, zones where $P_m < 10^{-4}$ are indicated in white. Four-branch series introduced in Subsubsection II–3.5.3, with $\mathbb{P}(G(X) < -4) \sim 5 \times 10^{-9}$.

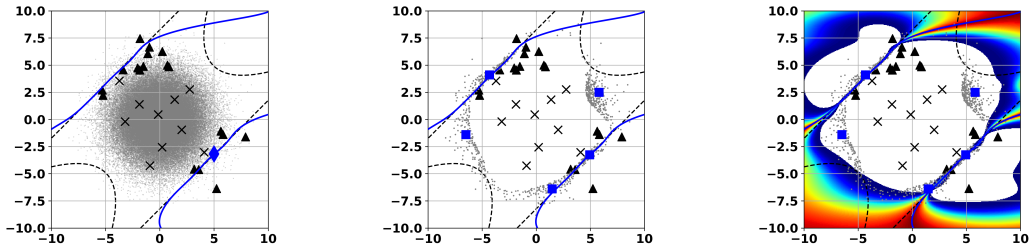

(a) Selection among $\mathcal{S}$ (b) Selection among $\mathbb{M}^{\bar{k}}(\hat{q}_2)$ (c) $P_m^{\hat{q}_2}$ Contours

Figure V.2 Refinement Illustration for $\hat{q} = \hat{q}_2 = \hat{q} = -3.99$. The blue line represents the level $\mu_{\hat{G}} = \hat{q}_2$. See Figure V.1 for legend settings. Four-branch series introduced in Subsubsection II–3.5.3, with $\mathbb{P}(G(X) < -4) \sim 5 \times 10^{-9}$.

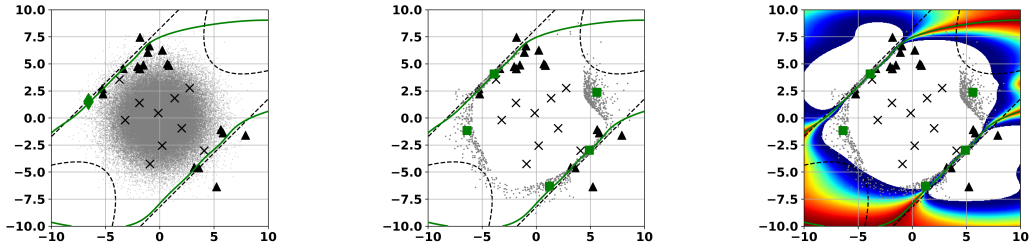

(a) Selection among $\mathcal{S}$ (b) Selection among $\mathbb{M}^{\bar{k}}(u)$ (c) $P_m^{\hat{q}_3}$ Contours

Figure V.3 Refinement Illustration for $\hat{q} = \hat{q}_3 = \hat{q}^+ = -3.66$. The green line represents the level $\mu_{\hat{G}} = \hat{q}_3$. See Figure V.1 for legend settings. Four-branch series introduced in Subsubsection II–3.5.3, with $\mathbb{P}(G(X) < -4) \sim 5 \times 10^{-9}$.

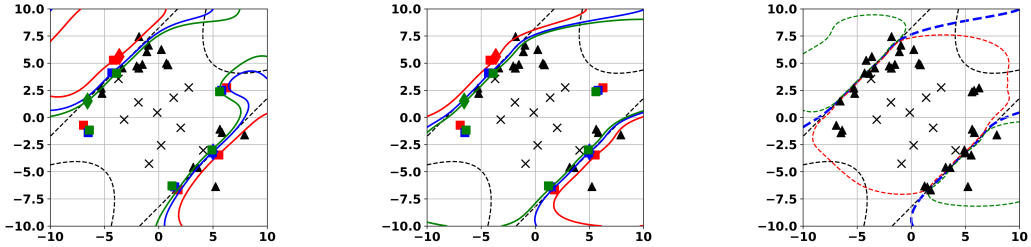

(a) Batch Selection (b) Updated Surrogate (c) Levels

Figure V.4 Illustrative Example: DoE and Surrogate. Settings in Figure V.1, with red, blue and green corresponding respectively to $\hat{q}_1$, $\hat{q}_2$, $\hat{q}_3$. Figure (c) represent the contours for $\mu_{\hat{G}} = q$, $\mu_{\hat{G}} + 2\sigma_{\hat{G}} = q$ and $\mu_{\hat{G}} - 2\sigma_{\hat{G}} = q$ represented respectively in blue, green and red dashed lines. Four-branch series introduced in Subsubsection II–3.5.3, with $\mathbb{P}(G(X) < -4) \sim 5 \times 10^{-9}$.

are considered: the reference quantile is hence the critical value of the problem of interest, while the level α is fixed to the failure probability very accurately estimated (CoV $< 0.05\%$), using either SS [Bect et al., 2017] or IS with a Gaussian mixture (Section III–3.2).

A classic 2D *single failure region* example and the three examples (2D and 6D) studied by Bect in [Bect et al., 2017], specifically designed for assessing very small failure probabilities ($\sim 10^{-8} - 10^{-9}$) using BSS are considered (Subsubsections II–3.5.1 II–3.5.3 II–3.5.5 II–3.5.6). To the best of the knowledge of the author, no other method is suitable for those challenging problems, hence QeAK-MCS is not compared against literature.

An analysis with $K_q K_p = 9$ ($K_q = K_p = 3$) samples selected at each refinement step is performed.

To assess the statistical significance of the proposed method (due to its stochastic nature), each test case is studied based on 50 independent runs. The number of calls N_{calls} to the performance function, the number of iterations N_{iter}, the estimation of the quantile $\hat{q}$, and the final *relative* error $\epsilon_q = \dfrac{|\hat{q} - q|}{q_{ref}}$ are consequently random variable illustrated by their empirical average. Note that for some analytical examples studied here, the true quantile q is null, so the classic relative error is not a suitable option. q_{ref} is chosen here as the standard deviation of the performance function σ_G, estimated on the analytical function using MCS with 10^7 samples. The initial DoE is supposed to be evaluated in 1 iteration. In the context of multiple independent runs, the CoV of $\hat{q}$, estimated from its realizations, is an indicator of the robustness of the method. The lowest is the CoV, the more likely is the algorithm to return an estimation of $\hat{q}$ which is closed to its asymptotic average. The tuning parameters are the ones provided in Table V.1. The average CoV of the estimation of the failure probability $\mathbb{E}[CoV[\hat{\alpha}]]$ based on IS (Eq. II.31) is also given in order the quantify the quality the IS procedure based on the ISD $f_{\mathcal{N}(0,\gamma^2 I_d)}$, hence the accuracy of the estimated quantile $\hat{q}$ based on the sampling procedure. It is worthy to point out that the latter is independent of the surrogate accuracy.

For each case, figures showing the average *relative* error ϵ_q, and the average estimate $\hat{q}$ as a function of the number of performance function calls are provided, where additional samples are added even after the stopping criterion is met, for a sake of illustration. The $2-\sigma$ confidence interval is represented with black dashed lines.

Since the parallel strategy refinement might propose strictly less than $K+1=8$ samples due to the *a posteriori* filtering procedure, a post-processing involving a linear interpolation procedure on ϵ_q and $\hat{q}$ is required at the end of the 50 runs. For two-dimensional examples, an illustration of the final DoE and refined metamodel is also provided, when the convergence criterion is satisfied, based on a single run.

V–4.1 Single Failure Region 2D

This single failure region example is introduced in Subsubsection II–3.5.1. In Table V.2, we compare the reference with the results of QeAK-MCS, based on 50 independent runs. For all runs, the algorithm QeAK-MCS stops after 1 refinement step (9 samples added to the initial DoE), yielding a very accurate estimate of the quantile, the average relative error being below 0.05%.

An illustration is provided in Figure V.5(a), showing the refined metamodel for a single run. The DoE selected is well clustered around the True LSS $G=q$, showing that both the quantile $\hat{q}$ and the surrogate are well estimated. This is further illustrated in the quantile history Figure V.5 (c) where the $2-\sigma$ confidence interval of $\hat{p}_{\tilde{f}}$ rapidly merge and converge toward the reference value. The relative error history Figure V.5 (b) demonstrates the convergence behaviour of the method in that case, where the mean error is below 0.01% after 60 calls. This convergence behavior is confirmed by the very low mean CoV of the failure probability estimate based on IS $\mathbb{E}[CoV[\hat{\alpha}]]$, which assesses the efficiency of the ISD is that low dimensional case. The method in that case is also very robust, with CoV$[\hat{q}]$<0.05%, which is further demonstrated with the $2-\sigma$ confidence interval rapidly merging to the reference value Figure V.5 (b).

The original function being a second order polynomial easily captured by the metamodel, this example is rather simple since also characterized by a single failure region and a low dimensionality. The low value of $\epsilon_{p_f}^{rel}$ can be explained by both the good quality of the surrogate, and the accuracy of the quantile based on the IS sampling method, illustrated by the low $\mathbb{E}[CoV[\hat{\alpha}]]$.

Table V.2 Results of the Single Failure Region 2D.

Method	$\mathbb{E}[N_{calls}]$	$\mathbb{E}[N_{iter}]$	$\mathbb{E}[\hat{q}]$	CoV$[\hat{q}]$	ϵ_q	$\mathbb{E}[CoV[\hat{\alpha}]]$
Reference[a]	10^7	-	0	-	0	$<0.04\%$
QeAK-MCS[b]	19.0	2.0	-1.023×10^{-3}	0.03%	0.02%	0.44%

Solving $\mathbb{P}(G(\boldsymbol{X})<\hat{q})=2.874\times10^{-5}$, with $q_{ref}=\sigma_G=121.334$.

[a] Reference: IS with a Gaussian mixture as ISD (Section III–3.2), 50 independent runs. CoV $<0.04\%$

[b] Initial DoE size: 10. 9 samples iteratively added. Based on 50 independent runs.

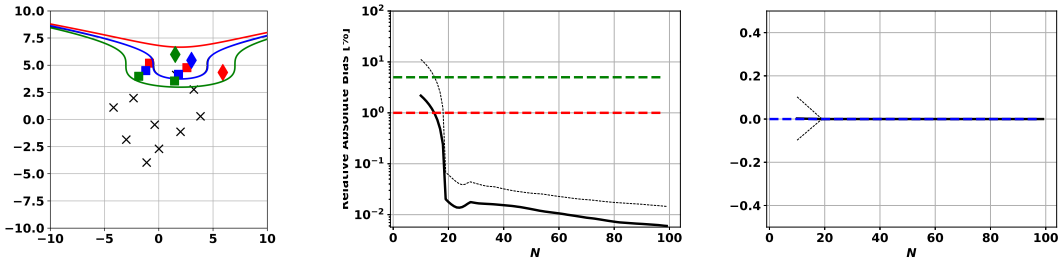

(a) Metamodel (b) *Relative* Error History (c) $\hat{q}$ History

Figure V.5 Results of the Single Failure Region 2D.
(a) Legend Settings in Figure V.4.
(b) Green and red thick dashed lines indicate respectively 5% and 1% relative error. The y-axis is logarithmic. The average relative error bias and the associated $2-\sigma$ confidence intervall are represented respectively in black thick line and black thin dashed lines.
(c) The normalized *predicted* quantile $\hat{q}$ and the associated $2-\sigma$ confidence intervall are represented respectively in black thick line and black thin dashed lines.

V–4.2 Four-branch series system 2D

This benchmark example characterized by two MPFPs, four failure domains and a very small failure probability ($\sim 5.6 \times 10^{-9}$) is introduced in Subsubsection II–3.5.3 ($u = -4$). It indeed represents a very challenging case, albeit low dimensional. The results are presented in Table V.3 and Figure V.6. QeAK-MCS stops after $\sim$ 99 calls ($\sim$ 11 iterations) in average, resulting in an very accurate and robust result, with respectively a mean relative error of 0.57% and a CoV of $\hat{q}$ of 0.82%. As seen in Figure V.6 (a), the True LSS is well estimated by the predicted LSS in the region characterized by high density of input distribution, where the ability of the surrogate to classify samples into the safe/unsafe domain is the most sensitive. Note also that in that zone, the upper/lower predicted LSS match the predicted LSS, indicating high predictability and the presence of DoE clustered in that zone. Figures V.6 (b) (c) illustrate respectively the average relative error and the quantile estimate history as a function of the number of performance calls, with corresponding $2-\sigma$ confidence intervall. One can note that after, in average 10 function calls (4-5 iterations), the average predicted quantile $\hat{q}$ is already of the same order of magnitude of the reference value, and the convergence is then rather fast, with a mean relative error lower that 1% after $\sim$ 90 function calls ($\sim$8 iterations). The average CoV associated to the IS estimate of the corresponding failure probability $\mathbb{P}(\mu_{\hat{G}} < \hat{q})$ is still low for this two-dimensional case, about 0.95 %. It illustrates the efficiency of the IS method with the Gaussian ISD $\mathcal{N}(0, \gamma^2 I_d)$ in this case, which translates in an accurate estimate of the quantile, for a given surrogate accuracy, which is confirmed by the convergence trend of the relative error which decreases as the surrogate is refined.

V–4.3 Deviation of a Cantilever Beam 2D

This two-dimensional example is characterized by a single failure region, with $p_f \sim 4 \times 10^{-6}$ and introduced in Subsubsection II–3.5.5. The results are presented in Table V.4 and Figure V.7. The eAK-MCS algorithm stops after $\sim$ 29 calls in average (3 iter-

Table V.3 Results of the Four-branch series system 2D.

Method	$\mathbb{E}[N_{calls}]$	$\mathbb{E}[N_{iter}]$	$\mathbb{E}[\hat{q}]$	CoV$[\hat{q}]$	ϵ_q	$\mathbb{E}[CoV[\hat{\alpha}]]$
Reference[a]	10^7	-	-4	-	0	$< 0.05\%$
QeAK-MCS[b]	98.4	10.9	-3.999	0.82%	0.57%	0.95%

Solving $\mathbb{P}(G(\boldsymbol{X}) < \hat{q}) = 5.596 \times 10^{-9}$, with $q_{ref} = \sigma_G = 0.6265$.

[a] Reference: SS [Bect et al., 2017], 100 independent runs. CoV $< 0.05\%$.

[b] Initial DoE size: 10. 9 samples iteratively added. Based on 50 independent runs.

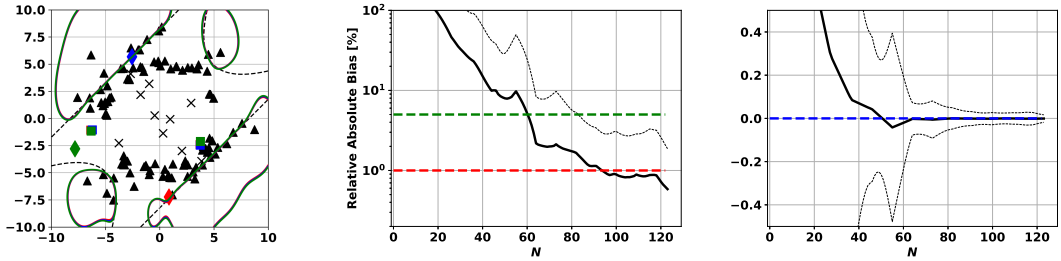

(a) Metamodel (b) *Relative* Error History. (c) $\hat{q}$ History

Figure V.6 Results of the Four-branch series system 2D. Legend Settings in Figure V.5.

ations), yielding a mean relative error lower than 1.2% at the end of the refinement algorithm, whose robustness is quantified by the final low CoV of $\hat{q}$<1.5%. Figure V.7 (b) shows that the average relative error is below 10% after one refinement step ($\sim$ 19 calls), which explains the sharp decrease to 0 of the mean normalized $\hat{q}$ in Figure V.7 (c). For a sake of illustration, the history is truncated to 35 calls. Indeed, for few runs characterized by very accurate metamodels, the enrichment algorithm proposes candidates that are too close to the existing DoE to be accepted, and the algorithm stops. The IS based quantile estimation shows a good efficiency, the average CoV of the failure probability estimated with IS being low $\mathbb{E}[CoV[\hat{\alpha}]] \sim 0.51\%$.

The final metamodel is represented V.7 (a).

Table V.4 Results of the Deviation of a Cantilever Beam 2D.

Method	$\mathbb{E}[N_{calls}]$	$\mathbb{E}[N_{iter}]$	$\mathbb{E}[\hat{q}]$	CoV$[\hat{q}]$	ϵ_q	$\mathbb{E}[CoV[\hat{\alpha}]]$
Reference[a]	10^7	-	$\sim -1.84615 \times 10^{-2}$	-	0	$< 0.04\%$
QeAK-MCS[b]	28.8	3.1	-1.84631×10^{-2}	1.44%	1.17%	0.51%

Solving $\mathbb{P}(G(\boldsymbol{X}) < -\frac{6}{325}) = 5.596 \times 10^{-9}$, with $q_{ref} = \sigma_G = 1.1501 \times 10^{-3}$.

[a] Reference: SS [Bect et al., 2017], 100 independent runs. CoV $< 0.04\%$.

[b] Initial DoE size: 10. 9 samples iteratively added. Based on 50 independent runs.

V–4.4 Response of a Nonlinear Oscillator 6D

The results for this six-dimensional example (introduced Subsubsection II–3.5.6) characterized by $\alpha \sim 1.5 \times 10^{-8}$ are presented in Table V.5 and Figure V.8. This example, due to the higher dimensionality and the very low level of the quantile sought, is rather

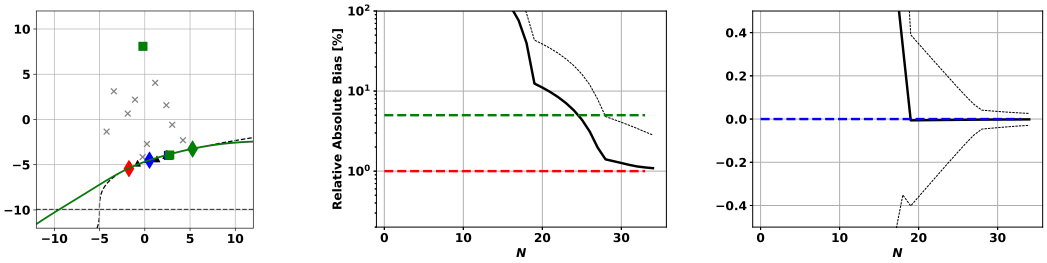

(a) Metamodel (b) *Relative* Error History. (c) $\hat{q}$ History

Figure V.7 Results of the Deviation of a Cantilever Beam 2D. Legend Settings in Figure V.5.

challenging. Interestingly, QeAK-MCS performs very well here, the algorithm stopping in average after ~ 41 calls (~ 2.2 iterations), which corresponds to 1 or 2 refinement steps only. The estimated quantile returned is subjected to a mean relative error of $\sim 1\%$, in a robust way with a CoV on $\hat{q}$ of $\sim 1.4\%$, which is remarkable. A look on the history of the mean relative error and $\hat{q}$ in Figures V.8 (a) and (b) respectively shows that the estimated quantile rapidly converge to the solution. The mean relative error reaches a plateau as the surrogate is refined, contrary to the other 2D examples for which it kept decreasing. This behavior can be explained by a deteriorated efficiency of the Gaussian ISD for the IS quantile estimation of the surrogate, for which the mean CoV of the failure probability estimator $\mathbb{E}[CoV[\hat{\alpha}]]$ is rather large, 2.52%, limiting the accuracy of the quantile based on the surrogate, independently of the latter's accuracy. This tendency would confirm the quality of the refinement algorithm proposed and the one of the final surrogate, even if this IS procedure cannot permit in this higher dimensional case to extract very accurately the quantile. This behavior also confirms a tendency observed in the related eAK-MCS example (Chapter IV), for which the surrogate itself seems accurate, but the Gaussian ISD could not permit to extract a highly accurate failure probability, despite an apparently accurate surrogate.

Table V.5 Results of Response of a Nonlinear Oscillator 6D.

Method	$\mathbb{E}[N_{calls}]$	$\mathbb{E}[N_{iter}]$	$\mathbb{E}[\hat{q}]$	CoV$[\hat{q}]$	ϵ_q	$\mathbb{E}[CoV[\hat{\alpha}]]$
Reference[a]	-	-	0	-	0	$< 0.05\%$
QeAK-MCS[b]	41.2	2.2	-2.46×10^{-4}	1.39%	1.01%	2.52%??

Solving $\mathbb{P}(G(\boldsymbol{X}) < \hat{q}) = 1.514 \times 10^{-8}$, with $q_{ref} = \sigma_G = 0.18267$.

[a] Reference: SS [Bect et al., 2017], 100 independent runs. CoV $< 0.05\%$.

[b] Initial DoE size: 30. 9 samples iteratively added. Based on 50 independent runs.

V–5 Conclusion

This study proposes an extension of AK-MCS as presented in [Schöbi et al., 2016] to make it suitable for the estimation of extreme quantiles. It uses a centered uncorrelated Gaussian distribution to sample candidate points and uses the IS method to estimate the quantile. The refinement algorithm of eAK-MCS permits to select candidate points to the DoE, based of the quantiles estimates. A parallel quantile selection

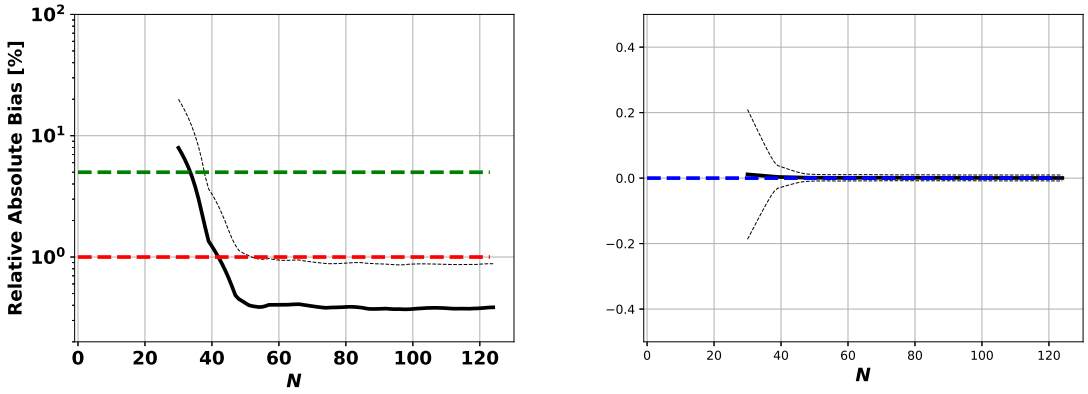

(a) *Relative* Error History

(b) $\hat{q}$ History

Figure V.8 Results of Response of a Nonlinear Oscillator 6D. Legend Settings in Figure V.5.

(also suitable for quantile estimation in the scope of [Schöbi et al., 2016]) is also proposed. The performance of the proposed algorithm is assessed and illustrated through some benchmark analytical functions, showcasing very satisfactory accuracy (relative error below $\sim 1\%$) and robustness (CoV$[\hat{q}] < 1.5\%$), in less than 100 evaluations of the original model, in average.

To the knowledge of the author, there is no algorithm in the literature able to estimate accurately such low quantiles, especially in problems with LSS characterized by multiple failure modes.

The first classic limitation of the method is inherent to the GP-surrogate itself: low dimensionality and moderate size of the DoE. It also depends on its ability to fit the performance function G. The second limitation is in the physical input distribution, that needs to be accurately mapped onto the standard space. The last concerns the accuracy of the IS-based quantile estimation: it strongly depends on the ability of the Gaussian ISD $f_{\mathcal{N}(0,\gamma^2 I_d)}$ to reduce the variance when estimating the failure probability $\hat{\alpha}$ based on the estimated quantile. The same problem occurs even when evaluating a reference value with an analytical function based on a given small quantile level α. This IS quantile estimation is expected to deteriorate as the input dimension rises, as identified in the 6D-oscillator example: the relative error reaches a stagnation value as the number of samples increases. Indeed, the IS CoV of α is significantly larger ($\sim 2.52\%$) than in the two-dimensional cases considered. This represents the main axis of improvement for the present method.

This work also illustrates the main advantage of the eAK-MCS method, as an extension of AK-MCS for the estimation of very small failure probabilities for which several algorithms are based and could be adapted in this context: quantile-based optimization [Moustapha et al., 2016] or quantile estimation [Schöbi et al., 2016] presented here. The key of this adaptation basically consisted on an IS based quantile estimation from the surrogate at a reasonable number of evaluations. A last contribution of this study is the proposition of parallel quantile selection that could also be applied for quantile estimation ($\alpha > 10^{-4}$) using the classic AK-MCS [Schöbi et al., 2016].

Part B

Robust Optimization Methods for ORC Turbine Cascade

Overview *This part aims at applying original* Robust Design Optimization *(RO) methods to the Shape Design of a supersonic ORC Turbine cascade. In particular, a comprehensive UQ analysis accounting for operational, fluid parameters and geometric (aleatory) uncertainties permits to provide a general overview over the impact of multiple effects and constitutes a preliminary study necessary for RO. Moreover, a failure scenario is analyzed by applying one of the methods illustrated in the first part of the manuscript. Several mono-objective RO formulations are considered in this work, including minimizing the mean or minimizing a high quantile of the* Objective Function. *(Robust) Optimal profiles are compared with each other, in terms of PDFs to account for the underlying variability of the input appropriately.* Deterministic Optimization *(DO) is also performed to showcase the advantages of RO over DO. The impact of the RO formulation is also investigated.*

Contribution *This work constitutes the basis of two journal articles (1 published, 1 submitted):*

1. *N. Razaaly, G. Gori, G. Persico, P.M. Congedo, Quantile-based robust optimization of a supersonic nozzle for Organic Rankine Cycle turbine, Submitted, April 2019.*

2. *N. Razaaly, G. Persico, P.M. Congedo, Impact of geometric, operational, and model uncertainties on the non-ideal flow through a supersonic ORC turbine cascade, Energy, Volume 169, Pages 213-227, 2019.*

Outline

This second Part is organized as follows. Chapter VI describes the models used for the simulation of the ORC turbine, including the governing equations, the blade parametrization, the numerical solver, the mesh deformation tool and the modeling of geometric uncertainties. In Chapter VII, several UQ analyses are carried out, studying the impact of different physical models and operational, model parameters and geometric uncertainties. It includes a reliability analysis applying the method for *unbiased* failure probability estimation MetaAL-OIS presented in Chapter III. In Chapter VIII, a mono-objective quantile-based RO approach is investigated illustrating its interest w.r.t. DO, and is compared to the classical formulation consisting of minimizing the mean of the objective function.

VI

ORC Turbine Cascade: Physical Model

Overview *This chapter introduces the turbine configuration of interest which is a well known axial-flow supersonic nozzle cascade operating with siloxane MDM, first presented in [Colonna et al., 2008]. The numerical framework including, the CFD solver, the parametrization and mesh tools, is described.*

Contribution *This chapter does not feature any original contribution w.r.t. the literature.*

Introduction

In the manuscript, the targeted ORC nozzle is the geometry of an existing ORC nozzle designed for a 300 kWe *Combined-Heat-and-Power* (CHP) axial turbogenerator employing siloxane MDM as working fluid and the combustion of biomass as a primary energy source. This supersonic axial-flow turbine stator characterized by converging-diverging blades features significant fluid-dynamic penalties due to a strong shock-wave forming on the rear suction side of the blade. This exemplary profile, originally presented in [Colonna et al., 2008] has been chosen because it is representative of typical difficulties encountered for cascade design in ORC turbines. It has been indeed extensively studied in the open literature of ORC, in particular, subject to several optimization trials in recent years [Pini et al., 2015, Rodriguez-Fernandez and Persico, 2015, Vitale et al., 2017]. The profile above is studied from an UQ and optimization under uncertainties perspective.

This Chapter describing the numerical framework associated to the ORC Turbine nozzle application [Colonna et al., 2008] is organized as follows. The governing equations and the numerical open-source solver SU2 permitting to compute the QoIs are

described in Section VI–1. A concise description of the thermodynamic model is provided in Section VI–2. The geometry parametrization based on B-splines is presented in Section VI–3. The baseline configuration is studied in Section VI–4, the mesh tools are finally exposed in Section VI–5.

VI–1 Governing equations and Flow Solver

The *Non-Ideal Computational Fluid Dynamics* (NICFD) solver included in the open-souce SU2 [Palacios et al., 2013, Economon et al., 2016, Pini et al., 2016, Palacios and al, 2014, Vitale and al, 2015] suite is employed to carry out the numerical analysis presented in this work. The reliability of solver predictions against experiments performed in a supersonic nozzle for organic vapours [Spinelli et al., 2018] was assessed in [Gori et al., 2017]. The SU2 NI-CFD solver relies on an embedded thermodynamic library which includes several *Equations Of State* (EOS) such as the *Van der Waals* (VdW) and the *Peng-Robinson-Stryjek-Vera* (PRSV) ones.

In the following, a brief overview of the main features of a NICFD solver are highlighted.

The three-dimensional Navier-Stokes equations for compressible flows read

$$\frac{\partial \mathbf{u}}{\partial t} + \nabla \cdot \mathbf{f}(\mathbf{u}) = \nabla \cdot \mathbf{d}(\mathbf{u}). \tag{VI.1}$$

The vector of the conserved variables $\mathbf{u} = (\rho, \mathbf{m}, E^t)^T$ includes the mass density $\rho \in \mathbb{R}^+$, the three components of momentum density $\mathbf{m} \in \mathbb{R}^3$, and the total specific energy $E^t \in \mathbb{R}^+$:

$$E^t = \rho\left(e + \frac{1}{2}||\mathbf{v}||^2\right), \tag{VI.2}$$

where e is the specific internal energy while $\mathbf{v} = \mathbf{m}/\rho$ is the velocity vector.

The function representing the advection and pressure fluxes reads

$$\mathbf{f}(\mathbf{u}) = [\mathbf{m}, (\mathbf{m} \otimes \mathbf{m})/\rho + P\mathbf{I}, \mathbf{m}(E^t + P)/\rho]^T, \tag{VI.3}$$

while the viscous and thermal fluxes are represented by the function

$$\mathbf{d}(\mathbf{u}) = [\mathbf{0}, \mathbf{\Pi}, \mathbf{v}^T \cdot \mathbf{\Pi} - \mathbf{q})]^T, \tag{VI.4}$$

with $\mathbf{d}(\mathbf{u}) \in \mathbb{R}^{5\times 3}$. In these latter functions, $P = P(\mathbf{u})$ is the pressure, $\mathbf{I}$ is the identity matrix of dimension 3, $\mathbf{\Pi} = \mathbf{\Pi}(\mathbf{v})$ is the viscous stress tensor and $\mathbf{q}$ is the thermal flux.

The system of equations is supplemented by constitutive relations that bound the state of the fluid to the thermodynamic and to the transport quantities. For a single-component fluid in single-phase conditions, two EoS are needed and provide the functional dependency of a state variable from any given pair of independent variables, for instance in the form of $P = P(T, v)$ and $e = e(T, v)$. These relations are invertible and therefore the functional forms $T = T(P, v)$ or $v = v(T, e)$ also exist. The structure of the numerical solver is strictly related to these functional relations. From a numerical perspective, when the Ideal Gas EoS is employed a set of simplifications are possible. When more complex EoS are considered, a generalized approach is needed.

The extension of the SU2 solver to make it suitable for NICFD is described in [Vitale et al., 2015].

Besides the structural changes required to accommodate the more complex EoS, NICFD solver must comply with the fulfillment of an additional consistency equation [Guardone and Vigevano, 2002a]:

$$\tilde{\chi}_{ij}(\rho_i - \rho_j) + \tilde{\kappa}_{ij}(\rho_i e_i - \rho_j e_j) = (P_i - P_j), \tag{VI.5}$$

where the pressure derivatives $\tilde{\chi}_{ij}$ and $\tilde{\kappa}_{ij}$, are defined as:

$$\chi = \left(\frac{\partial P}{\partial \rho}\right)_{\rho e} = \left(\frac{\partial P}{\partial \rho}\right)_{e} - \frac{e}{\rho}\left(\frac{\partial P}{\partial e}\right)_{\rho} \quad \text{and} \quad \kappa = \left(\frac{\partial P}{\partial \rho e}\right)_{\rho} = \frac{1}{\rho}\left(\frac{\partial P}{\partial e}\right)_{\rho}. \tag{VI.6}$$

According to Boussinesq, in the *Reynolds-Averaged Navier-Stokes* (RANS) equations the contribution of the so-called *turbulence* or *eddy* viscosity and of the turbulent thermal conductivity must be taken into account. Therefore, the transport coefficients μ, λ and κ, upon which the viscous stress tensor and the thermal fluxes depends on, must include also a turbulent contribution.

The SU2 framework relies on a standard edge-based structure. Starting from the original mesh, a dual grid is constructed using a median-dual vertex-based scheme. The semi-discretized integral form of PDE Equation VI.1 over the dual domain reads:

$$\int_{\Omega_i} \frac{\partial U}{\partial t}\, d\Omega + \sum_{j \in \mathcal{N}(i)} (\tilde{F}_{c_{ij}} + \tilde{F}_{v_{ij}}) \Delta S_{ij} - Q|\Omega_i| = \int_{\Omega_i} \frac{\partial U}{\partial t}\, d\Omega + R_i(U) = 0. \tag{VI.7}$$

In Eq. VI.7, $R_i(U)$ is the residual term while $\tilde{F}_{c_{ij}}$ and $\tilde{F}_{v_{ij}}$ represent the projected numerical approximations of the convective and viscous fluxes, respectively. ΔS_{ij} is the area of the face associated with the edge ij while Ω_i is the volume of the element. The $\mathcal{N}(i)$ index is related to the nodes surrounding node i. Following a standard practice, the convective and viscous fluxes are computed at the midpoint of each edge.

To increase the first-order accuracy of the numerical scheme, and to obtain a second-order accuracy in smooth flow regions, the SU2 solver relies on a limited construction of the flow variable, according to the MUSCL approach. Different flux limiters are available in SU2, to avoid the occurrence of spurious oscillations due to shocks and discontinuities typically occurring when second order-accurate schemes are employed.

In the analysis presented hereinafter, the inviscid fluxes are discretized using a second order approximate Riemann solver (ARS) of Roe upwind type [Roe, 1981, Vinokur and Montagné, 1990, Guardone and Vigevano, 2002b] along with the slope limiter proposed by van Albada; central differences are used for the viscous terms. The combination of such schemes guarantees high resolution in the numerical solution of the system of equations.

To retrieve the effects of turbulence in RANS simulations, the Menter's k-ω *Shear Stress Transport* (SST) [Menter, 1993] model is used, for its capability of resolving the near-wall region of the boundary layer as well as the free-stream region, making it widespread in turbomachinery applications.

As no wall functions are used, the near-wall region of the boundary layer is solved entirely by the simulation. To ensure a proper resolution in the near-wall region, the height of the first cell of the boundary layer grid was set to be equal to $\approx 2 \cdot 10^{-7}$, corresponding to a y^+ value lower than 1. The y^+ value was evaluated considering the

dynamic viscosity value assumed for the whole domain, and given in Table VI.1; the considered values of stream velocity and density are instead the ones resulting from simulations at the exit of the cascade, the reference length being the blade chord.

The SU2 suite is also equipped with *Non-Reflecting Boundary Conditions* (NRBC) [Giles, 1990] which are exploited throughout this work. NRBC are designed to avoid spurious pressure oscillations due to the reflection of pressure waves at the domain boundaries, and it is of particular relevance for the present study due to the strong shocks that establish downstream of the supersonic cascade.

VI–2 Working fluid and Thermodynamic model

The operating fluid is the siloxane (silicon oil) named octamethyltrisiloxane (MDM), whose properties are reported in Table VI.1 (γ, μ and k denote respectively the heat capacity ratio, the dynamic viscosity and the thermal diffusivity). Note that this working fluid is currently investigated during an on-going experimental campaign in Politecnico di Milano.

Concerning the thermodynamic model, a polytropic assumption is made, assuming constant heat capacity ratio: $\gamma = \frac{c_p}{c_v}$, c_p and c_v denoting the specific heat capacity at constant pressure and volume, respectively. The PRSV [Vitale and al, 2015] EOS is used to describe the thermodynamic behavior. The EOS constituted by two relations depending on the temperature T and the specific volume v is given hereafter:

$$\begin{aligned} \rho(T,v) &= \frac{rT}{v-b} - \frac{a\alpha^2(T)}{v^2+2bv-b^2} \\ e(T,v) &= c_v T - \frac{a\alpha(T)(k+1)}{b\sqrt{2}} \tanh^{-1}\left(\frac{b\sqrt{2}}{v+b}\right), \end{aligned} \tag{VI.8}$$

where

$$\begin{aligned} a &= 0.45724\frac{(rT_c)^2}{P_c} \\ b &= 0.0778\frac{rT_c}{P_c} \\ \alpha(T) &= 1+k\left(1-\sqrt{\frac{T}{T_c}}\right) \\ k &= 0.37464+1.54226\omega-0.26992\omega^2, \text{ if } \omega \le 0.49 \\ &= 0.379642+1.48503\omega-0.164423\omega^2+0.016666\omega^3, \text{ if } \omega > 0.49. \end{aligned} \tag{VI.9}$$

T_c, P_c denote respectively the critical temperature and pressure, and ω the acentric factor.

Uniform thermo-physical quantities are assigned, estimated as representative values for the entire transformation by resorting to the RefProp library. The inlet turbulent parameters are assigned considering a typical turbomachinery environment, namely a turbulence intensity of 3% and a turbulent-to-molecular viscosity ratio of 100.

Critical pressure	14.152 bar
Critical temperature	564.1 K
Critical density	256.82 $kg.m^{-3}$
γ	1.0165
Acentric factor ω	0.529
Gas constant	35.152 J/kg/K
μ	1.1517×10^{-5} Pa.s
k	0.03799 W/(m.K)

Table VI.1 Gas properties of the siloxane MDM

VI–3 Geometry Parametrization

In order to reconstruct the 2D blade profile employing a minimum number of variables, a unique B-spline curve is used to parametrize both pressure and suction sides of the cascade. An exhaustive description of B-splines curves/surfaces can be found in [Hoschek et al., 1993] [Farin, 2002]. The approach follows the one successfully applied in [Rodriguez-Fernandez and Persico, 2015]. The trailing edge is considered separated from the B-spline, which therefore has to be constrained to pass by the two control points that define the trailing edge, and is assumed to be a circular arc.

Notations Note that some variables introduced in this section, *i.e.* n, k, P, p, N, x, are indicated with a specific notation, not used elsewhere in the manuscript.

A B-spline curve $p(t)$ of degree n can be written as

$$p(t) = \sum_{i=0}^{n} N_{i,k}(t)\mathbf{a}_i, \tag{VI.10}$$

where $\mathbf{a}_i$ denotes the i-th control point (CP) with $i \in [\![0, n]\!]$. $N_{i,k}(t)$ is the corresponding $k-1$ degree polynomial B-Spline basis function, defined recursively by:

$$\begin{aligned} N_{i,1}(t) &= \mathbf{1}_{[t_i, t_{i+1}]}(t) \\ N_{i,k}(t) &= \frac{t - t_i}{t_{i+k-1} - t_i} N_{i,k-1}(t) + \frac{t_{i+k} - t}{t_{i+k} - t_{i+1}} N_{i+1,k-1}(t), \end{aligned} \tag{VI.11}$$

where $\{t_j\}_{j \in [\![0, n+k]\!]}$ denotes the increasing so-called knot sequence, and $t \in [t_{k-1}, t_{n+1}]$ is a scalar parameterizing the B-Spline curve.

Properties Some properties on B-splines are recalled:

- Polynomial Degree: $p(t)$ is a k degree polynomial curve on $]t_i, t_{i+1}[$.
- Regularity at junction points: $p(t)$ is $\mathcal{C}^{k-2}$ at junction points $p(t_i)$.
- Influence Range: CP $\mathbf{a}_i$ affects $p_{[t_i, t_{i+k}]}$.
- Local Control Property: $p_{[t_i, t_{i+1}]}$ is influenced by the k CP $(\mathbf{a}_{i-k+1}, ..., \mathbf{a}_i)$.

Baseline Approximation The first step is to approximate by a B-Spline curve the baseline geometry represented by $P+1$ data points p_l.
The polynomial degree k, the number of CP and the knot sequence $\{t_j\}_{j\in[\![0,n+k]\!]}$ are user defined.
The CP $\mathbf{a}_i$ can then be estimated minimizing the approximation error defined by:

$$f(x) = \sum_{l=0}^{P} \|p_l - x(\omega_l)\|^2, \tag{VI.12}$$

where x is the B-Spline curve obtained for a given set of control points $\{\mathbf{a}_i\}$. The sequence $\{\omega_l\}$ is computed as the curvilinear abscissae of the points $\{p_l\}_{l\in[\![0,P]\!]}$. $\|.\|$ is the Euclidian distance. Rewriting equation VI.12 using VI.10 results in a least squares minimization problem whose resolution leads to a linear symmetric system, composed by the following $n+1$ relations:

$$\sum_{i=0}^{n} \mathbf{a}_i \sum_{l=0}^{P} N_{i,k}(\omega_l) N_{j,k}(\omega_l) = \sum_{l=0}^{P} N_{j,k}(\omega_l) p_l, \ j \in [\![0, n+1]\!]. \tag{VI.13}$$

Each dimensional component of $\mathbf{a}_i$ can be solved independently, by means of Cholesky Decomposition for example. The B-Spline curve is constrained to pass through the first and last data points to create a closed curve along with the circular-shape trailing edge. $\mathcal{C}^{k-2}$ regularity is ensured by imposing the first (resp. last) data point to match the first CP $\mathbf{a}_0$ (resp. last CP $\mathbf{a}_n$) by selecting a knot sequence with a so-called multiplicity k at end points, namely $t_0 = ... = t_{k-1}$ (resp. $t_{n+1} = ... = t_{n+k}$).

Choice of knot sequence and impact on parametrization The knot sequence spacing, namely $\{t_{j+1} - t_j\}_{j\in[\![0,n+k-1]\!]}$, regulates the spacing between the control points, and is chosen following several guidelines:

1. to limit the geometrical error in the reconstruction;
2. to exploit the non-uniform distribution of CPs, reducing the distance between the CPs in regions of higher curvature;
3. to limit the CP number in interesting areas for the optimization, thus reducing the design dimension.

In this work, $n+1 = 30$ CP points are chosen and $k = 3$, resulting in $\mathcal{C}^1$ regularity at junction points and $p(t)$ is polynomial curve of degree 3 on $[t_i, t_{i+1}]$. 9 CPs are allowed to move in the direction normal to the blade (Figure VI.1), within a predefined range aimed at preventing unfeasible designs and mesh-deformation issues, while ensuring high design flexibility. Note that the displacements of the 4 CPs closest to the trailing edge are linked each other, so that only one CP is movable and the other ones move rigidly with the former; this allows reducing the design dimension while keeping constant geometrical parameters like the thickness and the wedge angle that are important for the structural integrity of the blade.

Fit the parametrization $\bar{\omega}_l$ Once the optimal CP positions $\mathbf{a}_i$ are evaluated solving Equation VI.13 based on an initial set (possibly large) of data points p_l representing the baseline, the sequence $\bar{\omega}_l$ has to be recovered to match the new set of points $\{\bar{p}_l\}_{l\in[\![0,\bar{P}]\!]}$ defining the blade geometry in the mesh used for optimization purpose. A 1D optimization problem has to be solved for each new point $\bar{p}_l$

$$\bar{\omega}_l = \arg\min_{\omega} \left\| \bar{p}_l - \sum_{i=0}^{n} N_{i,k}(\omega)\mathbf{a}_i \right\|^2 , \; l \in [\![0, \bar{P}]\!]. \tag{VI.14}$$

Parametrization Vector $\boldsymbol{x}$ In the following, $\boldsymbol{x}$ will denote the vector of normal displacements of the moving CP.

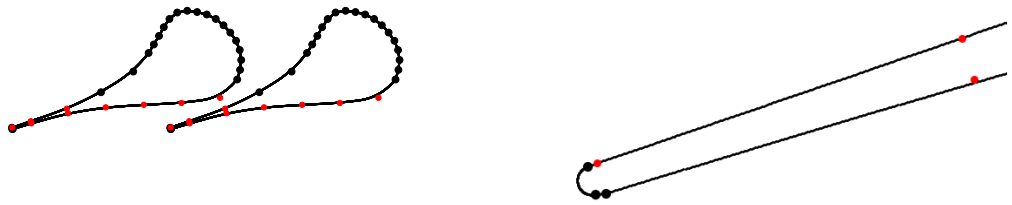

(a) Blade Parametrization (b) Zoom at the Trailing Edge.

Figure VI.1 Baseline profile approximated by B-splines: 30 CP, 9 Free CP (red), 21 Fixed CP (black).

VI–4 Baseline Configuration

Since this work aims at the aerodynamic optimization of the blade profile, the flow model focuses on the two-dimensional flow around the blade profiles at the midspan section of the cascade. Total Pressure P^t_{in}, total Temperature T^t_{in}, and axial flow direction are assigned at the inlet, while static pressure P^s_{out} is given at the outlet. The cascade operates with a design expansion ratio of about 7.5, expanding the organic fluid from 8 bar and 545 K as reported in Table VI.2.

	P^t_{in}	T^t_{in}	P^s_{out}
Nominal	8 bars	545.15 K	1.072 bars

Table VI.2 Nominal Operating Conditions.

To analyze the flow features at nominal conditions, the distribution of the Mach number is reported in Figure VI.2. It shows that high supersonic flows (with peak Mach number values of 2) are established in the rear sides of the cascade and the cascade-exit flow. As a result of the high Mach number of the free-streams (i.e., out

from the boundary layer) on both the suction and pressure sides of the blade, traditional fish-tail shock systems are generated at the blade trailing edge. The shock generated on the pressure side of the trailing edge impinges on the suction side of the adjacent blade, and it is reflected; this shock wave grows in strength when propagating downstream, as it merges with the compression occurring on the rear suction side of the blade, and due to the local concave shape of the blade. This phenomenon leads to the onset of a strong shock wave in the cascade-exit flow field. The QoIs related to that configuration, and used in the sequel are the total pressure loss $Y = \frac{P^t_{in} - P^t_{out}}{P^t_{in} - P^s_{out}}$ (where P^t_{out} denotes the mass-averaged total pressure at the outlet), and the mass flow rate per unit span $\dot{m}$. Another QoI used as a performance function to minimize is ΔP based on the pressure variability downstream of the cascade, and defined as the standard deviation of the azimuthal distribution of static pressure half an axial chord downstream the blade TE:

$$\Delta P = \sqrt{\frac{1}{n_p}\sum_{i=1}^{n_p}(P_i - \bar{P})} \tag{VI.15}$$

with

$$\bar{P} = \frac{1}{n_p}\sum_{i=1}^{n_p} P_i. \tag{VI.16}$$

n_p is the number of points $M_i = (x_0, y_i)$ chosen along the azimuthal direction on the downstream traverse, while $P_i = P(x_0, y_i)$ denotes the pressure interpolated linearly. Minimizing ΔP within the optimization is convenient for such highly supersonic cascade since it allows achieving a severe reduction of the shock strength, and hence of the shock loss, thus improving the cascade performance and, at the same time, reducing the perturbations entering the downstream rotor. However, also Y is evaluated because proper analysis of the cascades demands the quantification of an aerodynamic performance parameter.

VI–5 Mesh

During the optimization process, several blade profiles are progressively generated. Instead of re-generating it automatically, it is chosen in this work to modify the initial mesh at each design step. The dedicated mesh generation and deformation tools are described in the following. Additionally, a grid analysis is conducted for both Euler and RANS models, permitting to choose two grids respectively suitable for

- optimization purpose: coarse mesh resulting in a trade-off between accuracy and computational cost;
- stochastic assessment: fine mesh permitting to perform an accurate stochastic/deterministic analysis.

VI–5.1 Mesh Generation

The numerical grids are generated using an in-house tool developed at Politecnico di Milano, based on an advancing-front/Delaunay algorithm. Quadrilateral elements are first added over the solid walls, to build a boundary layer mesh, and to create hybrid grids suitable for viscous simulations. Afterwards, the advancing front algorithm

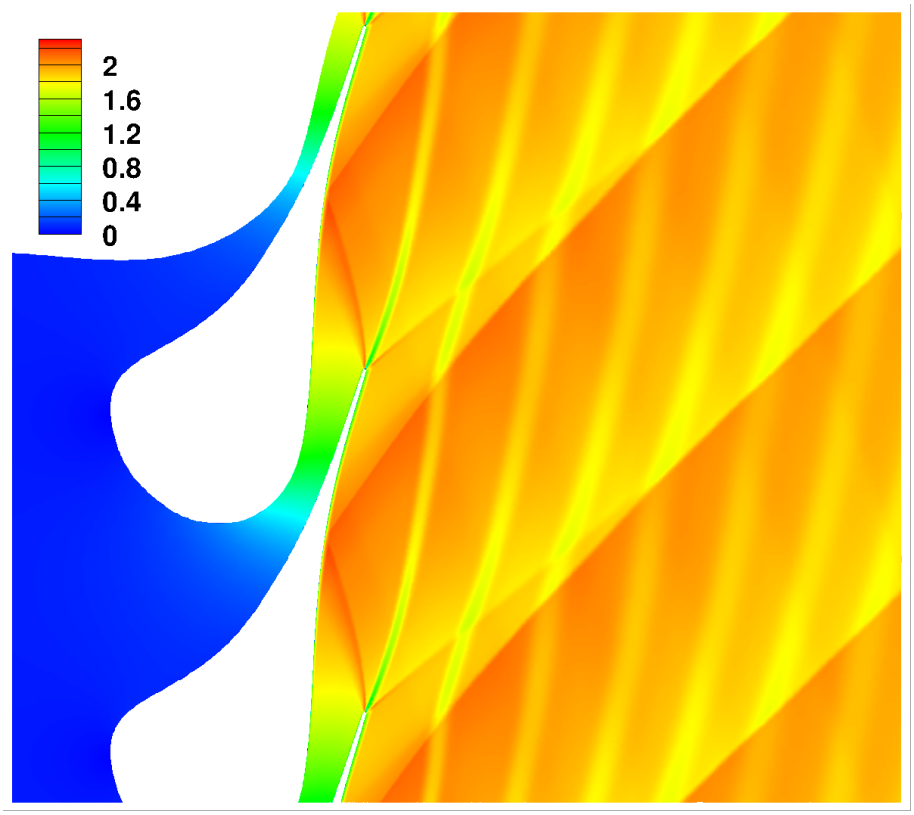

Figure VI.2 Mach contours at Nominal Conditions (Table VI.2) for the baseline profile.

triangulates the remaining portion of the computational domain. Due to the supersonic nature of the flow in the cascade of interest, relatively strong shocks arise in the rear suction side of the blade and at the *Trailing Edge* (TE), where the typical fish-tail shock pattern occurs [Colonna et al., 2008]. The grids were refined adequately in the regions where shock waves are expected to develop.

In the sequel, both inviscid models and high-fidelity RANS simulations are considered, with subsequent implications on the related meshes. Grids addressed to inviscid simulations require indeed a special treatment of the blade trailing edge section. The inherent artificial viscosity of numerical fluxes employed in inviscid simulations somehow allows simulating the separation that does occur at the trailing edge of a blade. However, as the artificial viscosity depends on the local cell size, the separation point also depends on the mesh resolution; with the typical refinement levels employed for transonic/transonic flows in turbine cascades, the separation point might be ill-predicted, leading to local non-physical states and even creating convergence issues. The truncation of the geometry at the trailing edge provides a significant advantage to mitigate these problems, as it introduces two sharp corners that enforce the separation of the flow, generally yielding to an improved convergence rate. For this reason, a truncated trailing edge was employed for all the inviscid simulations. Conversely, the original round trailing edge was retained for RANS simulations.

Rigorously, the lack of viscosity would forbid the flow to separate from any solid surface, independently from the curvature radius. A typical example is a low Mach number stream around a cylinder: the inviscid fluid model fails in predicting the development of the recirculation zone. In practical applications, the discretized formulation

of a partial differential equation, including the Euler equations, is generally affected by numerical dissipation. This numerical drawback somehow reproduces the role of viscosity and allows the flow to detach, at least in the proximity of very sharp edges.

The numerical diffusivity is strictly related to the numerical scheme employed and to the quality of the grid. In particular, the ill-prediction of separated flows is generally worse as one increases the resolution of the mesh, as the numerical viscosity decreases with it. This phenomenon typically occurs in the proximity of sharp geometrical curvatures, like for instance in inviscid turbo-machinery simulations, when a round trailing edge is present. As one refines the grid at the blade trailing, the separation is more and more prevented. This phenomenon usually causes local non-physical states to appear or makes simulations struggling to converge.

The truncation of the geometry at the trailing edge may help to overcome the issue. Indeed, it introduces two sharp corners that enforce the separation of the flow, and generally, it yields to an improved convergence rate. Clearly, for viscous simulations, the actual semi-circular representation of the round trailing edge is preserved.

In Navier-Stokes simulations, the height of the first cell of the boundary layer grid was set to $2 \cdot 10^{-7} m$, to ensure y^+ below unity. The y^+ value was evaluated starting from flat plate correlations considering the fluid viscosity provided in Table VI.1, the stream velocity and the density resulting from Euler simulations at the cascade-exit, and blade chord as reference length.

A representative NS mesh of the baseline profile, composed of 180 k cells, is reported in Figure VI.3, alongside two enlargements corresponding to the diverging channel and the trailing edge.

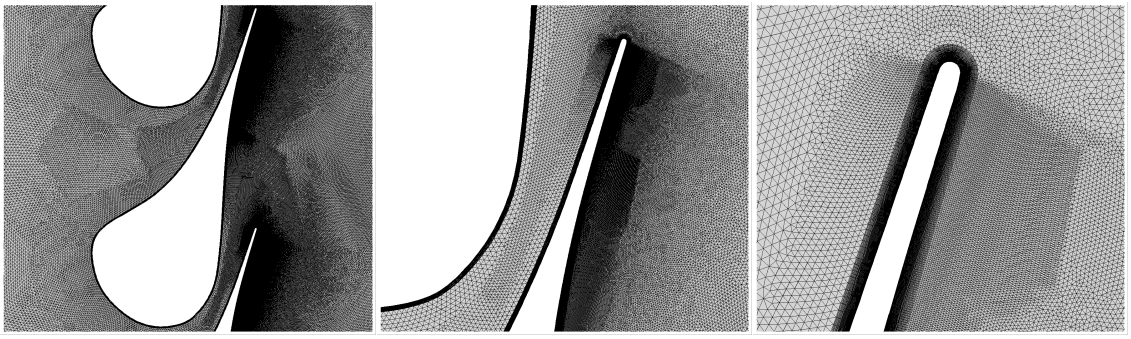

(a) Mesh (b) Diverging (c) TE

Figure VI.3 Example of a NS Mesh generated: 180 kcells.

VI–5.2 Mesh Deformation

A grid deformation tool is developed in order to accurately deform the grid for an assigned boundary displacement. The present approach follows the work of [De Boer et al., 2007], successfully applied in [Pini et al., 2015], to achieve a highly flexible and robust deformation tool for unstructured meshes, based on the interpolation of boundary nodes displacements to the whole mesh with *Radial Basis Functions* (RBF). A linear system of equations only involving boundary nodes has to be solved, and no grid connectivity information is needed. The following notations will be adopted in this *Subsection only*. d denotes the dimension space (here $d = 2$), $\boldsymbol{x} \in \mathbb{R}^d$ a node in

the mesh, $\boldsymbol{x}_{new} \in \mathbb{R}^d$ its new location, n_b the number of boundary nodes, $\{\boldsymbol{x}_{b_j}\}_{j\in[\![1,n_b]\!]}$ the set of nodes at the boundary, $p : \mathbb{R}^d \mapsto \mathbb{R}$ a polynomial.

The interpolation function $s : \mathbb{R}^d \to \mathbb{R}^d$, describing the displacement in the whole domain, can be written as a sum of basis functions:

$$s(\boldsymbol{x}) = \sum_{j=1}^{n_b} \alpha_j \Phi\left(\left\|\boldsymbol{x} - \boldsymbol{x}_{b_j}\right\|\right) + p(\boldsymbol{x}), \tag{VI.17}$$

where Φ is a given RBF. Coefficients of the linear polynomial p and α_j are determined by the interpolation conditions:

$$s(\boldsymbol{x}_{b_j}) = \mathbf{d}_{b_j} \tag{VI.18}$$

$$\sum_{j=1}^{n_b} \alpha_j q(\boldsymbol{x}_{b_j}) = 0, \tag{VI.19}$$

where $\mathbf{d}_{b_j}$ is the imposed displacement of the boundary node $\boldsymbol{x}_{b_j}$. Equation VI.19 has to be satisfied for all polynomials q with a degree less or equal than that of polynomial p. In our case, the displacement $\mathbf{d}_{b_j}$ is nullified for all boundary nodes, except the ones belonging to the blade. Independently for each spatial direction, the coefficients of the polynomial p and α_j are recovered solving a $(n_b + 4) \times (n_b + 4)$ symmetric positive definite linear system, using a Cholesky decomposition for instance.
The new position $\boldsymbol{x}_{new}$ of a node in the interior domain initially located in $\boldsymbol{x}$ is then directly derived:

$$\boldsymbol{x}_{new} = \boldsymbol{x} + s(\boldsymbol{x}). \tag{VI.20}$$

Each point is moved individually involving that no mesh-connectivity information is needed. The RBF retained in this work is the so-called *Volume* function, with global support, defined by $\Phi(r) = r$. This grid deformation tool is particularly easy to implement, robust, and computationally cheap, so perfectly suitable for the present work.

The baseline and two deformed Euler meshes composed by 36k cells are reported in Figure VI.4, alongside two enlargements corresponding to the diverging channel and to the trailing edge.

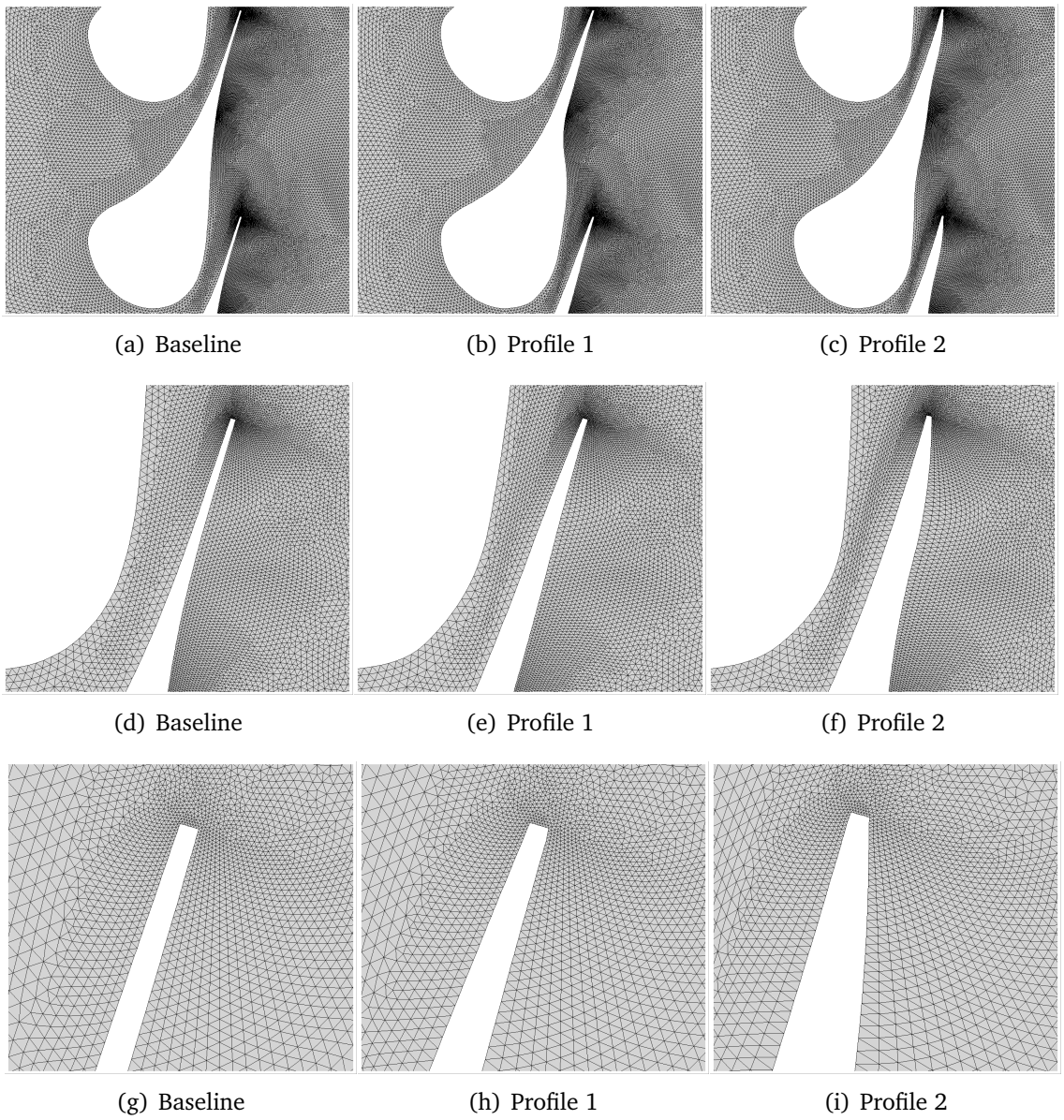

(a) Baseline (b) Profile 1 (c) Profile 2

(d) Baseline (e) Profile 1 (f) Profile 2

(g) Baseline (h) Profile 1 (i) Profile 2

Figure VI.4 Examples of Euler Meshes deformed: 36 kcells. Diverging chanel (d-f), Trailing Edge (g-i).

VII

Impact of geometric, operational, and model uncertainties on the non-ideal flow through a supersonic ORC turbine cascade

Overview *This chapter aims at presenting the outcomes of efficient surrogate-based uncertainty propagation methods applied to an ORC turbine, namely the axial supersonic turbine cascade introduced in Chapter VI. The impact of operational, fluid parameters and geometric uncertainties on different QoI such as the total pressure Y, ΔP or the mass-flow rate $\dot{m}$ is analyzed and provides a general overview over the influence of multiple effects and constitutes a preliminary study to RO. A failure scenario for ORC turbine is also analyzed by using one of the methods illustrated in the first part of this manuscript.*

Introduction

The present work, among the first studies in the Literature on ORC power systems, investigates the application of some advanced stochastic techniques to the analysis of a typical supersonic turbine cascade for ORC applications by considering a RANS turbulent solver and including a detailed characterization of the geometric uncertainties. Some recent works dealt with ANOVA-based analysis applied to the simulation of non-ideal gas flows, without an accurate characterization of geometric uncertainties:

i) using Euler solvers and considering uncertainties on operating conditions and thermodynamics models [Cinnella and Hercus, 2010, Geraci et al., 2016, Congedo et al., 2013a], ii) using turbulent solvers [Bufi and Cinnella, 2015].

Multiple sources of uncertainty are taken into account, related to the geometric tolerances of the blade and the operating conditions, and also considering those of some parameters of the thermodynamic model.

This Chapter is organized as follows. Section VII–1 provides in particular details on operating conditions considered and stochastic convergence studies for the calibration of the number of samples used in the stochastic space. Section VII–2 discusses uncertainties modeling, including a description of the geometric variability modelling. Results of the UQ study are analyzed in Section VII–3. A failure scenario is then illustrated in Section VII–4 . Finally, conclusions are discussed in Section VII–5.

VII–1 Operating Conditions and Numerical Settings

The configuration of interest is an axial-flow supersonic nozzle cascade operating with siloxane MDM, described in Chapter VI. In this work, blade-to-blade effects are investigated, considering a two-dimensional flow around the blade profiles at the midspan section of the cascade. Total Pressure P_{in}^t, total Temperature T_{in}^t, and axial flow direction are assigned at the inlet, while static pressure P_{out}^s is given at the outlet. Following [Colonna et al., 2008], we consider first a nominal (or full-load) operating condition for this nozzle cascade, characterized by an inlet thermodynamic state close to the saturation curve, and a high expansion ratio equal to ≈ 6. As well known, ORC power systems are requested to operate at part-load for long periods during their technical life, due to changes in the thermal power made available by the heat source and in the condenser temperature; this variation implies a large change in the turbine pressure ratio, resulting in a variation of aerodynamic loading on each cascade. In [Colonna et al., 2008], the implication of part-load operation for this cascades was estimated so to reduce the pressure ratio to ≈ 4, by an increase of cascade outlet pressure. Both full-load and part-load operating conditions are considered in this study, both of them reported in Table **??**.

Condition	P_{in}^t	T_{in}^t	P_{out}^s
Full-load	8.0 bars	543.65 K	1.33 bars
Part-Load	8.0 bars	543.65 K	2.0 bars

Table VII.1 Operating Conditions

Cascade Flow Field at Full- and Part-Load Conditions The RANS simulations were performed on a cluster equipped with Intel(R) Xeon(R) CPU X5650 at 2.67GHz. An adaptive CFL is selected to between 10 and 100. Simulations are assumed to be converged when residuals on the density are decreased by six orders of magnitude, or after 15000 iterations. Ill-converged simulations are re-run automatically with a minimal CFL of 1. Simulations run with 6 cores take about 8 hours for meshes composed by 180k cells.

A dedicated grid dependence analysis was performed at the full-load condition. Two quantities were used as metric for evaluating the mesh convergence, namely the total pressure loss Y and the mass flow rate per unit span $\dot{m}$. Figure VII.1 reports the relative percentage error on the performance estimators. In this study, grid independence was considered achieved with the mesh composed by 590k cells; on the basis of the quantitative results, the 180k cells mesh was considered as the optimal compromise between accuracy and computational cost (error of 2%) and, hence, it was employed to compute the blade performance in the UQ framework. We perform a posteriori assessment that the variability induced by the uncertainty quantification study is mainly predominant with respect to the mesh error.

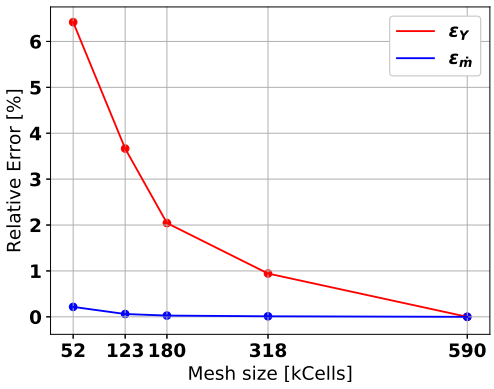

(a)

Figure VII.1 Grid Analysis on the baseline configuration (RANS), for the two QoI $\dot{m}$ and Y.

Calculations of the flow in the cascade for the full- and part-load conditions are now reported to properly show the most relevant flow features, in view of the UQ analysis which is the core of this study. Figure VII.2 reports the distribution of Mach number for the two conditions, and show that high supersonic flows (with peak Mach number values of 2) are established in the rear sides of the cascade and in the cascade-exit flow. As a result of the high Mach number of the free-streams (i.e., out from the boundary layer) on both the suction and pressure sides of the blade, classical fish-tail shock systems are generated at the blade trailing edge. The shock generated on the pressure side of the trailing edge impinges on the suction side of the adjacent blade, and it is reflected; this shock wave grows in strength when propagating downstream, as it merges with the compression occurring on the rear suction side of the blade, and due to the local concave shape of the blade. This leads to the onset of a strong shock wave in the cascade-exit flow field. A similar shock pattern can be observed for the two conditions, even though the main shock is stronger and slightly less inclined (with respect to the axial direction) in the part-load condition. The flow angle is also clearly different in the two conditions, as marked by the higher inclination of the wakes at part-load operation. This feature can be interpreted by considering that, in this latter condition, the converging-diverging nozzle becomes significantly over-expanded with respect to the outlet pressure; as a result, a post-compression takes place that, in cascade configuration, induces a flow turning in tangential direction (so to reduce the 'virtual' cross-section normal to the flow at the exit). The post-compression also explains the higher shock strength at part-load operation. The blade

wakes and, especially, the shocks contribute to the loss generation, which is quantified in this study in terms of the aforementioned total pressure loss Y. Y and the mass flow rate per unit span $\dot{m}$ are the QoIs considered in that work.

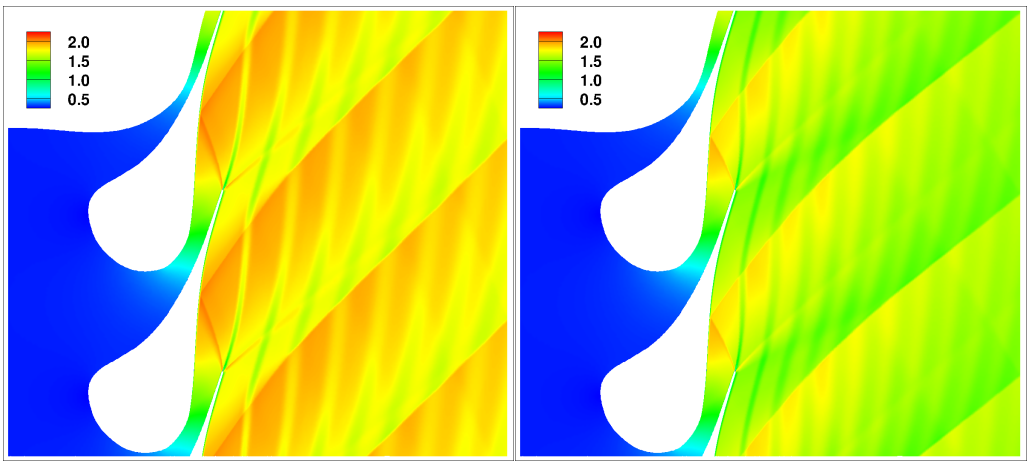

(a) Full Load (b) Part Load

Figure VII.2 Mach contours: Nominal Conditions

VII–2 Uncertainty Modeling

In this work, three classes of uncertainties are taken into account. At first, the geometric variability along the blade due to manufacturing tolerances was considered, discussed in Subsection VII–2.1 and modeled through the realization of a random vector of practical dimension ($N_\sigma = 7$ here), stemming from a infinite dimension Gaussian process. Moreover, uncertainties in operating conditions as well as in two parameters of the thermodynamic model were also considered and their quantification is discussed in Section VII–2.2.

VII–2.1 Modeling Geometric Variability

Various approaches have been introduced to model the geometric variations due to blade turbine manufacturing. Based on measurement data, *Principal Component Analysis* (PCA) can be used to build a probabilistic model of variability from the empirical mean and covariance of surface deviations at different locations on the blade [Garzon, 2003, Häcker, 2000, Lange et al., 2012]. Following [Dow and Wang, 2015, Dow and Wang, 2014], it is assumed that the geometric variability in manufactured turbine blades can be accurately described as a *non-stationary Gaussian Random Field* $e(s, \omega)$, ω being a coordinate in the sample space Ω, and $(\Omega, \mathcal{F}, \mathbb{P})$ a complete probability space. The arclength $s \in [0, 1]$ parametrizes the location on the blade surface, starting at the trailing edge ($s = 0$), going around the leading edge ($s = \frac{1}{2}$), and continuing back to the trailing edge on the opposite side of the blade ($s = 1$). This approach is somehow similar to the PCA [Garzon, 2003], except that in the present work, mean and covariance are provided in closed form rather than estimated from data. Indeed, random fields provide a convenient method for modeling spatially distributed uncertainty. Random fields have previously been used to model spatially distributed

uncertainty in a wide variety of systems, including natural variations in ground permeability [Christakos, 2012], random deviations in material properties for structural optimization problems [Chen et al., 2010], and geometric variability in airfoils [Borzì et al., 2010, Schillings et al., 2011].

Random Field

The Random field $e(s,\omega)$ represents the error between the manufactured surface and the nominal (perfect) one in the normal direction at the point parametrized by s. It is fully defined by its mean $\bar{e}(s)$ (null here) and autocovariance function $C(s,t)$: it captures the correlation between manufacturing errors at locations s and t along the blade surface, and describes the smoothness and correlation length of the random field. It is written as [Dow and Wang, 2014]:

$$C(s,t) = \sigma(s)\,\sigma(t)\,\rho(s,t) \tag{VII.1}$$

where $\sigma(s)$ is the standard deviation of the random field at location s, considered constant here: $\sigma(s) = \sigma_0$.
σ_0 quantifies le level of manufacturing variability. The non-stationary autocorrelation function ρ is defined by [Dow and Wang, 2014]:

$$\rho(s,t) = \exp\left(-\frac{|s-t|^2}{L^2(s,t)}\right), \tag{VII.2}$$

where the *square* correlation length $L^2(s,t)$ is defined by:

$$\begin{aligned} L^2(s,t) =& L(s)L(t) \\ L(s) =& L_0 + (L_{LE} - L_0)\exp\left(-\frac{|s-\frac{1}{2}|^2}{\omega^2}\right). \end{aligned} \tag{VII.3}$$

The values $L_0 = 0.1$, $\omega = 0.1$ [Dow and Wang, 2014] and $L_{LE} = 1.0 \times 10^{-2}$, all normalized by the blade half-arclength were used.

In that study, the TE is modeled as a circular arc, thus, the impact of manufacturing variability at the trailing edge is not addressed.

Discretization and Simulation

The Karhunen-Loeve (KL) expansion is used to represent the random field: it is based on a spectral decomposition of the autocovariance functions. The random field can be represented exactly by [Betz et al., 2014, Karhunen, 1947, Loeve, 1948]:

$$e(s,\omega) = \bar{e}(s) + \sum_{i=1}^{\infty} \sqrt{\lambda_i}\Phi_i(s)Z_i(\omega), \tag{VII.4}$$

where the λ_i are arranged in descending order. Z_i are standard uncorrelated normal random variables; $\lambda_i \in \mathbb{R}^+$ and $\Phi_i : [0,1] \to \mathbb{R}$ are respectively the eigenvalues and orthonormal eigenfunctions of the autocovariance function C, also referred to as the kernel function in this context, obtained by solving the homogeneous Fredholm integral equation of the second kind:

$$\int_{[0,1]} C(s,t)\Phi_i(t)\mathrm{d}t = \lambda_i \Phi_i(s), \ \forall s \in [0,1]. \tag{VII.5}$$

This integral equation is solved numerically on the discretized blade surface using the Nyström method [Betz et al., 2014, Nyström, 1930], with N_g Gauss quadrature points ($N_g = 500$ here) to approximate the integral. Discretized Eigenmodes are consequently evaluated solving a discrete eigenproblem, using for instance a *Singular Value Decomposition* (SVD). It results in a finite expansion further truncated to give a stochastic dimension of N_{KL}, determined by the decay of the eigenvalues. The normalized cumulative energy from the first p modes is defined by

$$E(p) = \frac{\sum_{i=1}^{p} \lambda_i}{\sum_{i=1}^{N_g} \lambda_i}. \tag{VII.6}$$

It is used to select the number of modes retained in the KL expansion:

$$N_{KL} = \arg\min\{k \in \mathcal{N}^* \ s.t. \ E(k) < \epsilon\}, \tag{VII.7}$$

where ϵ is a user defined parameter driving the accuracy of the expansion. $\epsilon = 99\%$ is chosen here.

Figures VII.4 and VII.3 illustrate the eigenmodes decay and selection. By analyzing the effects of the modes, it is evident that the odd modes alter, with different 'wavenumber', the blade thickness: mode 1 appears as a simple omothetic scaling of the blade, mode 3 increases the thickness in the trailing edge region and makes the blade more slender in the leading edge, mode 5 makes the blade more slender in the central part of the blade and increases the thickness both at leading edge and trailing edge, and so on for mode 7. Conversely, the even modes act mainly as blade rotation: mode 2 appears indeed as a rigid blade rotation centered close to the leading edge, mode 4 and mode 6 are more complex deformations in which the leading edge, the trailing edge and the central part of the blade 'deflect' (by a different amount) with respect to the original blade.

Figure VII.5 shows samples of geometric perturbation with the proposed method. Three levels of geometric variability are considered to study its impact on the QOI:

- No geometric variability: $\sigma_0 = 0$.
- Moderate geometric variability: $\sigma_0 = 3 \times 10^{-5} m$.
- Large geometric variability: $\sigma_0 = 6 \times 10^{-5} m$.

In the following, the unity of σ_0 will be skipped for a sake of brevity.

VII–2.2 Operating Conditions and Thermodynamic Model Uncertainties

Uncertainties associated to the operating conditions are considered in this work, namely on P^t_{in}, T^t_{in} and P^s_{out}, for both full-load and part-load turbine operation. The values of the uncertainties are reported in Tables VII.2 and VII.3. The uncertainties were estimated considering typical measurement errors in the monitoring devices of power systems; in particular, $\pm 5kPa$ of uncertainty in the pressure measurements and $\pm 0.35K$ of uncertainty in temperature measurements are assumed.

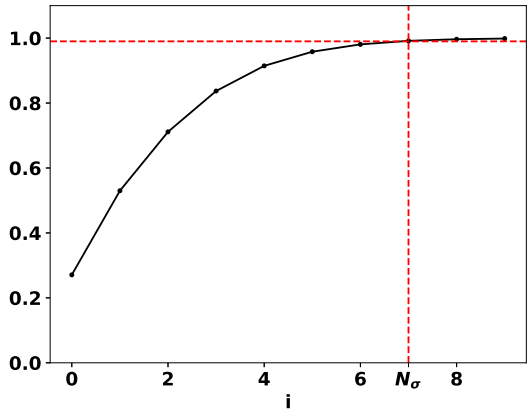

(a) Cumulative Energy $E(p)$ as a function of number of modes (Eq. VII.6). $\epsilon = 99\% \implies N_\sigma = 7$

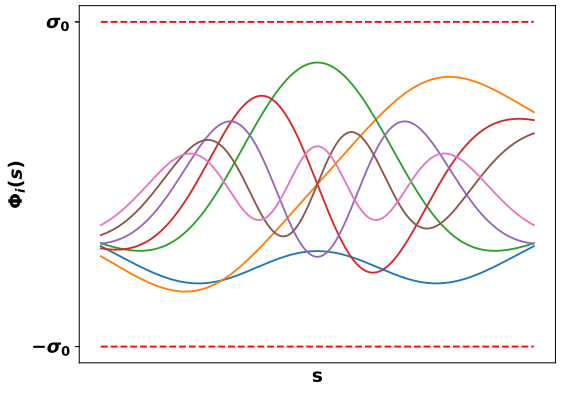

(b) Eigenmodes $\Phi_i(s)$ retained

Figure VII.3 Eigenmodes of the 1D random field.

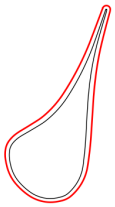

(a) Mode 1

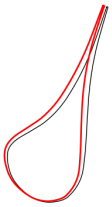

(b) Mode 2

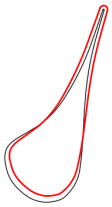

(c) Mode 3

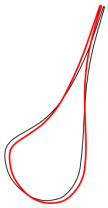

(d) Mode 4

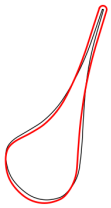

(e) Mode 5

(f) Mode 6

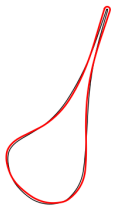

(g) Mode 7

Figure VII.4 Eigenmodes: illustration on the 2D Cascade (scale=50, $\sigma_0 = 6 \times 10^{-5} m$).

Two coefficients associated to the thermodynamic model of the fluid are also considered uncertain, namely the acentric factor ω and the heat capacity ratio γ of the fluid (which is considered polytropic in this study). A specific quantification of the

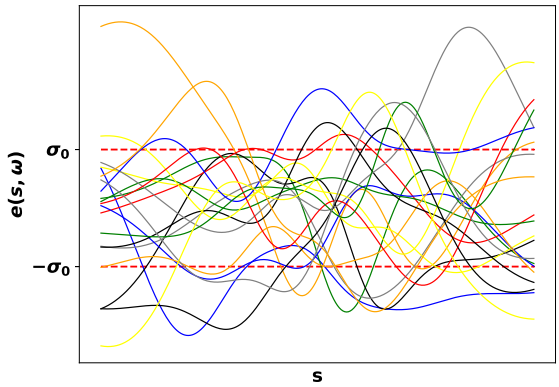

(a) Random Field

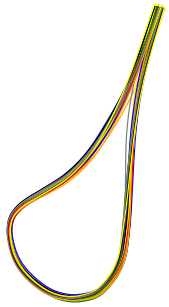

(b) scale=10, $\sigma_0 = 6 \times 10^{-5}$.

Figure VII.5 Geometric Variability Modeling: Samples.

variability of these parameters not being available, a uniform uncertainty of 5% is assumed for ω and a uniform range ± 0.004 ensuring thermodynamic consistency for γ. This is consistent with respect to other studies performed in literature over the coefficients of the thermodynamic models (see for example [Cinnella et al., 2011a, Cinnella et al., 2010, Congedo et al., 2013a]).

Tables VII.2 and VII.3 summarizes the scenarios corresponding respectively to full- and part-load, each considering three different geometric uncertainty levels.

Globally, the random vector is then denoted as $= (P^t_{in}, T^t_{in}, P^s_{out}, \gamma, \omega, \xi_1, ..., \xi_{N_\sigma})$, or $= (P^t_{in}, T^t_{in}, P^s_{out}, \gamma, \omega)$ if geometric variations are not taken into account.

Geometric Variations	No $\sigma_0 = 0$	Moderate $\sigma_0 = 3 \times 10^{-5}$	Large $\sigma_0 = 6 \times 10^{-5}$
P^s_{out} [bars]	$\mathcal{U}[1.28, 1.38]$	$\mathcal{U}[1.28, 1.38]$	$\mathcal{U}[1.28, 1.38]$
P^t_{in} [bars]	$\mathcal{U}[7.95, 8.05]$	$\mathcal{U}[7.95, 8.05]$	$\mathcal{U}[7.95, 8.05]$
T^t_{in} [K]	$\mathcal{U}[543.3, 544.0]$	$\mathcal{U}[543.3, 544.0]$	$\mathcal{U}[543.3, 544.0]$
γ [-]	$\mathcal{U}[1.012, 1.020]$	$\mathcal{U}[1.012, 1.020]$	$\mathcal{U}[1.012, 1.020]$
ω [-]	$\mathcal{U}[0.518, 0.540]$	$\mathcal{U}[0.518, 0.540]$	$\mathcal{U}[0.518, 0.540]$
ξ	-	$\mathcal{N}_7(0, \mathbf{I}_7)$	$\mathcal{N}_7(0, \mathbf{I}_7)$
Dimension	5	12	12

Table VII.2 Full Load: Uncertain Input, for different geometric variability levels

VII–2.3 Stochastic Convergence

An analysis of the convergence of statistics is performed considering full load and $\sigma_0 = 6 \times 10^{-5}$ in order to justify the number of samples necessary to conduct the UQ analysis based on the tools presented above. Three sets of LHS DOE of respective size 100, 200 and 400 are considered. Those sizes are chosen on a basis of similar studies conducted with a inviscid model, not presented here for a sake of brevity.

Geometric Variations	No $\sigma_0 = 0$	Moderate $\sigma_0 = 3 \times 10^{-5}$	Large $\sigma_0 = 6 \times 10^{-5}$
P^s_{out} [bars]	$\mathcal{U}[1.95, 2.05]$	$\mathcal{U}[1.95, 2.05]$	$\mathcal{U}[1.95, 2.05]$
P^t_{in} [bars]	$\mathcal{U}[7.95, 8.05]$	$\mathcal{U}[7.95, 8.05]$	$\mathcal{U}[7.95, 8.05]$
T^t_{in} [K]	$\mathcal{U}[543.3, 544.0]$	$\mathcal{U}[543.3, 544.0]$	$\mathcal{U}[543.3, 544.0]$
γ [-]	$\mathcal{U}[1.012, 1.020]$	$\mathcal{U}[1.012, 1.020]$	$\mathcal{U}[1.012, 1.020]$
ω [-]	$\mathcal{U}[0.518, 0.540]$	$\mathcal{U}[0.518, 0.540]$	$\mathcal{U}[0.518, 0.540]$
ξ	-	$\mathcal{N}_7(0, \mathbf{I}_7)$	$\mathcal{N}_7(0, \mathbf{I}_7)$
Dimension	5	12	12

Table VII.3 Part Load: Uncertain Input, for different geometric variability levels

Based on the three LHS sets, Figure VII.6 plots the PDFs of $\dot{m}$ and Y, while Figure VII.7 summarizes their total Sobol SI of input parameters. PDF's and total Sobol SI are in very good agreement for the different LHS sets; however, a slight error in the PDF of Y is observed when using 100 samples, hence all the UQ studies were conducted based on a LHS set of size $N_{LHS} = 200$.

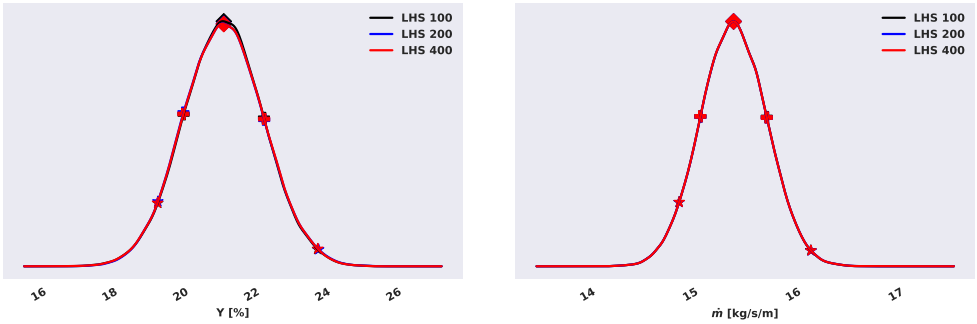

(a) Y PDFs (b) $\dot{m}$ PDFs

Figure VII.6 PDF Convergence analysis, based on LHS sets of size 100, 200 and 400. Stars indicate 5% and 95% quantiles, 'plus' indicate $\mu \pm \sigma$ and diamonds indicate μ.

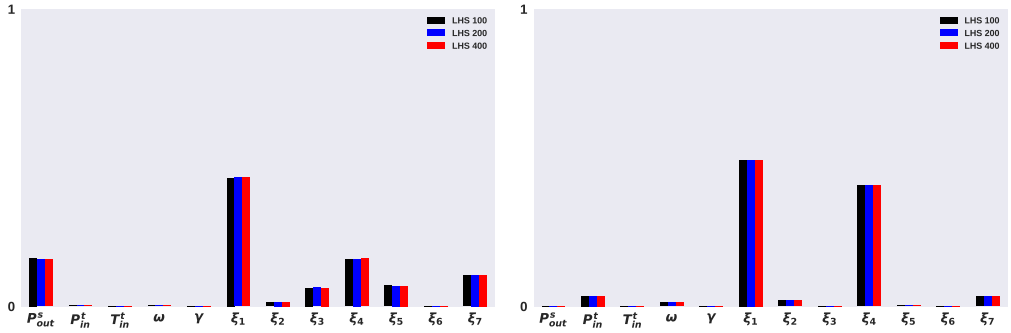

(a) Y (b) $\dot{m}$

Figure VII.7 Total Sobol SI Convergence analysis, based on LHS sets of size 100, 200 and 400.

VII–3 Results

This Section presents a comprehensive uncertainty quantification study based on the stochastic framework formulated above. Based on a LHS set of size $N_{LHS} = 200$ for each case, a comprehensive UQ analysis is performed. A sensitivity analysis (ANOVA) is carried out in Section VII–3.1. Marginal and joint PDF's of the QoI are then studied (Section VII–3.2), along with their statistics (Section VII–3.3). Finally, the impact of the uncertain input on the flow field is studied (Section VII–3.4).

VII–3.1 Sensitivity Analysis

A Sensitivity analysis was performed for the QOI Y and $\dot{m}$, and is presented in Figures VII.8 and VII.9 respectively, for both full- and part-load. First considering the influence of thermodynamic conditions in absence of geometric variability, the uncertainty in the outlet static pressure has the highest impact on the loss coefficient, especially in full-load condition; this is because the uncertainty in the outlet static pressure is relatively much higher than that on the inlet total pressure, and hence it dominates on the variability of pressure ratio; the variability of pressure ratio, in turns, induces a variation of shock strength and, hence, aerodynamic losses. In part-load condition, the inlet total pressure grows in relevance on Y; as a matter of fact, for this off-design condition the difference between the inlet and the outlet pressures reduces, while the uncertainty remains the same, so both the uncertainties contribute in a measurable way to the variability of pressure ratio. The outlet static pressure does not have any impact on the flow rate, as expected since the cascade is chocked in both full- and part-load conditions. Conversely, the uncertainty in inlet total pressure dominates the variability of flow rate in both the conditions, as the inlet total pressure determines the value of fluid density; this latter, in turn, is only marginally influenced by the inlet total temperature in the conditions of interest.

The uncertainties in the two parameters of the thermodynamic model have a minimal impact on the variability of Y. Conversely, the ratio of specific heat capacities has a relevant impact on the flow rate, as it influences the relationship between the mass flow rate and the expansion ratio in chocked-flow conditions. The acentric factor does not have a measurable effects on both the QoIs. The relevance of operational and model uncertainties is drastically reduced when manufacturing tolerances are plugged into the flow model, even though the mutual hierarchy of the former remains the same, and the considerations reported above still apply. If geometric variability is large, manufacturing tolerances dominate the variability of the QoIs. In particular, it is observed that mode 1 and mode 4 are responsible for most of the variability of flow rate, and also have the highest impact on the variability of loss coefficient. An analysis of the geometric modes reveals that Mode 1 induces a net variation of geometric throat and also mode 4 has a large impact on the throat, as it is associated to a rotation which alters significantly both the leading edge and the rear side of the blade, which define the geometric throat of the cascade. These considerations justify the relevance of mode 1 and 4 on the flow rate; however, in a supersonic configuration a variation of the geometric throat without a corresponding change in expansion ratio makes the nozzle to operate in off-design conditions, leading to the onset of stronger shocks and, hence, modifying the cascade performance. This may explain why mode 1 and mode 4 also dominate the variability of Y. This latter, however, is influenced by all the modes; as a matter of fact, the development of boundary layer and the onset

of the leading shock depend on the detailed shape of the blade, both in the diverging part of the bladed duct and in the region of un-guided turning, and all the modes alter the blade in the rear part. As a further consideration, it is well known in cascade aerodynamics that trailing edge thickness has a relevant impact on the wake width and, hence, on the viscous loss; this contributes to explain the relative relevance of all the odd modes on Y, as all of them alter the trailing edge thickness; this is particularly visible in full-load condition, for that viscous effects contribute more than shocks to the aerodynamic loss, as at full-load the shocks have lower strength.

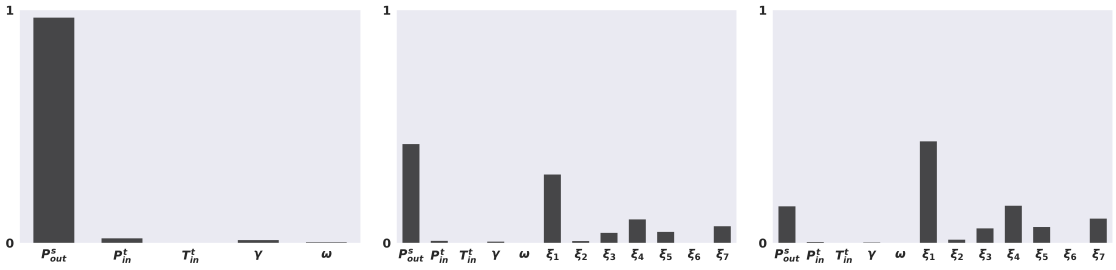

(a) Full Load: $\sigma_0 = 0$ (b) Full Load: $\sigma_0 = 3 \times 10^{-5}$ (c) Full Load: $\sigma_0 = 6 \times 10^{-5}$

(d) Part Load: $\sigma_0 = 0$ (e) Part Load: $\sigma_0 = 3 \times 10^{-5}$ (f) Part Load: $\sigma_0 = 6 \times 10^{-5}$

Figure VII.8 Sensitivity Analysis Y: Total Sobol SI

VII–3.2 PDF Comparisons

The PDFs of Y and $\dot{m}$ are provided in Figure VII.10 for the three different geometric variations, in both full-load and part-load cases. In an alternative two-dimensional representation, the joint PDFs are also provided in Figure VII.11.

In absence of geometric variability, the PDFs of Y have a complex non-Gaussian shape with different mean values and support; in particular, the support is narrow enough to make the full-load conditions always outperforming the part-load one. Conversely, the PFDs of $\dot{m}$ are of Gaussian type with very narrow support; this result had been already observed and discussed in detail in [Romei et al., 2018], and is motivated by the combination of inlet pressure and temperature uncertainties. As the cascade is chocked in the two conditions, and the uncertainties in the inlet conditions are the same, the PDFs appear identical.

The influence of geometric tolerances is, again, very significant from both the qualitative and quantitative point of view. At first, the introduction of geometric variability makes the PDFs of Y to become of Gaussian type. This is probably because the geometric variability itself is modeled as Gaussian process; however, this indicate the dominant effect of manufacturing tolerances, when they are plugged into the un-

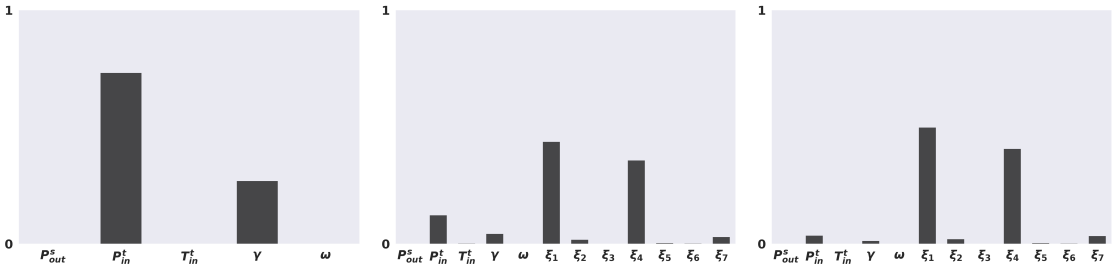

(a) Full Load: $\sigma_0 = 0$ (b) Full Load: $\sigma_0 = 3 \times 10^{-5}$ (c) Full Load: $\sigma_0 = 6 \times 10^{-5}$

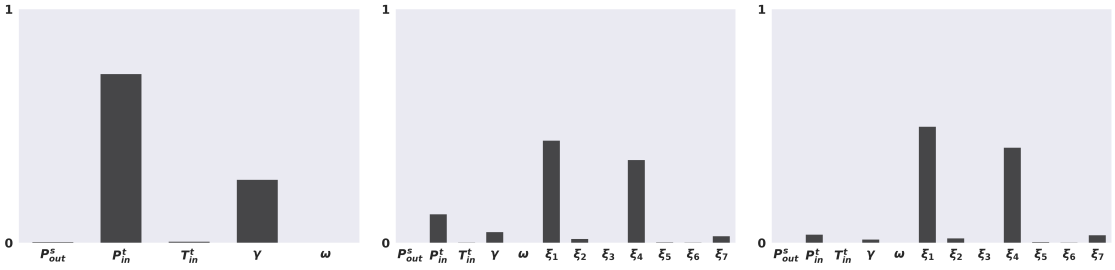

(d) Part Load: $\sigma_0 = 0$ (e) Part Load: $\sigma_0 = 3 \times 10^{-5}$ (f) Part Load: $\sigma_0 = 6 \times 10^{-5}$

Figure VII.9 Sensitivity Analysis $\dot{m}$: Total Sobol SI.

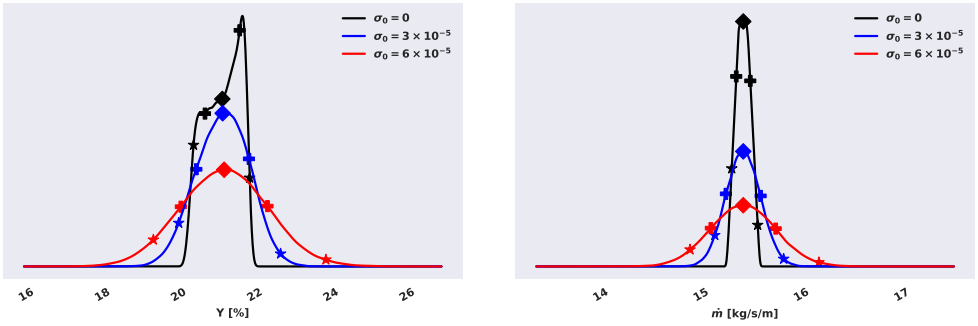

(a) Full Load: Y (b) Full Load: $\dot{m}$

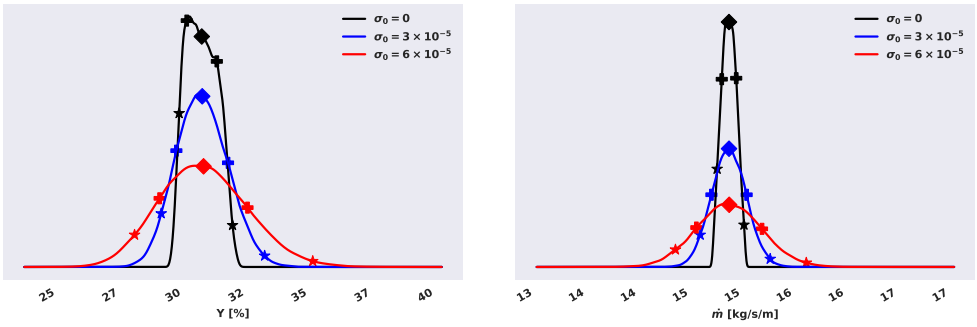

(c) Part Load: Y (d) Part Load: $\dot{m}$

Figure VII.10 PDF of Y and $\dot{m}$ at full and partial load: comparison between no/moderate/high geometric variations.

certainty framework. On the quantitative ground, the geometric variability clearly enlarges the support of the PDFs in all the conditions and for both the QoIs. In particular, the variability in loss coefficient increases from about 2% in absence of tolerances to about 4-6% for the largest tolerance. Despite this, the mean of the PDFs undergoes a slight change (only visible for part-load condition) which does not alter the ranking between full-load and part-load conditions in terms of mean performances; however, when considering the actual realizations of the flow process in presence of the largest geometric variability, a significant overlapping between the PDFs in the two conditions exists (between 21.5% and 24.5%) making the two operating conditions equivalent from the performance perspective for a relatively large percentage of realizations.

The impact of manufacturing tolerances on the flow rate is identical for the two conditions and simply enlarges by a factor ≈ 5 the support of the PDF.

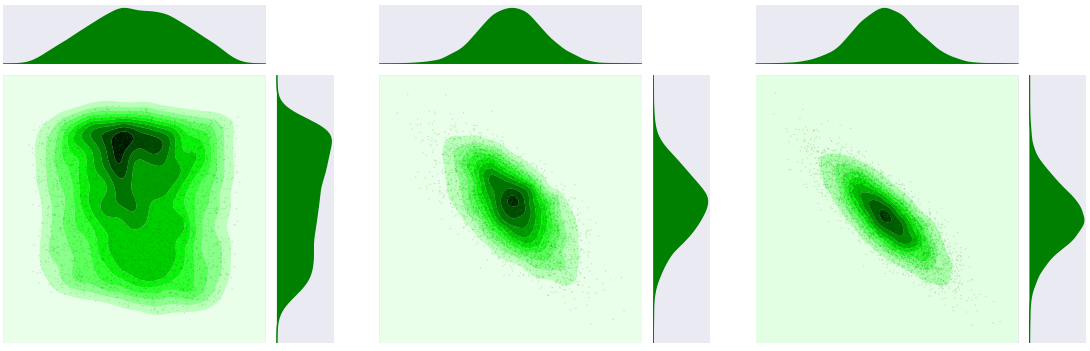

(a) Full Load: $\sigma_0 = 0$ (b) Full Load: $\sigma_0 = 3 \times 10^{-5}$ (c) Full Load: $\sigma_0 = 6 \times 10^{-5}$

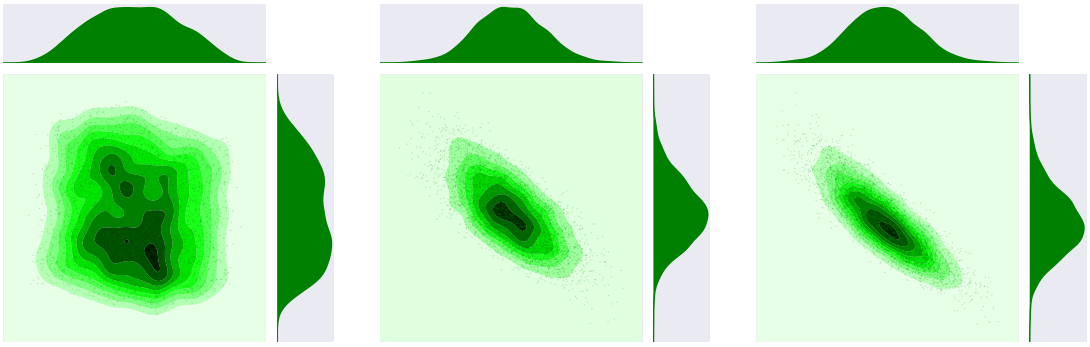

(d) Part Load: $\sigma_0 = 0$ (e) Part Load: $\sigma_0 = 3 \times 10^{-5}$ (f) Part Load: $\sigma_0 = 6 \times 10^{-5}$

Figure VII.11 Joint PDF $(\dot{m}, Y)$

VII–3.3 Statistics

On the basis of the PDFs reported in the previous Subsection, the most relevant statistics (mean, variance, 5-quantile, and 95-quantile) were computed and are reported in Table VII.4. They show, in more quantitative terms, the features already observed when commenting the PDFs in terms of mean, variance, and support (which is roughly given by the difference between the two quantiles). The interference between the PDFs of Y at large geometric variability is confirmed by the 5-quantiles and 95-quantiles, thus confirming that it is not just a matter of tail probabilities. The analysis also con-

firms that the quantitative equivalence between the flow rate in the full- and part-load conditions does not hold only for the mean properties but it is valid for the whole stochastic framework. This result, which is physically consistent, might be considered as a further proof of the validity of the proposed statistic methodology based on surrogates.

		$\sigma_0 = 0$	$\sigma_0 = 3 \times 10^{-5}$	$\sigma_0 = 6 \times 10^{-5}$
Full Load (μ,σ,q_5,q_{95})	Y[%]	(20.91, 0.45, 20.15, 21.54)	(20.91, 0.69, 19.75, 22.01)	(20.94, 1.14, 19.09, 22.83)
	$\dot{m}$[kg/s/m]	(15.33, 0.07, 15.22, 15.44)	(15.33, 0.17, 15.04, 15.61)	(15.33, 0.32, 14.80, 15.86)
Part Load (μ,σ,q_5,q_{95})	Y[%]	(30.77, 0.60, 29.87, 31.75)	(30.79, 1.02, 29.16, 32.53)	(30.84, 1.74, 28.10, 33.83)
	$\dot{m}$[kg/s/m]	(15.38, 0.07, 15.26, 15.49)	(15.38, 0.17, 15.10, 15.66)	(15.38, 0.32, 14.86, 15.90)

Table VII.4 Scalar Statistics (mean, standard deviation, 5% and 95% quantiles) of the QoI Y and $\dot{m}$, for the three geometric noise levels.

VII–3.4 Physical Analysis

In this Subsection, QoI of high dimension variability is conducted using the UQ tools described in Subsection I–3.2 to perform a physical analysis of the flow. The distributions of Mach number over the entire flow domain and its variability are now discussed, by resorting to the mean and the Coefficient of Variance.

The QoI here shown refer to Mach number at *node location* of the initial mesh, the latter allowed to be deformed conserving the initial nodes connectivity. Prescribing the QoI to assigned spatial location would require a cumbersome interpolation/extrapolation, adding numerical inaccuracies of the QoI, in the vicinity of the blade wall, due geometric blade perturbations.

The distributions of mean and CoV of the Mach number on the computational domain is shown Figures VII.12 and VII.13, corresponding respectively to the full- and part-load conditions. The mean Mach number distributions are actually very similar each other and to the deterministic ones. This is probably because the uncertainties are relatively small and are symmetric with respect to the deterministic values; moreover, the manufacturing tolerances are also assumed to be Gaussian processes whose mean correspond to the original blade shape. However, the same uncertainties produce significant perturbations, that grow significantly when activating the geometric variability. CoV values slightly exceeding 2% are found, with the highest values concentrated in the wakes and in the shock fronts.

In case of no geometric variability, almost null CoV is found in the bladed channel up to the shock on rear suction side of the blade; after that, high CoV is observed in the whole rear suction side up to the trailing edge, where local peaks of CoV occur in the wake and in the fishtail shock system. Moving downstream, the wake width increases due to turbulent and viscous diffusion, resulting in a cascade of wide regions of moderate CoV; in correspondence to the main shock front, the CoV remains locally high and increases moving downstream, as the leading shock grows in strength. As already commented, the main shock grows in magnitude moving downstream as the compression waves generated in the rear suction side, and induced by the local concave shape of the blade, coalesce in a shock front at a certain distance from the blade, enforcing the weak reflected shock coming from the trailing edge of the adjacent blade. The variability in operating conditions (in outlet pressure, in particular) and in the specific heat capacity ratio influence the shock strength justifies the local high values of CoV.

When geometric variability is plugged into the uncertainty framework, the character of the CoV distribution does not change but some evident quantitative effects appear; similar features take place for the two operating conditions. At first, progressively higher CoV values are found upstream of the blade when the manufacturing tolerance increases; the CoV reduces in the accelerating region of the bladed nozzle, and especially in the supersonic divergent, where the mean Mach number grows significantly. This suggests that manufacturing tolerances induce a nearly uniform variance in this region, so that the CoV distribution is dominated by that of the mean. On the rear suction side of the blade and in the cascade-exit flow field high CoV values are observed in the wakes and in the shock regions, as already observed in absence of geometric variability; however, wider areas of high CoV appear, and, at a certain distance from the blade, moderate-to-high CoV cover the entire flow field. The larger extension of high CoV regions downstream of the cascade can be explained by considering that the modes alter significantly the blade shape in the rear part. In particular, the compression wave generated on the concave part of the rear suction side is perturbed by the local variability in the blade shape, altering both the shock strength and the shock inclination; this contributes to explain the wider high CoV region observed across the shock in presence of manufacturing tolerances. Beside that, the wake appears even more sensitive than the shock to geometric uncertainty; this is probably motivated by the fact that the geometric variability, and in particular the odd modes, alter the trailing edge thickness, which has a direct impact on the wake width.

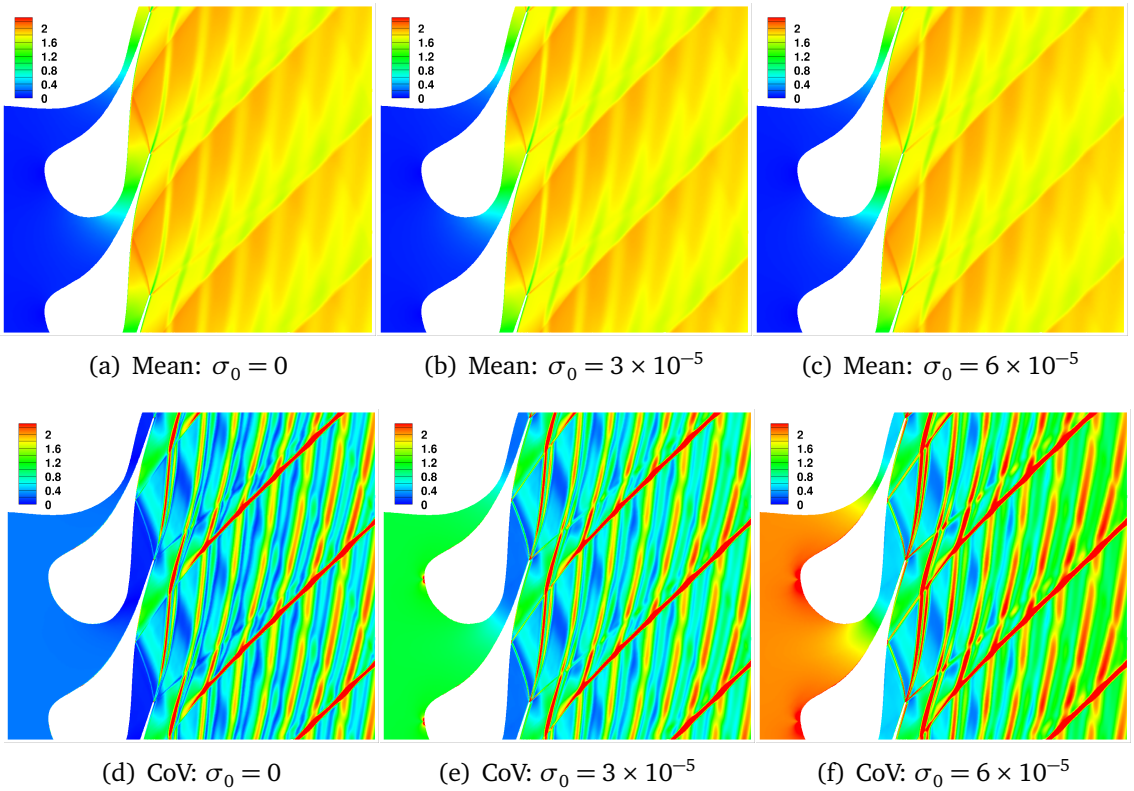

(a) Mean: $\sigma_0 = 0$ (b) Mean: $\sigma_0 = 3 \times 10^{-5}$ (c) Mean: $\sigma_0 = 6 \times 10^{-5}$

(d) CoV: $\sigma_0 = 0$ (e) CoV: $\sigma_0 = 3 \times 10^{-5}$ (f) CoV: $\sigma_0 = 6 \times 10^{-5}$

Figure VII.12 Mean and CoV[%] Mach contours for full load.

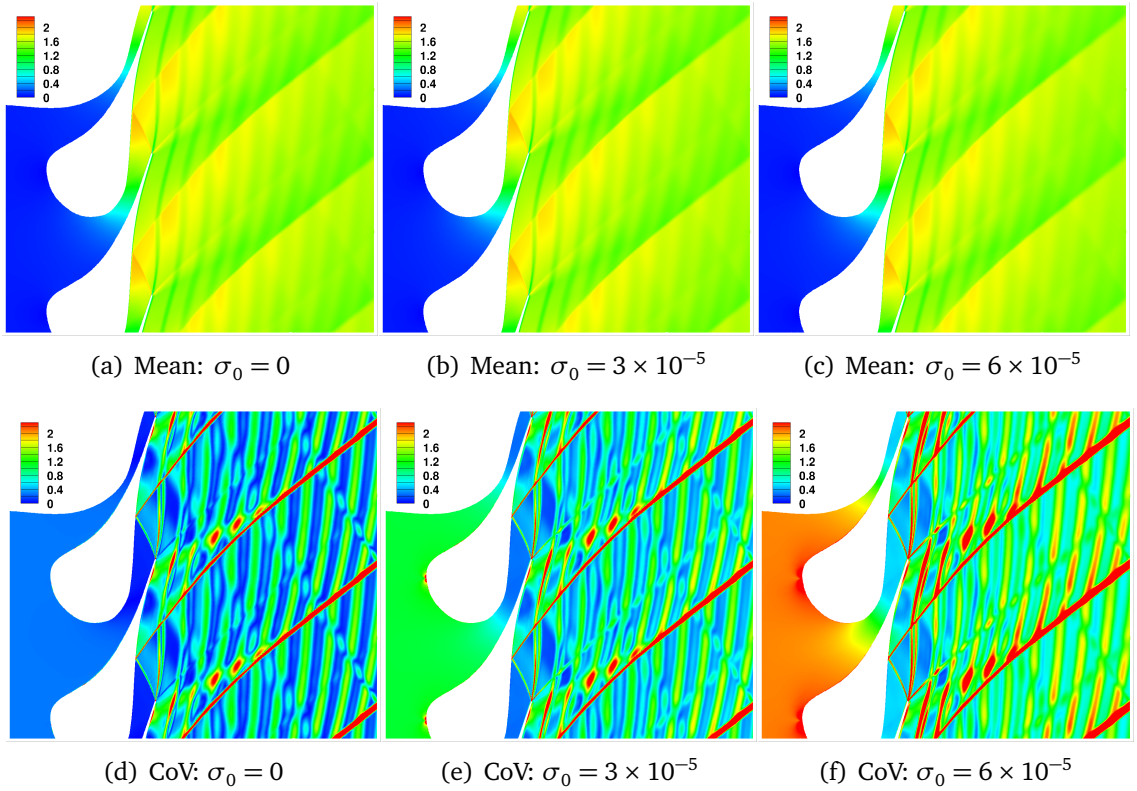

(a) Mean: $\sigma_0 = 0$ (b) Mean: $\sigma_0 = 3 \times 10^{-5}$ (c) Mean: $\sigma_0 = 6 \times 10^{-5}$

(d) CoV: $\sigma_0 = 0$ (e) CoV: $\sigma_0 = 3 \times 10^{-5}$ (f) CoV: $\sigma_0 = 6 \times 10^{-5}$

Figure VII.13 Mean and CoV[%] Mach contours for part load.

VII–4 Computation of a failure scenario

In this section, we illustrate a study about a failure scenario, where we consider a failure probability in the form $p_f = \mathbb{P}(\Delta P(\boldsymbol{Y}) > \Delta P_{crit})$, that is written as:

$$p_f = \mathbb{P}(J(\boldsymbol{Y}) < 0), \tag{VII.8}$$

where J denotes the performance function in the physical space. It is defined as:

$$J(\boldsymbol{Y}) = \Delta P_{crit} - \Delta P(\boldsymbol{Y}), \tag{VII.9}$$

where, as mentioned before, ΔP is the standard deviation of the azimuthal pressure distribution evaluated half an axial chord downstream the blade trailing edge [Rodriguez-Fernandez and Persico, 2015]. Then, we investigate a failure scenario, defined here as the QOI exceeding a given critical value of ΔP_{crit}.

The source of uncertainty depends on nine independent uniform random variables denoted as $\boldsymbol{Y}$, listed in Table VII.5, with their corresponding nominal conditions. A first source of uncertainty is associated to the operating conditions, namely the inlet total pressure P^t_{in} and temperature T^t_{in}, the static outlet pressure P^s_{out}, following [Pini, 2013, Pini et al., 2014b]. As a second source of uncertainty, we consider the coefficients associated to the thermodynamic model, depending on the fluid: the acentric factor ω, the heat capacity ratio γ, the gas constant $\mathcal{R}$, the critical pressure P_{crit}, temperature T_{crit} and density ρ_{crit}. A uniform uncertainty of 2% is assumed except for γ: a range ensuring thermodynamic consistency for this parameter is selected.

The failure analysis is performed by using a mesh of 7000 cells for the CFD computation [Razaaly et al., 2017], where the estimated performance function CPU cost is of 30 seconds (with a i7-6820HQ CPU, architecture x86-64). The choice of this coarse mesh is dictated by the will to compare the performances of the MetaAL-OIS method to a Monte Carlo Sampling, so requiring a vast number of computations.

Two scenarios are considered with two different critical values ΔP_{crit_1} and ΔP_{crit_2}:

- ΔP_{crit_1} is chosen such that $p_f \sim 10^{-3}$ (i.e. $\Delta P_{crit_1} = 19594$ kPa). The result is assessed by comparing with MCS.
- ΔP_{crit_2} is chosen such that $p_f < 10^{-5}$ (i.e. $\Delta P_{crit_2} = 20138$ kPa). In practice, ΔP_{crit_2} is selected as the maximal ΔP value sampled by means of MCS when considering $\mathbb{P}(\Delta P(\boldsymbol{Y}) > \Delta P_{crit_1})$.

A Monte Carlo Sampling is performed with a sampling size equal to $N_{MCS} = 10^5$, thus obtaining a CoV of $\delta_{MCS} = 10\%$ when evaluating $\mathbb{P}([\Delta P(\boldsymbol{Y}) > \Delta P_{crit_1}])$. The proposed approach MetaAL-OIS is compared to MCS in Table VII.6 and VII.7 considering the critical values ΔP_{crit_1} and ΔP_{crit_2}, respectively.

Variable	P_{in}^t	T_{in}^t	P_{out}^s	ω	γ	$\mathcal{R}$	P_{crit}	T_{crit}	ρ_{crit}
PDF	Uniform	Uniform	Uniform	Uniform	Uniform	Uniform	Uniform	Uniform	Uniform
Minimum	7.6 bar	541.15 K	1 bar	0.518	1.01	34.45 J/kg/K	13.87 bar	552.82 K	251.7 kg/m^3
Maximum	8.4 bar	549.15 K	2 bar	0.540	1.02	35.86 J/kg/K	14.44 bar	575.38 K	261.9 kg/m^3
Nominal	8 bar	545.15 K	1.072 bar	0.529	1.016	35.15 J/kg/K	14.15 bar	564.1 K	256.8 kg/m^3

Table VII.5 Random Variables.

	Metamodel-based Estimation		Unbiased Estimation			
Method	N_{calls}	$\hat{p}_{\tilde{G}}$	N_{calls}	$\hat{p}_f$	$\hat{\delta}_f$	$3-\hat{\sigma}_f$ Interval
MCS			100,000	1.000×10^{-3}	10.0%	$[0.700, 1.299] \times 10^{-3}$
MetaAL-OIS	**109**	$\mathbf{1.198 \times 10^{-3}}$	$\mathbf{109+200}$	$\mathbf{1.198 \times 10^{-3}}$	$\mathbf{< 0.097\%}$	$\mathbf{[1.194, 1.201] \times 10^{-3}}$
MetaAL-OIS (IS)			$109+200$	1.197×10^{-3}	<0.10%	$[1.193, 1.200] \times 10^{-3}$
MetaAL-OIS (CV+IS)			$109+200$	1.198×10^{-3}	$< 0.097\%$	$[1.194, 1.201] \times 10^{-3}$

Table VII.6 Comparison of the performances of the MetaAL-OIS with MCS: ΔP_{crit_1}

	Metamodel-based Estimation		Unbiased Estimation			
Method	N_{calls}	$\hat{p}_{\tilde{G}}$	N_{calls}	$\hat{p}_f$	$\hat{\delta}_f$	$3-\hat{\sigma}_f$ Interval
MCS			100,000	1.000×10^{-5}	100.0%	$[0.000, 3.000] \times 10^{-5}$
MetaAL-OIS	**131**	$\mathbf{4.002 \times 10^{-6}}$	$\mathbf{131+200}$	$\mathbf{4.002 \times 10^{-6}}$	**0.13%**	$\mathbf{[3.986, 4.017] \times 10^{-6}}$
MetaAL-OIS (IS)			$131+200$	3.982×10^{-6}	<0.14%	$[3.965, 3.998] \times 10^{-3}$
MetaAL-OIS (CV+IS)			$131+200$	4.002×10^{-6}	0.13%	$[3.986, 4.017] \times 10^{-6}$

Table VII.7 Comparison of the performances of the MetaAL-OIS with MCS: ΔP_{crit_2}

Considering the first critical value ΔP_{crit_1}, 109 CFD evaluations (i.e. evaluations of the performance function) are necessary to build the metamodel. The unbiased estimation provided with only 200 additional evaluations and a CoV lower of 0.10% is the same as the metamodel based estimation. It indicates that the metamodel is very accurate in the failure region. The unbiased estimation lies in the $3-\sigma$ range obtained using MCS evaluation. A similar accuracy with MCS would require about 10^9 CFD evaluations.

Moreover, based on the CPU costs of the CFD evaluations and of the proposed algorithm, the degree of parallelism required to obtain an estimation for p_f using MCS with a CoV of 5% with the same amount of time than MetaAL-OIS can be computed. A number of processors $N_{proc} = 1.3 \times 10^5$ is obtained in this case.

When using the critical value ΔP_{crit_2}, the metamodel building requires 131 CFD evaluations. Also, in this case, a sharp accuracy in the failure region is observed, since only 200 additional evaluations are necessary to provide an unbiased estimation associated with a CoV of 0.13%. A similar accuracy with MCS would require about 1.5×10^{11} CFD evaluations.

In this case, about $N_{proc} = 3 \times 10^7$ processors would be required to obtain an estimation for p_f using MCS with a CoV of 5% with the same amount of time than MetaAL-OIS.

Even if a single failure region characterizes this test-case, it gives some hints about the potential interest in using the MetaAL-OIS method for the analysis of ORC turbines.

VII–5 Conclusion

This study has proposed an uncertainty quantification analysis applied to the simulation of a turbulent non-ideal flow within a supersonic turbine cascade for Organic Rankine Cycle applications. In particular, a Kriging-based method has been coupled with a Computational Fluid Dynamic solver permitting to consider multiple sources of uncertainties associated with operating conditions, fluid parameters and an accurate representation of geometric tolerances. Two main scenarios are considered, *i.e.* a full-load (a high expansion ratio equal to ≈ 6) and a part-load (pressure ratio to ≈ 4) operating conditions.

The primary outcome of the study is an accurate statistical study of two quantities of interest, namely the total pressure loss and the mass flow rate. In particular, the total Sobol SIs, the probability density functions, and the statistical moments are computed.

Concerning the sensitivity analysis, results confirm the findings of previous work; the uncertainty in the outlet static pressure has the highest impact on the loss coefficient and is predominant with respect to the thermodynamic model uncertainties; the inlet total conditions, instead, dominate on the mass flow rate. With respect to the present state-of-the art, a novel result has been observed, *i.e.* the impact of operational and model uncertainties is drastically reduced when manufacturing tolerances are considered. The modal representation of manufacturing uncertainties and the related statistical analysis allow to highlight the most relevant modes, suggesting that specific areas of the blade have the highest impact on the overall uncertainty. The support of the probability density functions of the quantities of interest enlarges significantly when the manufacturing tolerances are plugged into the uncertainty analysis, and the functions take a regular Gaussian shape (differently from what observed if only operative and model uncertainties are considered). On a distributed basis, the flow released by the cascade exhibits relevant sensitivity to all sources of uncertainty, but again its statistical moments grow significantly in presence of manufacturing tolerances; as the dominating modes alter the blade shape in the rear suction side and the trailing edge thickness, the strength and inclination of the main rear shock undergoes significant variability, so as the width and defect of the blade wake.

A final study shown here concerns the analysis of a failure scenario for ORC turbines. The efficiency of the MetaAL-OIS method is assessed by comparison with a MCS sampling. The parsimonious behavior of MetaAL-OIS makes it particularly suitable for costly calculations. This preliminary study can be extended in the future to more realistic scenarios in the analysis of ORC turbine behavior.

VIII

Robust Optimization: a nested quantile approach

Overview *A quantile-based mono-objective RO formulation is applied to the design of the 2D profile of a supersonic turbine cascade, under a probabilistic constraint: the mean mass-flow rate is constrained to be with a prescribed range. Comparison with constrained DO and a classical RO approach,* i.e. *minimizing the mean of the performance function subject to the same constraint, exhibits advantages of such a method.*

VIII–1 Introduction

Small-medium scale ORC power plants ($O(10^1 - 10^4)$ kW) have received great interest in both the technical and academic community, in particular due to its ability to recover mechanical energy from low-grade heat sources such as, solar, geothermal energy, biomass or waste heat. As well known, the performance of the ORC power system is strongly linked to the efficiency of the turbine. The turbine aerodynamics is complicated by the use of organic fluids, which combine low enthalpy drops, high-expansion ratio per stage and low speed of sound, leading to transonic or supersonic ORC turbines, which demand the use of converging-diverging cascades and are commonly prone to strong shock waves and chocked flow conditions.

Recent advances of fluid dynamic simulation tools accounting for so-called *dense gas* effects, induced by the use of organic fluid described by complex Equation of State (EOS), has permitted the development of Fluid-dynamic Shape Optimization (FSO) approaches for automated design of ORC blade cascades. Nevertheless, in ORC applications, the operational variability of the hot and cold sources often results in significant variations of inflow and outflow conditions at the turbine, having a detrimental influence of the machine performance. The fluid-dynamic design of ORC turbines could benefit for automated design methodologies, possibly integrating uncertainties.

This work presents the results of the application of a *robust* shape optimization method to the design of a typical converging-diverging turbine nozzle for ORC applications (Chapter VI), aiming at minimizing a QoI quantifying the performance of the cascade, the QoI itself being a random variable.

Even though nowadays established and fully demonstrated, RO aimed at minimizing the mean of a QoI might suffer from a lack of control of this latter variability. Alternative formulations are possible to enhance the control of the variability, taking into account the QoI's standard deviation, for example by formulating the objective function as $\mu \pm k\sigma$, or Min σ s.t. $\mu < \mu_0$ for instance, where μ, σ denote the QoI's mean

and standard deviation respectively. However, such methods suffer from the fact that the user-defined parameters k, μ_0 have a substantial impact on the final design. Moreover, including explicitly the standard deviation in the objective function induces an increase in the computation burden in the stochastic space with respect to the mean. [Pisaroni et al., 2018] considers single- and multi-objective evolutionary algorithms involving in particular quantiles, a.k.a. value at risk, and conditional value at risk of objective or constraint functions, using a continuation multilevel Monte Carlo methodology. For ORC-driven problems, essentially multi-objective optimization have been proposed on both the mean and the standard deviation [Congedo et al., 2013a, Bufi et al., 2017, Bufi and Cinnella, 2017], a multi-point approach was proposed [Pini et al., 2014a].

In this study, we propose to minimize a high quantile of the performance function in the context of the ORC turbine blade optimization. It has the advantage of being highly interpretable: the QoI's 95% quantile is the threshold below which 95% of the QoI's realizations lie, involving that designer may choose a specific quantile level according to some technical constraints. The quantile can be easily evaluated as a function of the standard deviation σ, once the probability density functions (PDF) is assigned (for example, 2σ represents q_{95} for a Gaussian QoI). However, in robust optimization problems applied to aerodynamic design, which feature significant uncertainties and severe non-linear effects, the PDF of the QoI is not known a priori. As a second consideration, evaluating the quantile with classical Monte-Carlo methods is not cost-effective with respect to σ evaluation; however, state-of-the-art surrogate-based techniques permits the leverage this issue, by using a learning technique which exploits the local nature of the quantile, whose assessment can be seen as an inverse problem for tail probability computation. As shown in this study, the cost to evaluate the quantile can be even lower, or in any case of the same order of magnitude as the cost of assessing the average for example. The use of quantile can, however, be particularly beneficial in controlling the PDF of the optimal design, compared to optimizing an integral quantity such as the mean or the standard deviation.

The proposed method relies on a double-loop algorithm coupling the efficient quantile estimation (Chapter V), and a Bayesian optimization technique [E. Brochu and de Freitas, 2010]. The proposed approach is applied here to the constrained robust optimization of a well-known supersonic turbine nozzle for ORC applications [Colonna et al., 2008], that was considered for deterministic optimization with both inviscid [Pini et al., 2015] and Reynolds-Averaged Navier-Stokes (RANS) [Rodriguez-Fernandez and Persico, 2015, Vitale et al., 2017] models. It requires an automatized sequence of operations consisting of the parametrization of the blade, mesh generation and finally the CFD evaluation to compute the quantity of interest. A mesh-convergence study is presented to assess the CFD solution and the influence of the numerical error within the optimization process. We systematically use an inviscid flow solver for the robust optimization; alongside the inviscid robust optimization, also a deterministic optimization is performed using a RANS turbulent solver, for comparison with available high-fidelity optimization. All the optimal configurations are subsequently analyzed and compared by computing their QoI statistics with the RANS solver. In this study, we show therefore that for the ORC application, the use of a robust optimization method with a low-fidelity solver produces more efficient designs than those that could be obtained using a classical deterministic optimization with

a higher-fidelity solver. This study, therefore, proposes a concrete alternative to the optimization of ORC turbines with a systematic consideration of the uncertainties of the system.

The study is organized as follows. The problem of interest and a sketch of the numerical framework is illustrated in Section VIII–2. Section VIII–2.2 is devoted to the description of the CFD simulations, design parameterization and numerical verification. In Section VIII–3, the stochastic and optimization algorithms are described in details. In Section VIII–4, the optimization results are discussed, and the evidence about the interest of the proposed framework is provided. Conclusions and some perspectives are then provided in Section VIII–5.

VIII–2 Problem Formulation and numerical framework

VIII–2.1 RO Formulation

A classical single-objective optimization problem with constraints can be formulated as follows

$$\begin{aligned} \text{Minimize} \quad & f(\boldsymbol{x}) \\ \text{s.t.} \quad & g(\boldsymbol{x}) \in [g_{min}, g_{max}] \\ & \boldsymbol{x} \in \Omega, \end{aligned} \tag{VIII.1}$$

where f is a scalar QoI depending on a design vector $\boldsymbol{x}$ belonging to the design space Ω, and g is a constraint, which can assume values in the interval $[g_{min}, g_{max}]$.

If the problem is affected by some sources of uncertainties, then functions f and g are dependent also on a random vector, denoted as $\boldsymbol{\xi}$. In this case, a very common way of extending the problem mentioned in VIII.1, is to consider some meaningful statistics of the function f and g. For example, the *mean-based optimization* problem consists in:

$$\begin{aligned} \text{Minimize} \quad & \mathbb{E}_{\xi}[f(\boldsymbol{x}, \boldsymbol{\xi})] \\ \text{s.t.} \quad & \mathbb{E}_{\xi}[g(\boldsymbol{x}, \boldsymbol{\xi})] \in [g_{min}, g_{max}] \\ & \boldsymbol{x} \in \Omega, \end{aligned} \tag{VIII.2}$$

where $\mathbb{E}_{\xi}[\cdot]$ represents the expectation operator conditioned w.r.t. the random vector $\boldsymbol{\xi}$.

The idea of optimizing a combination of statistics stems from the need of limiting the variability of the QoI; alternatively from the aforementioned approach based on the mean objective function, we propose to solve the following *quantile-based optimization* problem:

$$\begin{aligned} \text{Minimize} \quad & q_{95}^{\xi}[f(\boldsymbol{x}, \boldsymbol{\xi})] \\ \text{s.t.} \quad & \mathbb{E}_{\xi}[g(\boldsymbol{x}, \boldsymbol{\xi})] \in [g_{min}, g_{max}] \\ & \boldsymbol{x} \in \Omega, \end{aligned} \tag{VIII.3}$$

where $q_{95}^{\xi}[f(\boldsymbol{x}, \boldsymbol{\xi})]$ represents 95% quantile of f under the probability measure of the random vector $\boldsymbol{\xi}$, satisfying a probabilistic constraint on g.

In this study, we illustrate the interest of such formulation of robust optimization comparing mean-based and quantile-based optimization in terms of computational cost and robustness of optimal individuals.

We denote here with f and g the outcomes of the CFD-based simulation, which is constituted by several steps, described in Subsection VIII–2.2, including a verification analysis about the mesh convergence.

All the optimization and UQ analyses reported in this study are based on Gaussian Process (GP) surrogates. Surrogates are systematically built over the space of design parameters $\boldsymbol{x}$, making use of different functions according to the metrics used for the optimization problem: deterministic optimization (f), quantile-based robust optimization (q_{95}), and also a mean-based robust optimization (μ) implemented and performed in order to have a benchmark for the novel quantile-based optimization here proposed.

Note also that a GP surrogate of the constraint function g over the space of design parameters $\boldsymbol{x}$ is built. An Expected Improvement (EI)-based strategy is then applied for solving the optimization problem, which is presented in Subsection VIII–3.

VIII–2.2 CFD-based simulation

The evaluation of the QoIs, *i.e.* f and g, is the outcome of a CFD evaluation for given vectors of design parameter $\boldsymbol{x}$ and uncertainties ξ. This evaluation requires the fulfillment of several steps, which are depicted in Figure VIII.1. Note that f refers either to Y or ΔP, and g to the mass-flow rate $\dot{m}$.

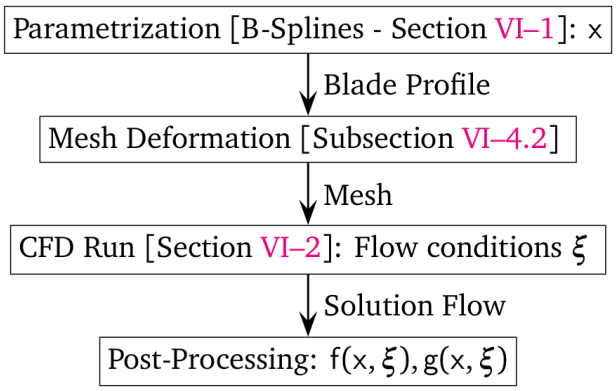

Figure VIII.1 CFD-based evaluation: $f(\boldsymbol{x}, \xi)$

The numerical simulations are performed using the NICFD solver described in Section VI–1 using the PRSV EOS to describe the non-ideal behavior of the organic fluid MDM.

Mesh Convergence Analysis

The spatial resolution of the computational mesh was selected as a result of a dedicated grid dependence study, based on the two performance parameters ΔP and Y.

In the following, the robust optimizations are performed using the inviscid model, while the deterministic optimizations and the *a-posteriori* assessment of all the optimal individuals are performed using both the inviscid and the RANS model. Therefore, two

different grid dependence analyses were carried out, and different alternative mesh resolutions were ultimately adopted for the two models. They are discussed separately in the following.

Euler Analysis The grid sensitivity analysis for the inviscid simulations was carried out considering ΔP only as QoI. This choice is motivated by the fact that the value of Y is of limited quantitative relevance in inviscid models (in such simulations the viscous contribution only depends on the artificial viscosity) Figure VIII.2(a) reports the percentage errors of 5 different meshes, the most refined one (250k cells) is taken as reference. The trend shows that the grid dependence of the solutions obtained using meshes composed by 36k cells or more is relatively low (below 1% difference with respect to the reference), with the mesh composed by 112k cells very close to the reference one (0.3% difference with respect to the reference). In light of these results, the 36k cell mesh was considered to provide the best trade-off between computational cost and accuracy; the reliability of the 36k cell mesh is further demonstrated by the pressure distribution along the blade sides, which reproduces with reasonable accuracy the one obtained with the reference mesh as reported in Figure VIII.2(b). Therefore, the 36k mesh was employed to carry out the deterministic and robust optimization procedures.

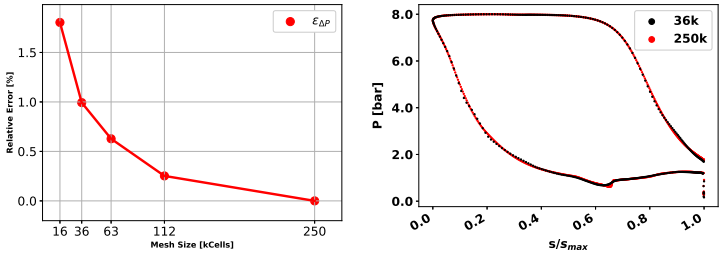

(a) ΔP Relative Error.

(b) Pressure Distribution comparison between 36k and 250k cells meshes.

Figure VIII.2 Euler Grid Analysis at Nominal Conditions on the baseline configuration.

RANS Analysis Simulations based on the RANS model are used to perform a benchmark deterministic optimization and are employed to assess the performances of all the optimized profiles. A grid analysis was again performed, to correctly set the mesh spatial discretization, for meshes ranging from 52k cells to 590k cells, with this latter taken as reference. Figure VIII.3(a) reports the percentage error computed on the performance estimators ΔP and Y. The 180k cells mesh show the best compromise between computational cost and accuracy, namely less than 1.5% and 0.3% of deviations for the objective functions Y and ΔP respectively, with respect to the finest mesh. This mesh is consequently used in the UQ framework to assess the different blade profiles resulting, CFD simulations being run in parallel. On the other hand, the deterministic optimization (Eq. VIII.1) algorithm (except in the initialization step) is substantially sequential. It is chosen to resort to the 52k cells mesh to perform the optimization in a reasonable amount of time, providing less accurate results (slightly

less than 5.5% and 2% deviations for the objective functions Y and ΔP respectively) for an acceptable computational cost. Figure VIII.3(b) plots the pressure distribution over the blade as resulting from using the 180k and the 590k elements mesh.

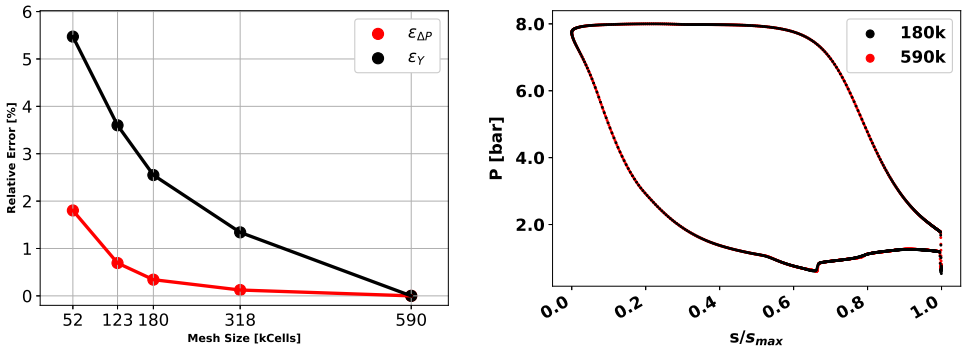

(a) ΔP and Y Relative Error.

(b) Pressure Distribution comparison between 180k and 590k cells meshes.

Figure VIII.3 RANS Grid Analysis on the baseline configuration.

Inviscid computations are performed using the 36k cells mesh. Convergence is assumed when either the density residuals are decreased by 10 orders of magnitude, while a maximal number of 5000 iterations is considered. Turbulent simulations used for DO are achieved using the 52k cells mesh, the CFD convergence being assumed when density residuals are decreased by 5 orders of magnitude or the maximal number of iterations of 7000 is reached. Final UQ assessments are conducted with the 180k cells mesh, with a maximal number of 15000 iterations. All simulations are performed using an adaptive CFL between 2.5 and 100.

Operating Conditions

As already recalled in the Introduction, ORC power systems operate in a context of continuous variability that alter the thermodynamic conditions both at the inlet and at the outlet of the turbine. Such variability propagates within the turbine and results in a change of boundary conditions for each cascade. Following [Pini et al., 2014a], in this study we model the operational variability as independent and uniform uncertainties on all the thermodynamic conditions, resulting in the random vector $\xi = [P^t_{in}, T^t_{in}, P^s_{out}]$. The range of these uncertainties is also reported in Table VIII.1. Note that the selection of the test-cases and the prescribed ranges of variability are based on previous experiences of the authors and on the very few information on the topic available from literature. However, the aim of the study is not to optimize a specific technical case but to investigate a challenging optimization problem for which robust design has an evident technical relevance.

	P^t_{in}	T^t_{in}	P^s_{out}
Nominal	8 bars	545.15 K	1.072 bars
Random	$\mathcal{U}[7.6, 8.4]$ bars	$\mathcal{U}[541.15, 549.15]$ K	$\mathcal{U}[1, 2]$ bars

Table VIII.1 Operating Conditions: Nominal and Random (Uniform and independent).

Note that we neglect the uncertainties on the parameters of the thermodynamic model since previous studies (Chapter VII) provided evidence about their limited impact with respect to the uncertainties on operating conditions for turbine cascades.

VIII–3 Algorithms Description

We perform four different optimizations in this study. The first two are under a deterministic constraint: one based on the inviscid flow model and aimed at minimizing ΔP and the other based on the RANS flow model and using Y as QoI. For both cases, the mass flow rate is the constraint function. Note that in the RANS-based optimization, the fitness function to optimize is Y and not ΔP, since this is a more traditional choice for RANS optimization. This case is introduced as a benchmark for illustrating the usefulness of using an inviscid model for driving the optimization, which could yield optimal design with efficient performances also for RANS simulations. The RANS-based optimization is made feasible by the relatively low cost of the deterministic formulation. The algorithmic details for deterministic optimization are given in Subsection VIII–3.1.

The two latter are robust optimizations, using the inviscid flow model, with the following formulations: the first one is based on a classical formulation, and it is focused on the minimization of the mean of ΔP (Subsection VIII–3.2); the second one is based on the novel approach proposed in this study, and aims at minimizing the 95% quantile of ΔP (Subsection VIII–3.3). Both robust optimizations are formulated under a mean-based probabilistic constraint on the mass flow rate.

VIII–3.1 Constrained Deterministic Optimization

For an n-dimensional problem, we are concerned with solving the following single-objective optimization problem:

$$\begin{aligned} \text{Minimize} \quad & f(\boldsymbol{x}) \\ \text{s.t.} \quad & g(\boldsymbol{x}) \in [g_{min}, g_{max}] \\ & \boldsymbol{x} \in \Omega, \end{aligned} \tag{VIII.4}$$

where f and g denote respectively the objective and constraint functions, and $\boldsymbol{x}$ is the vector of design variables corresponding to a blade parametrization, Ω being the design space, tensor product of intervals defined by upper and lower limits of each component of $\boldsymbol{x}$.

We employ a classic Bayesian framework for Surrogate-Based Optimization (SBO):

1. Set an initial DoE and build initial surrogates for the objective and the constraint functions.

2. Generate a new design solving a sub-optimization problem based on the surrogates. It aims at either further explore the design space or exploit a promising region. The new design is evaluated by means of the original objective function f (CFD). Surrogate models are updated.

3. Repeat Step 2 until a stopping criterion is satisfied or a maximal evaluation budget is reached.

A general sketch of the proposed framework for tackling robust optimization problems is provided in Figure VIII.4.

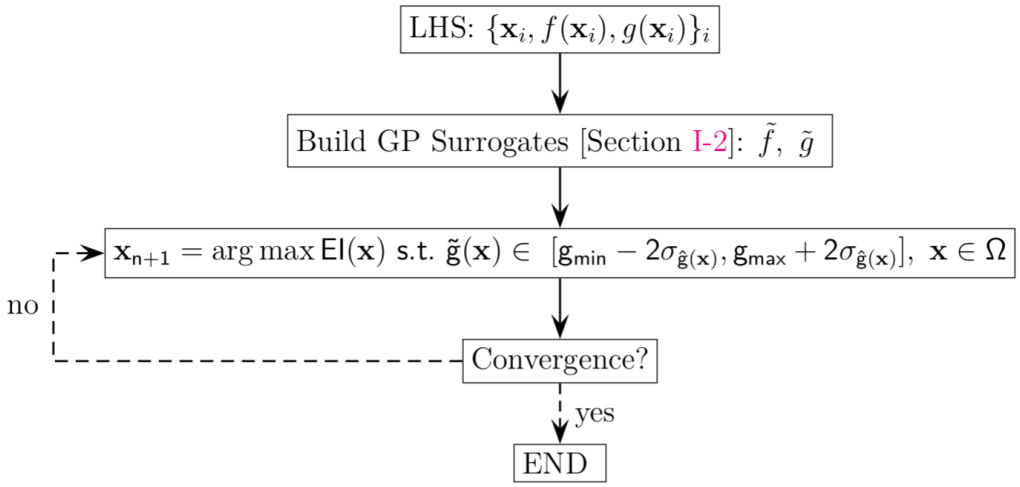

Figure VIII.4 General Sketch of the Expected Improvement [E. Brochu and de Freitas, 2010]-based algorithm used for Deterministic Optimization (Eq. VIII.2).

Initial DoE An initial DoE of size $N^{\boldsymbol{x}}_{LHS}$ is generated using LHS over the design space $[\boldsymbol{x}_{min}, \boldsymbol{x}_{max}]$, for which the objective and constraint functions are evaluated (CFD): $\{\boldsymbol{x}_i, f(\boldsymbol{x}_i), g(\boldsymbol{x}_i)\}_{i \in [\![1, N^{\boldsymbol{x}}_{LHS}]\!]}$. Surrogates of f and g are then built (Section I–2).

Sample Infill Criterion and Sub-optimization We focus on one of the most popular criterion in Efficient Global Optimization (EGO) [E. Brochu and de Freitas, 2010]: the Expected Improvement (EI).

For a given untried sample $\boldsymbol{x}$, the Improvement is defined as

$$I(\boldsymbol{x}) = \max(0, f_{min} - \hat{f}(\boldsymbol{x})), \tag{VIII.5}$$

f_{min} denoting the minimum objective function value observed so far. $\hat{f}(\boldsymbol{x})$ is the Gaussian predictor of the GP based surrogate of f at the sample $\boldsymbol{x}$. Note that $I(\boldsymbol{x})$ is a random scalar value which is positive when the prediction is lower than the best value known thus far, set to 0 otherwise. The new query point is found by maximizing the expected improvement:

$$\boldsymbol{x}^* = \arg\max EI(\boldsymbol{x}). \tag{VIII.6}$$

$EI(\boldsymbol{x}) = \mathbb{E}_{\hat{f}(\boldsymbol{x})}[I(\boldsymbol{x})]$ denotes the so-called *Expected Improvement* at $\boldsymbol{x}$, whose analytical expression is given by [E. Brochu and de Freitas, 2010]:

$$\begin{aligned} EI(\boldsymbol{x}) &= (\mu_{\hat{f}(\boldsymbol{x})} - f_{min})\Phi(Z) + \sigma_{\hat{f}(\boldsymbol{x})}\phi(Z) && \text{if } \sigma_{\hat{f}(\boldsymbol{x})} > 0 \\ &= 0 && \text{if } \sigma_{\hat{f}(\boldsymbol{x})} = 0, \end{aligned} \tag{VIII.7}$$

$Z = \dfrac{\mu_{\hat{y}(\boldsymbol{x})} - y_{min}}{\sigma_{\hat{y}(\boldsymbol{x})}}$, Φ (resp. ϕ) is the univariate Gaussian standard cumulative (resp. probability) density function.

The original EI infill criterion [E. Brochu and de Freitas, 2010] in Equation VIII.6 is slightly modified in order to take into account for the constraint. The new query point thus reads:

$$\begin{aligned} \boldsymbol{x}^* = & \arg\max EI(\boldsymbol{x}) \\ & \text{s.t. } \tilde{g}(\boldsymbol{x}) \in [g_{min} - 2\sigma_{\hat{g}(\boldsymbol{x})}, g_{max} + 2\sigma_{\hat{g}(\boldsymbol{x})}] \\ & \boldsymbol{x} \in \Omega. \end{aligned} \tag{VIII.8}$$

The sub-optimization problem Equation VIII.8 can be solved by means of any gradient-free[1] optimizer, e.g. using Covariance Matrix Adaptation (CMA) [Nikolaus Hansen, 2018] in Python. $\boldsymbol{x}^*$ is then evaluated with CFD, and surrogate models are updated.

The Bayesian optimization framework is summarized in Algorithm VIII.1 for a sake of clarity.

Algorithm VIII.1 Bayesian Optimization

Input: $N^{\boldsymbol{x}}_{LHS}$, $N^{\boldsymbol{x}}$

$N^{\boldsymbol{x}}_{LHS}$ samples: $\{\boldsymbol{x}_i, f(\boldsymbol{x}_i), g(\boldsymbol{x}_i)\}_i$

Build GP and EI (Eq. VIII.7): $\tilde{f}(\boldsymbol{x})$, $\tilde{g}(\boldsymbol{x})$, $EI(\boldsymbol{x})$

$i = N^{\boldsymbol{x}}_{LHS}$

while $i < N^{\boldsymbol{x}}$, **do**

  Selection: $\boldsymbol{x}_{i+1} = \arg\max EI(\boldsymbol{x})$ s.t. $\tilde{g}(\boldsymbol{x}) \in [g_{min} - 2\sigma_{\hat{g}(\boldsymbol{x})}, g_{max} + 2\sigma_{\hat{g}(\boldsymbol{x})}]$, $\boldsymbol{x} \in \Omega$

  Evaluation: $f(\boldsymbol{x}_{i+1}), g(\boldsymbol{x}_{i+1})$

  Update GP, EI

  $i \leftarrow i + 1$

Return $\boldsymbol{x}_i$

VIII–3.2 Robust Optimization: Mean Minimization

We describe the approach used to perform the following classical mean robust optimization:

$$\begin{aligned} \text{Minimize } & \mathbb{E}_{\xi}[f(\boldsymbol{x}, \boldsymbol{\xi})] \\ \text{s.t. } & \mathbb{E}_{\xi}[g(\boldsymbol{x}, \boldsymbol{\xi})] \in [g_{min}, g_{max}] \\ & \boldsymbol{x} \in \Omega, \end{aligned} \tag{VIII.9}$$

where f and g are scalar random functions, f representing the objective to minimize and g the constraint. $\boldsymbol{\xi}$ is the random vector, and $\boldsymbol{x}$ is the vector of design variables. A very similar approach w.r.t. the robust optimization consisting in minimizing a quantile is considered, the only difference consisting in computing the estimation $e_f(\boldsymbol{x})$ of the mean $\mathbb{E}_{\xi}[f(\boldsymbol{x}, \boldsymbol{\xi})]$, for each design sample $\boldsymbol{x}$ using the surrogate-based method described in Subsection I–3.1 based on $N^{\boldsymbol{\xi}}_{LHS} = 24$ LHS samples. The LHS sample size is selected based on stochatic convergence study not shown here for a sake of brevity.

[1] A gradient-based optimizer could be used, but would require derivatives of $EI(\boldsymbol{x})$.

The method is summarized in Algorithm VIII.2, based on the mean estimation (Subsection I–3.1).

Algorithm VIII.2 Robust Optimization: Mean Formulation

Input: N^x_{LHS}, N^x, N^ξ_{LHS}, N_{MC}
Sample N^x_{LHS} LHS profiles: $\{\boldsymbol{x}_i\}_i$
Evaluate Means $e_f(\boldsymbol{x}_i)$, $e_g(\boldsymbol{x}_i)$: Subsection I–3.1
Build GP and EI (Eq. VIII.7): $\tilde{q}_f(\boldsymbol{x})$, $\tilde{e}_g(\boldsymbol{x})$
$i = N^x_{LHS}$
while $i < N^x$ **do**
  Selection: $\boldsymbol{x}_{i+1} = \arg\max EI(\boldsymbol{x})$ s.t. $\tilde{e}_g(\boldsymbol{x}) \in [g_{min} - 2\sigma_{\hat{e}_g(\boldsymbol{x})}, g_{max} + 2\sigma_{\hat{e}_g(\boldsymbol{x})}]$
  Evaluate Means $e_f(\boldsymbol{x}_{i+1})$, $e_g(\boldsymbol{x}_{i+1})$: Subsection I–3.1
  Update GP and EI
  $i \leftarrow i + 1$

The parameters related to the constrained deterministic/robust optimization used here are summarized in Table VIII.2.

n	N^x_{LHS}	N^ξ_{LHS}	$\dot{m}_{min}$ [%]	$\dot{m}_{max}$ [%]	N	N^x
9	$5n$	24	98	102	10^6	300

Table VIII.2 Parameters for the Deterministic and Robust Optimizations (Subsubsection VIII–3.1 and VIII–3.3).

VIII–3.3 Robust Optimization: Quantile Minimization

Here we are concerned with solving the following single-objective optimization problem:

$$\begin{aligned} \text{Minimize} \quad & q^\xi_{95}[f(\boldsymbol{x},\boldsymbol{\xi})] \\ \text{s.t.} \quad & \mathbb{E}_\xi[g(\boldsymbol{x},\boldsymbol{\xi})] \in [g_{min}, g_{max}] \\ & \boldsymbol{x} \in \Omega, \end{aligned} \tag{VIII.10}$$

where f and g are scalar random functions, f representing the objective to minimize and g the constraint. $\boldsymbol{\xi}$ is the random vector, and $\boldsymbol{x}$ is the vector of design variables.

To solve this optimization problem, we propose a nested approach combining the SBO framework described in Subsection VIII–3.1, scalar UQ tools described Subsection I–3.1 and the efficient quantile estimation algorithm QeAK-MCS (Chapter V).

- For each design sample $\boldsymbol{x}_0$, the estimation $q_f(\boldsymbol{x}_0)$ of the 95-quantile $q^\xi_{95}[f(\boldsymbol{x}_0,\boldsymbol{\xi})]$ is carried out running CFD evaluations in the *stochastic space* (Chapter V), the latters being used to evaluate the estimation $e_g(\boldsymbol{x}_0)$ of the mean $\mathbb{E}_\xi[g(\boldsymbol{x}_0,\boldsymbol{\xi})]$ (Subsection I–3.1).
- The functions $q_f(\boldsymbol{x})$ and $e_g(\boldsymbol{x})$ are directly plugged-in the SBO framework described in Subsection VIII–3.1.

The present method is summarized in Algorithm VIII.3.

Algorithm VIII.3 Robust Optimization: Quantile Formulation

Input: N^x_{LHS}, N^ξ_{LHS}, N^x, ϵ, q_{ref}
Sample N^x_{LHS} profiles: $\{\boldsymbol{x}_i\}_i$
Evaluate Quantile $q_f(\boldsymbol{x}_i)$: Chapter V
Evaluate Mean $e_g(\boldsymbol{x}_i)$: Subsection I–3.1
Build GP and EI (Eq. VIII.7): $\tilde{q}_f(\boldsymbol{x})$, $\tilde{e}_g(\boldsymbol{x})$
$i = N^x_{LHS}$
while $i < N^x$ **do**
  Selection: $\boldsymbol{x}_{i+1} = \arg\max EI(\boldsymbol{x})$ s.t. $\tilde{e}_g(\boldsymbol{x}) \in [g_{min} - 2\sigma_{\hat{e}_g(\boldsymbol{x})}, g_{max} + 2\sigma_{\hat{e}_g(\boldsymbol{x})}]$
  Evaluate Quantile $q_f(\boldsymbol{x}_{i+1})$: Chapter V
  Evaluate Mean $e_g(\boldsymbol{x}_{i+1})$: Subsection I–3.1
  Update GP and EI
  $i \leftarrow i + 1$

VIII–4 Results

The capabilities of the methods described in Section VIII–3 are demonstrated by re-designing the supersonic cascade first investigated in [Colonna et al., 2008] and optimized under deterministic assumptions in [Pini et al., 2015], [Rodriguez-Fernandez and Persico, 2015], and [Vitale et al., 2017]. Four formulations are compared:

- *Euler-Based Deterministic Optimization*: the blade is optimized considering fixed operating conditions (nominal design point, as defined in Table VIII.1) under the constraint of preserving the baseline mass-flow within a 2% range. This case is performed following the deterministic optimization algorithm described in Subsection VIII–3.1, based on inviscid simulations where the QoI is ΔP. The resulting profile is referred to as the *O-E* profile.

- *RANS-Based Deterministic Optimization*: this case is similar to the former, but based on RANS simulations where the QOI is Y. The resulting profile is referred to as the *O-NS* profile.

- *Robust Optimization - Mean Formulation*: This case accounts for the environmental variability modeled by a random vector $\boldsymbol{\xi}$ (as defined in Table VIII.1), using a classic robust optimization formulation, namely minimizing the QoI mean using the method described in Subsection VIII–3.2, under the constraint of preserving the mean mass-flow rate within 2% of the baseline value. This profile is referred to as the *RO-E-*μ profile and is based on inviscid simulations.

- *Robust Optimization - Quantile Formulation*: This optimization also accounts for environmental variability modeled by a random vector $\boldsymbol{\xi}$ (as defined in Table VIII.1), solving the quantile-based optimization problem described in Subsection VIII–3.3, referring to the 95% quantile, under the constraint of preserving the mean mass-flow rate within 2% of the baseline value. This profile is referred to as the *RO-E-*q_{95} profil and is based on inviscid simulations.

ΔP is the best candidate as QoI for the euler-based optimization of this cascade, for several reasons. Previous studies [Colonna et al., 2008, Pini et al., 2015] indicate that the baseline cascade features a strong shock released downstream, whose mixing contributes significantly to the loss generation. Minimizing ΔP means primarily to minimize the shock losses, and hence indirectly to minimize the impact of shock-boundary layer interaction. Moreover, differently from Y, ΔP is properly quantified by both the inviscid and the RANS models, and hence it is more suitable for the present study as most of the optimizations performed are based on inviscid simulations. Finally, minimizing ΔP is also beneficial for the subsequent rotor aerodynamics, as a more uniform pressure field at the rotor inlet implies a lower stator-rotor interaction and, hence, a weaker rotor aerodynamic forcing, that in transonic/supersonic turbine might produce relevant performance degradation [Denos et al., 2001, Miller et al., 2003].

The optimal profiles that we obtained from the various optimizations are systematically compared with each other using the RANS solver.

This Section is organized as follows. A preliminary study about mesh and statistics convergence is presented in Subsection VIII–4.1. In Subsections VIII–4.2-VIII–4.3-VIII–4.4, the results of the optimization are documented: convergence, geometry profiles, mesh deformation, UQ assessment, the comparison between RANS and inviscid based results are discussed. In Subsection VIII–4.5, a physical analysis of the optimized cascades is performed.

VIII–4.1 Mesh and statistics convergence

The spatial resolution of the computational mesh is selected as a result of a dedicated grid dependence study, based on the two performance parameters previously introduced, *i.e.* ΔP and Y.

In the following analysis, the robust optimizations are performed using the inviscid model, while the deterministic optimizations and the *a-posteriori* assessment of all the optimal individuals are performed using both the inviscid and the RANS model. Therefore, two different grid dependence analyses are carried out, and two alternative mesh resolutions are ultimately adopted for the two models.

Euler Analysis The 36 kcell mesh is considered to provide the best trade-off between computational cost and accuracy. Therefore, the 36k mesh is employed to carry out the deterministic and robust optimization procedures. For the *a-posteriori* UQ analysis performed with inviscid flow assumption, lower restrictions in computational cost hold and the 112 kcell grid is employed. Still regarding the inviscid UQ analysis, different LHS sets (dimension 50, 100, 150) are considered to compute the performances of the blade. Results show that the convergence on the statistical quantities is reached with a LHS of dimension 100.

RANS Analysis Simulations based on the RANS model are used to perform a benchmark deterministic optimization and are employed to assess the performances of all the optimized profiles. Given the good compromise between accuracy and computational cost, the 180k cells mesh is retained to compute the blade performances in the UQ framework, while the 52k cells mesh is retained in the optimization procedure for solving Eq. VIII.1.

The performance statistics of the baseline profile are evaluated by performing an UQ analysis using LHS (off-design experiments) of dimension 50, 100 and 150. The PDF of Y (Total pressure loss) is plot (Figure VIII.5): the stochastic convergence is satisfactory reached with a LHS size of 100. The results of this post-processing procedure is detailed in Subsections I–3.1 and I–3.2.

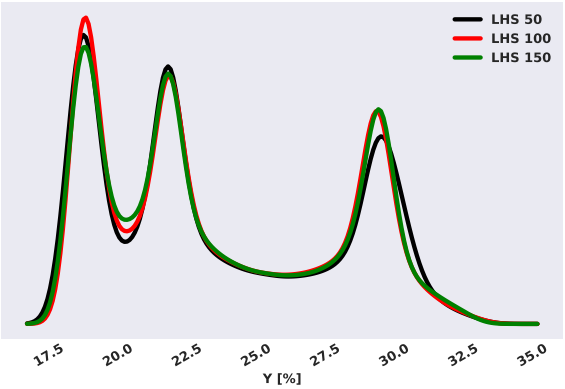

Figure VIII.5 RANS Grid Analysis on the baseline configuration: Y PDF obtained on the 180k cells mesh, for different LHS size.

VIII–4.2 Optimization Process

All the optimization problems are started with DoE consisting in $5d = 45$ profiles, the design space dimension being $d = 9$. The influence of the number of initial sample designs (in the context of bayesian deterministic optimization) has been studied by Han et al. [Han et al., 2015], along with the effect of randomness of the initial sampling (considering five LHS samples of the same size generated with different seeds). For 40 design variables, as a rule of thumb, they suggested to use between $0.5d$ and $2d$ as the size of the initial DoE, and found very similar convergence histories for the different LHS seeds. In the present study, we decided to exceed significantly with the DoE size ($5d$) with respect to the recommendations reported in [Han et al., 2015], with the aim of enhancing the reliability of the surrogate optimization. After the DoE, the EI optimization algorithm stops after a maximal number of runs (300) or if the same designs (or very close) are proposed by the optimizer. A review of the optimization processes is reported in this Subsection.

Euler-based deterministic optimization During the optimization, the best profile is obtained after 279 CFD evaluations, with $\Delta P = 1.70$kPa (285 designs are considered in total). Simulations are run in parallel using 8 processors, except when evaluating the initial DoE where each processor is devoted to one CFD simulation, in parallel though. The convergence curve shown in Figure VIII.6 (a) indicates a sharp reduction of QoI at the end of the DoE, thus suggesting that the initialization provides a very good approximation of response surface. Then, most of the minimization takes place in the first 50 CFD runs after the DoE. The mass flow rate constraint for the optimal profile (O-E) is satisfied at nominal conditions (See Table VIII.3).

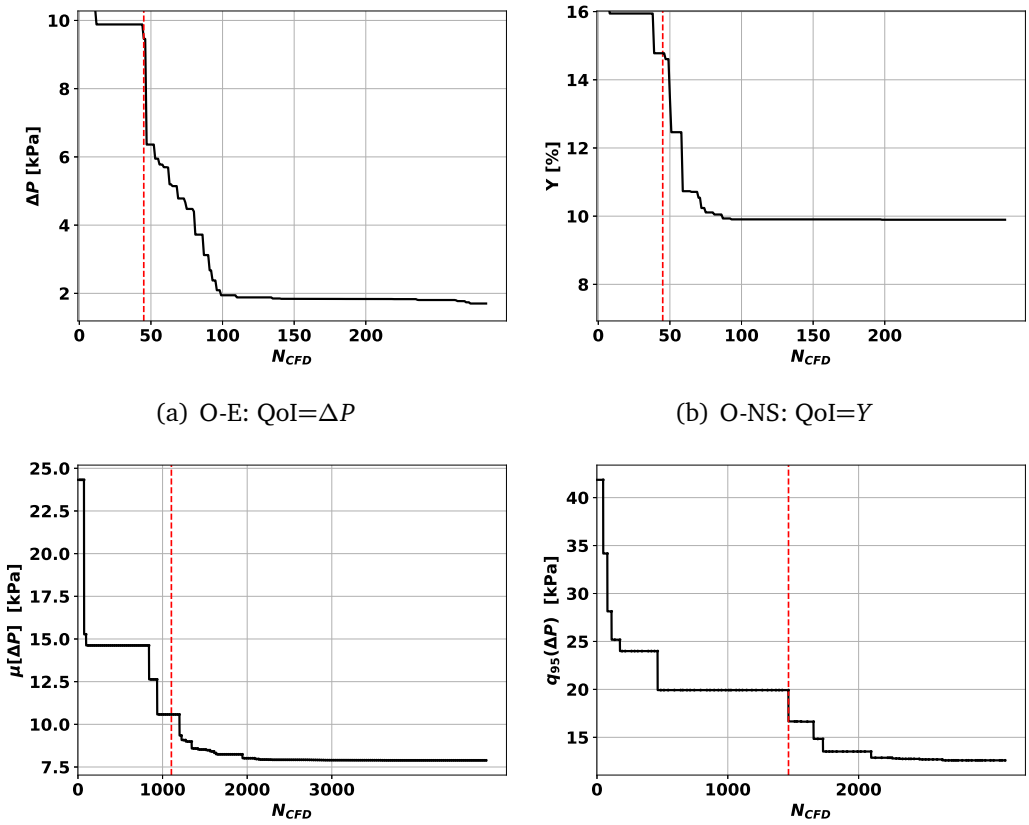

(a) O-E: QoI=ΔP (b) O-NS: QoI=Y

(c) RO-E-μ: QoI=$\mathbb{E}(\Delta P)$ (d) RO-E-q_{95}: QoI=$q_{95}(\Delta P)$

Figure VIII.6 Convergence curves during the optimization. Best QoI as a function of the number of CFD evaluations. The red vertical line indicates the optimization process start and corresponds to the number of CFD evaluations required for the LHS initial configurations.

RANS-based deterministic optimization During the optimization, the best profile is obtained after 198 CFD evaluations, with $Y = 9.9$ % (285 designs are considered in total). Also for the RANS optimization, the convergence curve shown in Figure VIII.6 (b) suggests a proper initialization and a quick convergence, as most of the minimization is achieved in less then 100 CFD runs. The mass flow rate constraint for the optimal profile (O-NS) is not satisfied at nominal conditions ($\dot{m} = 103.9\%\dot{m}_b$), when using the RANS model (Table VIII.3). This might be due to the 'weak' formulation of the constraint, which makes use of the predictive standard deviation based on the Kriging surrogate VIII.1.

Robust Optimization with Mean-based Formulation An initial DoE of 45 designs is considered (which require 1080 CFD evaluations, since a stochastic evaluation has to be performed for each profile). The best profile is obtained after 157 designs (requiring 3068 CFD evaluations), with $\mu^{\xi}(\Delta P) = 7.9$ kPa (201 blade configurations are considered in total, whose stochastic evaluations require 4824 CFD simulations). The convergence curve Figure VIII.6 (d) shows that a few high-performance designs are found already in the DoE phase, and the identification of the optimum in the following convergence process is relatively fast.

Robust Optimization with Quantile-based Formulation The Robust Optimization is initialized with a DoE of 45 designs (which in the stochastic framework requires 1416 CFD evaluations). The best profile is obtained after 83 designs (2640 CFD evaluations), with $q_{95}^{\xi}(\Delta P) = 12.6$ kPa. 103 designs are considered (3120 CFD evaluations). The convergence curve in Figure VIII.6 (c) shows again that the DoE is effective in finding few individuals with relatively low q_{95}, followed by a fast process. It is to be noted that the minimization based on the quantile is less demanding than that based on the mean, as almost the half of the blade configurations are required to find the optimum.

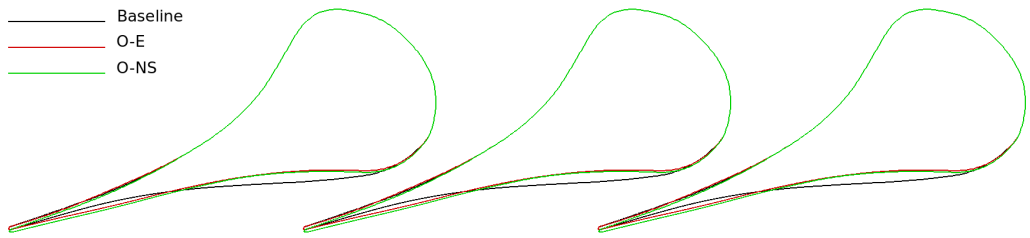

(a) Deterministic

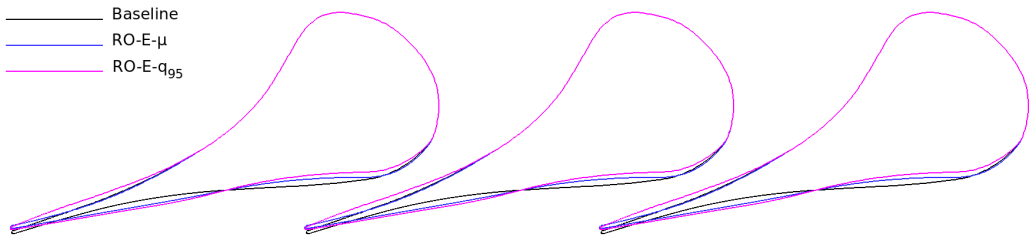

(b) Robust

Figure VIII.7 Blade profiles comparison; top: baseline compared to deterministic optimal blades; bottom: baseline compared to robust optimal blades.

VIII–4.3 Optimal blade profiles

The optimal blade profiles obtained with the four optimization processes discussed above are shown in Figure VIII.7 in comparison to the baseline configuration, with frame VIII.7(a) reporting the two deterministic designs and VIII.7(b) the two robust designs.

The two deterministic optimal blades are very similar each other and much different with respect to the baseline layout, especially on the suction side of the blade downstream of the (sonic) throat. The present optimal blades resemble the ones documented in previous design exercises performed on this cascade (e.g., [Pini et al., 2015],[Rodriguez-Fernandez and Persico, 2015],[Vitale et al., 2017]). The deterministic optimization drives the design towards blades featuring an accentuated curvature in the diverging section of the bladed channel, i.e. between the sonic throat and the cascade opening, and an almost straight profile in the region of unguided turning. As it will be discussed in the later Subsection on aerodynamic analysis, such shape allows eliminating the strong shock originated in the baseline cascade flow, with beneficial effects on both the uniformity of the pressure field downstream of the cascade and the

cascade loss. This also explains why the two optimizations lead to very similar optimal blades; as a further consideration, the similarity between results obtained with Euler and RANS optimizations indicates that, in the present case, the inviscid model is able to capture the main flow features and hence it is a suitable choice for the more advanced, and more computationally-intensive, robust optimizations.

The two robust designs differ significantly from both the baseline and the deterministic ones. The general action of the optimization is similar to the one commented above, with both the robust-optimal blades featuring a larger curvature on the suction side downstream of the throat and a straight rear suction side. Nonetheless, the area ratio between the cross-sections at the throat and at the opening is lower than that of the deterministic-optimal blades. This can be explained considering that almost all the realizations in the uncertain scenario feature a lower pressure ratio with respect to the nominal one. Since the cross-section at the (sonic) throat is nearly fixed by the constraint on the mass flow rate, the reduction of area-ratio implies a lower area of the cross-section at the blade opening for both the robust-optimal blades with respect to the deterministic-optimal ones. The two blades also feature minor but visible differences, mostly concentrated in the shape of the divergent part of the bladed channel, which also lead to a slight difference in the area-ratio across the divergent, which is higher for the quantile-based optimal blade than for the mean-based one. Instead, the two blade profiles nearly overlap in the rear suction side downstream of the cascade opening and in the trailing edge region, where indeed the flow effects most affecting the QoI (ΔP) take place.

VIII–4.4 Analysis of the statistics

A UQ analysis is conducted on the four optimal profiles obtained to assess their performances with the RANS high fidelity model with a 180k cells mesh. As mentioned in Subsection VIII–4.1, $N_{LHS} = 100$ samples are used. A similar analysis is conducted with the inviscid model with 36k cells mesh, used in the optimization process.
The UQ analysis statistics results are summarized in Table VIII.3, obtained using the scalar UQ analysis tools presented in Subsection I–3.1 and commented below.

		Profiles				
Performances		Baseline	O-E	O-NS	RO-E-μ	RO-E-q_{95}
Nominal (Euler)	ΔP [kPa]	17.1	1.7	-	12.7	12.2
	Y [%]	16.0	5.4	-	12.1	12.1
	$\dot{m}$ [%]	100.8	100.5	-	101.7	98.3
Nominal (RANS)	ΔP [kPa]	17.5	2.3	2.3	13.6	13.1
	Y [%]	19.0	9.4	9.1	15.5	15.5
	$\dot{m}$ [%]	100.4	100.6	103.9	101.6	98.2
μ, σ, q_{95} (Euler)	ΔP [kPa]	25.7, 6.7, 35.2	16.5, 10.1, 30.4	-	7.9, 3.9, 13.4	8.2, 3.0, 12.7
	Y [%]	20.7, 4.4, 27.8	13.9, 7.1, 26.7	-	8.6, 2.0, 12.8	10.3, 2.2, 14.6
	$\dot{m}$ [%]	100.9, 3.2, 105.9	100.3, 3.2, 105.2	-	101.2, 3.2, 106.3	98.0, 3.1, 102.8
μ, σ, q_{95} (RANS)	ΔP [kPa]	25.4, 6.4, 34.4	16.6, 10.0, 29.5	16.7, 9.9, 29.7	8.2, 3.9, 14.1	8.4, 3.1, 13.2
	Y [%]	23.5, 4.2, 30.0	17.7, 6.8, 29.5	17.6, 7.0, 29.8	12.4, 1.8, 16.1	13.8, 2.1, 18.0
	$\dot{m}$ [%]	100.5, 3.2, 105.4	100.5, 3.2, 105.5	103.9, 3.2, 109.0	101.3, 3.2, 106.3	98.0, 3.1, 102.8

Table VIII.3 Scalar Statistics Analysis for the optimized and baseline profiles. Euler (resp. RANS) quantities are based on CFD evaluations on 36k (resp. 180k) cells meshes. Random scalars are evaluated using $N_{LHS} = 100$ CFD evaluations. $\dot{m}$ is expressed in percentage of $\dot{m}_b = 15.23$ kg/s/m.

Nominal Conditions At nominal conditions, the profiles *O-NS* and *O-E* clearly outperform the other ones with the lowest total pressure loss Y and ΔP. This values of minimal loss and pressure variation are consistent with those obtained in previous deterministic optimization performed on the very same profile [Pini et al., 2015], [Rodriguez-Fernandez and Persico, 2015], and [Vitale et al., 2017]. Moreover, the two deterministic-optimal blades feature very similar losses and identical pressure variability downstream of the cascade, as a further proof of the reliability of inviscid model for the present configuration. Note that also the robust profiles, *RO-E-*μ and *RO-E-*q_{95}, perform similarly at nominal conditions and slightly better than the baseline one with a total pressure loss Y of 15.5%. Even though a probabilistic mass flow constraint is prescribed in the Robust Optimization problems, both *robust* profiles satisfy the deterministic mass flow constraint.

Uncertain Conditions Mean, standard deviation and 95% quantile of the QoIs ΔP, Y, and the mass flow rate $\dot{m}$ are evaluated for each blade profile using consecutively inviscid and RANS models (Table VIII.3). For each profile, the random mass flow rate shows a rather similar behavior, with a mean value very close to the nominal one and a standard deviation close to 3% of $\dot{m}_b$. It is interesting to note that the performance of the baseline and of the deterministic-optimal profiles deteriorate significantly at off-design conditions. In particular, the *O-E* exhibits $\mathbb{E}[\Delta P] = 16.5\%$ with a large variability associated, quantified by a standard deviation of 10.1% (even larger than that of the baseline one), against an optimal $\Delta P = 2.3kPa$ in nominal conditions; similarly, for the *O-NS* the UQ analysis reveals that $\mathbb{E}[Y] = 17.6\%$ with standard deviation 9.9%, to be compared to $Y = 9.1\%$ at nominal conditions. It is, however, to be noted that the deterministic profiles have been designed for a nominal point which is far from the mean of uncertain conditions (Table VIII.1). This represent a typical scenario of ORC power systems, in which the design (nominal) condition does not correspond to the average of the expected variability; hence, for this technology a robust design approach is particularly beneficial for reducing the sensitivity of the design from the expected variability.

The potential advantages of robust design can be fully appreciated by considering the statistics of the RO-E-μ and RO-E-q_{95} profiles. Considering the inviscid UQ analysis and focusing on ΔP as QoI (for consistency with the model used throughout the optimization), the RO-E-μ profile has the lowest mean value 7.9 kPa and a standard deviation of 3.9%, comparably lower w.r.t. both the deterministic designs. The low variability of the 'conventional' robust optimization is further improved by the here-proposed novel quantile-based design, as the RO-E-q_{95} profile feature both the lowest 95-quantile and the lowest standard deviation of 3.0%, with only a slight increase of mean value (8.2 kPa) w.r.t. the mean-based design. The lowest variability of the RO-E-q_{95} blade is confirmed by the RANS analysis, which provides nearly identical results of the inviscid one in terms of ΔP; this, once again, indicates that the inviscid model is able to provide a reliable design when combined with a proper selection of QoI.

Focusing now on the blade performance in terms of loss coefficient, and considering the RANS UQ analysis, the two robust-optimal blades behave almost equivalently, the RO-E-μ blade slightly outperforming the RO-E-q_{95} one both in terms of both mean value and variability. This is not in contradiction with the optimization, which used another QoI as fitness function. The results of the present robust optimization indicates that a quantile-based approach has the potential to minimize the variability of loss coefficient, if set with Y as QoI and using the RANS model, at the expense of a

significant increase of computational cost Note that the 36k Euler simulation takes 500s; the 52k RANS simulation takes 1200s, on 8 procs. Roughly, the CPU time is then multiplied by 16. In light of the present results, the similar performance of the two robust-optimal blades might not justify such increased effort.

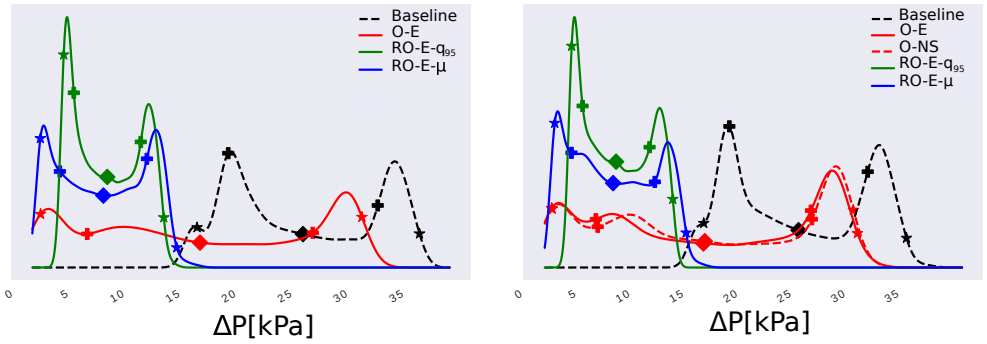

(a) ΔP: Euler 36kcell mesh

(b) ΔP: RANS 180kcell mesh

Figure VIII.8 PDF comparison between the optimized and baseline profiles. "Plus" dots indicate $\mu \pm \sigma$, square dots indicate μ, star dots indicate respectively 5% and 95% quantiles. $N_{LHS} = 100$ samples considered.

The complete picture of the stochastic properties of the baseline and optimal blades is provided by the plots of the PDF for ΔP, Y and $\dot{m}$, reported in Figures VIII.8, VIII.9, and VIII.10 respectively. In these figures, the PDFs computed with Euler and RANS models are reported in separate frames, the former considering only the baseline and the optimal blades obtained with inviscid optimization process (i.e., *O-E*, RO-E-μ, and RO-E-q_{95}) and the latter featuring also the *O-NS* one. First considering ΔP as QoI, it is evident that the baseline blade has a relatively large variability (which, in such PDF plots, can be visualized as the PDF 'support' which is, in turn, quantified as the difference between the 5% and the 95% quantiles). This illustration of the difference between 5% and 95% quantiles provides a good representation of the PDF support. The deterministic-optimal blades, which feature a very similar PDF when evaluated with a RANS model, perform generally better than the baseline one but exhibit a very large variability, so that their support overlaps the one of the baseline in a large region ($16kPa \leq \Delta P \leq 32kPa$); this means that in a very significant fraction of the possible realizations of the process, the baseline can actually outperform the deterministic-optimal blades. From this perspective, the robust-optimal blades provide a crucial improvement with respect to deterministic-optimal ones; not only the mean value of QoI is much lower than that of the other blades, but the entire support of their PDFs is significantly reduced and, especially, it is almost completely decoupled from that of the baseline blade; this ensures that the robust-optimal blades outperform the baseline configuration in almost all the possible realizations of the process within the variability range. When comparing the PDFs of the robust-optimal blades, some differences emerge in a context of global similarity; in particular, the quantile-based approach guarantees not only to minimize the 95% quantile, but in general to slightly reduce the support of the PDF, and so the variability as already seen in terms of the standard deviation. From this perspective, the novel quantile-based approach is competitive

w.r.t. the more standard mean-based approach both in terms of computational cost (as already commented) and in terms of the stochastic performance of the optimization outcome.

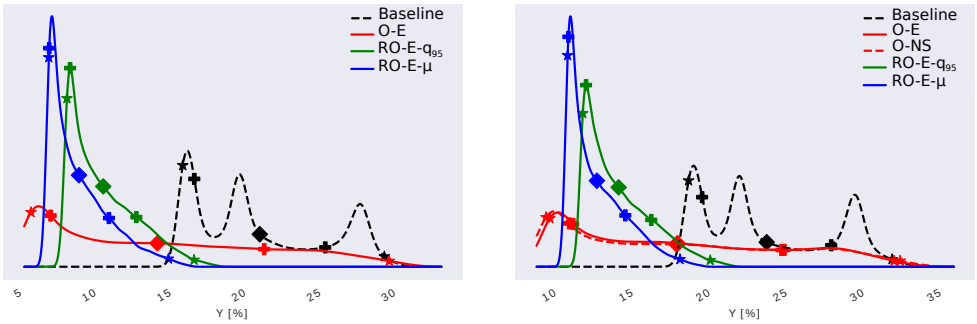

(a) Y: Euler 36kcell mesh (b) Y: RANS 180kcell mesh

Figure VIII.9 PDF comparison between the optimized and baseline profiles. "Plus" dots indicate $\mu \pm \sigma$, square dots indicate μ, star dots indicate respectively 5% and 95% quantiles. $N_{LHS} = 100$ samples considered.

The considerations reported above also hold for the PDFs of Y. The two deterministic-optimal blades are still equivalent and with a large support which overlaps largely with the one of the baseline; again, the robust-optimal blades provide a much smaller support w.r.t. the baseline one, with an almost complete decoupling. As already noted when commenting the statistics, the two robust-optimal blades feature similar stochastic properties, with the RO-E-μ blade providing a slightly smaller mean value and 95% quantile; however, the two supports are almost entirely overlapped, demonstrating that the two robust-optimal blades are practically equivalent in terms of loss coefficient.

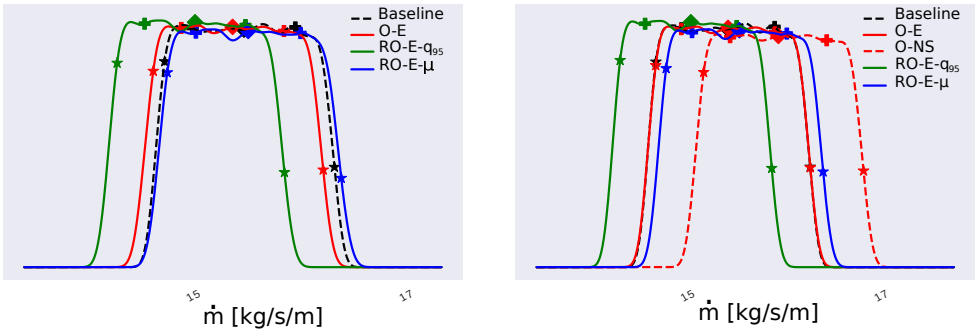

(a) $\dot{m}$: Euler 36kcell mesh (b) $\dot{m}$: RANS 180kcell mesh

Figure VIII.10 PDF comparison between the optimized and baseline profiles. "Plus" dots indicate $\mu \pm \sigma$, square dots indicate μ, star dots indicate respectively 5% and 95% quantiles. $N_{LHS} = 100$ samples considered.

Finally considering the flow rate, all the PDFs are qualitatively similar and exhibit a nearly identical support. As for the entire range of variability considered the cascades is always in choked-flow conditions, the shape and the support of the PDFs directly

depend of the variability in the inlet total conditions and the PDF takes a trapezoidal shape, as discussed in detail in [Romei et al., 2019]. Some of the PDFs are slightly shifted, with the RO-E-q_{95} blade featuring a slightly smaller mean and quantiles and the *O-NS* blade exhibiting a slightly higher mean and quantiles, but most of the realizations of all the optimal blades are within the acceptability range of probabilistic constraint. Note that for all blades, all the realizations are not within the acceptability range of the probabilistic constraint, since, finally, only the mean is constrained to be within that range.

VIII–4.5 Physical Analysis

This Subsection discusses the aerodynamics of the baseline and optimal blades under uncertain flow conditions, considering RANS simulations, with the aim of explaining the properties of the optimal blades on the basis of physical considerations. Three classes of quantities are considered. The Mach number contour fields at nominal conditions are first shown in Figure VIII.11. Then, the UQ framework for vector statistics presented in Subsection I–3.2 and the CFD evaluations performed in Subsection VIII–4.4 are used to evaluate statistics of flow fields; in particular, the contours of mean and CoV of the Mach number are considered and are reported in Figures VIII.12 and VIII.13 respectively. 73 modes out of 100 PCA modes are retained in the analysis, corresponding to a cumulative energy conservation beyond 99.99%.

The figures of this Subsection show the contours for the baseline and for all the optimal blades, and are supplemented by corresponding isentropic Mach number distributions over the blade surface. The isentropic Mach number is evaluated assuming an isentropic expansion from total upstream condition to the local static pressure on the blades, and is commonly used in turbomachinery application to highlight relevant cascade features such as shocks, over-speeds, and adverse pressure gradients.

Nominal Mach contours At nominal conditions, the baseline blade exhibits the onset of a strong shock resulting from the coalescence of a train of compression waves generated on the curved rear suction side. The strong shock is responsible for both the high loss and the large pressure gradients affecting the cascade-exit flow field. When the blade is optimized for the nominal condition only, the optimization removes the main shock by identifying optimal blades with straight shape in the rear part; since the trailing edge of the blade is geometrically constrained, the optimization cannot eliminate the fish-tail shock system generated at the trailing edge. Considering the M_{is} profiles, the comparison between the deterministic-optimal blades and the baseline one clearly shows that the latter features a higher over-speed, followed by a shock (which is the reflection on the blade surface of one trailing edge shock generated on the adjacent blade) and by a diffusion which ultimately leads to the generation of the main shock; while the reflected shock is present also in the optimal blades, and depends on the constraint in the trailing edge thickness, the subsequent diffusion is absent from the pressure distribution of the deterministic-optimal blades. The two deterministic-optimal blades are shown, once again, to perform equivalently even though obtained with different flow models.

The flow uniformity provided by the deterministic optimization is not achieved with the robust-optimal blades, which instead exhibit the onset of a strong shock in the cascade-exit flow field. However, the origin of this shock is completely different

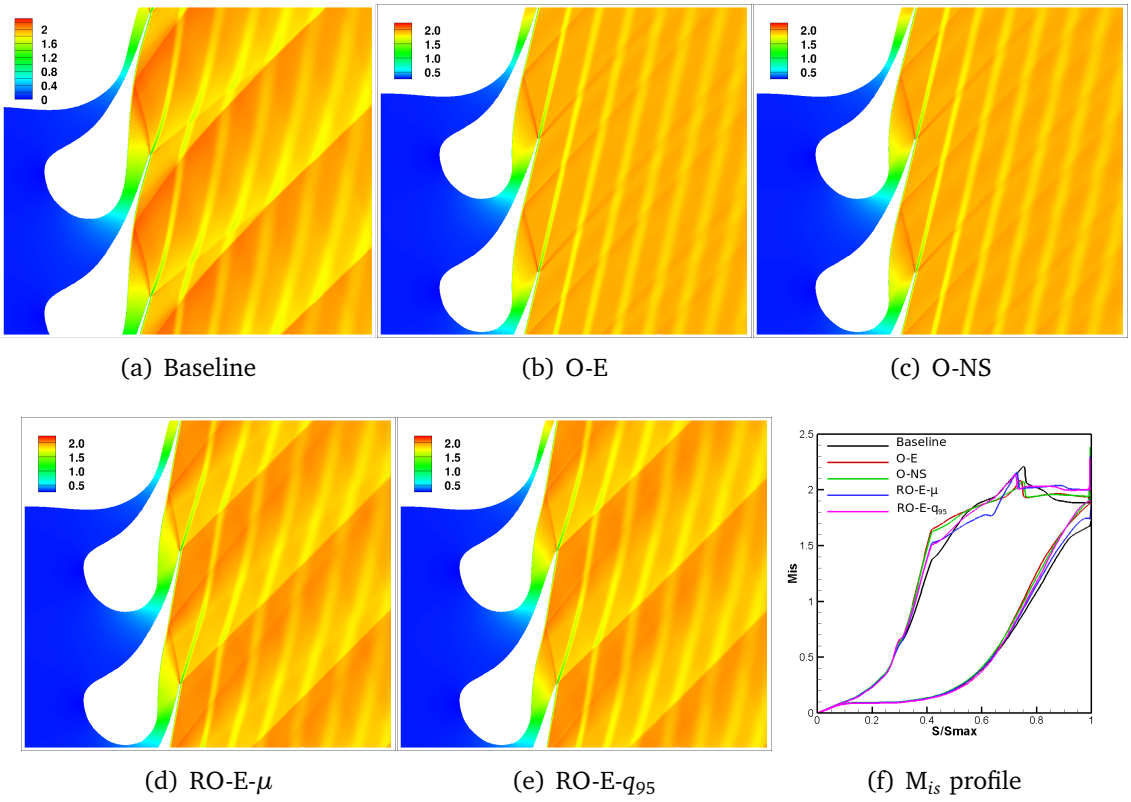

(a) Baseline (b) O-E (c) O-NS

(d) RO-E-μ (e) RO-E-q_{95} (f) M_{is} profile

Figure VIII.11 Mach contours at Nominal conditions. [RANS, 180k cells mesh]

from that of the baseline shock. As a matter fact, the shock is generated on the suction side of the trailing edge and not as a result of a diffusion on the blade. This is further confirmed by the M_{is} profiles, which show no diffusion on the suction side downstream of the reflected shock for both the robust-optimal profiles. The shock is simply originated by the fact that the robust-optimal blade are designed for having good performance in a range of conditions which feature, in average, lower expansion ratio than in the nominal condition. As already commented when discussing the blade shape, the robust-optimal blades have a lower area-ratio across the divergent w.r.t. the deterministic-optimal ones. As a result, when operated in nominal condition, the robust-optimal blades are in fact in post-expansion, which as well known leads to the onset of a shock at the trailing edge.

Mean Mach contours In light of the flow features emerging in nominal conditions, it is interesting to analyze the mean aerodynamics of the optimal blades. It is worth noticing, at first, that commenting a mean contour is not straightforward, as each point in the mesh is result of a statistical procedure and, hence, the field is not reproducing the flow in a specific condition; therefore, only the general trends can be commented while the analysis of detailed features might be misleading. The distribution computed for the baseline blade shows a similar character of that commented for the nominal condition, even though with smeared gradients. This indicates that the baseline blade suffers from the effects of the rear-shock in whole variability range; this is reasonable since the flow in the rear suction side of the blade remains supersonic for all considered

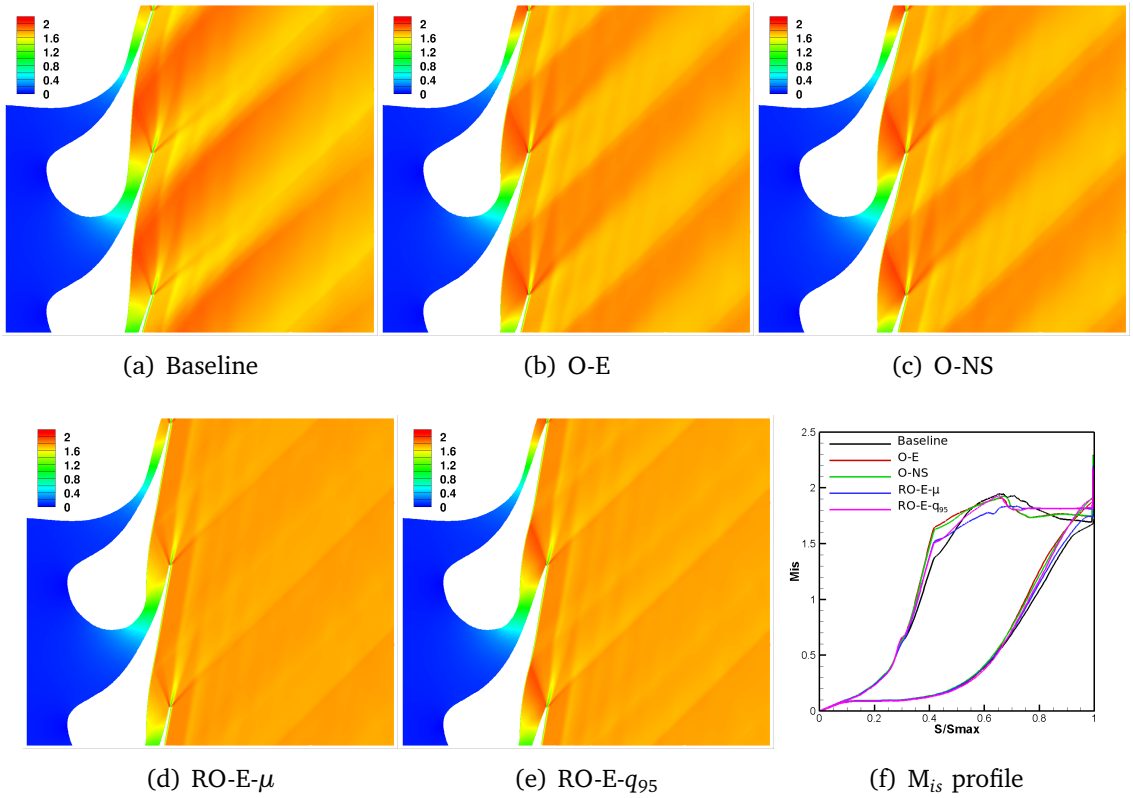

(a) Baseline (b) O-E (c) O-NS

(d) RO-E-μ (e) RO-E-q_{95} (f) M_{is} profile

Figure VIII.12 Mach contours mean considering uncertain operating conditions, evaluated by means of PCA UQ (Subsection I–3.2) [RANS, 180k cells mesh, $N_{LHS} = 100$]

conditions, so the curved shape always leads to the onset of the rear shock. As a further confirmation of what above, the mean profile of M_{is} shows a large diffusion region downstream of the mean over-speed.

The deterministic-optimal blades improve the behavior of the baseline one, but the uniformity observed in nominal condition is not visible anymore; conversely, clear variations in mean Mach number appear in the cascade-exit flow field, which seem to be correlated to the shock-pattern generated at the trailing edge. This is motivated by the area-ratio of both the deterministic-optimal blades, which is too large for most of the realizations occurring within the prescribed variability; as a result, the cascade often operates in post-compression condition, which leads to the onset of relatively strong shocks at the trailing edge.

The robust optimization is able to greatly reduce the effects discussed above; in particular, RO-E-μ blade features an almost uniform mean Mach number distribution at the cascade exit, proving that the mean-based optimization is able to select the most suitable blade configuration over the range of variability. Interestingly, the RO-E-q_{95} blade provides a similar flow uniformity at the cascade exit, even though the quantile-based optimization does not consider explicitly the mean values in the optimization algorithm. Differences between the two robust-optimal cascade exist and are concentrated in the divergent, with the RO-E-q_{95} blade featuring a higher over-speed; however, in the rear suction side downstream of the reflected shock the M_{is} profiles of the two blades become nearly identical, thus leading to a very similar cascade-exit mean flow field.

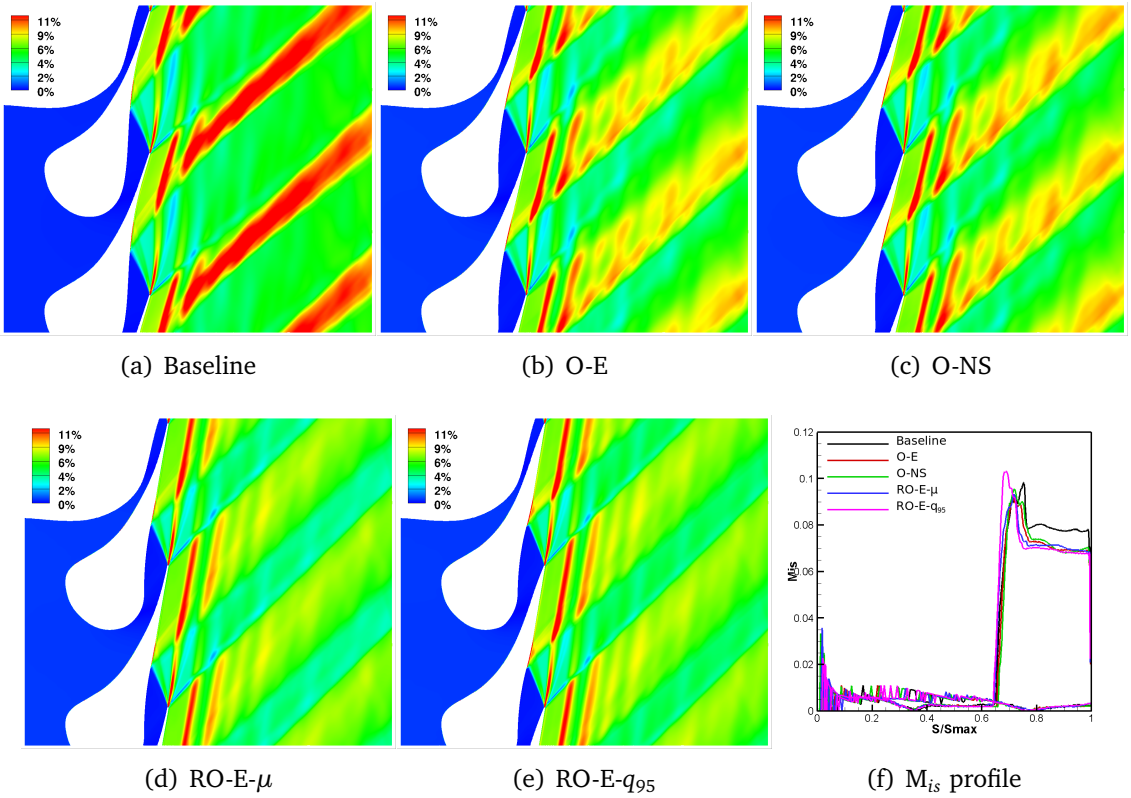

(a) Baseline (b) O-E (c) O-NS

(d) RO-E-μ (e) RO-E-q_{95} (f) M_{is} profile

Figure VIII.13 Mach contours CoV [%] considering uncertain operating conditions, evaluated by means of PCA UQ (Subsection I–3.2) [RANS, 180k cells mesh, $N_{LHS} = 100$]

CoV Mach contours In order to highlight the local distribution of variability over the flow field, the CoV coefficient (defined as the ratio between the standard deviation and the mean) is now analyzed. First considering the baseline blade, very high CoV is established in the region interested by the compression wave / shock, suggesting that the main shock featuring this blade undergoes a significant evolution across the considered range of variability. A somehow similar patter is found for the deterministic-optimal blades with a generally high CoV in the region comprised between the reflected shock and the trailing edge shock. A net reduction of CoV is found when analyzing the robust-optimal blades, which anyway exhibit a CoV distribution similar to that of the other blades. This result suggests that, when a proper QoI is selected, the application of the robust design allows reducing the variability in the entire flow field.

VIII–4.6 Computational Cost

In the present Subsection, details about the CPU cost during the optimization process are discussed. All computations are done on a standard laptop with an i7-6820HQ CPU at 2.70GHz equipped with 8 processors. Detailed information is available in Table VIII.4. In the four optimization cases, $N^{\boldsymbol{x}}_{LHS} = 45$ profiles are considered for the initial DoE, that can be considered independently. Then, the EI loop sequentially provides a new profile to be analysed.

Deterministic Optimization: Euler The initial DoE is evaluated in parallel. $N_{iter} =$ 246 iterations are totally required. The best profile is obtained after 279 CFD simulations.

Deterministic Optimization: NS $N_{iter} = 285$ iterations are totally required. During the optimization loop, each RANS simulation is run with 8 processors. The best profile is optained after 198 simulations.

Quantile-Based Optimization The initial DoE step requires 1808 CFD calls. For a given profile, ~ 32 CFD calls corresponding to ~ 4 iterations are necessary to evaluate the so-called 95% quantile. In total, $N_{profiles} = 103$ profiles are considered requiring 3120 CFD calls, in $N_{iter} = 390$ iterations. The 83^{th} profile is the best, requiring 2640 CFD calls.

Mean-Based Optimization The quantile-based optimization initial DoE is used in order to compare the two robust strategies from the same initial designs. For any given profile, 24 CFD calls corresponding to 3 iterations are necessary to evaluate the mean, leading to a total number of $N_{iter} = 603$ iterations. The 157^{th} profile is the best, requiring 3768 CFD calls.

Note that this cost is about $\sim 50\%$ more than for the quantile-based optimization). For the present case, 16 CFD runs in the stochastic space for evaluating the mean is very conservative, but necessary for the proposed algorithm. As a general comment, a relevant point to raise is the interest in optimizing a quantile since a higher control of the PDF variability is possible with a comparable cost of computing a quantile with respect to the mean.

	O-E	O-NS	RO-E-q_{95}	RO-E-μ
Initial DoE	45(45)	45(45)	45(1416)	45(1080)
$N_{profiles}(N_{CFD})$	285(285)	285(285)	103(3120)	201(4824)
N_{iter} (8 PROC)	246	285	390	603
Time/iteration	500s	1200s (8 procs)	500s	500s

Table VIII.4 CPU cost required during the optimization process for the three profiles in terms of time and number of CFD calls. $N_{profiles}$ is the number of profiles considered during optimization, N_{CFD} the number of CFD evaluations required to assess the corresponding profiles and N_{iter} the number of iterations necessary assuming parallel computations with 8 processors.

VIII–5 Conclusion

A Robust optimization method based on a quantile formulation is fully documented and applied to the design of supersonic ORC cascade operating in the non-ideal regime. We provide evidence about the advantages of a quantile-based formulation with respect to a conventional mean-based robust optimization. By applying the novel quantile-based procedure, we obtain a RO-E-q_{95} profile, which has the lowest 95-quantile and the smallest standard deviation of 3.0%, with only a slight increase of mean value (8.2

kPa) w.r.t. the mean-based design. In the case of interest here, a significant control about the variability of the PDF through the quantile formulation is obtained with a lower computational cost with respect to the mean. More generally, it seems that even in a case when the computational cost could be of the same order of magnitude, the choice of a quantile formulation should be preferred.

Concerning the optimal blades, the flow uniformity provided by the deterministic optimization is not achieved with the robust-optimal blades, which exhibit the onset of a sharp shock in the cascade-exit flow field. This shock comes from the fact that the robust-optimal blades are designed for having good performance in a range of conditions which have a lower expansion ratio than in the nominal state. When operated in nominal condition, the robust-optimal blades are in fact in post-expansion, which as well known leads to the onset of a shock at the trailing edge. The two robust designs differ significantly, the area ratio between the cross-sections at the throat and the opening is lower than that of the deterministic-optimal blades. This behavior can be explained considering that almost all the realizations in the uncertain scenario feature a lower pressure ratio with respect to the nominal one. The two blades also feature minor but visible differences mostly concentrated in the shape of the divergent part of the bladed channel, which also leads to a slight difference in the area-ratio across the divergent.

Another relevant point observed is that the robust optimization with low-fidelity solver can yield a design with better performances (on both Euler and RANS evaluations) than the one coming from a purely deterministic optimization using a high-fidelity RANS solver. This behavior has a great interest in ORC turbine optimization since it could provide a concrete alternative approach with respect to the current procedures to guarantee better the robustness of the design at a moderate computational cost.

Globally, in this study, high-fidelity RANS analysis provides nearly identical results of the inviscid one in terms of ΔP. This behavior shows that the inviscid model can provide a reliable design when combined with a proper selection of QoI.

IX

Conclusion and Perspectives

This thesis is divided into two parts. The first is dedicated to the calculation of rare events, while the second is focused on the modeling, simulation and optimization of ORC turbines. In the following, the conclusions are drawn on the studies carried out, also providing some prospects for future work.

IX–1 Part 1: Rare Events

The first part of this manuscript is devoted to some contributions related to the computation of Rare Events. Three surrogate[1]-based algorithms are developed for the problems of small failure probabilities and extreme quantiles. Those contributions are primarily motivated with the aim to extend existing RBDO methods for extreme (rare) events. It is emphasized that the three methods proposed rely on a surrogate-based adaptive sampling strategy. They are in particular depending on the Gaussian assumption satisfied by the underlying Gaussian Process at the basis of the Kriging metamodel, to use the local *U-criterion* introduced by [Echard et al., 2011] which exploits the mentioned gaussianity to estimate the so-called probability of misclassification. Consequently, any surrogate method could in theory be used, provided it includes a Gaussian prediction error measure, similarly to the Kriging predicitive variance. The local *U-criterion* could be also in theory, replaced by a more elaborate (and computationally expensive) criterion such as the so-called *Stepwise Uncertainty Reduction* (SUR) (see [Bect et al., 2017]), as the proposed algorithms focus mainly on providing suitable (*already good*) candidate samples based on which the ranking performed by means of a local/global criterion is less influential for their efficiency.

In Chapter III, the surrogate-based method for the computation of tail probabilities features a sequential efficient refinement strategy and is characterized by an innovative ISD based on Gaussian Mixtures permitting the accurate estimation of very small failure probabilities in a reasonable number of calls (several million in practice). Moreover, a new estimator inspired by [Dubourg et al., 2013] combining Control Variate and Importance Sampling permits the unbiased computation of probabilities of failure. The proposed method has been tested until six uncertainties, providing accurate metamodels exploited by Gaussian Mixture ISDs in less than approximately 150 evaluations. In all test-cases considered, MetaAL-OIS performed better than compared methods, or at worst, with a computational cost of the same order of magnitude of

[1] Kriging also referred to as Gaussian Processes, described in Section I–2.

the best method for the test-case of interest. An unbiased estimation is then obtained using *only* hundred additional evaluations (from an already accurate surrogate, easing the latter part).

In Chapter IV, an extension of the popular AK-MCS [Echard et al., 2011, Schöbi et al., 2016] is presented for the estimation of small probabilities. The proposed algorithm is compared to the more sophisticated BSS [Bect et al., 2017] method, which combines bayesian SUR strategies and Subset Simulation. Its efficiency is illustrated on challenging test-cases from [Bect et al., 2017] specifically dedicated for small failure probabilities (in the range $10^{-5} - 10^{-9}$). The efficiency of eAK-MCS, concerning both the number of performance function calls and accuracy, seems to be of the same order of magnitude of BSS, which is to the best of the author' knowledge, one of the most efficient methods for assessing very small failure probabilities. There are two clear advantages of eAK-MCS over BSS. The adaptive refinement of eAK-MCS aims at directly refine the LSS, a natural consequence being that an estimate of the failure probability accounting for the epistemic uncertainty handled by Kriging is available at each step of the algorithm (making it in particular, *in theory*, suitable for RBDO algorithms [Moustapha et al., 2016]). On the contrary in BSS, the user should wait for the refinement to reach the last threshold to have an estimate of the failure probability. Moreover, for reliability, eAK-MCS is more comfortable to implement w.r.t. BSS, with a clear parallelization strategy.

Additionally, numerical studies conducted with particularly *unfavorable* initial DoE (no LSS detected at the initialization) and with sequential strategy, show the ability of eAK-MCS to identify multiple failure regions, providing some hints about its robustness. The main advantage of eAK-MCS is its substantial similarity to the popular AK-MCS: AK-MCS derived methods could be with limited efforts adapted to *extreme* events. This distinctive feature is in particular illustrated in this thesis (Chapter V), since the AK-MCS based [Schöbi et al., 2016] quantile estimation algorithm has been extended for extreme quantile (level in the range $10^{-5}-10^{-9}$) successfully, at the price of minor additional developments. A tuned isotropic Gaussian ISD is used to estimate the quantile-based on the current Kriging surrogate, while the parallel refinement algorithm of eAK-MCS provides several samples to enrich the DoE. Its performance is assessed and illustrated through the benchmark analytical functions (up to six uncertainties) used for eAK-MCS, showcasing very satisfactory accuracy (relative error below $\sim 1\%$) and robustness, in less than 100 evaluations of the original model, in average. Moreover, a multi-quantile selection permits an additional level of parallelization.

The limitations of the developed methods consist first in the assumption that the input model can be *exactly* recast in the standard space. Secondly, only a limited number of uncertainties can be considered (up to ten approximately) due to the Kriging surrogate construction and to reduced efficiency of both MCMC and Gaussian Mixture ISD in higher dimensions. Finally, the proposed methods depend strongly on the ability to fit the performance function by the surrogate.

Future Work The main direction of improvement for the reliability analysis tools presented in the sequel resides in the combinaison of the adaptive sampling scheme, from MetaAL-OIS and eAK-MCS, featuring respectively an elaborate but sequential strategy and a parallel and straightforward to implement one. This potential approach would permit to significantly reduce the number of evaluations of the performance function. The Gaussian Mixture ISD would exploit the surrogate for accurate small

failure probability estimates, in a more efficient way than the tuned isotropic Gaussian used in eAK-MCS. The adaptive refinement of the quantile estimation as presented in QeAK-MCS would obviously benefit from this improved sampling strategy for failure probability. However, for extreme quantiles, another direction of improvement would lie in a very accurate estimation of the quantile associated to the current surrogate model. On-going work is performed in that direction. Consequently, it is expected to improve both eAK-MCS and QeAK-MCS in terms of efficiency[2] and accuracy[3]. Such improvements would then attain their limits in the framework described in the sequel, and would not address the following limitations:

- Need to recast the rare event formulation in the standard space;
- Fitting Kriging hyperparameters limits the input dimensionality and the number of the performance function evaluations;
- The methods depends strongly of the ability for the surrogate to fit the performance function.

Besides the guidelines aforementioned, it is worthy to point out that eAK-MCS and QeAK-MCS are robust and efficient methods that can be used for small failure probability and extreme quantile estimation with an outstanding trade-off between ease of implementation and accuracy/efficiency. Both methods are expected to significantly help the extension of RBDO approaches for extreme (rare) events.

IX–2 Part 2: Robust Optimization Methods for ORC Turbine Cascade

The second part of this manuscript focused on shape optimization methods for ORC turbomachinery applications. An analysis of the combined effects of different uncertainties on a typical supersonic turbine nozzle is proposed. Then, a numerical framework for Robust Optimization under a probabilistic constraint is illustrated and applied to design under uncertainties of the latter cascade.

Chapter VII investigates the application of advanced stochastic techniques to the analysis of a typical supersonic turbine cascade. The uncertainties considered include operating conditions (total inlet pressure and temperature), fluid closure parameters describing the PRSV EOS in SU2, and geometric variability modeling deviations from manufacturing operations, based on RANS simulations. Such preliminary analyses are of crucial importance for Robust Optimization as this permit to rank and quantify uncertainties. The following comments are valid on the basis on the different input variability (or *scenarios*) investigated. The primary outcome of the study concerning the sensitivity analysis, results confirm the findings of previous work; the uncertainty in the outlet static pressure has the highest impact on the loss coefficient and is predominant with respect to the thermodynamic model uncertainties; the total conditions at the inlet, instead, dominate on the mass flow rate. Modeling of manufacturing tolerances is performed combining random field (non-stationary Gaussian Process with

[2]Number of calls of the performance function.
[3]More efficient IS strategy for suitable exploitation of surrogate when dealing with extreme events.

null mean) modeling and its low dimensional parametrization using a Karhunen-Loeve (KL) expansion [Dow and Wang, 2014]. The modal representation of manufacturing uncertainties and the related statistical analysis allow for highlighting the most relevant modes, suggesting that specific areas of the blade have the highest impact on the overall uncertainty. The support of the probability density functions of the quantities of interest enlarges significantly when the manufacturing tolerances are plugged into the uncertainty analysis, and the functions take a regular Gaussian shape (differently from what observed if only operative and model uncertainties are considered). A high dimensional output UQ propagation method is reported, permitting the investigation of the impact of uncertainties on the physical flow. The flow released by the cascade exhibits relevant sensitivity to all sources of uncertainty, but again its statistical moments grow significantly in the presence of manufacturing tolerances. As the dominating modes alter the blade shape in the rear suction side and the trailing edge thickness, the strength and inclination of the main rear shock undergoes significant variability, so as the width and defect of the blade wake.

Moreover, the performance of the advanced reliability analysis method for the computation of *unbiased* failure probabilities MetaAL-OIS has been assessed on an original configuration, considering nine random variables combining operating and fluid parameters uncertainties. A surrogate-based estimation of the failure probability is obtained accurately in less than 150 CFD evaluations, while an additional 200 CFD simulations result in an unbiased estimate. It provides hints of the applicability of such a method in a real industrial context.

Because of the lack of data available in this delicate topic (e.g. measurements of existing cascades are confidential), the approach intended to consider several *realistic*[4] uncertainty models in order to showcase the possible outcomes of such a surrogate-based UQ (cost-effective) framework. Indeed, the outcomes of the UQ analysis is strongly linked to the input variability. For instance, increasing the range of variability of the inlet total temperature is expected to increase its sensitivity indices w.r.t. some performance output measure as well. As stated in Chapter I, characterizing uncertainties related to operating conditions, model parameters and geometric imperfection[5] is both of paramount importance, and not straighforward to achieve. Industry might benefit from systematic methods aiming to reach such objectives, and obviously significant efforts should be addressed towards that direction. In Chapter VIII, a Robust optimization method based on a quantile formulation is fully documented and applied to the design of supersonic ORC cascade operating in the non-ideal regime. In particular, the mean mass-flow rate is constrained to be within a prescribed range, which slightly complicates the RO process. Advantages of a quantile-based formulation with respect to a conventional mean-based robust optimization are showcased. By applying the novel quantile-based procedure, we obtain a RO-quantile optimal profile, which has the lowest 95-quantile and the smallest standard deviation, with only a slight increase of mean value w.r.t. the mean-based design. In the case of interest here, a significant control about the variability of the PDF through the quantile formulation is obtained with a lower computational cost with respect to the mean. More generally,

[4] To some extent.

[5] Out of scope of the present manuscript

it seems that even in a case when the computational cost could be of the same order of magnitude, the choice of a quantile formulation should be preferred due to this variability control.

Future Work In the context of RO, several improvements are desirable. As illustrated, the RO formulation has a significant impact on the final *robust* profiles. Multi-objective RO formulations partially address this issue, usually with a detrimental effect in term of computational cost, since it would provide not only one *robust* optimal design but a set of *non-dominated* solutions denoted as *Pareto* optimal solutions. The expert judgment could potentially help in selecting the most promising designs, based on suitable UQ analyses or engineering considerations. To avoid such studies involving extra human time and computational cost, some investigation in the mathematical formulation of the RO itself could be of interest.

The RO optimization methods presented in the manuscript could benefit from several improvements in term of computational cost. Indeed, in the bi-level approach considered, for each design a full UQ analysis (evaluation of mean/quantile) is *too accurately* performed: restricting the accuracy of the UQ analysis only for *promising designs* could dramatically save computational cost. Coupling very promising *Bounding Boxes*-based approaches [Rivier and Congedo, 2018a, Rivier and Congedo, 2018b] to the present framework could significantly reduce the computational effort. Moreover, using suitable surrogates (e.g. co-Kriging) able to deal with CFD simulations of different levels of fidelity (and computational cost) is of critical interest when dealing with the cost-effectiveness of RO or even DO methods. Low CFD models such as inviscid alongside coarse meshes, fast to evaluate, could permit, at low CPU cost, to explore the design space while capturing, even loosely, the flow physics. Subsequently, a reduced number of high CFD models evaluations (e.g. RANS) would be necessary to consider promising design regions. Essential features of surrogate-based RO or DO methodology lie indubitably in the accuracy of the surrogate model and its ability to capture the underlying physical model. GP-based methods such as Kriging usually suffer from the input dimensionality, thus limiting the design space. Gradients of QoIs (e.g. using the adjoint) could be integrated into Kriging and significantly improve its accuracy [Han et al., 2010]; however, reducing efficiently the dimensionality is still a crucial question. Recent works consisting in either perform a deterministic shape optimization in a design space of reduced dimensionality [Lukaczyk et al., 2014] or perform a GP-based surrogate suitable with high dimensional input [Lataniotis et al., 2018] paves a promising way to this end.

IX–3 Long-term perspectives

One critical aspect of RO and rare event methods which is not addressed here is the question of the uncertainties modeling. Indeed, it has been assumed that the random vector modeling UQ is parametric (aleatory) and perfectly known. In [Garzon, 2003], the geometric variability due to manufacturing processes is parametrized by a random vector of moderate size (10-20) from 150 accurate measurements of compressor blades using PCA. Such an approach might be corrupted with uncertainties, possibly influencing the RO or the UQ assessment process. This question is particularly es-

sential when a reliability analysis needs to be performed[6] since the resulting failure probability might be vitiated by uncertainties related to the random vector modeling. In [Chabridon et al., 2017], the impact of *uncertain* random input vector on the failure probability is partially investigated, the failure probability is then considered as a random variable.

Shape design methods, for turbomachinery, accounting for uncertainties are becoming increasingly popular; industry, in particular, should benefit from systematic and reliable methods for the modeling of uncertainties. The results presented in this manuscript highlight the advantages of a robust formulation for the design of an ORC turbine. Much remains to be done. Following the works presented here, two tracks look promising. Primarily, some of the techniques presented here can potentially be used for UQ studies in more complex ORC configurations, such for example using more complex geometries (3D cascades, full stage or multiple stages), or investigating transient effects. A second possibility is to extend the optimization techniques presented here to include an estimate of the errors of the thermodynamic and turbulence models. This action could be particularly relevant for ORCs given the lack of experimental data with which to calibrate the models.

[6] or more generally when a UQ assessment of a design needs to be evaluated, e.g. PDF reconstruction of a given QoI.

Bibliography

[Alauzet et al., 2019] Alauzet, F., Dervieux, A., Frazza, L., and Loseille, A. (2019). Numerical uncertainties estimation and mitigation by mesh adaptation. In *Uncertainty Management for Robust Industrial Design in Aeronautics*, pages 89–107. Springer.

[Angelino and Di Paliano, 1998] Angelino, G. and Di Paliano, P. C. (1998). Multicomponent working fluids for organic rankine cycles (orcs). *Energy*, 23(6):449–463.

[Angelino et al., 1984] Angelino, G., Gaia, M., and Macchi, E. (1984). A review of italian activity in the field of organic rankine cycles. *VDI-Berichte*, (539):465–482.

[Au and Beck, 1999] Au, S. and Beck, J. L. (1999). A new adaptive importance sampling scheme for reliability calculations. *Structural safety*, 21(2):135–158.

[Au and Beck, 2001] Au, S. K. and Beck, J. (2001). Estimation of small failure probabilities in high dimensions by subset simulation. *Prob. Eng. Mech.*, 16:263–277.

[Avramidis and Wilson, 1998] Avramidis, A. N. and Wilson, J. R. (1998). Correlation-induction techniques for estimating quantiles in simulation experiments. *Operations Research*, 46(4):574–591.

[Babuska and Oden, 2004] Babuska, I. and Oden, J. T. (2004). Verification and validation in computational engineering and science: basic concepts. *Computer methods in applied mechanics and engineering*, 193(36):4057–4066.

[Basudhar et al., 2008] Basudhar, A., Missoum, S., and Sanchez, A. H. (2008). Limit state function identification using support vector machines for discontinuous responses and disjoint failure domains. *Probabilistic Engineering Mechanics*, 23(1):1–11.

[Bect et al., 2012] Bect, J., Ginsbourger, D., Li, L., Picheny, V., and Vazquez, E. (2012). Sequential design of computer experiments for the estimation of a probability of failure. *Statistics and Computing*, 22(3):773–793.

[Bect et al., 2017] Bect, J., Li, L., and Vazquez, E. (2017). Bayesian subset simulation. *SIAM/ASA Journal on Uncertainty Quantification*, 5(1):762–786.

[Bethe, 1998] Bethe, H. A. (1998). On the theory of shock waves for an arbitrary equation of state. In *Classic papers in shock compression science*, pages 421–495. Springer.

[Betz et al., 2014] Betz, W., Papaioannou, I., and Straub, D. (2014). Numerical methods for the discretization of random fields by means of the karhunen–loève expansion. *Computer Methods in Applied Mechanics and Engineering*, 271:109–129.

[Bichon et al., 2005] Bichon, B., Eldred, M., Swiler, L., Mahadevan, S., and McFarland, J. (2005). Efficient global reliability analysis for nonlinear implicit performance functions. *AIAA J*, 46(10):2459–68.

[Bichon et al., 2008] Bichon, B. J., Eldred, M. S., Swiler, L. P., Mahadevan, S., and McFarland, J. M. (2008). Efficient global reliability analysis for nonlinear implicit performance functions. *AIAA journal*, 46(10):2459–2468.

[Borzì et al., 2010] Borzì, A., Schulz, V., Schillings, C., and Von Winckel, G. (2010). On the treatment of distributed uncertainties in pde-constrained optimization. *GAMM-Mitteilungen*, 33(2):230–246.

[Bourinet, 2016] Bourinet, J.-M. (2016). Rare-event probability estimation with adaptive support vector regression surrogates. *Reliability Engineering & System Safety*, 150:210–221.

[Bourinet, 2018] Bourinet, J.-M. (2018). *Reliability analysis and optimal design under uncertainty-Focus on adaptive surrogate-based approaches*. PhD thesis, Université Clermont Auvergne.

[Breitung, 1984] Breitung, K. (1984). Asymptotic approximations for multinormal integrals. *Journal of Engineering Mechanics*, 110(3):357–366.

[Bucher, 1988] Bucher, C. G. (1988). Adaptive sampling—an iterative fast monte carlo procedure. *Structural safety*, 5(2):119–126.

[Bucher and Bourgund, 1990] Bucher, C. G. and Bourgund, U. (1990). A fast and efficient response surface approach for structural reliability problems. *Structural safety*, 7(1):57–66.

[Bufi and Cinnella, 2015] Bufi, E. and Cinnella, P. (2015). Efficient uncertainty quantification of turbulent flows through supersonic orc nozzle blades. *Energy Procedia*, 82:186 – 193. 70th Conference of the Italian Thermal Machines Engineering Association, ATI2015.

[Bufi et al., 2017] Bufi, E. A., Camporeale, S. M., and Cinnella, P. (2017). Robust optimization of an organic rankine cycle for heavy duty engine waste heat recovery. *Energy Procedia*, 129:66 – 73. 4th International Seminar on ORC Power SystemsSeptember 13-15th 2017POLITECNICO DI MILANOBOVISA CAMPUSMILANO, ITALY.

[Bufi and Cinnella, 2017] Bufi, E. A. and Cinnella, P. (2017). Robust optimization of supersonic orc nozzle guide vanes. *Journal of Physics: Conference Series*, 821(1):012014.

[by: Nicholas Lange, 1997] by: Nicholas Lange, R. (1997). Neural networks for pattern recognition. *Journal of the American Statistical Association*, 92:1642–1645.

[C. E. Rasmussen, 2006] C. E. Rasmussen, C. W. (2006). *Gaussian Processes for Machine Learning*. the MIT Press.

[Cacuci, 2003] Cacuci, D. G. (2003). *Sensitivity Uncertainty Analysis, Volume 1: Theory*, volume V. 2. Chapman and Hall/CRC, 1 edition.

[Cadini et al., 2015] Cadini, F., Gioletta, A., and Zio, E. (2015). Improved metamodel-based importance sampling for the performance assessment of radioactive waste repositories. *Reliability Engineering and System Safety*, 134:188–197.

[Cadini et al., 2014] Cadini, F., Santos, F., and Zio, E. (2014). An improved adaptive kriging-based importance technique for sampling multiple failure regions of low probability. *Reliability Engineering and System Safety*, 131:109–117.

[Cardoso et al., 2008] Cardoso, J. B., de Almeida, J. R., Dias, J. M., and Coelho, P. G. (2008). Structural reliability analysis using monte carlo simulation and neural networks. *Advances in Engineering Software*, 39(6):505–513.

[Chabridon et al., 2017] Chabridon, V., Balesdent, M., Bourinet, J.-M., Morio, J., and Gayton, N. (2017). Evaluation of failure probability under parameter epistemic uncertainty: application to aerospace system reliability assessment. *Aerospace Science and Technology*, 69:526–537.

[Chen et al., 2010] Chen, S., Chen, W., and Lee, S. (2010). Level set based robust shape and topology optimization under random field uncertainties. *Structural and Multidisciplinary Optimization*, 41(4):507–524.

[Christakos, 2012] Christakos, G. (2012). *Random field models in earth sciences*. Courier Corporation.

[Cinnella et al., 2011a] Cinnella, P., Congedo, P., Pediroda, V., and Parussini, L. (2011a). Sensitivity analysis of dense gas flow simulations to thermodynamic uncertainties. *Physics of Fluids*, 23:116101.

[Cinnella et al., 2010] Cinnella, P., Congedo, P. M., Pediroda, V., and Parussini, L. (2010). Quantification of thermodynamic uncertainties in real gas flows. *International Journal of Engineering Systems Modelling and Simulation*, 2(1):12–24.

[Cinnella and Hercus, 2010] Cinnella, P. and Hercus, S. (2010). Robust optimization of dense gas flows under uncertain operating conditions. *Computers & Fluids*, 39(10):1893 – 1908.

[Cinnella et al., 2011b] Cinnella, P., Marco Congedo, P., Pediroda, V., and Parussini, L. (2011b). Sensitivity analysis of dense gas flow simulations to thermodynamic uncertainties. *Physics of Fluids*, 23(11):116101.

[Colonna, 1996] Colonna, P. (1996). *Fluidi di lavoro multi componenti per cicli termodinamici di potenza (Multicomponent working fluids for power cycles)*. PhD thesis, Ph. D. thesis, Politecnico di Milano, Milano, Italy.

[Colonna et al., 2015] Colonna, P., Casati, E., Trapp, C., Mathijssen, T., Larjola, J., Turunen-Saaresti, T., and Uusitalo, A. (2015). Organic Rankine Cycle Power Systems: From the Concept to Current Technology, Applications, and an Outlook to the Future. *Journal and Engineering for Gas Turbines and Power*, 137(100801).

[Colonna et al., 2008] Colonna, P., Harinck, J., Rebay, S., and Guardone, A. (2008). Real-gas effects in organic rankine cycle turbine nozzles. *Journal of Propulsion and Power*, 24(2):282–294.

[Congedo et al., 2013a] Congedo, P., Geraci, G., Abgrall, R., Pediroda, V., and Parussini, L. (2013a). Tsi metamodels-based multi-objective robust optimization. *Engineering Computations (Swansea, Wales)*, 30(8):1032–1053.

[Congedo et al., 2013b] Congedo, P. M., Geraci, G., Abgrall, R., Pediroda, V., and Parussini, L. (2013b). TSI metamodels-based multi-objective robust optimization. *Engineering Computations*.

[Cramer, 1991] Cramer, M. (1991). On the mach number variation in steady flows of dense hydrocarbons. *Journal of fluids engineering*, 113(4):675–680.

[Cramer and Best, 1991] Cramer, M. and Best, L. (1991). Steady, isentropic flows of dense gases. *Physics of Fluids A: Fluid Dynamics*, 3(1):219–226.

[Cressie, 1992] Cressie, N. (1992). Statistics for spatial data. *Terra Nova*, 4(5):613–617.

[Curran, 1981] Curran, H. (1981). Organic working fluids in rankine engines. *Journal of Energy*, 5(4):218–223.

[Dai et al., 2012] Dai, H., Zhang, H., Wang, W., and Xue, G. (2012). Structural reliability assessment by local approximation of limit state functions using adaptive markov chain simulation and support vector regression. *Computer-Aided Civil and Infrastructure Engineering*, 27(9):676–686.

[De Boer et al., 2007] De Boer, A., Van der Schoot, M., and Bijl, H. (2007). Mesh deformation based on radial basis function interpolation. *Computers & structures*, 85(11-14):784–795.

[Deheeger and Lemaire, 2006] Deheeger, F. and Lemaire, M. (2006). Reliability analysis by support vector machine classification. In *Integrating Structural Analysis, Risk & Reliability, 3rd ASRANet colloquium-Glasgow*.

[Del Moral et al., 2006] Del Moral, P., Doucet, A., and Jasra, A. (2006). Sequential monte carlo samplers. *Journal of the Royal Statistical Society: Series B (Statistical Methodology)*, 68(3):411–436.

[Denos et al., 2001] Denos, R., Arts, T., Paniagua, G., Michelassi, V., and Martelli, F. (2001). Investigation of the Unsteady Aerodynamics in a Transonic Turbine Stage. *ASME J. Turbomach.*, 123(1):81–89.

[Der Kiureghian and Dakessian, 1998] Der Kiureghian, A. and Dakessian, T. (1998). Multiple design points in first and second-order reliability. *Structural Safety*, 20(1):37–49.

[Diaconis and Shafer, 1978] Diaconis, P. and Shafer, G. (1978). A mathematical theory of evidence. *Journal of the American Statistical Association*, 73(363):677.

[Ditlevsen, 1979] Ditlevsen, O. (1979). Generalized second moment reliability index. *Journal of Structural Mechanics*, 7(4):435–451.

[Dow and Wang, 2014] Dow, E. A. and Wang, Q. (2014). Optimal design and tolerancing of compressor blades subject to manufacturing variability. In *16th AIAA Non-Deterministic Approaches Conference*, page 1008.

[Dow and Wang, 2015] Dow, E. A. and Wang, Q. (2015). The implications of tolerance optimization on compressor blade design. *Journal of Turbomachinery*, 137(10):101008.

[Draper, 1997] Draper, N. (1997). Response surface methodology: Process and product optimization using designed experiments. *Journal of Statistical Planning and Inference*, 59:185–186.

[Dubourg, 2011] Dubourg, V. (2011). *Adaptive surrogate models for reliability analysis and reliability-based design optimization*. PhD Thesis.

[Dubourg et al., 2013] Dubourg, V., Sudret, B., and Deheeger, F. (2013). Metamodel-based importance sampling for structural reliability analysis. *Probabilistic Engineering Mechanics*, 33:47–57.

[Dubrule, 1983] Dubrule, O. (1983). Cross validation of kriging in a unique neighborhood. *Journal of the International Association for Mathematical Geology*, 15(6):687–699.

[E. Brochu and de Freitas, 2010] E. Brochu, V. M. C. and de Freitas, N. (2010). A tutorial on bayesian optimization of expensive cost functions, with application to active user modeling and hierarchical reinforcement learning. *arXiv:1012.2599*.

[Echard et al., 2011] Echard, B., Gayton, N., and Lemaire, M. (2011). Ak-mcs: an active learning reliability method combining kriging and monte carlo simulation. *Structural Safety*, 33(2):145–154.

[Echard et al., 2013] Echard, B., Gayton, N., Lemaire, M., and Relun, N. (2013). A combined inportance sampling and kriging reliability method for small failure probabilities with time-demanding numerical models. *Reliability Engineering and System Safety*, 111:232–240.

[Economon et al., 2016] Economon, T. D., Mudigere, D., Bansal, G., Heinecke, A., Palacios, F., Park, J., Smelyanskiy, M., Alonso, J. J., and Dubey, P. (2016). Performance optimizations for scalable implicit {RANS} calculations with {SU2}. *Computers & Fluids*, 129:146 – 158.

[Elhewy et al., 2006] Elhewy, A. H., Mesbahi, E., and Pu, Y. (2006). Reliability analysis of structures using neural network method. *Probabilistic Engineering Mechanics*, 21(1):44–53.

[Enevoldsen and Sørensen, 1993] Enevoldsen, I. and Sørensen, J. D. (1993). Reliability-based optimization of series systems of parallel systems. *Journal of structural engineering*, 119(4):1069–1084.

[Faravelli, 1989] Faravelli, L. (1989). Response-surface approach for reliability analysis. *Journal of Engineering Mechanics*, 115(12):2763–2781.

[Farin, 2002] Farin, G. (2002). *Curves and Surfaces for CAGD: A Practical Guide*. Morgan Kaufmann Publishers Inc., San Francisco, CA, USA, 5 edition.

[Feller, 1958] Feller, W. (1958). An introduction to probability theory and its applications. *Journal of the Franklin Institute*, 265(1):73–74.

[Fenrich and Alonso, 2017] Fenrich, R. W. and Alonso, J. J. (2017). Reliable multidisciplinary design of a supersonic nozzle using multifidelity surrogates. In *18th AIAA/ISSMO Multidisciplinary Analysis and Optimization Conference*, page 3826.

[Ferson et al., 2008] Ferson, S., Oberkampf, W. L., and Ginzburg, L. (2008). Model validation and predictive capability for the thermal challenge problem. *Computer Methods in Applied Mechanics and Engineering*, 197(29-32):2408–2430.

[Fishman, 1996] Fishman, G. S. (1996). *Monte-Carlo: concepts, algorithms and applications*. New York: Wiley.

[Freeny, 1988] Freeny, A. (1988). Empirical model building and response surfaces. *Technometrics*, 30:229–231.

[Garzon, 2003] Garzon, V. E. (2003). *Probabilistic aerothermal design of compressor airfoils*. PhD thesis, Massachusetts Institute of Technology.

[Geraci et al., 2016] Geraci, G., Congedo, P., Abgrall, R., and Iaccarino, G. (2016). High-order statistics in global sensitivity analysis: Decomposition and model reduction. *Computer Methods in Applied Mechanics and Engineering*, 301:80 – 115.

[Ghanem et al., 2017] Ghanem, R., Higdon, D., and Owhadi, H. (2017). *Handbook of uncertainty quantification*. Springer.

[Giles, 1990] Giles, M. B. (1990). Nonreflecting boundary conditions for euler equation calculations. *AIAA journal*, 28(12):2050–2058.

[Glimm and Sharp, 1999] Glimm, J. and Sharp, D. (1999). Prediction and the quantification of uncertainty. *Physica D: Nonlinear Phenomena*, 133(1-4):152–170.

[Glynn, 1996] Glynn, P. W. (1996). Importance sampling for monte carlo estimation of quantiles. In *Mathematical Methods in Stochastic Simulation and Experimental Design: Proceedings of the 2nd St. Petersburg Workshop on Simulation*, pages 180–185. Publishing House of St. Petersburg University.

[Gori et al., 2017] Gori, G., Zocca, M., Cammi, G., Spinelli, A., and Guardone, A. (2017). Experimental assessment of the open-source su2 cfd suite for orc applications. *Energy Procedia*, 129(Supplement C):256 – 263.

[GPy, 2012] GPy (since 2012). GPy: A gaussian process framework in python. http://github.com/SheffieldML/GPy.

[Guardone and Vigevano, 2002a] Guardone, A. and Vigevano, L. (2002a). Roe Linearization for the van der Waals Gas. *Journal of Computational Physics*, 175(10):50–78.

[Guardone and Vigevano, 2002b] Guardone, A. and Vigevano, L. (2002b). Roe linearization for the van der Waals gas. *J. Comput. Phys.*, 175:50–78.

[Häcker, 2000] Häcker, J. (2000). Statistical analysis of manufacturing deviations and classification methods for probabilistic aerothermal design of turbine blades. *Master's degree thesis*.

[Han et al., 2015] Han, Z.-H., Abu-Zurayk, M., Görtz, S., and Ilic, C. (2015). Surrogate-based aerodynamic shape optimization of a wing-body transport aircraft configuration. In *Symposium on AeroStructures*, pages 257–282. Springer.

[Han et al., 2010] Han, Z.-H., Zimmermann, R., and Goretz, S. (2010). A new cokriging method for variable-fidelity surrogate modeling of aerodynamic data. In *48th AIAA Aerospace sciences meeting including the new horizons forum and Aerospace exposition*, page 1225.

[Hanson, 1999] Hanson, K. M. (1999). A framework for assessing uncertainties in simulation predictions. *Physica D: Nonlinear Phenomena*, 133(1-4):179–188.

[Harinck, 2010] Harinck, J. (2010). Super-and transcritical fluid expansions for next-generation energy conversion systems.

[Hasofer and Lind, 1974] Hasofer, A. M. and Lind, N. C. (1974). Exact and invariant second-moment code format. *Journal of the Engineering Mechanics division*, 100(1):111–121.

[Helton and Davis, 2003] Helton, J. C. and Davis, F. J. (2003). Latin hypercube sampling and the propagation of uncertainty in analyses of complex systems. *Reliability Engineering & System Safety*, 81(1):23–69.

[Hesterberg and Nelson, 1998] Hesterberg, T. C. and Nelson, B. L. (1998). Control variates for probability and quantile estimation. *Management Science*, 44(9):1295–1312.

[Hoschek et al., 1993] Hoschek, J., Lasser, D., and Schumaker, L. L. (1993). *Fundamentals of computer aided geometric design*. AK Peters, Ltd.

[Hsu and Nelson, 1990] Hsu, J. C. and Nelson, B. L. (1990). Control variates for quantile estimation. *Management Science*, 36(7):835–851.

[Huang et al., 2006] Huang, D., Allen, T. T., Notz, W. I., and Zeng, N. (2006). Global Optimization of Stochastic Black-Box Systems via Sequential Kriging Meta-Models. *Journal of Global Optimization*, 34(3):441–466.

[Huang et al., 2016] Huang, X., Chen, J., and Zhu, H. (2016). Assessing small failure probabilities by ak–ss: An active learning method combining kriging and subset simulation. *Structural Safety*, 59:86–95.

[Hurtado and Alvarez, 2000] Hurtado, J. E. and Alvarez, D. A. (2000). Reliability assessment of structural systems using neural networks. In *Proc. European Congress on Computational Methods in Applied Sciences and Engineering, ECCOMAS*, volume 2000.

[Iaccarino et al., 2011] Iaccarino, G., Pecnik, R., Glimm, J., and Sharp, D. (2011). A qmu approach for characterizing the operability limits of air-breathing hypersonic vehicles. *Reliability Engineering & System Safety*, 96(9):1150–1160.

[Jameson et al., 1998] Jameson, A., Martinelli, L., and Pierce, N. (1998). Optimum aerodynamic design using the navier–stokes equations. *Theoretical and Computational Fluid Dynamics*, 10(1):213–237.

[Janusevskis and Le Riche, 2013] Janusevskis, J. and Le Riche, R. (2013). Simultaneous kriging-based estimation and optimization of mean response. *Journal of Global Optimization*, 55(2):313–336.

[Jin et al., 2003] Jin, R., Du, X., and Chen, W. (2003). The use of metamodeling techniques for optimization under uncertainty. *Structural and Multidisciplinary Optimization*, 25(2):99–116.

[Kang et al., 2010] Kang, S.-C., Koh, H.-M., and Choo, J. F. (2010). An efficient response surface method using moving least squares approximation for structural reliability analysis. *Probabilistic Engineering Mechanics*, 25(4):365–371.

[Karellas and Schuster, 2008] Karellas, S. and Schuster, A. (2008). Supercritical fluid parameters in organic rankine cycle applications. *International Journal of Thermodynamics*, 11(3).

[Karhunen, 1947] Karhunen, K. (1947). *Über lineare Methoden in der Wahrscheinlichkeitsrechnung*, volume 37. Sana.

[Kaymaz, 2005] Kaymaz, I. (2005). Application of kriging method to structural reliability problems. *Structural Safety*, 27(2):133–151.

[Keshavarzzadeh et al., 2017] Keshavarzzadeh, V., Fernandez, F., and Tortorelli, D. A. (2017). Topology optimization under uncertainty via non-intrusive polynomial chaos expansion. *Computer Methods in Applied Mechanics and Engineering*, 318:120 – 147.

[Kleiber and Hien, 1994] Kleiber, M. and Hien, T. D. (1994). The stochastic finite element method (basic perturbation technique and computer implementation), journal = Applied Stochastic Models and Data Analysis. 10(4):297–297.

[Kluwick, 2004] Kluwick, A. (2004). Internal flows of dense gases. *Acta mechanica*, 169(1-4):123–143.

[Knio and Le Maitre, 2006] Knio, O. and Le Maitre, O. (2006). Uncertainty propagation in cfd using polynomial chaos decomposition. *Fluid dynamics research*, 38(9):616.

[Kullback and Leibler, 1951] Kullback, S. and Leibler, R. A. (1951). On information and sufficiency. *The annals of mathematical statistics*, 22(1):79–86.

[Lange et al., 2012] Lange, A., Voigt, M., Vogeler, K., and Johann, E. (2012). Principal component analysis on 3d scanned compressor blades for probabilistic cfd simulation. In *53rd AIAA/ASME/ASCE/AHS/ASC Structures, Structural Dynamics and Materials Conference 20th AIAA/ASME/AHS Adaptive Structures Conference 14th AIAA*, page 1762.

[Larjola, 1995] Larjola, J. (1995). Electricity from industrial waste heat using high-speed organic rankine cycle (orc). *International journal of production economics*, 41(1-3):227–235.

[Lataniotis et al., 2018] Lataniotis, C., Marelli, S., and Sudret, B. (2018). Extending classical surrogate modelling to ultrahigh dimensional problems through supervised dimensionality reduction: a data-driven approach. *arXiv preprint arXiv:1812.06309*.

[Law et al., 1991] Law, A. M., Kelton, W. D., and Kelton, W. D. (1991). *Simulation modeling and analysis*, volume 2. McGraw-Hill New York.

[Lebrun and Dutfoy, 2009] Lebrun, R. and Dutfoy, A. (2009). An innovating analysis of the nataf transformation from the copula viewpoint. *Probabilistic Engineering Mechanics*, 24(3):312–320.

[LEE and PARK, 2006] LEE, K.-H. and PARK, G.-J. (2006). A global robust optimization using kriging based approximation model. *JSME International Journal Series C Mechanical Systems, Machine Elements and Manufacturing*, 49(3):779–788.

[Lelièvre et al., 2018] Lelièvre, N., Beaurepaire, P., Mattrand, C., and Gayton, N. (2018). Ak-mcsi: A kriging-based method to deal with small failure probabilities and time-consuming models. *Structural Safety*, 73:1–11.

[Liang et al., 2008] Liang, J., Mourelatos, Z. P., and Tu, J. (2008). A single-loop method for reliability-based design optimisation. *International Journal of Product Development*, 5(1-2):76–92.

[Loeve, 1948] Loeve, M. (1948). Functions aleatoires du second ordre. *Processus stochastique et mouvement Brownien*, pages 366–420.

[Lootsma, 1996] Lootsma, F. A. (1996). Monte carlo: Concepts, algorithms, and applications. *Journal of Computational and Applied Mathematics*, 75(2):N3–N4.

[Lootsma, 1997] Lootsma, F. A. (1997). Fuzzy set theory and its applications, 3rd edition. *European Journal of Operational Research*, 101(1):227–228.

[Lophaven et al., 2002] Lophaven, S. N., Nielsen, H. B., Sondergaard, J., and Dace, A. (2002). A matlab kriging toolbox. *Technical University of Denmark, Kongens Lyngby, Technical Report No. IMM-TR-2002-12*.

[Lukaczyk et al., 2014] Lukaczyk, T. W., Constantine, P., Palacios, F., and Alonso, J. J. (2014). Active subspaces for shape optimization. In *10th AIAA multidisciplinary design optimization conference*, page 1171.

[Macchi, 2017] Macchi, E. (2017). *Theoretical basis of the Organic Rankine Cycle*, pages 3–24. Woodhead Publishing.

[MacQueen, 1967] MacQueen, J. (1967). *Some methods for classification and analysis of multivariate observations*. Proceedings of the Berkeley symposium on mathematical statistics and probability, vol.1. Berkeley.

[Marelli and Sudret, 2014] Marelli, S. and Sudret, B. (2014). Uqlab: A framework for uncertainty quantification in matlab. In *Vulnerability, uncertainty, and risk: quantification, mitigation, and management*, pages 2554–2563.

[Marrel et al., 2008] Marrel, A., Iooss, B., Van Dorpe, F., and Volkova, E. (2008). An efficient methodology for modeling complex computer codes with gaussian processes. *Computational Statistics & Data Analysis*, 52(10):4731–4744.

[Mehta, 1991] Mehta, U. B. (1991). Some aspects of uncertainty in computational fluid dynamics results. *Journal of Fluids Engineering*, 113(4):538–543.

[Menter, 1993] Menter, F. (1993). Zonal two equation kw turbulence models for aerodynamic flows. In *23rd fluid dynamics, plasmadynamics, and lasers conference*, page 2906.

[Merle and Cinnella, 2015] Merle, X. and Cinnella, P. (2015). Bayesian quantification of thermodynamic uncertainties in dense gas flows. *Reliability Engineering & System Safety*, 134:305–323.

[Merle and Cinnella, 2019] Merle, X. and Cinnella, P. (2019). Robust prediction of dense gas flows under uncertain thermodynamic models. *Reliability Engineering & System Safety*, 183:400–421.

[Metropolis et al., 1953] Metropolis, N., Rosenbluth, A. W., Rosenbluth, M. N., Teller, A. H., and Teller, E. (1953). Equation of state calculations by fast computing machines. *The journal of chemical physics*, 21(6):1087–1092.

[Miller et al., 2003] Miller, R., Moss, R., Ainsworth, R., and Harvery, N. (2003). Wake, Shock, and Potential Field Interactions in a 1.5 Stage Turbine—Part I: Vane-Rotor and Rotor-Vane Interaction. *ASME J. Turbomach.*, 125(1):33–39.

[Miranda et al., 2008] Miranda, A. A., Le Borgne, Y.-A., and Bontempi, G. (2008). New routes from minimal approximation error to principal components. *Neural Processing Letters*, 27(3):197–207.

[Montomoli et al., 2015] Montomoli, F., Carnevale, M., D'Ammaro, A., Massini, M., and Salvadori, S. (2015). *Uncertainty quantification in computational fluid dynamics and aircraft engines*. Springer.

[Morio, 2012] Morio, J. (2012). Extreme quantile estimation with nonparametric adaptive importance sampling. *Simulation Modelling Practice and Theory*, 27:76–89.

[Most, 2007] Most, T. (2007). An adaptive response surface approach for structural reliability analyses based on support vector machines. In *Proceedings of the eleventh international conference on civil, structural and environmental engineering computing, BHV Topping*.

[Most and Bucher, 2008] Most, T. and Bucher, C. (2008). New concepts for moving least squares: An interpolating non-singular weighting function and weighted nodal least squares. *Engineering analysis with boundary elements*, 32(6):461–470.

[Moustapha et al., 2016] Moustapha, M., Sudret, B., Bourinet, J.-M., and Guillaume, B. (2016). Quantile-based optimization under uncertainties using adaptive kriging surrogate models. *Structural and multidisciplinary optimization*, 54(6):1403–1421.

[Nataf, 1962] Nataf, A. (1962). Determination des distribution don t les marges sont donnees. *Comptes Rendus de l Academie des Sciences*, 225:42–43.

[Nelson, 1999] Nelson, R. B. (1999). Lecture notes in statistics: An introduction to copulas.

[Nikolaus Hansen, 2018] Nikolaus Hansen (2018). CMA. https://pypi.python.org/pypi/cma.

[Nyström, 1930] Nyström, E. J. (1930). Über die praktische auflösung von integralgleichungen mit anwendungen auf randwertaufgaben. *Acta Mathematica*, 54(1):185–204.

[Oberkampf and Barone, 2006] Oberkampf, W. L. and Barone, M. F. (2006). Measures of agreement between computation and experiment: validation metrics. *Journal of Computational Physics*, 217(1):5–36.

[Oberkampf and Trucano, 2002] Oberkampf, W. L. and Trucano, T. G. (2002). Verification and validation in computational fluid dynamics. *Progress in Aerospace sciences*, 38(3):209–272.

[Pai and Hong, 2006] Pai, P.-F. and Hong, W.-C. (2006). Software reliability forecasting by support vector machines with simulated annealing algorithms. *Journal of Systems and Software*, 79(6):747–755.

[Palacios and al, 2014] Palacios, F. and al (2014). Stanford university unstructured (su2): Open-source analysis and design technology for turbulent flows. *AIAA SciTech*, 52nd Aerospace Sciences Meeting.

[Palacios et al., 2013] Palacios, F., Colonno, M. F., Aranake, A. C., Campos, A., Copeland, S. R., Economon, T. D., Lonkar, A. K., Lukaczyk, T. W., Taylor, T. W. R., and Alonso, J. J. (2013). Stanford University Unstructured (SU2): An open-source integrated computational environment for multi-physics simulation and design. In *51st AIAA Aerospace Sciences Meeting and Exhibit*.

[Papadopoulos et al., 2012] Papadopoulos, V., Giovanis, D. G., Lagaros, N. D., and Papadrakakis, M. (2012). Accelerated subset simulation with neural networks for reliability analysis. *Computer Methods in Applied Mechanics and Engineering*, 223:70–80.

[Papadrakakis and Lagaros, 2002] Papadrakakis, M. and Lagaros, N. (2002). Reliability-based structural optimization using neural networks and monte carlo simulation. *Comput Methods Appl Mech Eng*, 191(32):3491–507.

[Pasquale et al., 2013] Pasquale, D., Ghidoni, A., and S., R. (2013). Shape optimization of an Organic Rankine Cycle radial turbine nozzle. *Journal and Engineering for Gas Turbines and Power*, 135(042308).

[Persico, 2017] Persico, G. (2017). Evolutionary Optimization of Centrifugal Nozzles for Organic Vapours. *Journal of Physics: Conference Series*, 821(012015).

[Persico and Pini, 2017] Persico, G. and Pini, M. (2017). *Fluid dynamic design of Organic Rankine Cycle turbines*, pages 253–297. Woodhead Publishing.

[Picheny et al., 2010a] Picheny, V., Ginsbourger, D., and Richet, Y. (2010a). Noisy Expected Improvement and on-line computation time allocation for the optimization of simulators with tunable fidelity. working paper or preprint.

[Picheny et al., 2010b] Picheny, V., Ginsbourger, D., Roustant, O., Haftka, R. T., and Kim, N.-H. (2010b). Adaptive designs of experiments for accurate approximation of a target region. *Journal of Mechanical Design*, 132(7):071008.

[Picheny et al., 2010c] Picheny, V., Kim, N. H., and Haftka, R. T. (2010c). Application of bootstrap method in conservative estimation of reliability with limited samples. *Structural and Multidisciplinary Optimization*, 41(2):205–217.

[Pini, 2013] Pini, M. (2013). *Turbomachinery Design Optimization using Adjoint Method and Accurate Equations of State*. PhD thesis, Politecnico di Milano.

[Pini et al., 2014a] Pini, M., Persico, G., and Dossena, V. (2014a). Robust adjoint-based shape optimization of supersonic turbomachinery cascades. In *ASME Turbo Expo 2014: Turbine Technical Conference and Exposition*, pages V02BT39A043–V02BT39A043. American Society of Mechanical Engineers.

[Pini et al., 2014b] Pini, M., Persico, G., and Dossena, V. (2014b). Robust adjoint-based shape optimization of supersonic turbomachinery cascades. In *ASME Turbo Expo 2014: Turbine Technical Conference and Exposition*, pages V02BT39A043–V02BT39A043. American Society of Mechanical Engineers.

[Pini et al., 2015] Pini, M., Persico, G., Pasquale, D., and Rebay, S. (2015). Adjoint method for shape optimization in real-gas flow applications. *ASME Journal of Engineering for Gas Turbines and Power*, 137(3).

[Pini et al., 2016] Pini, M., Vitale, S., , Colonna, P., Gori, G., Guardone, A., Economon, T., Alonso, J., and Palacios, F. (2016). Su2: the open-source software for non-ideal compressible flows. In *NICFD 2016: 1st International Seminar on Non-Ideal Compressible-Fluid Dynamics for Propusion & Power*, Varenna, Italy.

[Pironneau, 1974] Pironneau, O. (1974). On optimum design in fluid mechanics. *Journal of Fluid Mechanics*, 64(1):97–110.

[Pisaroni et al., 2018] Pisaroni, M., Nobile, F., and Leyland, P. (2018). Continuation multilevel monte carlo evolutionary algorithm for robust aerodynamic shape design. *Journal of Aircraft*, pages 1–16.

[Proppe, 2008] Proppe, C. (2008). Estimation of failure probabilities by local approximation of the limit state function. *Structural Safety*, 30(4):277–290.

[Rajashekhar and Ellingwood, 1993] Rajashekhar, M. R. and Ellingwood, B. R. (1993). A new look at the response surface approach for reliability analysis. *Structural safety*, 12(3):205–220.

[Ranjan et al., 2008] Ranjan, P., Bingham, D., and Michailidis, G. (2008). Sequential experiment design for contour estimation from complex computer codes. *Technometrics*, 50(4):527–541.

[Rasmussen and Williams, 2006] Rasmussen, C. E. and Williams, C. (2006). *Gaussian Processes for Machine Learning*. the MIT Press.

[Razaaly and Congedo, 2018] Razaaly, N. and Congedo, P. M. (2018). Novel algorithm using active metamodel learning and importance sampling: application to multiple failure regions of low probability. *Journal of Computational Physics*, 368:92–114.

[Razaaly et al., 2017] Razaaly, N., Persico, G., and Congedo, P. M. (2017). Uncertainty Quantification of Inviscid Flows Through a Supersonic ORC Turbine Cascade. *Energy Procedia*.

[Rivier and Congedo, 2018a] Rivier, M. and Congedo, P. M. (2018a). Surrogate-Assisted Bounding-Box Approach Applied to Constrained Multi-Objective Optimisation Under Uncertainty. Research Report RR-9214, Inria Bordeaux Sud-Ouest ; Inria Saclay.

[Rivier and Congedo, 2018b] Rivier, M. and Congedo, P. M. (2018b). Surrogate-Assisted Bounding-Box Approach for Optimization Problems with Approximated Objectives. Research Report RR-9155, Inria.

[Roache, 1997] Roache, P. J. (1997). Quantification of uncertainty in computational fluid dynamics. *Annual review of fluid Mechanics*, 29(1):123–160.

[Rodriguez-Fernandez and Persico, 2015] Rodriguez-Fernandez, P. and Persico, G. (2015). Automatic design of ORC turbine profiles using evolutionary algorithms. *3rd International Seminar on ORC Power Systems*, (133).

[Roe, 1981] Roe, P. L. (1981). Approximate riemann solvers, parameter vectors, and difference schemes. *J. Comput. Phys.*, 43(2):357–372.

[Romei et al., 2019] Romei, A., Congedo, P. M., and Persico, G. (2019). Assessment of deterministic shape optimizations within a stochastic framework for supersonic organic rankine cycle nozzle cascades. *Journal of Engineering for Gas Turbines and Power*, 141(7):071019.

[Romei et al., 2018] Romei, A., Persico, G., and Congedo, P. M. (2018). Assessment of deterministic shape optimizations within a stochastic framework for supersonic organic rankine cycle nozzle cascades. *Journal of Engineering for Gas Turbines and Power*, Under Review.

[Roustant et al., 2012] Roustant, O., Ginsbourger, D., and Deville, Y. (2012). Dicekriging, diceoptim: Two r packages for the analysis of computer experiments by kriging-based metamodeling and optimization.

[Roy, 2005] Roy, C. J. (2005). Review of code and solution verification procedures for computational simulation. *Journal of Computational Physics*, 205(1):131–156.

[Rubino et al., 2018] Rubino, A., Pini, M., Colonna, P., Albring, T., Nimmagadda, S., Economon, T., and Alonso, J. (2018). Adjoint-based fluid dynamic design optimization in quasi-periodic unsteady flow problems using a harmonic balance method. *Journal of Computational Physics*.

[Rubinstein, 1981] Rubinstein, R. Y. (1981). *Simulation and the Monte-Carlo method*. New York: Wiley.

[Rubinstein and Kroese, 1996] Rubinstein, R. Y. and Kroese, D. P. (1996). Monte carlo: Concepts, algorithms, and applications. *Journal of Computational and Applied Mathematics*, 75(2):N3–N4.

[Saltelli et al., 2004] Saltelli, A., Tarantola, S., and Campolongo, F. (2004). *Sensitivity Analysis in Practice*. Wiley.

[Santner et al., 2013] Santner, T., Williams, B., and Notz, W. (2013). *The design and analysis of computer experiments*. New York: Springer.

[Sauret and T Gu, 2014] Sauret, E. and T Gu, Y. (2014). 3d cfd simulations of a candidate r143a radial-inflow turbine for geothermal power applications. volume 2.

[Schillings et al., 2011] Schillings, C., Schmidt, S., and Schulz, V. (2011). Efficient shape optimization for certain and uncertain aerodynamic design. *Computers & Fluids*, 46(1):78–87.

[Schmelzer et al., 2019] Schmelzer, M., Dwight, R. P., Edeling, W., and Cinnella, P. (2019). Estimation of model error using bayesian model-scenario averaging with maximum a posterori-estimates. In *Uncertainty Management for Robust Industrial Design in Aeronautics*, pages 53–69. Springer.

[Schöbi et al., 2016] Schöbi, R., Sudret, B., and Marelli, S. (2016). Rare event estimation using polynomial-chaos kriging. *ASCE-ASME Journal of Risk and Uncertainty in Engineering Systems, Part A: Civil Engineering*, 3(2):D4016002.

[Sciacovelli et al., 2018] Sciacovelli, L., Cinnella, P., and Gloerfelt, X. (2018). A priori tests of rans models for turbulent channel flows of a dense gas. *Flow, Turbulence and Combustion*, 101(2):295–315.

[Sciacovelli et al., 2017] Sciacovelli, L., Cinnella, P., Gloerfelt, X., and Grasso, F. (2017). Dns of turbulent flows of dense gases. In *Journal of Physics: Conference Series*, volume 821, page 012018. IOP Publishing.

[Shi and Lin, 2016] Shi, L. and Lin, S.-P. (2016). A new rbdo method using adaptive response surface and first-order score function for crashworthiness design. *Reliability Engineering & System Safety*, 156:125–133.

[Soave, 1972] Soave, G. (1972). Equilibrium constants from a modified redlich-kwong equation of state. *Chemical engineering science*, 27(6):1197–1203.

[Sobol, 2001] Sobol, I. M. (2001). Global sensitivity indices for nonlinear mathematical models and their monte carlo estimates. *Mathematics and computers in simulation*, 55(1-3):271–280.

[Spinelli et al., 2018] Spinelli, A., Cammi, G., Gallarini, S., Zocca, M., Cozzi, F., Gaetani, P., Dossena, V., and Guardone, A. (2018). Experimental evidence of non-ideal compressible effects in expanding flow of a high molecular complexity vapor. *Experiments in Fluids*, 59(8).

[Spinelli et al., 2017] Spinelli, A., Cammi, G., Zocca, M., Gallarini, S., Cozzi, F., Gaetani, P., Dossena, V., and Guardone, A. (2017). Experimental observation of non-ideal expanding flows of siloxane mdm vapor for orc applications. *Energy Procedia*, 129:1125–1132.

[Stein, 2012] Stein, M. L. (2012). *Interpolation of spatial data: some theory for kriging*. Springer Science & Business Media.

[Stern et al., 2001] Stern, F., Wilson, R. V., Coleman, H. W., and Paterson, E. G. (2001). Comprehensive approach to verification and validation of cfd simulations—part 1: methodology and procedures. *Journal of fluids engineering*, 123(4):793–802.

[Stryjek and Vera, 1986] Stryjek, R. and Vera, J. (1986). Prsv: An improved peng—robinson equation of state for pure compounds and mixtures. *The canadian journal of chemical engineering*, 64(2):323–333.

[Tang et al., 2015] Tang, K., Congedo, P., and Abgrall, R. (2015). Adaptive surrogate modeling by ANOVA and sparse polynomial dimensional decomposition for global sensitivity analysis in fluid simulation. *Journal of Computational Physics*, 314(1):557–589.

[Thompson, 1971] Thompson, P. A. (1971). A fundamental derivative in gasdynamics. *The Physics of Fluids*, 14(9):1843–1849.

[Trevor Hastie, 2009] Trevor Hastie, Robert Tibshirani, J. F. (2009). *The elements of statistical learning: Data mining, inference, and prediction*. Springer Series in Statistics. Springer, 2nd ed. 2009. corr. 3rd printing 5th printing. edition.

[Tvedt, 1989] Tvedt, L. (1989). Second order reliability by an exact integral. In *Reliability and Optimization of Structural Systems' 88*, pages 377–384. Springer.

[Vazquez, 2005] Vazquez, E. (2005). *Modélisation comportementale de systèmes non-linéaires multivariables par méthodes à noyaux et applications*. PhD thesis, Université Paris Sud-Paris XI.

[Verneau, 1978] Verneau, A. (1978). Application of organic fluids in solar turbines [l'emploi des fluides organiques dans les turbines solaires]. *Entropie*, 14(82):9–18.

[Victoria C. P. Chen and Shoemaker, 1999] Victoria C. P. Chen, D. R. and Shoemaker, C. A. (1999). Applying experimental design and regression splines to high-dimensional continuous-state stochastic dynamic programming. *Operations Research*, 47:38–53.

[Vinokur and Montagné, 1990] Vinokur, M. and Montagné, J. L. (1990). Generalized flux-vector splitting and roe average for an equilibrium real gas. *J. Comput. Phys.*, 89:276.

[Vitale and al, 2015] Vitale, S. and al (2015). Extension of the SU2 Open Source CFD code to the simulation of turpinibulent flows of fluids modelled with complex thermophysical laws. *AIAA Aviation*, 22nd AIAA Computational Fluid Dynamics Conference.

[Vitale et al., 2017] Vitale, S., Albring, T. A., Pini, M., Gauger, N. R., Colonna, P., et al. (2017). Fully turbulent discrete adjoint solver for non-ideal compressible flow applications. *Journal of the Global Power and Propulsion Society*, 1:Z1FVOI.

[Vitale et al., 2015] Vitale, S., Gori, G., Pini, M., Guardone, A., Economon, T. D., Palacios, F., Alonso, J. J., and Colonna, P. (2015). Extension of the su2 open source cfd code to the simulation of turbulent flows of fuids modelled with complex thermophysical laws. *AIAA Paper*, 2760:2015.

[Wheeler and Ong, 2013] Wheeler, A. P. and Ong, J. (2013). The role of dense gas dynamics on organic rankine cycle turbine performance. *Journal of Engineering for Gas Turbines and Power*, 135(10):102603.

[Youn et al., 2003] Youn, B. D., Choi, K. K., and Park, Y. H. (2003). Hybrid analysis method for reliability-based design optimization. *Journal of Mechanical Design*, 125(2):221–232.

[Zaki et al., 2014] Zaki, M. J., Meira Jr, W., and Meira, W. (2014). *Data mining and analysis: fundamental concepts and algorithms*. Cambridge University Press.

[Zeldovich, 1946] Zeldovich, J. (1946). On the possibility of rarefaction shock waves. *ZHURNAL EKSPERIMENTALNOI I TEORETICHESKOI FIZIKI*, 16(4):363–364.

[Zhang et al., 2017] Zhang, J., Taflanidis, A., and Medina, J. (2017). Sequential approximate optimization for design under uncertainty problems utilizing kriging metamodeling in augmented input space. *Computer Methods in Applied Mechanics and Engineering*, 315:369 – 395.

[Zhao et al., 2015] Zhao, H., Yue, Z., Liu, Y., Gao, Z., and Zhang, Y. (2015). An efficient reliability method combining adaptive importance sampling and kriging metamodel. *Applied Mathematical Modelling*, 39:1853–66.

[Zocca et al., 2018] Zocca, M., Spinelli, A., Cozzi, F., and Guardone, A. (2018). Influence of a recessed step at the throat section of a supersonic nozzle. *The Aeronautical Journal*, 122(1251):715–732.

[Zuev et al., 2012] Zuev, K. M., Beck, J. L., Au, S.-K., and Katafygiotis, L. S. (2012). Bayesian post-processor and other enhancements of subset simulation for estimating failure probabilities in high dimensions. *Computers & structures*, 92:283–296.

université PARIS-SACLAY | École doctorale de mathématiques Hadamard (EDMH)

Titre : Méthodes d'estimation d'événements rares et d'optimisation robuste avec application aux turbines ORC

Mots Clefs : Processus gaussiens • Evénements rares • Probabilité de défaillance • Quantile extrême • Optimisation Robuste • Turbine ORC • Variabilité géométrique

Résumé :
Cette thèse vise à formuler des méthodes innovantes de quantification d'incertitude (UQ) à la fois pour l'optimisation robuste (RO) et l'optimisation robuste et fiable (RBDO). L'application visée est l'optimisation des turbines supersoniques pour les Cycles Organiques de Rankine (ORC). Les sources d'énergie typiques des systèmes d'alimentation ORC sont caractérisées par une source de chaleur et des conditions thermodynamiques entrée/sortie de turbine variables. L'utilisation de composés organiques, généralement de masse moléculaire élevée, conduit à des configurations de turbines sujettes à des écoulements supersoniques et des chocs, dont l'intensité augmente dans les conditions *off-design*; ces caractéristiques dépendent également de la forme locale de la pâle, qui peut être influencée par la variabilité géométrique induite par les procédures de fabrication. Il existe un consensus sur la nécessité d'inclure ces incertitudes dans la conception, nécessitant ainsi des méthodes UQ et un outil permettant l'optimisation de form adapté. Ce travail est décomposé en deux parties principales. La première partie aborde le problème de l'estimation des événements rares en proposant deux méthodes originales pour l'estimation de probabilité de défaillance (metaAL-OIS et eAK-MCS) et un pour le calcul quantile (QeAK-MCS). Les trois méthodes reposent sur des stratégies d'adaptation basées sur des métamodèles (Kriging), visant à affiner directement la région dite *Limit-State-Surface* (LSS), contrairement aux methodes de type *Subset Simulation* (SS). En effet, ces dernières considèrent différents seuils intermédiaires associés à des LSSs devant être raffinés. Cette propriété de raffinement *direct* est cruciale, car elle permet la compatibilité de couplage à des méthodes RBDO existantes. En particulier, les algorithmes proposés ne sont pas soumis à des hypothèses restrictives sur le LSS (contrairement aux méthodes de type FORM/SORM), tel que le nombre de modes de défaillance, cependant doivent être formulés dans l'espace standard. Les méthodes eAK-MCS et QeAK-MCS sont dérivées de la méthode AK-MCS, et d'un échantillonnage adaptatif et parallèle basé sur des algorithmes de type *K-Means pondéré*. MetaAL-OIS présente une stratégie de raffinement séquentiel plus élaborée basée sur des échantillons MCMC tirés à partir d'une densité d'échantillonage d'importance (ISD) quasi optimale. Par ailleurs, il propose la construction d'une ISD de type mélange de gaussiennes, permettant l'estimation précise de petites probabilités de défaillance lorsqu'un grand nombre d'échantillons (plusieurs millions) est disponible, comme alternative au SS. Les trois méthodes sont très performantes pour des exemples analytiques 2D à 8D classiques, tirés de la littérature sur la fiabilité des structures, certaines présentant plusieurs modes de défaillance, et tous caractérisés par une très faible probabilité de défaillance/niveau de quantile ($O(10^{-5} - 10^{-9})$). Des estimations précises sont obtenues pour les cas considérés en un nombre raisonnable d'appels à la fonction de performance ($\sim 15 - 150$). La deuxième partie de ce travail aborde les méthodes originales d'optimisation robuste (RO) appliquées à la conception de forme d'une pâle de turbine supersonique ORC. Une analyse UQ prenant en compte des incertitudes géométriques (aléatoires), liées aux conditions de fonctionnement et aux paramètres du fluide est conduite et permet de donner de quantifier l'impact de différentes variables d'entrée variables et constitue une étude préliminaire nécessaire à la conception robuste. Ensuite, plusieurs formulations RO mono-objectif sous contrainte probabiliste sont considérées dans ce travail, notamment en considérant la moyenne ou un quantile élevé de la fonction objectif.

Title: Rare Event Estimation and Robust Optimization Methods with Application to ORC Turbine Cascade

Keywords: Gaussian Processes • Failure Probability • Extreme Quantile • Robust Optimization • ORC Turbine • Geometric Manufacturing Variability

Abstract:
This thesis aims to formulate innovative Uncertainty Quantification (UQ) methods in both Robust Optimization (RO) and Reliability-Based Design Optimization (RBDO) problems. The targeted application is the optimization of supersonic turbines used in Organic Rankine Cycle (ORC) power systems. Typical energy sources for ORC power systems feature variable heat load and turbine inlet/outlet thermodynamic conditions. The use of organic compounds with a heavy molecular weight typically leads to supersonic turbine configurations featuring supersonic flows and shocks, which grow in relevance in the aforementioned off-design conditions; these features also depend strongly on the local blade shape, which can be influenced by the geometric tolerances of the blade manufacturing. A consensus exists about the necessity to include these uncertainties in the design process, so requiring fast UQ methods and a comprehensive tool for performing shape optimization efficiently. This work is decomposed in two main parts. The first one addresses the problem of rare events estimation, proposing two original methods for failure probability (metaAL-OIS and eAK-MCS) and one for quantile computation (QeAK-MCS). The three methods rely on surrogate-based (Kriging) adaptive strategies, aiming at refining the so-called Limit-State Surface (LSS) directly, unlike Subset Simulation (SS) derived methods. Indeed, the latter consider intermediate threshold associated with intermediate LSSs to be refined. This direct refinement property is of crucial importance since it enables the adaptability of the developed methods for RBDO algorithms. Note that the proposed algorithms are not subject to restrictive assumptions on the LSS (unlike the well-known FORM/SORM), such as the number of failure modes, however need to be formulated in the Standard Space. The eAK-MCS and QeAK-MCS methods are derived from the AK-MCS method and inherit a parallel adaptive sampling based on the weighted K-Means algorithm. MetaAL-OIS features a more elaborate sequential refinement strategy based on MCMC samples drawn from a quasi-optimal ISD. It additionally proposes the construction of a Gaussian mixture ISD, permitting the accurate estimation of small failure probabilities when a large number of evaluations (several millions) is tractable, as an alternative to SS. The three methods are shown to perform very well for 2D to 8D analytical examples popular in structural reliability literature, some featuring several failure modes, all subject to very small failure probability/quantile level ($O(10^{-5} - 10^{-9})$). Accurate estimations are performed in the cases considered using a reasonable number of calls to the performance function (15-150). The second part of this work tackles original Robust Optimization (RO) methods applied to the Shape Design of a supersonic ORC Turbine cascade. A comprehensive Uncertainty Quantification (UQ) analysis accounting for operational, fluid parameters and geometric (aleatoric) uncertainties is illustrated, permitting to provide a general overview over the impact of multiple effects and constitutes a preliminary study necessary for RO. Then, several mono-objective RO formulations under a probabilistic constraint are considered in this work, including the minimization of the mean or a high quantile of the Objective Function. A critical assessment of the (Robust) Optimal designs is finally investigated.

Université Paris-Saclay
Espace technologique / Immeuble Discovery
Route de l'Orme aux Mérisiers, RD 128/91190 Saint-Aubin, France